CHARACTERIZATION OF THE STRAIN HARDENING RESPONSE OF AMORPHOUS POLYMERS

by

Ellen M. Arruda

B.S., Engineering Science, Pennsylvania State University (1985)
M.S., Engineering Mechanics, Pennsylvania State University (1988)

SUBMITTED IN PARTIAL FULFILLMENT
OF THE REQUIREMENTS FOR THE
DEGREE OF
DOCTOR OF PHILOSOPHY
IN MECHANICAL ENGINEERING

at the

MASSACHUSETTS INSTITUTE OF TECHNOLOGY
May, 1992

Signature of Author _____

Department of Mechanical Engineering
May 21, 1992

Certified by _____

Professor Mary C. Boyce
Thesis Supervisor

Accepted by _____

Professor Ain Ants Sonin, Chairman
Department Committee on Graduate Studies

Characterization of the Strain Hardening Response of Amorphous Polymers

by

Ellen M. Arruda

Submitted to the Department of Mechanical Engineering

on May 21, 1992 in partial fulfillment of the

requirements for the Degree of Doctor of Philosophy in

Mechanical Engineering

Abstract

The term glassy polymers refers to non-crystalline polymeric materials below their glass transition temperatures. Glassy polymers are used extensively in engineering applications which often exploit the anisotropic characteristics which arise during solid phase deformation processing of these materials. Effects of existing anisotropy include the familiar elastic anisotropy as well as several highly anisotropic yield and post yield features such as direction dependent flow strengths, strain hardening characteristics and shape deformation responses. This thesis establishes a thorough experimental study of the evolution of anisotropy during strain hardening in two glassy polymers, polymethylmethacrylate and polycarbonate, with temperature, strain rate, and state of deformation. The effects of initial anisotropy are also extensively investigated through isolation of the individual effects of these same processing variables in further experimental testing of preoriented materials.

Above the glass transition temperature amorphous polymers are in a rubbery state for which their response to large strain deformations contains the characteristic evolution of anisotropy during loading but is essentially elastic. A constitutive model has been developed which fully captures the three dimensional characteristics of the evolving anisotropy in rubbery polymers. This model is then implemented into an existing kinematic framework for the large strain deformation response of glassy polymers and is used with the experiments discussed above to both characterize the evolution of anisotropy in glassy polymers and predict the effects of initial anisotropy in preoriented glassy materials.

Thesis Advisor: Dr. Mary C. Boyce, Associate Professor of Mechanical Engineering

Acknowledgements

The author wishes to thank her thesis advisor, Mary C. Boyce, for her continued support throughout the term of this thesis project, for her superior mentorship skills, for instilling a strong sense of academic ethics, for never compromising thoroughness in favor of a quick turnaround to publication and for her tremendous energy, enthusiasm and input. I would also like to thank my committee members, Professors Ali S. Argon of Mechanical Engineering, E.L. (Ned) Thomas of Materials Science and Engineering and Robert E. Cohen of Chemical Engineering, for their keen interest in my thesis work and for the feedback they've provided at various times throughout my tenure at MIT. The financial support of the MIT Bradley Foundation and The National Science Foundation are also gratefully acknowledged.

To those 007 cellar dwellers and my office collegues, past and present, among them future Nobel Laureates whom it has been my salubrious fortune to have befriended including: Christine Allan, Mehrdad Haghi, Antonis Zavaliangos, Surya Kalidindi, Fred Haubensak, Tresa Pollack, Simona Socrate, and Omar Hasan. Thank you for making the MIT years fun ones.

To my first and closest MIT friend, Naomi Super Fried, for her continued encouragement and expert counseling skills. Our lunchtime therapy sessions were much needed, welcomed escapes from the lab.

I thank the Marlborough Arrudas and their descendents: Marcelle and Tony, Elizabeth and Mark Carlin, John, Tim, Elise and Christine, for their help and support over the past four years. I feel very lucky to be associated with such a close, loving family.

This thesis is dedicated with all my love to my family, Frank and Fran Perkoski, Julianne Perkoski, Alan and Robin Perkoski, and Susan and Tom Hazelton, for always encouraging me to continue in school, for believing in me and for bragging about me to all your friends.

I most especially thank my daughter, Nicole, for almost never getting sick the night before my tests or deadlines, for understanding why Mommy was always going to work, and for being so happy to see me when I returned. Finally to my husband, Tony, the only person who worked harder on my education than I did, to whom I owe this thesis, my PhD degree and my sanity. Thank you for being a wonderful daddy and husband, for your countless weekends with Nicole, trips to the grocery store, and cancelled engagements owing to my impossible schedule, and for doing it all without a single complaint, ever. I love you.

Contents

Chapter 1

Introduction

Solid phase deformation processing refers to a range of operations which together constitute one of the most widely used methods for producing glassy polymer components. These important manufacturing operations utilize the strengthening features associated with large deformation processes involving the glassy polymer in the solid state. Conventionally the polymer processing operation has been optimized by a costly, trial-and-error procedure because of the lack of full understanding of polymer deformation behavior. The three dimensional evolution of anisotropy has not previously been investigated beyond strain levels associated with yield. No thorough investigation of the evolution of anisotropy during strain hardening and the effects of anisotropy on polymer behavior has previously been undertaken.

The aim of this thesis is two-fold: An extensive experimental study was conceived and undertaken which isolated the evolution of anisotropy during straining of initially isotropic materials and identified effects of initial anisotropy on the response of two preoriented glassy polymers, polycarbonate (PC) and polymethylmethacrylate (PMMA). Secondly, this thesis is concerned with modelling of the three dimensional effects of evolving and existing anisotropies during large strain deformation processes. The use of state variables in a physically based constitutive model of large strain glassy polymer behavior was explored.

Central to the modelling of the glassy polymer response is the notion that the clues to the mechanisms of developing anisotropy in the glassy polymer can be inferred from the statistical mechanics of rubber elasticity provided the rubber elasticity theory correctly provides for three dimensional anisotropic effects. In Chapter 2 the rubber elasticity literature is reviewed for the purpose of evaluating the ability of existing rubber deformation models to predict the three dimensional effects of rubber materials. Finding none to satisfy the criteria of being (i) physically based, (ii) requiring a minimal number of material properties and (iii) capturing the three dimensional aspects of rubber deformation, a new model of rubber deformation is developed. The discussion of this model emphasizes its ability to characterize and predict the large strain deformation response of several commercially available rubber products in ad-

dition to data in the literature.

Chapter 3 includes isothermal experiments on initially isotropic PC and PMMA which illustrate the evolution of anisotropy with plastic straining in these glassy polymer materials. The rubber deformation model developed in Chapter 2 is used within an existing kinematic framework for the large strain deformation of glassy polymers to predict the experimentally observed development of anisotropy in glassy polymers during strain hardening. The effects of initial anisotropy in glassy polymers include the well known effects on the elastic constants of these materials. Chapter 4 details the effects of initial anisotropy on the yield and subsequent large strain response of preoriented glassy PC. Extensive three dimensional experimental results on preoriented PC are presented and discussed. The rubber elasticity model implemented into the isotropic glassy polymer deformation model in Chapter 3 is used in Chapter 4 to predict the experimentally obtained anisotropic effects.

The effects of strain rate and temperature on the strain hardening response of glassy PC and PMMA are investigated in Chapter 5. Experimental testing over a range of strain rates and temperatures which included isothermal and approximately adiabatic test conditions isolate the temperature and strain rate effects. Once again testing of preoriented materials is used to gather great insight into the nature of the influence of temperature and strain rate on the observed stress-strain responses of these glassy polymers. The glassy polymer model of the preceeding chapters is modified in Chapter 5 to include the effects of strain rate and temperature on the response of PC and PMMA.

Chapter 6 briefly summarizes the work presented in this thesis, highlighting the significance of the results obtained and suggesting future efforts in polymer deformation and processing problems.

Chapter 2

The State of Deformation Dependence of Rubber Elastic Materials

Mathematical models which attempt to describe the stress-stretch relation for rubber elastic materials can be classified as either of the phenomenological invariant-based approach or the statistical mechanics approach. The well-known models which will be discussed herein have been used to describe nonlinear rubber elastic deformation with various degrees of success, however most fail to fully capture the response of a macromolecular network under different states of deformation. Treloar [1], in a review of the phenomenological models, was prompted to write that any of the invariant-based models 'which deviate from statistical mechanics should take into account the properties of a rubber not only in simple extension and compression, but also in other types of strain'. Advancements in the fifteen years since have failed to produce either invariant or statistical mechanics-based models with the sophistication to simply and accurately capture this tensorial characteristic.

In this Chapter, we briefly review many of the existing models for rubber elastic deformation which vary greatly in both conceptual and mathematical complexity. In our evaluation of the existing statistically based models we acknowledge that such models provide a basis for the appearance of physically mimicing a macromolecular structure. These are compared to the rubber deformation data of Treloar [2] for a vulcanized material in uniaxial extension, biaxial extension and pure shear, and are shown to be unable to accurately account for the polymer behavior under different states of deformation. The earlier review of rubber elasticity by Treloar [1] showed most invariant-based models to also fail in this regard with the exception of the empirical six-parameter Ogden [3] model. We repeat this observation of the ineffectiveness of the invariant based models in predicting the correct state of deformation dependence for purposes of completeness. Our additional discontent with these models is the absence of a physical description of deformation mechanisms associated with

the invariant based models. We then propose a new model to capture the direction dependent strain hardening response of rubbery polymers and compare its ability to describe nonlinear rubber elastic deformation against the existing models described earlier and against Treloar's experimental data.

The last section of this Chapter investigates the state of deformation dependence of three commercially available rubber products: neoprene, gum and silicone rubber. Results of our experimental tests on these materials in uniaxial compression and plane strain compression are presented. The eight chain model proposed and developed in this Chapter is shown to correctly predict the state of deformation dependence of all three materials over the entire range of deformation of the materials. The usefulness of this model is seen to result from its requiring one test to determine two physically based properties of the rubber in order to fully characterize rubber deformation.

2.1 Review of invariant based models

Excellent historical perspectives of the phenomenological invariant-based models have been given by Treloar [4,1]. The original theories of this genre were aimed at obtaining an expression for the network deformation response in terms of general stretches. Eventually it was accepted by investigators in this field that such an approach would have to yield an expression for the elastic strain energy which is of the form dictated by continuum mechanics as concerns an initially isotropic, incompressible, hyperelastic solid. The restricted form for the strain energy is

$$W = \hat{W}(\lambda_1, \lambda_2, \lambda_3) \tag{2.1}$$

where the λ_i are the principal stretches. The following independent functions of the stretches, which are constant under an orthogonal transformation and fully describe the system, are therefore called stretch invariants.

$$I_1 = \lambda_1^2 + \lambda_2^2 + \lambda_3^2 \tag{2.2}$$

$$I_2 = \lambda_1^2\lambda_2^2 + \lambda_2^2\lambda_3^2 + \lambda_1^2\lambda_3^2 \tag{2.3}$$

$$I_3 = \lambda_1^2\lambda_2^2\lambda_3^2 \tag{2.4}$$

Incompressibility, generally taken to hold for rubbers, requires that I_3 retain the value of

$$I_3 = 1 \tag{2.5}$$

Consequently the general form for the strain energy may be written as

$$W = \hat{W}(I_1, I_2) \tag{2.6}$$

The persistent invariant based theories are usually written in a form which follows directly from Equation 2.1 or 2.6 and represents a specific case of these forms. The most prominent theories are discussed below.

2.1.1 Mooney-Rivlin

An analysis by Rivlin [5] which was loosely based on continuum mechanics postulates showed that the earlier result of Mooney [6] is actually the most general first-order expression for strain energy in I_1 and I_2 as prescribed by Equation 2.6. Rivlin's treatment of Mooney's result gives

$$W = C_1(I_1 - 3) + C_2(I_2 - 3) \tag{2.7}$$

where the constants C_1 and C_2 are the two parameters of the model. A deformation test in which one invariant is held constant while the other is varied systematically with strain would yield values for C_1 and C_2 if they were indeed constants as originally formulated in the Mooney-Rivlin model. Experiments by Obata, Kawabata and Kawai [7] showed C_1 and especially C_2 to vary with both I_1 and I_2 when the strain energy is forced to follow the form of Equation 2.7.

2.1.2 Ogden

Ogden [3] pointed out that while Rivlin's analysis was rigorously correct for treating mathematical abstractions it was unnecessarily restrictive for describing actual physical systems. Ogden proposed a strain energy function of the form

$$W = \sum_n \frac{\mu_n}{\alpha_n}(\lambda_1^{\alpha_n} + \lambda_2^{\alpha_n} + \lambda_3^{\alpha_n} - 3) \tag{2.8}$$

in which the μ_n and the α_n are constants and may have any values including non-integer values. The degree of the sum may be adjusted as needed to fit the data at hand. The model easily lends itself to be tailored in this manner; reasonable fits to data from three states of deformation have been achieved by Ogden [3] for $n \geq 3$ in which case the minimum number of independently adjustable parameters is six. Here, data from all three states of deformation must be used to fit the six parameters.

2.1.3 Valanis-Landel

These investigators posed in Valanis and Landel [8] that the form for the elastic strain energy should be separable functions of the stretches.

$$W = \sum_{i=1}^{3} w(\lambda_i) \tag{2.9}$$

The three functions $w(\lambda_i)$ are all of the same form although a satisfactory analytic expression for the form of the $w(\lambda_i)$ was not given by the authors. As proposed the model did not contain adjustable parameters per se, any biaxial test in which one of the stretches could be held at a constant value while another varied was used to experimentally characterize the data as $(\lambda_i, w(\lambda_i))$ pairs for $\lambda_j = constant$, $j \neq i$.

2.1.4 Comments on these models

The phenomenological theories lack a direct physical connection to the mechanisms of deformation. Furthermore these models either do not fit even uniaxial extension data, as in the case of Equation 2.7, or lack the connection to real structural descriptors which would enable them to be useful under conditions of complex loading during deformation as occurs in processing operations.

The Ogden [3] model is quite complex, and although it has been shown to best capture the state of deformation dependence of rubber materials for the entire range of stretches except near the limiting stretch regimes, to do so the model requires six parameters completely devoid of physical insight into the mechanics governing that state of deformation dependence. Appendix A gives the stress-stretch relationships in uniaxial extension, biaxial extension and pure shear for the Mooney-Rivlin and Ogden models. The model constants used to fit published data by Treloar [2] are also reported in Appendix A. It is instructive to note that with the first four parameters listed in Appendix A for the Ogden model the uniaxial data is well fit, but the biaxial response predicted does not differ from the uniaxial prediction beyond a stretch of $\lambda = 4.0$. The model requires data from more than one state of deformation in order to determine the number of terms and their parameters needed to capture the state of deformation dependence. Upon searching for an analytical description for the $w(\lambda_i)$ functions in the Valanis-Landel model, Treloar [1] found that the form was one which simply reduces to the Ogden model with six parameters. The Valanis-Landel model was also shown to be accurate in the low to moderate stretch regions for empirically capturing the deformation response of many rubber materials using the six parameters of Ogden plus an adjustable rubbery modulus.

2.2 Statistical mechanics approaches to rubber deformation

Historically, the statistical mechanics models which have approached the ability to capture the tensorial response of polymers have also approached prohibitively difficult mathematical complexity. The statistical models will be described in terms of their strain energy formulations where possible both for comparison with the phenomenological theories discussed above and also because the stress-stretch relations are easily formulated from the strain energy when the strain energy has an analytic form. The stress-stretch relations for these models are given in Appendix A for the three states of deformation contained in Treloar's 1944 data. Model parameters used to fit this data are also given.

The first statistical mechanics approach to describing the force on a deforming polymeric network assumed Gaussian statistics to apply, that is the chains never approached their fully extended length $r = lN$ where N is the number of statistical

links of length l in the chain between chemical crosslinks. Gaussian statistics yields

$$W = \frac{1}{2}G(\lambda_1^2 + \lambda_2^2 + \lambda_3^2 - 3) \qquad G = nk\Theta \tag{2.10}$$

for the strain energy where the rubbery modulus G is a function of the chain density, n, Boltzmann's constant, k, and temperature, Θ. Using the form given by Equation 2.6 the strain energy is written

$$W = C_1(I_1 - 3) \qquad C_1 = \frac{nk\Theta}{2} \tag{2.11}$$

The use of networks comprised of chains which are essentially described by Equation 2.10 has been the focus of investigators using the statistical mechanics approach to rubber elasticity. The various models to be described in this section originally took the Gaussian chain of Equation 2.10 as a building block in a rubber network; the ends of chains such as this then formed the junction points of the network. In building models the networks have been comprised of three, four or an infinite number of chains. Network junction points have been commissioned to deform affinely with the imposed deformation of the material or given the phantom characteristic of free vibration with which to statistically sample space without impinging on other chain regions. In many of the models, the chain statistics themselves have been modified to allow larger stretches than are afforded by the assumptions of Gaussian statistics. Many of the statistical mechanics models have been discussed by Mark and Erman [9] also by Treloar [4] and will be outlined below for purposes of historic perspective and later comparison with a new model and experimental results.

2.2.1 Wang and Guth

The Wang and Guth [10] network consists of three orthogonal non-Gaussian chains which deform affinely with the imposed bulk deformation. This system is sketched in Figure 2.1 for (a) undeformed, (b) uniaxial extension and (c) biaxial extension load geometries. Wang and Guth employed Langevin statistics to account for large stretch behaviors, the principal stress-stretch relations for the network have the form

$$\sigma_1 - \sigma_2 = \frac{nk\Theta}{3}\sqrt{N}\left(\lambda_1\mathcal{L}^{-1}\left\{\frac{\lambda_1}{\sqrt{N}}\right\} - \lambda_2\mathcal{L}^{-1}\left\{\frac{\lambda_2}{\sqrt{N}}\right\}\right) \tag{2.12}$$

where σ_1 is the stress in the chain along the 1 direction, λ_1 is the stretch in the same chain, the subscript 2 similarly refers to the quantities in the 2 direction, N is the number of rigid statistical links between crosslinks, and $\mathcal{L}^{-1}\left(\frac{\lambda_i}{\sqrt{N}}\right)$ is the inverse Langevin function for $i = 1, 2$ or 3 defined by

$$\mathcal{L}(\beta) = \coth\beta - \frac{1}{\beta} \qquad \mathcal{L}^{-1}\left(\frac{\lambda_i}{\sqrt{N}}\right) = \beta \tag{2.13}$$

The functional dependence of the inverse Langevin on λ_i is such that the function asymptotically increases as the stretch in the i_{th} chain, λ_i, approaches its limiting, or locking stretch, value $\lambda_L = \sqrt{N}$. The individual principal stresses are resolved for any particular state of deformation by the boundary conditions and by incompressibility, Equation 2.5. The approximate strain energy is calculated from the first three terms of the Wang and Guth [10] expression for the probability distribution function as

$$W = nk\Theta \left[b_1 \frac{I_1}{3} + b_2 \frac{\left(I_1^2 - 4\frac{I_2}{3}\right)}{5} + b_3 \frac{\left(I_1^3 - 12\frac{I_1 I_2}{5}\right)}{7} + C \right] \tag{2.14}$$

where the coefficients b_1, b_2 and b_3 are functions of the number of statistical links, N, and C is a constant. Additional terms include higher order functions of I_1 and I_2. This expression reduces to a form equivalent to Equation 2.10 for Gaussian chains. The model simply requires two parameters, the rubbery modulus and the chain locking stretch parameter defined by specifying λ_L or N.

2.2.2 Flory and Rehner

A four chain regular tetrahedron model was proposed by Flory and Rehner [11] for Gaussian chains linked together at the center of a right regular tetrahedron initially. The chains' free ends formed the corners of the tetrahedron and deformed affinely. This network model is sketched in Figure 2.2 for undeformed and deformed configurations. If the junction point is stationary then the deformation is affine and the strain energy of this system of Gaussian chains is functionally equivalent to that given by Equation 2.10. Treloar [12] further explored this system for the case of non-Gaussian chains and allowed the central junction point of the network to deform non-affinely. The model requires two parameters which represent the rubbery modulus and the network locking stretch. An explicit expression for the strain energy is not given for this case since during non-affine deformation of the junction point its position of maximum probability density is not at the center of the deforming tetrahedron and can not be easily described analytically. Because the network is not affine, the strain energy of this system of Langevin chains can not be described in terms of a functionally equivalent form to Equation 2.14.

Our analysis of the four chain model followed an earlier method by Treloar [13] which allowed the 'floating' junction point to seek an equilibrium position for affine displacements of the tetrahedron corners. Equilibrium was found in the present study for the condition of no net force on the junction point using an iterative Newton scheme, the stress-stretch relations were determined numerically at each stretch increment once equilibrium was achieved for that increment. The present treatment uses the floating junction point numerical formulation to simulate the response of the four chain network. Analytical stress-stretch expressions for the four chain model included are in Appendix A for the condition of a *stationary* junction point.

2.2.3 Flory and Erman

Flory and Erman [14] consider a network in which the chain junction points are constrained from a phantom characteristic via interactions with other chains. The elastic strain energy of the network is found from the sum of phantom and constraint contributions

$$W = W_{ph} + W_c \tag{2.15}$$

where W_{ph} of phantom Gaussian chains is

$$W_{ph} = \frac{1}{2}\xi k\Theta(I_1 - 3) \tag{2.16}$$

Note that Equation 2.16 differs from Equation 2.10 by the parameter ξ where

$$\xi = \left(1 - \frac{2}{\phi}\right) n \tag{2.17}$$

The parameter n is the number of network chains and ϕ is the number of chains meeting at a junction. When $\phi = 4$ the junction is tetrafunctional and the strain energy of the phantom network in Equation 2.16 is one-half of the affine strain energy in Equation 2.10. The contribution of constraints to the free energy is given as

$$W_c = \frac{1}{2}nk\Theta \sum_i [B_i + D_i - \ln(B_i + 1) - \ln(D_i + 1)] \tag{2.18}$$

for

$$B_i = \kappa^2(\lambda_i^2 - 1)(\lambda_i^2 + \kappa)^{-2} \tag{2.19}$$

$$D_i = \lambda_i^2 \kappa^{-1} B_i \tag{2.20}$$

and where κ is a measure of the strengths of the constraints which depends on the relative sizes of free (phantom) fluctuations and actual constrained fluctuations. This model depends on the parameters n, ϕ and κ. In it $\kappa \to \infty$ for completely constrained junctions and $\kappa \to 0$ in the phantom chain limit, n can take on any large, positive value and ϕ must be greater than two.

2.2.4 Edwards and Vilgis

These investigators assume that the chains in a rubber never approach their fully extended lengths during deformation and use an entanglement network to describe a primitive path which evolves with stretch and does reach full extension in Edwards and Vilgis [15].

$$W = \frac{1}{2}N_c k\Theta\left[\frac{\sum_{i=1}^{3}(1-\alpha^2)\lambda_i^2}{1-\alpha^2\sum\lambda_i^2} - \log(1-\alpha^2\sum_{i=1}^{3}\lambda_i^2)\right] + \frac{1}{2}N_s\left[\sum_{i=1}^{3}\left(\frac{\lambda_i^2(1+\eta)(1-\alpha^2)}{(1+\eta\lambda_i^2)(1-\alpha^2\sum\lambda_i^2)} + \log(1+\eta\lambda_i^2)\right)\right] - \frac{1}{2}N_s\sum_{i=1}^{3}\left[\log(1-\alpha^2\sum\lambda_i^2)\right] \quad (2.21)$$

Here the four parameters are α, a measure of the inextensibility of the network, η, a slippage measure, N_c, the number of crosslinks and N_s, the number of sliplinks.

2.2.5 Comments on these models

The three chain model of Wang and Guth and the four chain tetrahedron of Flory and Rehner provide for a three-dimensional representation of the stress-stretch relations. These models appear to provide a basis for physically mimicing a real polymer macromolecular network. The three chain model does not exhibit the cooperative nature of chain deformations which must be characteristic of real networks but is instead dominated by the behavior of the chain having the greatest extension. The four chain tetrahedron model with the moving junction point captures the cooperative nature of network deformation but shows a marked deviation from initial orthogonal symmetry especially for short chains, Treloar [13], and therefore exhibits a strong dependence on loading direction as well as loading state. Flory and Rehner also recognized the anisotropy of their proposed four chain network and recommended averaging the results of all possible network orientations to relieve this deficiency. The Flory-Erman model uses Gaussian statistics for the phantom chain contribution which does not allow the stretches to reach those associated with fully extended chains. The contribution of the constraints as modelled by Flory and Erman results in a form for the total strain energy which is actually quite similar functionally to the non-Gaussian affine networks for which the first three terms are described by Equation 2.14. The Flory-Erman approach succeeds in describing a network which is without an initial direction dependence unlike the four chain model. Their truly initially isotropic network is achieved at the expense of a third parameter, κ, which is difficult to characterize and adds mathematical complexity as well as physical ambiguity to modelling efforts. Finally in the Edwards and Vilgis model the assumption that the chains do not fully extend is not valid for the short polymer networks. Note the similarity in form of Equation 2.21 to the Flory-Erman model and also to Equation 2.14. In this case the model requires four parameters.

Comparisons of the strain energy expressions of Wang and Guth, Flory and Erman, and Edwards and Vilgis reveal that the latter two expressions are similar to what one may achieve by properly weighting the coefficients b_1, etc. in the Wang and

Guth strain energy expression (Equation 2.14 + higher order terms) in order that certain functions of the invariants dominate. This is reminiscent of earlier empirical attempts to improve the Mooney-Rivlin formulation by adding higher order terms in I_1 and/or I_2 to the strain energy, see for example Treloar [4]. The proper weighting of the invariants required to obtain the best fit may be achieved by: an empirical fit which returns the problem to the methods of the invariant based models; the addition of parameters connected to the physics of the deformation; or by an educated choice for a simple network configuration which will retain a two parameter description and provide an initially symmetric network. This third approach will yield a truly useful constitutive model provided the mathematical complexity of the resulting model does not increase. The next section describes such a model.

2.3 Proposed "eight" chain model

2.3.1 Requirements of a model

The existing models referenced above have merit and are frequently used in treating rubber deformation problems. Many of the early models capture the 'S'-shaped load versus stretch curve exhibited by rubber materials in uniaxial tension. A relative dearth of experimental evidence exists in the literature for the response of rubbers in other deformation states up to very large stretches save for the work of Treloar [2], in uniaxial extension, biaxial extension and shear, considered by many to be the quintessential rubber data[1], and the extensive biaxial experiments of Jones and Treloar [16]. Consequently, many of the existing models fail the task of describing the response of a rubber material under different states of deformation without changing the model parameters. In other cases the models are prohibitive in the number of parameters required to fit the data or the mathematical complexity they represent. The need for a constitutive relationship which possesses mathematical simplicity, requires one test to characterize the material and has a limited number of parameters has prompted the development of the following model.

2.3.2 Langevin chain statistics

The statistical mechanics approach to rubber elasticity models the rubber chain segment between chemical crosslinks as a number N of rigid links of equal length l. The rigid link is that segment length of the actual chain which undergoes rigid body motion in response to an imposed strain, depending on the actual rubber material the statistical rigid link may span one or several repeat molecular units. The initial

[1]Some debate has persisted over whether the characteristic upturn in the observed stress-stretch behavior is solely due to crystallization and therefore, not present in all rubbers. In this Chapter we offer additional experimental results on three rubber materials which exhibit the same basic, characteristic behavior as that of Treloar's data.

chain length is taken from a random walk consideration of N steps of length l, and is denoted r_0.

$$r_0 = \sqrt{N}\, l \tag{2.22}$$

The fully extended chain has approximate length lN so that the limiting extensibility (or chain locking stretch), defined as the final length divided by initial length, is given in terms of the statistical parameters as $\lambda_L = \sqrt{N}$. At any value of chain length the most probable angular distribution of rigid links about the chain vector length may be found. Following the use of Langevin statistics by Kuhn and Grün [17], the probability of the most probable link angle distribution about a given vector length is taken to be equal to the probability of that vector length. The chain vector length is denoted r_{chain}. In this way Kuhn and Grün obtain an expression for the probability density function for chain lengths and subsequently the configurational entropy of a stretched chain of current length r_{chain}

$$s_{chain} = k\left[c - N\left(\frac{r_{chain}}{Nl}\beta + \ln\frac{\beta}{\sinh\beta}\right)\right] \tag{2.23}$$

where c is a constant, k is Boltzmann's constant and β is the inverse Langevin function, $\beta = \mathcal{L}^{-1}\left[\frac{r_{chain}}{Nl}\right]$, for the Langevin function defined as $\mathcal{L}[\beta] = \coth\beta - \frac{1}{\beta}$. The use of Langevin statistics properly accounts for the limiting chain extensibility. The work of deformation is proportional to the entropy change on stretching the chains from the unstretched state and may be written in terms of the chain length as:

$$W = nk\Theta N\left(\frac{r_{chain}}{Nl}\beta + \ln\frac{\beta}{\sinh\beta}\right) - \Theta c' \tag{2.24}$$

where n is the chain density, c' is a combination of constants and the remaining terms are as defined previously. The material is considered to be incompressible and the principal stresses can be determined from the work of deformation to within an arbitrary pressure, p,

$$\sigma_i = \lambda_i\frac{dW}{d\lambda_i} + p\,, \tag{2.25}$$

where the λ_i are the principal stretches and the pressure may be determined from the boundary conditions. The stress–stretch relations are frequently written in terms of the difference in two principal stresses to eliminate the pressure term.

$$\sigma_1 - \sigma_2 = \lambda_1\frac{dW}{d\lambda_1} - \lambda_2\frac{dW}{d\lambda_2} \tag{2.26}$$

2.3.3 Use of Langevin chain networks

The use of Langevin chain statistics in networks has been considered by Wang and Guth [10] in their three chain model and by Treloar [12] in his extension of the tetrahedron model of Flory and Rehner [11]. Treloar [4] and later Treloar and Riding [18] also considered a model of a large assembly of chains which were averaged by integrating over many spatial orientations. Analytical results of non-Gaussian three chain, tetrahedron and total assembly of chains models are presented in Treloar [4] for uniaxial tension.

These models were also previously considered for their general predictive capabilities of the characteristic 'S'-shaped uniaxial response by Treloar [4]. He observed that the response of the tetrahedron model was slightly dependent upon the orientation of the volume element with respect to the extension direction. In their 1952 paper, Wang and Guth [10] stipulated that the faces of the three chain cube element be aligned with the principal stretch space during deformation. Treloar [4] concluded that these models possess an inherent anisotropy which could be eliminated by a system of a large assembly of chains, each of length equal to the root-mean-square chain length, $r_0 = \sqrt{N}\, l$, which occupy random orientations in space. In this manner the contributions from chains in several orientations may be averaged to give the overall response. His proposed total assembly of chains model requires integration over the distribution of chains for each subjected stretch state, a procedure which was mathematically prohibitive fifteen years ago and remains cumbersome today.

We agree with Treloar's assessments of the existing network models except for his reluctance to restrict the orientation of a model to some specific relationship with respect to principal stretch space as Wang and Guth had done. Motivated by Treloar's assertion to present a model which averages several spatial orientations, but recognizant of the need for a mathematically concise representation, we have proposed a model which possesses the cubic symmetry of principal stretch space as it averages eight orientations of that space in determining the network response. The clear advantage of this technique is its ability to simulate a true network response of cooperative chain stretching which presents a clear picture of the deformation process with mathematical ease.

2.3.4 Proposed model geometry

The proposed model considers eight orientations of chains in space which may be envisioned by the eight chain network system sketched in Figure 2.3 for undeformed, uniaxial extension and biaxial extension loaded configurations. The chain length, r_{chain}, is sought for each of the chains in the eight chain model as a function of the imposed principal global stretches λ_1, λ_2, λ_3 in order that Equation 2.24 may be differentiated to obtain the stress-stretch relations of Equation 2.26. Consider the cube containing the eight chain configuration in Figure 2.4. The cube edges are taken

to remain aligned with principal stretch space during deformation, chains linked at the center of the cube extend to the eight corners. In principal space the cube is allowed expansion along each principal direction subject only to incompressibility which may be expressed as

$$\lambda_1\lambda_2\lambda_3 = 1 \tag{2.27}$$

Note that the restriction to principal stretch space does not limit the usefulness of the model to axisymmetric deformations. For example, in pure shear the principal stretches are $\lambda_1 = \lambda$, $\lambda_2 = 1$ and $\lambda_3 = \lambda^{-1}$. The directions in which these stretches act rotate continuously with the deformation and this rotation is monitored by the standard kinematics of finite strain deformation making use of the polar decomposition and subsequent extraction of the stretch tensor eigenvalues from the general deformation gradient tensor. See for example the discussion by Hopkins in Treloar [1] or Fardshisheh and Onat [19]. The eight chain model is always stretched in the principal frame and is in general oriented differently from the laboratory frame. The rationale for use of the model in this manner follows from the consideration that in response to any deformation a principal stretch frame exists and the chains in that reference frame will undergo stretches describable by the principal values of stretch, λ_1, λ_2 and λ_3.

The unstretched network includes eight chains of length $r_0 = \sqrt{N}\,l$ inside a cube of dimension a_0. From this geometry

$$a_0 = \frac{2}{\sqrt{3}} r_0 \tag{2.28}$$

In Figure 2.5 the cube is stretched by $\lambda_1\hat{\imath}$, $\lambda_2\hat{\jmath}$ and $\lambda_3\hat{k}$ so that the cube edges measure $\lambda_1 a_0$, $\lambda_2 a_0$ and $\lambda_3 a_0$ in the $\hat{\imath}$, $\hat{\jmath}$ and $\hat{k}$ directions, respectively. A chain vector from the center of the cube to a corner may be written for one chain as

$$\mathbf{c}_1 = \frac{a_0}{2}\lambda_1\hat{\imath} + \frac{a_0}{2}\lambda_2\hat{\jmath} + \frac{a_0}{2}\lambda_3\hat{k}\,. \tag{2.29}$$

This chain has vector length

$$r_{chain} = \frac{a_0}{2}\left(\lambda_1^2 + \lambda_2^2 + \lambda_3^2\right)^{\frac{1}{2}} \tag{2.30}$$

as do all remaining chains in the given network geometry, regardless of deformation state. Substitution from Equations 2.28 and 2.22 into Equation 2.30 gives the chain length in terms of the statistical parameters and the principal stretches

$$r_{chain} = \frac{1}{\sqrt{3}}\sqrt{N}\,l\left(\lambda_1^2 + \lambda_2^2 + \lambda_3^2\right)^{\frac{1}{2}}\,. \tag{2.31}$$

In this form the expression for the chain vector length is suitable for substitution into Equation 2.24 which with Equation 2.26 yields the following stress–stretch relation for the proposed model

$$\sigma_1 - \sigma_2 = \frac{nk\Theta}{3}\sqrt{N}\,\mathcal{L}^{-1}\left[\frac{\lambda_{chain}}{\sqrt{N}}\right]\frac{(\lambda_1^2 - \lambda_2^2)}{\lambda_{chain}} \tag{2.32}$$

where the chain stretch, $\lambda_{chain} = \frac{r_{chain}}{r_0}$, is the same in each chain and is given by

$$\lambda_{chain} = \frac{1}{\sqrt{3}}\left(\lambda_1^2 + \lambda_2^2 + \lambda_3^2\right)^{\frac{1}{2}} . \tag{2.33}$$

Because each chain in the system undergoes a stretch equivalent to that in every other network chain, the model is likened to averaging the contributions of a single chain over eight spatial orientations.

The expression for chain stretch is seen to reduce to a function of the first stretch invariant, I_1, and Equation 3.23 may be rewritten as

$$\lambda_{chain} = \frac{1}{\sqrt{3}}\, I_1^{\frac{1}{2}} . \tag{2.34}$$

The strain energy of the proposed model may be found from integration of Equation 3.16 using the series expansion form for the inverse Langevin function given for example in Treloar [13]. The first five terms for the strain energy of this model are

$$\begin{aligned} W &= nk\Theta\left[\frac{1}{2}(I_1 - 3) + \frac{1}{20N}(I_1^2 - 9) + \frac{11}{1050N^2}(I_1^3 - 27)\right] \\ &\quad + nk\Theta\left[\frac{19}{7000N^3}(I_1^4 - 81) + \frac{519}{673750N^4}(I_1^5 - 243)\right] + \cdots \end{aligned} \tag{2.35}$$

Note that the strain energy in Equation 2.35 exhibits a nonlinear I_1 dependence as a result of the chain stretch being defined in terms of I_1 only. Debate has persisted in the literature over the presence of the principal stretch invariants I_1 and I_2 in the strain energy function. The role of higher order I_1 type terms in predicting a state of deformation dependence is discussed in Appendix B.

In Rivlin's [5] continuum mechanics approach, the difference in principal stresses of an initially isotropic, incompressible hyperelastic solid is written as the following function of the principal stretch invariants

$$\sigma_1 - \sigma_2 = 2\left[\frac{\delta W}{\delta I_1} + {\lambda_3}^2\frac{\delta W}{\delta I_2}\right]\left({\lambda_1}^2 - {\lambda_2}^2\right) \tag{2.36}$$

Because the strain energy of the eight chain model in Equation 2.35 is a function only of I_1, Equations 2.32 and 2.36 can be directly compared resulting in the following

$$\frac{\delta W}{\delta I_1} = \frac{nk\Theta}{6}\sqrt{N}\,\mathcal{L}^{-1}\left[\frac{\lambda_{chain}}{\sqrt{N}}\right]\frac{1}{\lambda_{chain}} \tag{2.37}$$

The Cauchy stress, $\mathbf{T}$, is related to the left Cauchy-Green deformation tensor, $\mathbf{B}$, as follows [20][2] for a so called Cauchy-Green material in which an expression for the strain energy is assumed to exist

[2]The notation adopted for this section is from the standard continuum mechanics literature which gives $\mathbf{B} = \mathbf{F}\mathbf{F}^{\mathbf{T}}$. In Chapter 3 we define the backstress tensor by the symbol $\mathbf{B}$. Any confusion over the two uses of $\mathbf{B}$ is regretted.

$$\mathbf{T} = \rho_0 \left[\frac{2}{J} \left(\frac{\delta W}{\delta I_1} + I_1 \frac{\delta W}{\delta I_2} \right) \mathbf{B} - \frac{2}{J} \frac{\delta W}{\delta I_2} \mathbf{B}^2 + 2J \frac{\delta W}{\delta I_3} \mathbf{I} \right] \tag{2.38}$$

where ρ_0 is the initial volume, $J = det\mathbf{F}$, and $\mathbf{I}$ is the identity tensor. For an incompressible material, $J = 1$ and this expression reduces to

$$\mathbf{T} = -p\mathbf{I} + 2\frac{\delta W}{\delta I_1} \mathbf{B} - 2\frac{\delta W}{\delta I_2} \mathbf{B}^2 \tag{2.39}$$

and when the form of the strain energy does not include an I_2 dependence as in Equation 2.35, the expression is further reduced. Substitution of Equation 2.37 into Equation 2.39 with $\frac{\delta W}{\delta I_2} = 0$ gives

$$\mathbf{T} = \frac{nk\Theta}{3} \sqrt{N}\, \mathcal{L}^{-1} \left[\frac{\lambda_{chain}}{\sqrt{N}} \right] \frac{1}{\lambda_{chain}} \mathbf{B} - p\mathbf{I} \tag{2.40}$$

Recalling Equation 2.34 where $I_1 = tr\mathbf{B}$, the deviatoric Cauchy stress tensor may be written as

$$\mathbf{T}' = \frac{nk\Theta}{\sqrt{3}} \sqrt{N}\, \mathcal{L}^{-1} \left[\frac{{I_1}^{1/2}}{\sqrt{3N}} \right] \frac{1}{{I_1}^{1/2}} \left(\mathbf{B} - \frac{1}{3} I_1 \mathbf{I} \right) \tag{2.41}$$

The symmetry of the network of "eight" chains with respect to principal stretch directions is the key to the success of this model and is found to greatly reduce the complexity of the strain energy function as compared to the three chain model. The resulting stress-stretch relations are simpler than those obtained for the four chain Flory-Rehner model because the eight chain model effectively reduces to computing the stretch of one single chain. In other words, all chains are found to stretch equally while still satisfying the force equilibrium and incompressibility requirements of the network.

2.4 Comparison of rubber elasticity models with Treloar's 1944 data

The models discussed herein were used to assess their respective abilities to predict the response of a rubber material in two states of deformation based on the model parameters determined by a third deformation state. The data chosen were taken from Treloar [2] and are plotted together as force versus stretch in Figure 2.6. The data include uniaxial extension, equi-biaxial extension and pure shear (plane strain compression)[3]. Except for the Ogden model, each model was fit to the uniaxial

[3]Although described as a pure shear deformation by Treloar [2], these results were actually achieved by the equilavent plane strain deformation state. Treloar reports the maximum principal stretch versus the corresponding normal force, and not the shear force. The simulations of this deformation state follow accordingly; the maximum principal stretch and the force which corresponds to this stretch are calculated as described in Appendix A.

extension data; the constants determined from this fit were then used to simulate biaxial extension and pure shear. The constants needed for each model are listed on the figures corresponding to the results of each model. The model constants are also given in Appendix A which contains the individual stress versus stretch relations for most of the models discussed in this Chapter. In the case of the Ogden model the six parameters were taken from his 1972 paper. Since only the first four constants are needed to predict the uniaxial response it is likely that at least two states of deformation were considered in determining the six model parameters. The results appear in Figure 2.7 for the invariant models of Mooney and Rivlin and of Ogden, Figure 2.8 for the statistical three chain model, Figure 2.9 for the statistical four chain model, Figure 2.10 for the Flory-Erman model and Figure 2.11 for the proposed eight chain model. The Valanis-Landel model was not included because it would give virtually the same results as the Ogden model. The Edwards-Vilgis model was also not included because it is mathematically too complex to easily obtain a good fit using its four parameters.

2.4.1 Explanation of the experimental data

The data on Treloar's vulcanized rubber include tests in uniaxial extension, biaxial extension and pure shear to very large extension ratios and are plotted as load normalized by initial area versus stretch. The strong state of deformation dependence of the large and limiting stretch behavior of the rubbery polymeric network material remains a primary obstacle to true characterization of rubber elasticity. The equi-biaxial extension data in Figure 2.6 varies significantly from either the uniaxial extension or pure shear data. The divergence of the biaxial data is due to the nature of the molecular chain stretching in equi-biaxial extension versus uniaxial extension. Biaxial extension offers two venues of principal tensile stretch ($\lambda_1 = \lambda$, $\lambda_2 = \lambda$, $\lambda_3 = \lambda^{-2}$); an initially isotropic network of chains will reach limiting chain extension due to stretching in both directions providing a planar state of orientation. In uniaxial tensile deformation the chains extend along one direction only ($\lambda_1 = \lambda$, $\lambda_2 = \lambda^{-1/2}$, $\lambda_3 = \lambda^{-1/2}$), additional stretch is thus allotted through the drawing of material from the transverse directions, and the onset of limiting chain extension is delayed with respect to the biaxial deformation locking. The pure shear data are plotted in terms of the maximum principal stretch, λ_1, vs. the corresponding normal force (ie not the shear force) which acts in the direction of λ_1. Pure shear deformation is more closely related to uniaxial extension than to equi-biaxial extension because chain stretch occurs due to stretching along one principal direction ($\lambda_1 = \lambda$, $\lambda_2 = 1$, $\lambda_3 =, \lambda^{-1}$) with chains being drawn from one direction transverse to the extension direction in pure shear. Thus a pure shear experiment yields a limiting stretch value which is similar to that obtained in uniaxial extension. A true constitutive model should be able to capture the observed differences between biaxial and uniaxial tensile behavior as well

as the similarities in behavior between uniaxial deformation and shear.

2.4.2 Explanation of simulations

The results of the invariant model simulations show that the Mooney-Rivlin equation can only be fit to the uniaxial extension data to a stretch of 4.5 at which point the upturn in the characteristic 's' shape of the rubber deformation curve occurs and the first order approximation is no longer valid. The Ogden model provides a good fit to the data for all but the very highest stretches and all three states of deformation are captured by the six parameters used in the Ogden model. Clearly Ogden's approach offers the best fit to the data but it does so with the greatest empiricism.

The three chain model shows no state of deformation dependence beyond a stretch of 4.0 for the three stretch states examined; the results of the simulations for three states of deformation converge at large stretches whereas the data diverge. The failure of the three chain model to capture the state of deformation dependence lies in the absence of a cooperative nature of network chain deformation in this model except through the imposition of incompressibility. In uniaxial extension, depicted in Figure 2.1, the chain parallel to the extension direction stretches until it reaches the locking stretch. The remaining two chain stretches are determined by incompressibility and do not contribute significantly to the force. Under equi-biaxial extension, two coplanar chains extend independently until simultaneously reaching the locking stretch and the third chain stretch is determined by consideration of incompressibility. Therefore the limiting stretch in equi-biaxial extension as predicted by the three chain model has the same value as that obtained in uniaxial extension and in pure shear, the result is convergence of the load vs. stretch predictions for the three different stretch states rather than the actual divergence of these curves which the data shows.

The four chain Flory-Rehner model shows a slight state of deformation dependence at small stretches which is retained at large stretches. This model has some success in predicting a state of deformation dependence because the chains in this network do respond cooperatively to the deformation, see Figure 2.2. Four chains stretch along the extension direction in uniaxial extension resulting in an overall network limiting tensile stretch which exceeds the locking stretch of a single chain ($\lambda_L = \sqrt{N}$). In biaxial extension perpendicular to one chain in the Flory-Rehner tetrahedron the remaining three chains undergo stretching. The result is again increased network extensibility over the single chain limiting stretch to a value which differs from the tensile locking stretch. The different values for locking in uniaxial and biaxial extension are manifested in the load–stretch predictions of the four chain model which reach asymptotes at different values of stretch for different states of deformation.

The four chain model does not possess symmetry with respect to the principal stretch space. The load versus stretch predictions depend upon the orientation of the

four chain tetrahedron with respect to λ_1, λ_2 and λ_3 in addition to the magnitudes of the λ_i.

The Flory-Erman model predicts deformation dependence for stretches below 4.5. The best fit to the Flory-Erman model in uniaxial extension was achieved for a large value for their parameter, κ, the measure of constraint strength. This represents a condition of highly constrained junction points which in the limit of $\kappa \rightarrow \infty$ approaches affine junction points. The model is similar in this case to Gaussian chains with affine junction points, a situation which is also described by the Mooney-Rivlin equation. The restriction of Gaussian statistics on the chain stretches prevents the model from capturing the high stretch regime of any of the deformations. The force-extension expressions given by the Flory-Erman and Mooney-Rivlin models differ in the weighting of I_1 and I_2 type terms hence the actual state of deformation dependence predicted by these models differs. A discussion of the role of the invariants I_1 and I_2 in the state of deformation dependence predicted by the various models addressed here is presented in Appendix B.

The eight chain model is clearly superior to the other statistical models in the state of deformation dependence predicted. Of the models considered here it is rivaled only by Ogden's in terms of overall fit to all of the data. The eight chain model requires two parameters which are mechanistically linked to the physics of the deformation, a rubbery modulus which explicitly accounts for the temperature dependence of rubber elasticity and a network locking stretch. These parameters can be determined from a single test. The advantages of the eight chain model are its proximity in kind to a system which is initially isotropic, the use of Langevin chains which capture the effects of limiting chain extensibility and a network configuration which responds cooperatively to an imposed deformation, thereby physically mimicing the response of an actual networked solid. These features allow for mechanically simulating the state of deformation dependence of the behavior during large deformation while retaining mathematical simplicity. The features of the eight chain model as seen in Figure 2.3 combine the favorable aspects of the previous three chain and four chain network models. The model possesses symmetry with respect to the principal stretch space which was required by Wang and Guth [10] in their discussion. All eight chains stretch uniaxially in response to an imposed uniaxial extension deformation as is true for the four chains in the Flory-Rehner [11] model. Again the limiting network stretch of the eight chain network exceeds the extensibility of a single chain in extension. In biaxial extension all eight chains extend identically due to stretching in two principal directions. The resulting limiting stretch is something other than either the individual chain locking stretch and the limiting stretch in uniaxial extension. A significant feature of the eight chain model is that all chains stretch equally under biaxial extension as well as uniaxial extension. The chain stretch is always the root–mean–square of the global principal stretch state. This unique feature of the eight chain model is true for other deformation states; all chains stretch equally in response

to any given deformation state. The stretch in each chain can be interpreted as an *averaged* stretch and is a function of I_1 but not I_2. Because the chains are Langevin springs higher order I_1 terms appear in the strain energy expression. The importance of higher order I_1 terms in predicting a state of deformation dependence to rubber elastic deformation is discussed in Appendix B.

2.5 Experiments on commercially available rubber products

The uniaxial compression test and plane strain compression test represent near extremes in the behavior of polymeric networks under biaxial deformation states. During uniaxial compression the polymer chains in the material stretch freely in all directions within a plane perpendicular to the load axis. Under plane strain compression the specimen is held within a channel die which completely constrains the material in one direction while allowing expansion in a second direction perpendicular to the first. The material flows along the expansion direction as a result of the compressive load applied perpendicular to the plane containing the constrained and expansion directions. In the plane strain compression die apparatus sketched in Figure 2.12 expansion occurs along the X axis, the material is constrained along the Z axis and Y is the load direction. Polymer network stretching occurs only along the axis of free expansion in plane strain. The resulting stress versus stretch curve in plane strain compression differs from that in uniaxial compression because of the vastly different chain stretch behaviors in these two compression geometries.

Three commonly available rubber materials were chosen for this study: silicone rubber (40 durometer), neoprene rubber (60 durometer) and gum rubber (hardness unknown)[4]. Uniaxial cubes of length 12 mm and plane strain specimens measuring 12 mm×9 mm×12 mm were cut from these materials. In the plane strain compression tests the 9 mm dimension was constrained. Uniform deformations on the order of -200% strain were achieved in uniaxial compression and -150% strain in plane strain compression. The specimen (and die, in the case of plane strain) was placed between flat plates on the ends of the load train on an Instron model 1350 servohydraulic testing machine. Liberal lubrication was applied on all specimen surfaces in contact with plates or die walls to insure uniform deformations; a MoS_2 based paste made by Dow Corning was deemed sufficient for lubricating these materials. Linear ramp tests were performed on all three materials for both deformation states at displacement rates of approximately 1 mm/second. The load and displacement output responses of the testing machine were converted to digital signals by a Kiethly A/D board then transferred to a Macintosh personal computer for storage. The raw load versus displacement data were corrected for the testing machine compliance before

[4]These three materials were obtained at the Greene Rubber Company of Cambridge, MA.

being converted to nominal load (that is, load divided by initial area) versus stretch information. The results of ramp tests in uniaxial compression and plane strain compression are presented in Figures 2.13, 2.14, and 2.15 for silicone, gum and neoprene rubber, respectively. Each of the three materials shows the basic characteristic response of a limiting stretch which is dependent upon the state of deformation. The three materials differ significantly in their initial moduli and/or locking stretch values.

The proposed model was used to predict the plane strain compression responses of the three materials examined in this study based on the constants derived from their corresponding uniaxial compression responses. Results of these simulations appear in Figures 2.16, 2.17 and 2.18 for the silicone, gum and neoprene rubber materials previously described. The model parameters used to fit the uniaxial compression data are listed for each material on the corresponding figure. The model accurately captures the state of deformation dependence of all three materials. Each of these materials differs in the modulus and/or locking stretch value needed by the model to fit the uniaxial compression response. A direct comparison of the uniaxial compression responses of the three materials has been made in Figure 2.19, here the differences in actual material moduli and limiting extensibilities are easily seen. Including Treloar's data the model has been shown to characterize four materials representing a range of material properties. Previous network models considered contained the same basic parameters of an initial modulus and a measure of finite extensibility, but were unable to predict a state of deformation dependence because of inabilities of the models to effectively represent a network response. In the case of the eight chain model the successful prediction is a result of correct usage of the finite extensibility parameter as that of an averaged measure of applied stretches over eight spatial orientations. The mathematically tractable eight chain model of Equation 3.16 represents a true constitutive relationship for rubber deformation which is able to correctly account for the large stretch deformation response in one state of deformation, then with that characterization, predict other states of deformation.

2.6 Summary

A physically based constitutive model for large stretch rubber deformation has been proposed in this Chapter which has been specifically designed to account for the three dimensional state of deformation dependence in networked solids. The eight chain model presented here is formulated such that the nature of the state of deformation dependence is clearly seen to be the result of a network of chains reaching the individual chain extensibility limit at different imposed global stretch levels for different stretch states. The eight chain model successfully accounts for the state of deformation dependence using a rubbery modulus and a locking stretch as its only two parameters, both of which can be determined from a single experiment. Present in all statistical models, these parameters are physically linked to the polymeric network

and therefore provide a basis for including other aspects of rubber elastic behavior such as temperature dependence, swelling and Mullin's effect. Indeed, the rubbery modulus term explicitly includes temperature.

Experiments were conducted on three rubber materials to illustrate the state of deformation dependence of these materials and to determine the predictive capability and effectiveness of the proposed model. In addition the model was compared to existing rubber elasticity models in the ability to capture the response of data in the literature, Treloar [2], in three states of deformation. The eight chain model was shown to be superior in its overall ability to successfully account for the three dimensional nature to the underlying mechanics of network solid deformation for a total of four materials representing a range in material hardnesses and extensibilities.

The eight chain model contains many attractive features of concern in modelling the complicated deformation procedures involved in the finite straining of amorphous polymeric solids. It retains mathematical feasibility as a two parameter model and also contains the ability to respond to an imposed deformation state in a manner which simulates the actual mechanism governing the state of deformation response of rubber materials. This model is expected the accurately capture the state of deformation dependence on the strain hardening response of amorphous polymers below their glass transition temperatures. In the next Chapter the eight chain rubber elasticity model developed here will be implemented into an existing framework for the large strain deformation dependence of glassy polymers to determine whether it indeed captures this same tensorial dependence on deformation seen for materials in the glassy state.

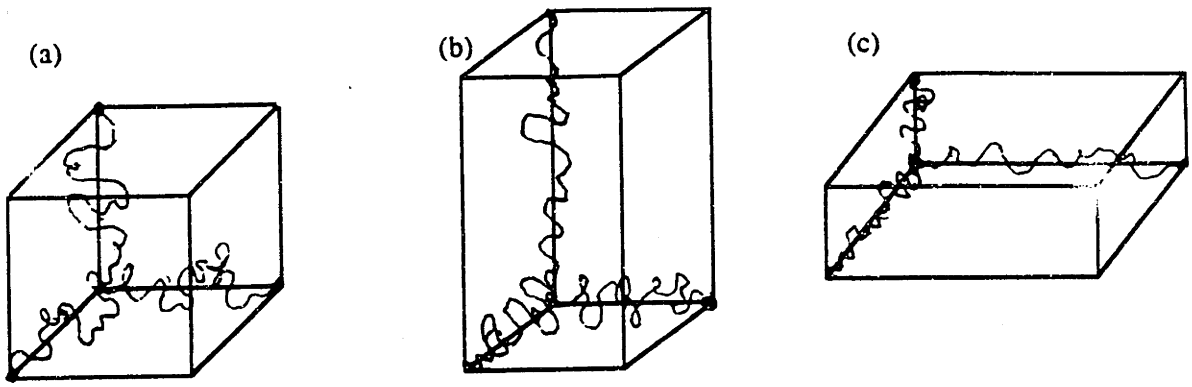

Figure 2.1: Three chain rubber elasticity model for (a) undeformed, (b) uniaxial extension and (c) biaxial extension configurations.

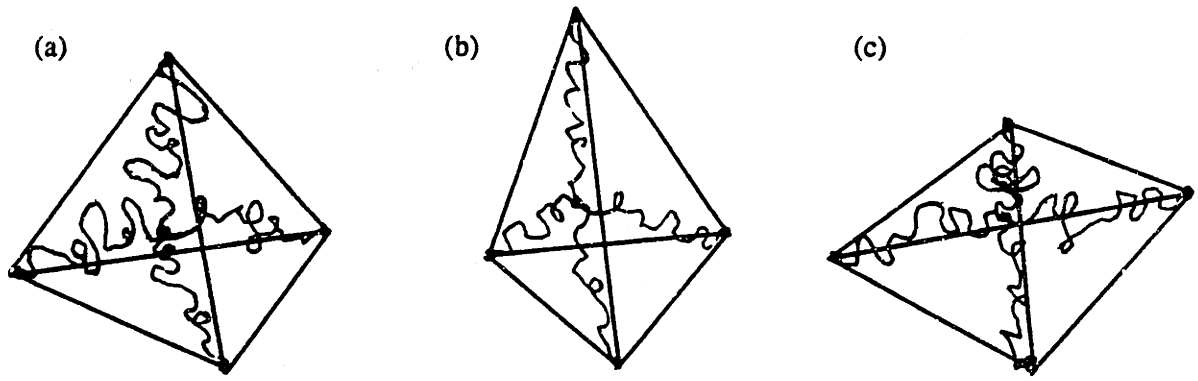

Figure 2.2: Four chain rubber elasticity model for (a) undeformed, (b) uniaxial extension and (c) biaxial extension configurations.

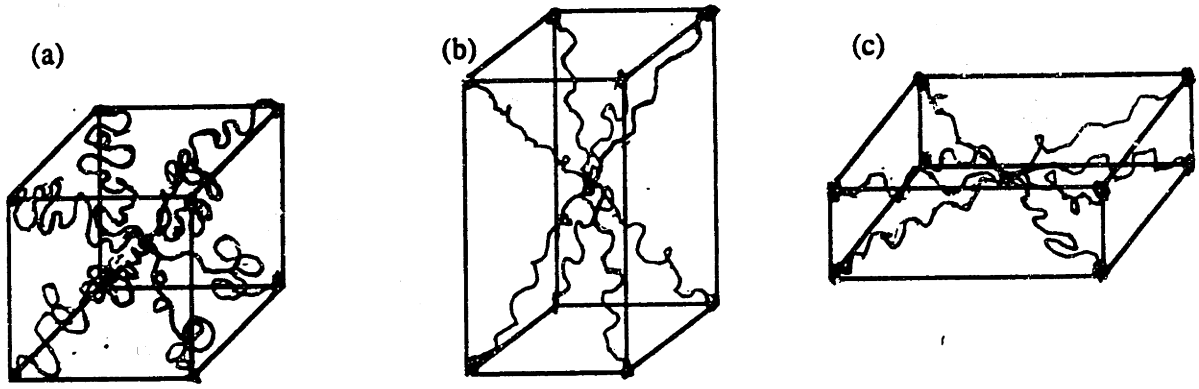

Figure 2.3: Eight chain rubber elasticity model for (a) undeformed, (b) uniaxial extension and (c) biaxial extension configurations.

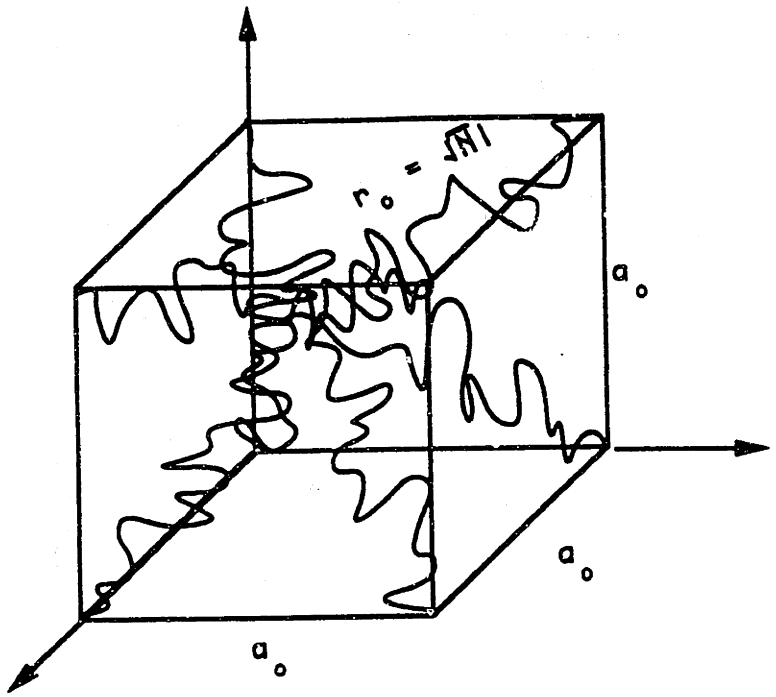

Figure 2.4: The unstretched network for the proposed eight chain model.

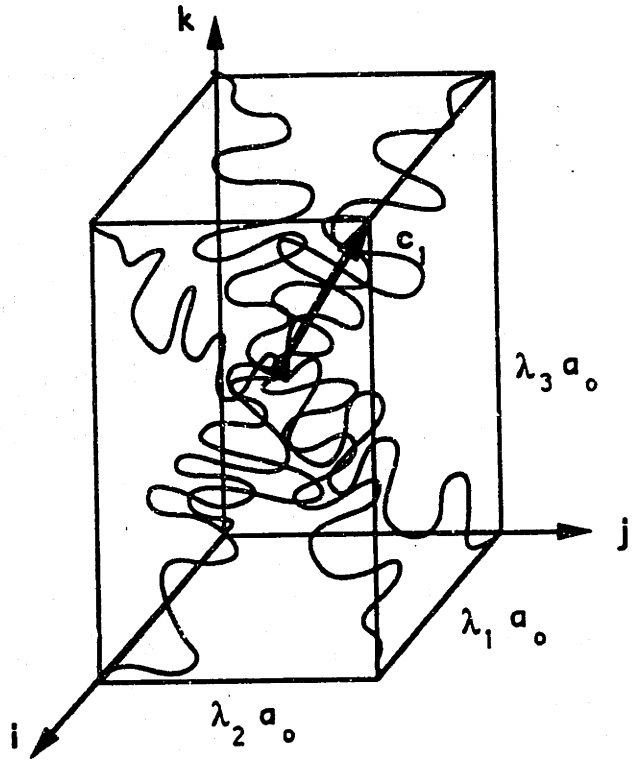

Figure 2.5: The eight chain network in a stretched configuration.

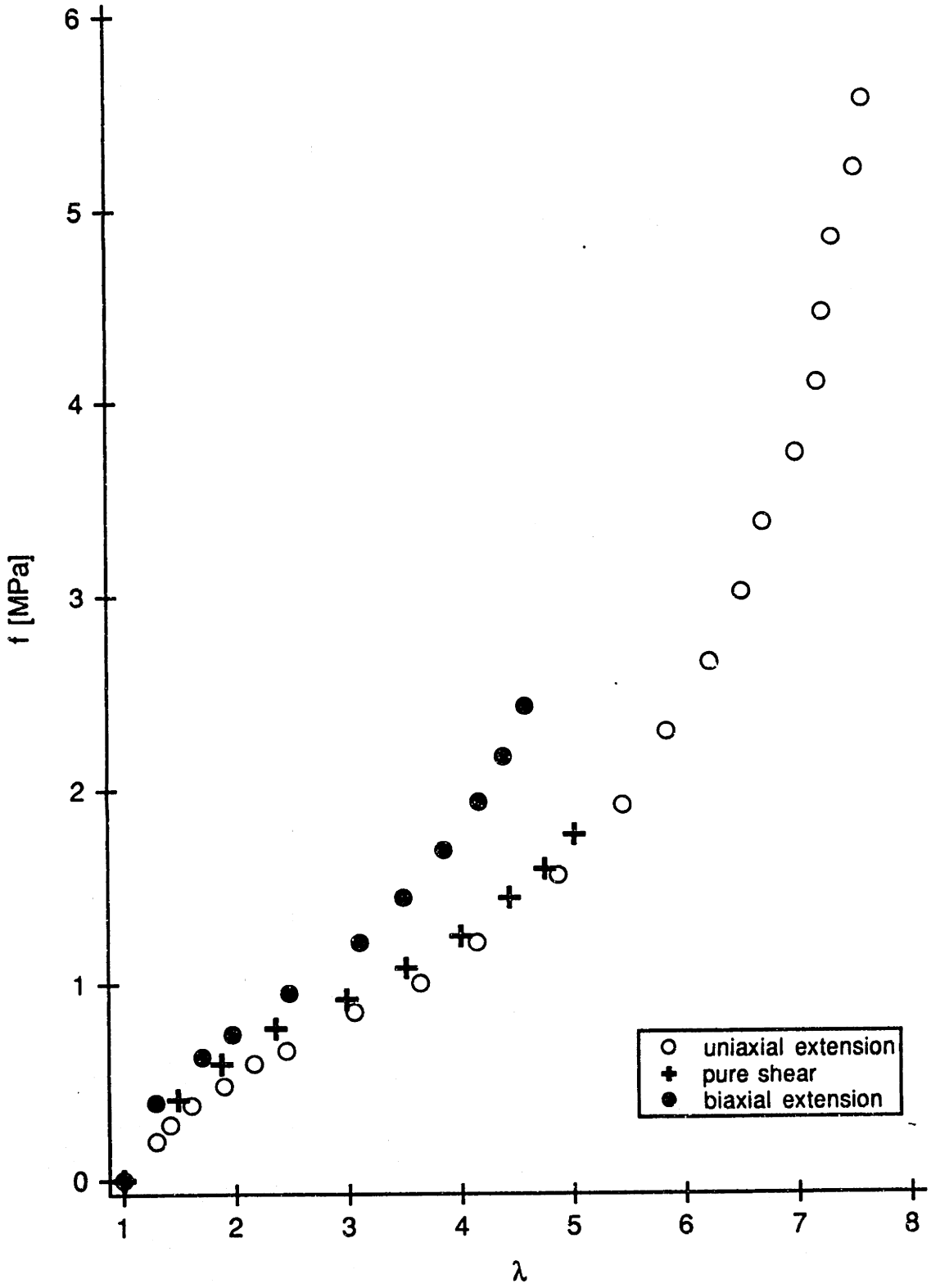

Figure 2.6: Data from Treloar (1944), plotted as force per unit unstrained area versus stretch, showing the state of deformation dependence of a rubber material in uniaxial extension, biaxial extension and shear.

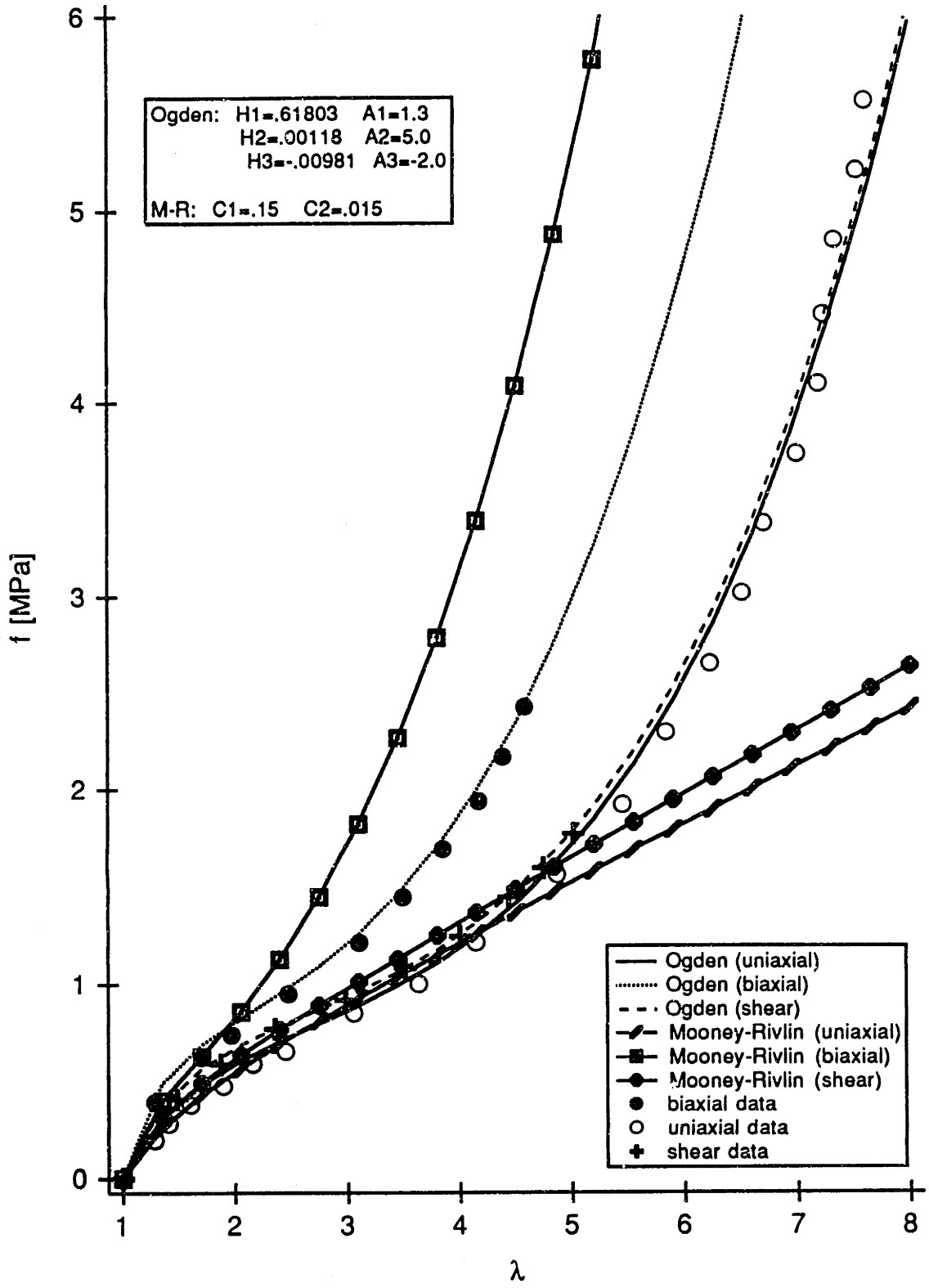

Figure 2.7: Results of simulations using the Mooney-Rivlin and Ogden models versus data from Treloar (1944) in uniaxial extension, biaxial extension and shear.

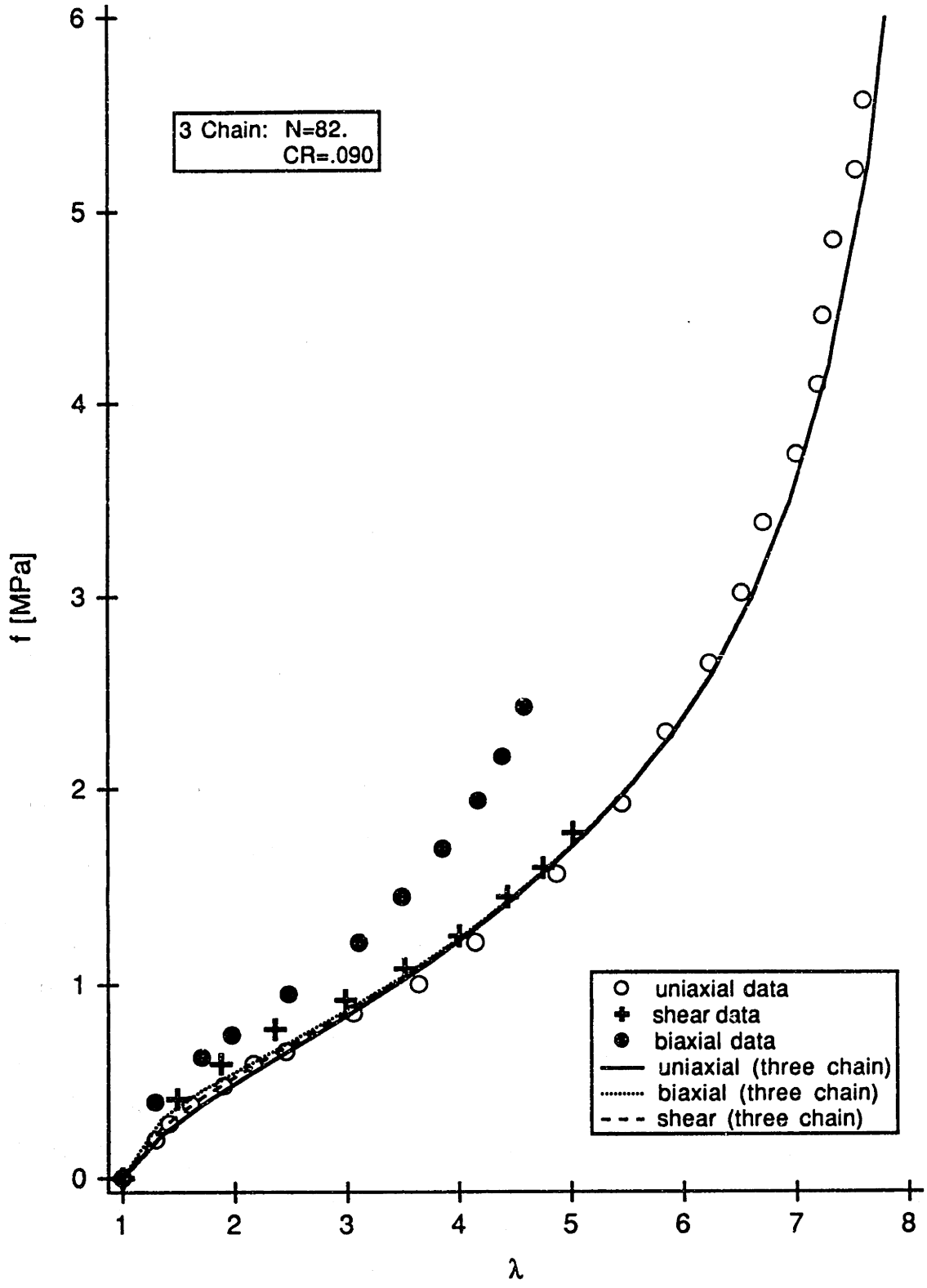

Figure 2.8: Results of simulations using the Wang and Guth model versus data from Treloar (1944) in uniaxial extension, biaxial extension and shear.

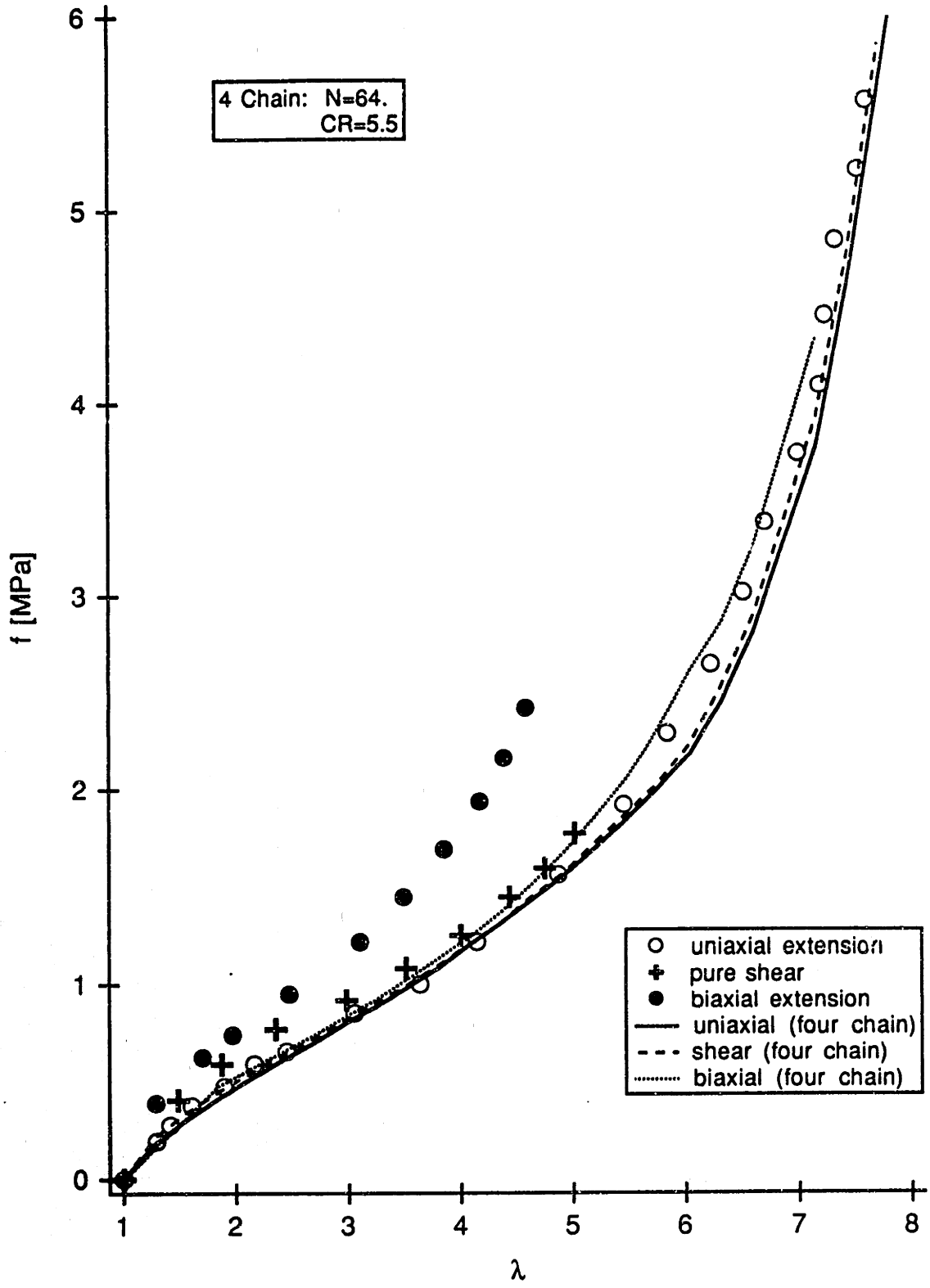

Figure 2.9: Results of simulations using the four chain model versus data from Treloar (1944) in uniaxial extension, biaxial extension and shear.

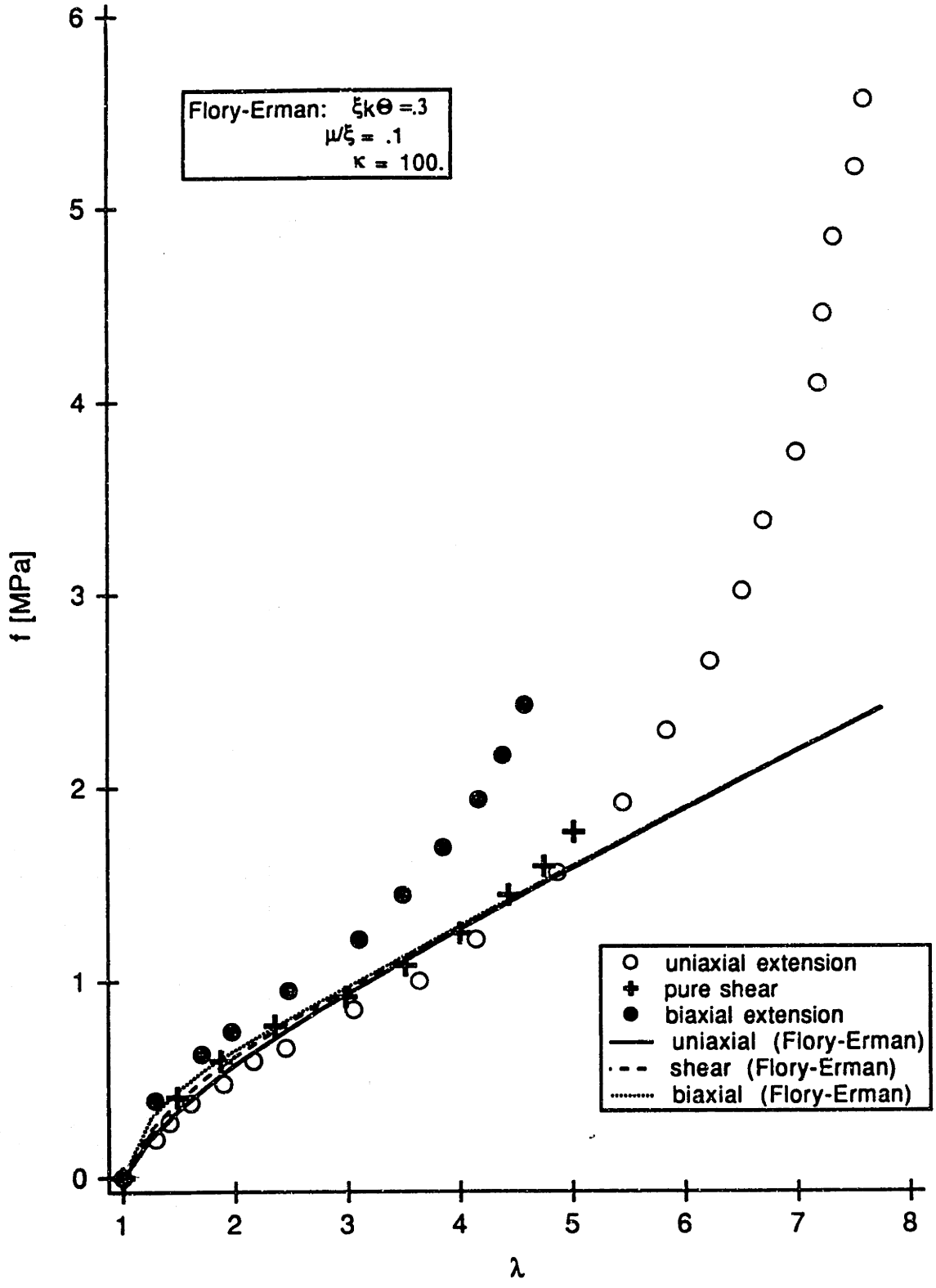

Figure 2.10: Results of simulations using the Flory and Erman model versus data from Treloar (1944) in uniaxial extension, biaxial extension and shear.

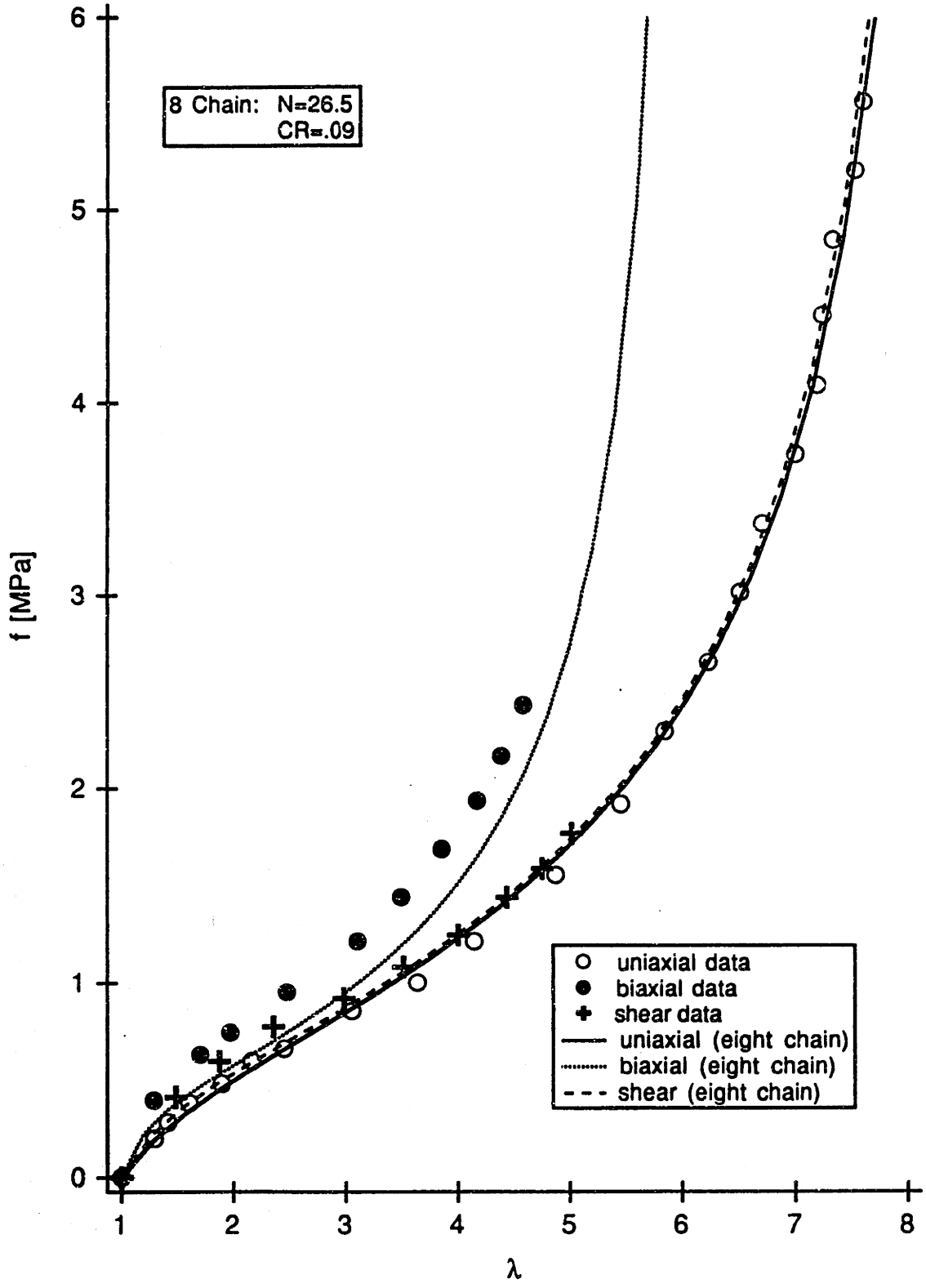

Figure 2.11: Results of simulations using the eight chain model versus data from Treloar (1944) in uniaxial extension, biaxial extension and shear.

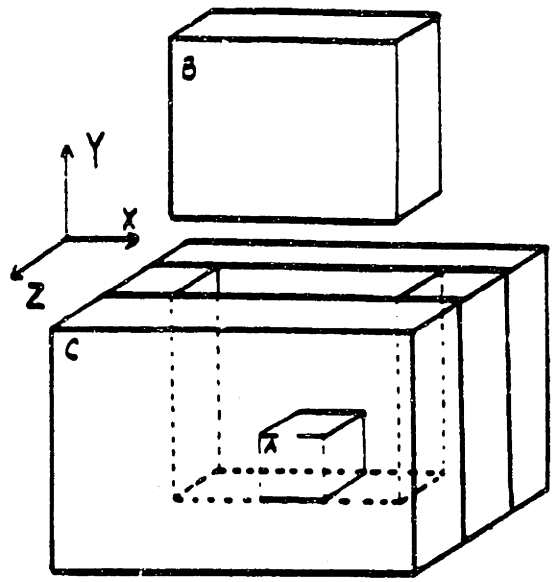

Figure 2.12: Sketch of plane strain compression testing apparatus. Specimen (A) is compressed by punch (B) in the Y direction and expands in the X direction. The die (C) constrains the specimen along the Z axis.

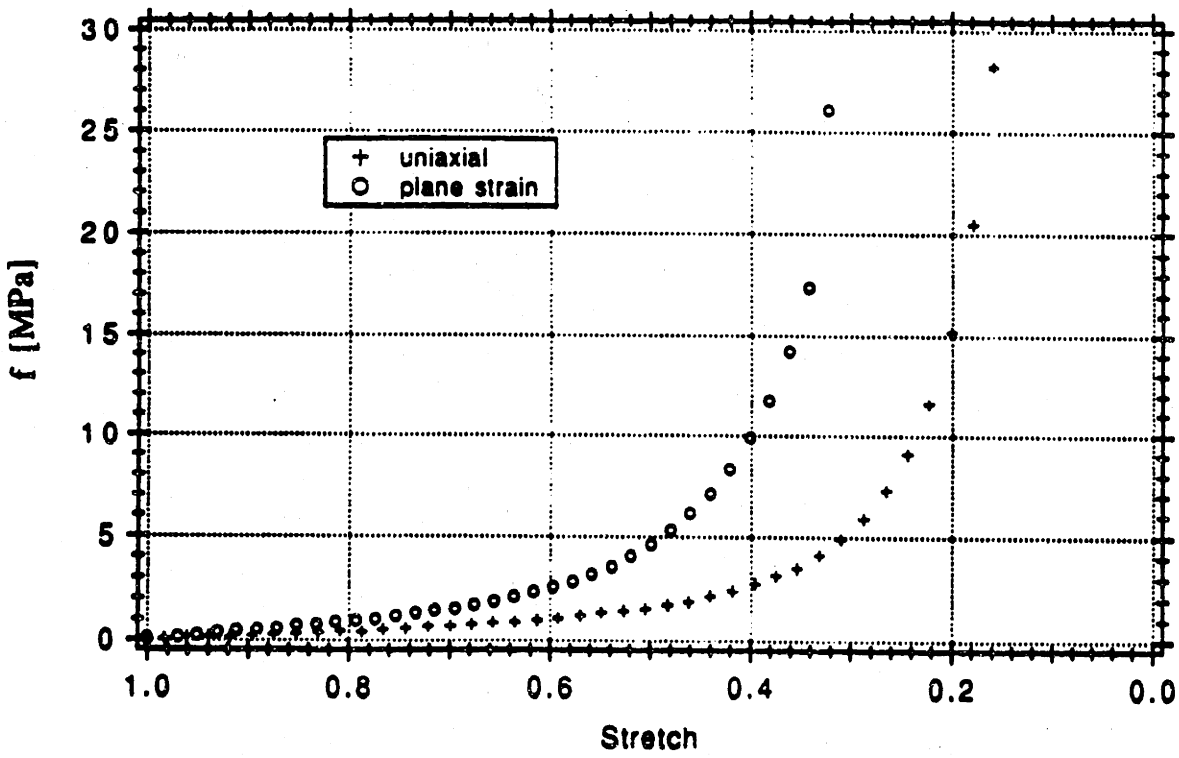

Figure 2.13: Ramp tests in uniaxial compression and plane strain compression for silicone rubber.

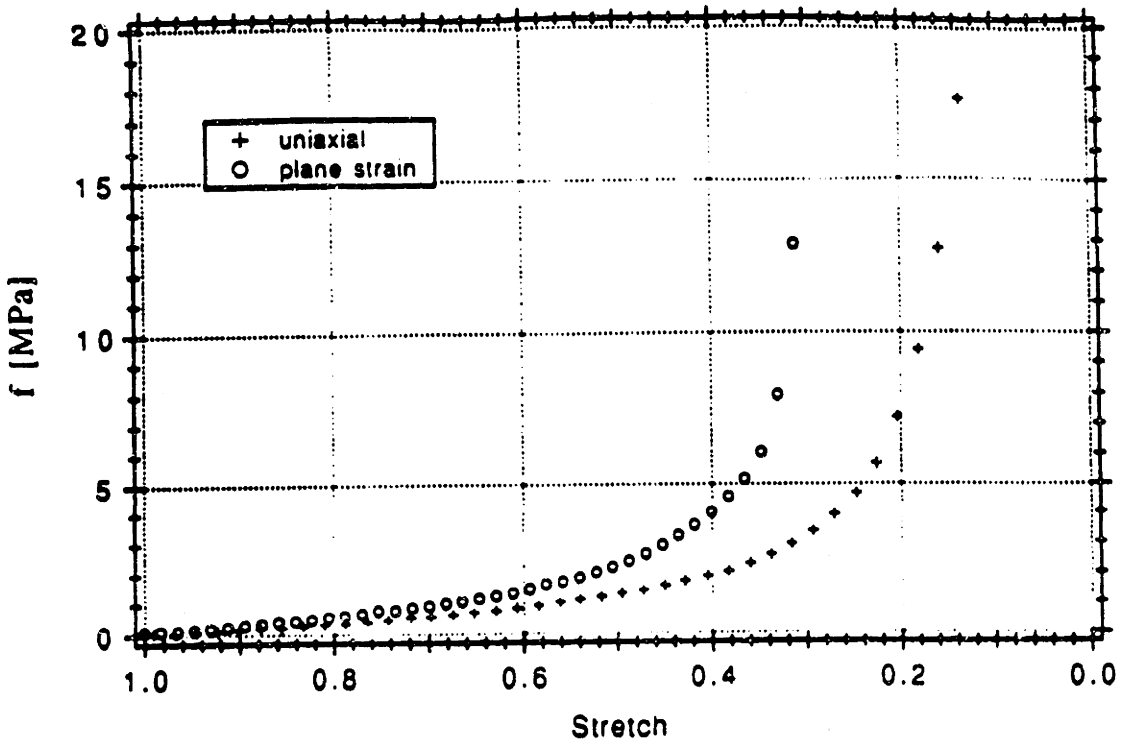

Figure 2.14: Ramp tests in uniaxial compression and plane strain compression for gum rubber.

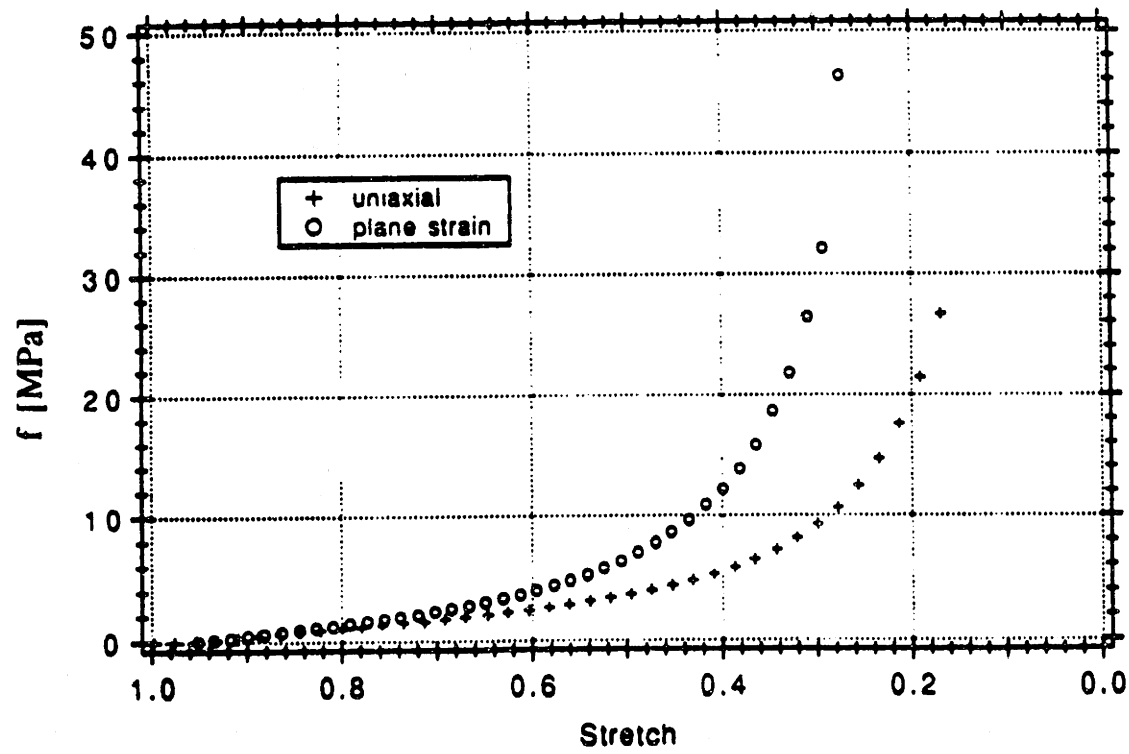

Figure 2.15: Ramp tests in uniaxial compression and plane strain compression for neoprene rubber.

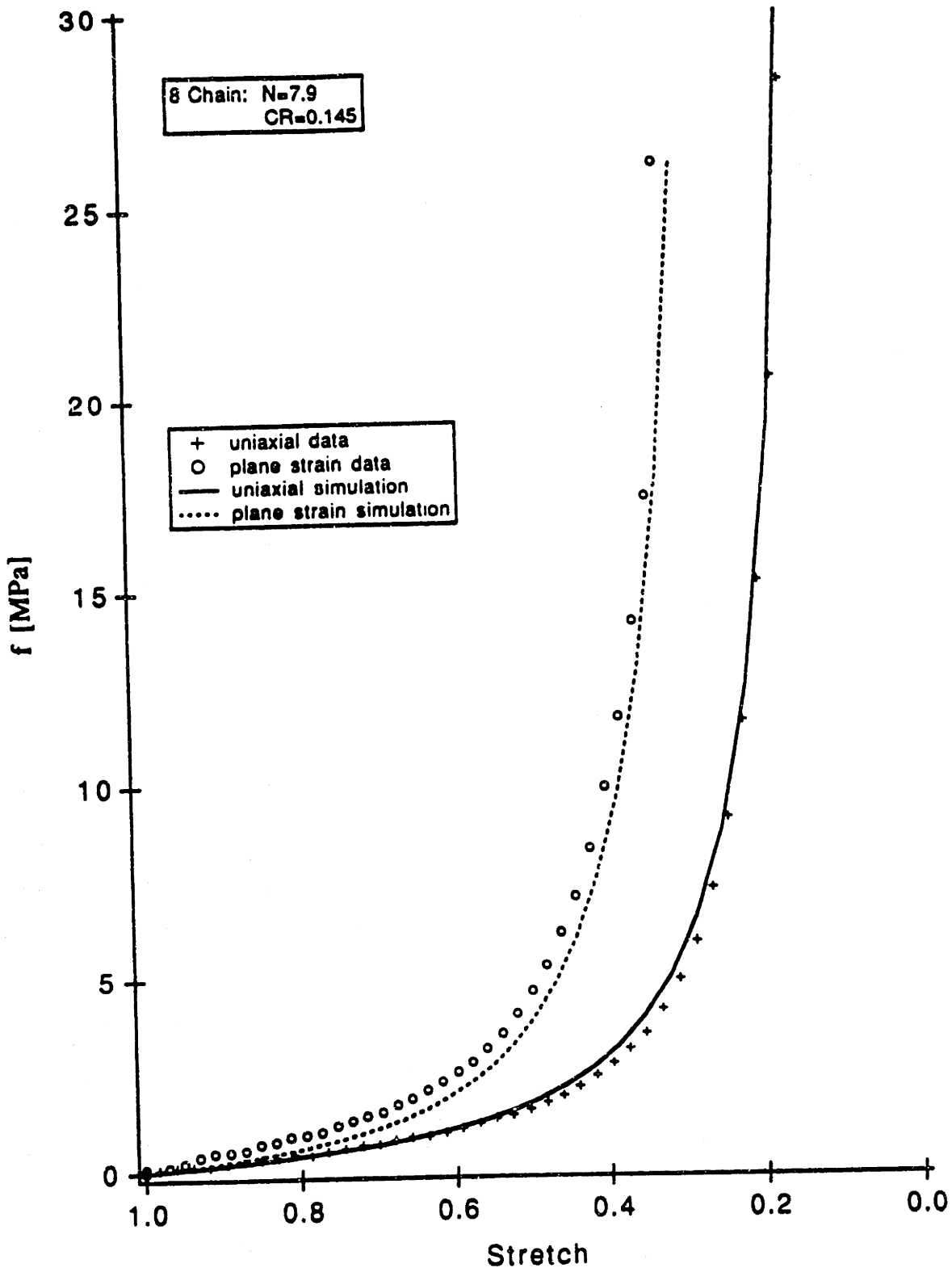

Figure 2.16: Results of simulations using the eight chain model and data on silicone rubber.

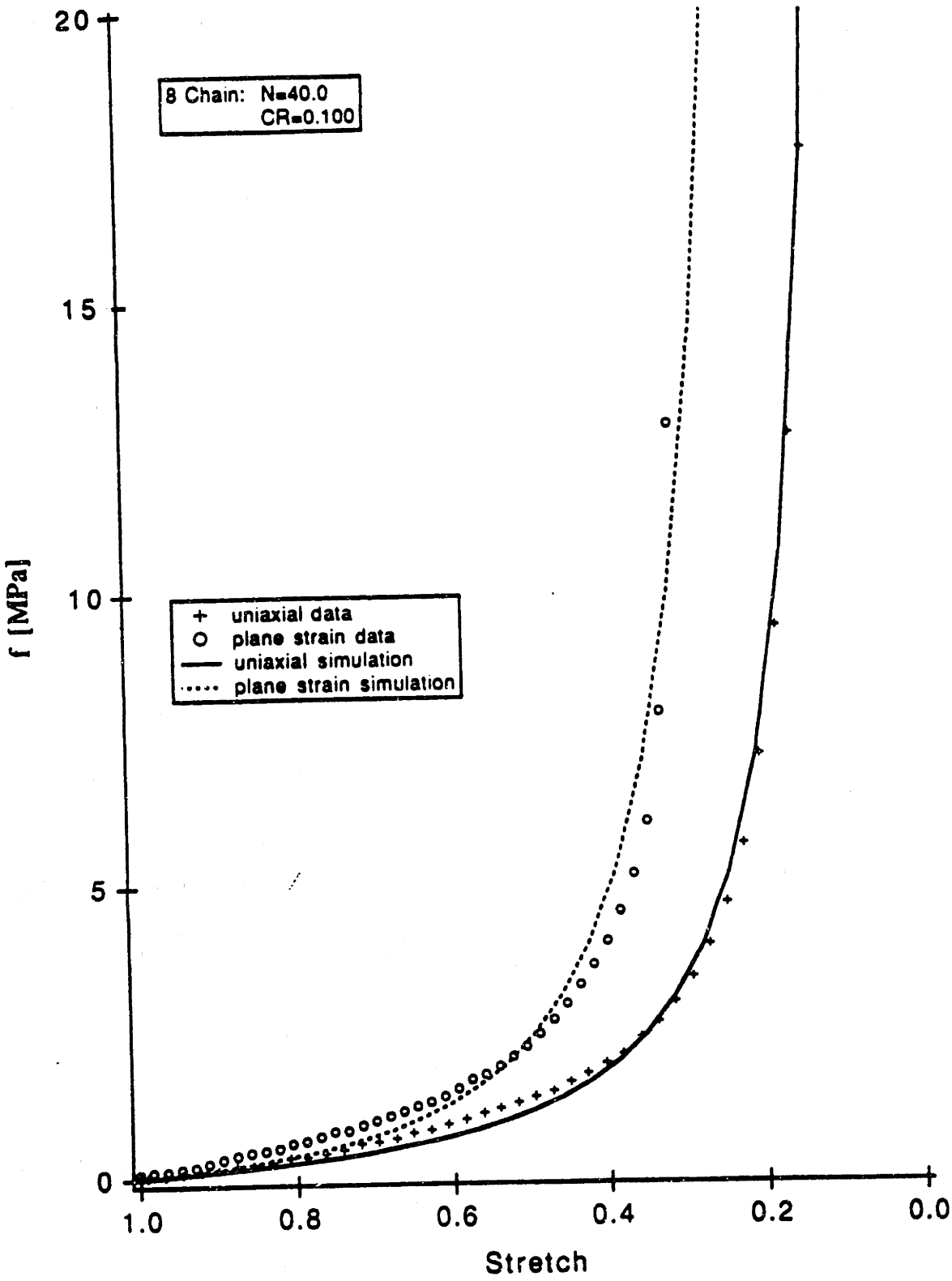

Figure 2.17: Results of simulations using the eight chain model and data on gum rubber.

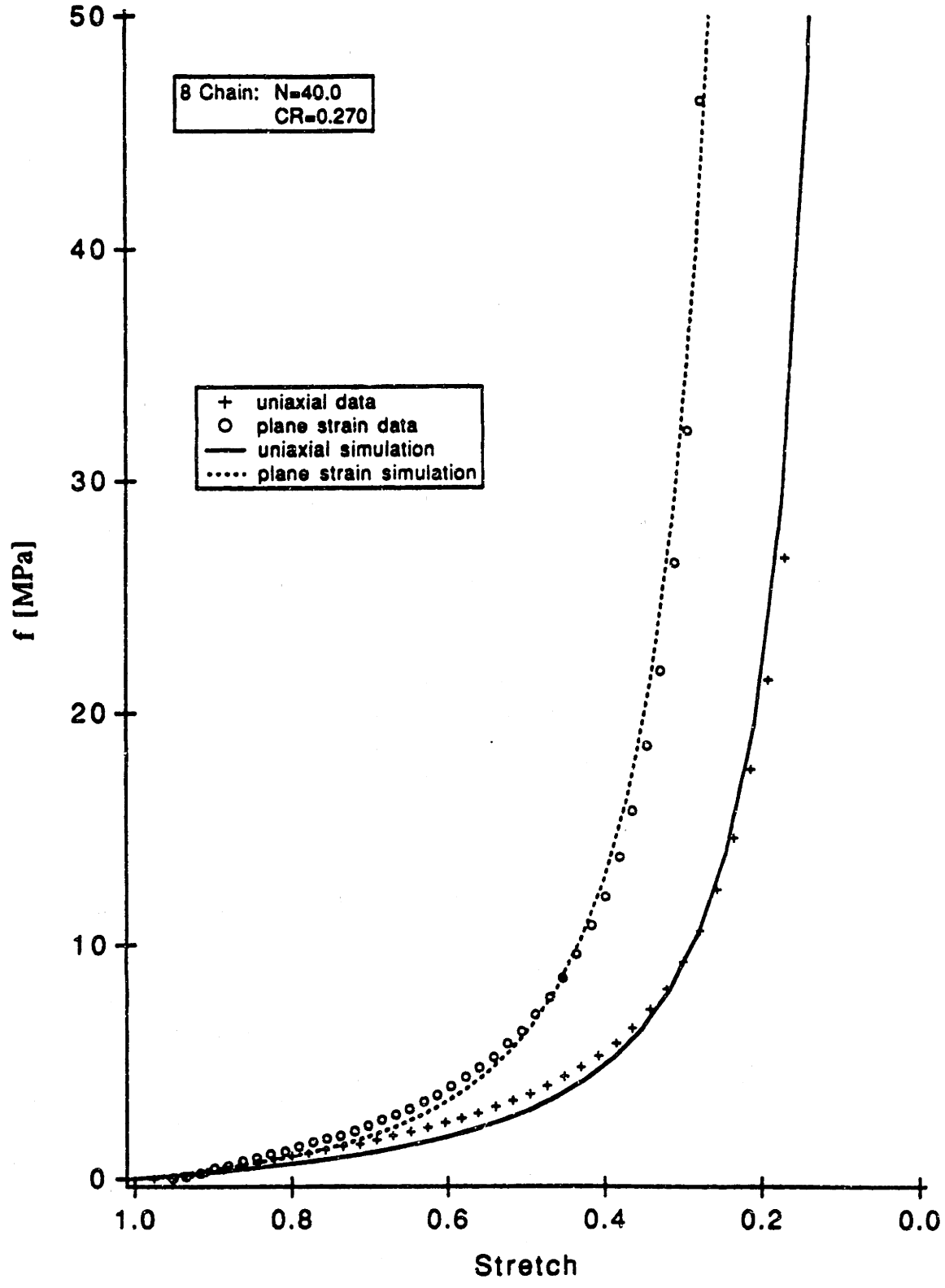

Figure 2.18: Results of simulations using the eight chain model and data on neoprene rubber.

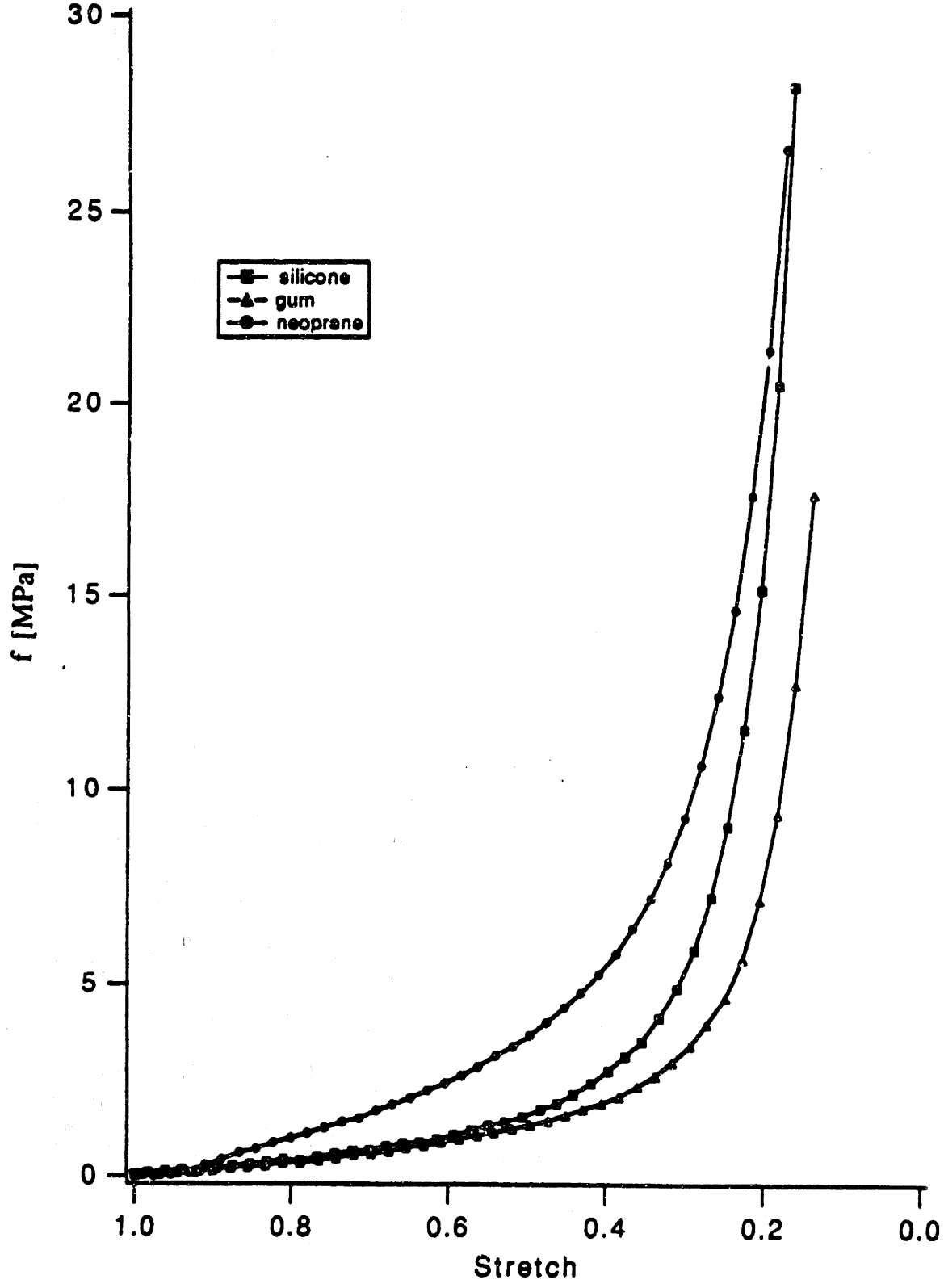

Figure 2.19: Direct comparison of the uniaxial compression responses of silicone, gum and neoprene rubbers.

Chapter 3

Evolution of Plastic Anisotropy in Glassy Polymers During Finite Straining

The mechanical behavior of glassy polymers subjected to large strain deformations is primarily governed by the evolution of the polymer chain network with deformation state and temperature from that of an initially random configuration to a highly oriented state. As the chain network orients the polymer exhibits extensive strain hardening. A typical isothermal stress-stretch response of an amorphous polymer below the glass transition temperature is sketched in Figure 3.1. The strain hardening response of the glassy polymer is seen to be similar to that which occurs during rubbery deformation as examined in the previous Chapter. This stress-stretch response of the rubbery polymer is sketched in Figure 3.2. In the glassy polymer the strain induced orientation acts to preferentially strengthen the polymer, much of the orientation is locked into the polymer after unloading, producing an anisotropic material. This orientation hardening phenomenon is often exploited in the processing of strengthened polymeric components.

In this Chapter we present a series of experiments which describes the anisotropic nature of the inelastic behavior of amorphous polymers, devoting particular attention to the three dimensional state of deformation dependence of the evolution of anisotropy during large strain deformations. We offer a model for the large strain behavior of glassy polymers and examine three representations from the previous Chapter for the tensorial characterization of the evolution of the anisotropic strain hardening in glassy polymers. The two materials considered are polycarbonate (PC) and polymethylmethacrylate (PMMA)which undergo the glass transition at 150°C, respectively. This Chapter includes isothermal tests on each material in the temperature ranges of the glassy regimes of each. The effects of an initial orientation on such aspects of the subsequent anisotropic response as flow strengths, deformation patterns and finite extensibilities will be discussed in Chapter 4.

3.1 Previous experimental studies

Several experimental studies on the large strain deformation of polymers have been reported. However, each study focuses its attention on a single type of test. The most popular method of testing has been the uniaxial tension test, those successful in producing large strain deformations in such tests on glassy polymers include: Haward and Thackray [21] for polyvinylchloride (PVC), plasticized cellulose nitrate and plasticized cellulose acetate; Hope, Ward and Gibson [22] for PMMA; Stokes and Nied [23] for PC, polybutylene terephthalate (PBT) and polyetherimide (PEI); G'Sell and Jonas [24] for PVC and high density polyethylene (HDPE); Kahar, Duckett and Ward [25] for PMMA; and Heymans [26] for PC. In the uniaxial tension test the limit of elastic deformation is usually followed either by brittle failure of the polymer, as is the case for PMMA at 23°C, or by the onset of localized deformation through necking. G'Sell and Jonas monitored the deformation of the neck, and through closed loop control obtained locally constant strain rate conditions for more accurate stress-strain data than had been previously obtained. The occurrence of necking and its associated difficulties in monitoring true strains and strain rates has prompted some investigators to develop methods of testing in other modes of deformation. Bowden and Raha [27] used plane strain compression tests on PMMA and polystyrene (PS) to moderate levels of strain, G'Sell, Boni and Shrivastava [28] developed a simple shear apparatus for tests on polyethylene (PE) and Wang and Parks [29] performed uniaxial compression tests on PC. In these tests uniform deformations could be obtained for the full range of material extensibility.

In this Chapter the uniaxial compression and plane strain compression tests are used extensively for the purpose of illustrating the state of deformation dependence of PC and PMMA. These two tests allow for globally homogeneous deformations at constant strain rates for the full range of extensibilities, ie. in excess of 100% strain for PC and PMMA. The plane strain compression test and uniaxial compression test represent examples of near extreme conditions of polymer network orientation morphologies. During plane strain compression deformation, molecular chain alignment occurs along a single flow direction, whereas in uniaxial compression the molecular chains are free to stretch along all directions in a plane normal to the compression axis. This results in a planar state of orientation. These two states of deformation will be used to evaluate the ability of several constitutive models, including the model proposed in Chapter 2, to predict the state of deformation dependence of strain hardening in the glassy polymers PC and PMMA.

An important polymer forming operation is cold drawing, which produces unidirectionally strengthened polymer components along the drawing axis. The cold drawing polymer forming operation is rather simply conducted using a servohydraulic testing machine. This operation includes the formation and stabilization of a necked region prior to drawing, and involves non-homogeneous deformation. This forming

operation was conducted on glassy PC and simulated using the eight chain model for strain hardening to illustrate and further emphasize the vast opportunity for understanding the polymer deformation process afforded by the model developed in this thesis work.

3.2 Overview of polymer deformation constitutive models

The onset of inelastic deformation in glassy polymers is believed to occur once individual polymer chain segments overcome a local resistance to rotation [30,31,32]. This initial yield depends on temperature, strain rate and pressure. The continuing plastic flow is characterized by strain softening followed by strain hardening, the latter is considered to be the result of an evolving resistance to chain alignment [21,33,31,34,35,36].

Previous elastic-viscoplastic models of glassy polymers have attempted to describe the yield event in terms of a barrier to plastic flow which is based on the nature of the macromolecule. The initial yield event in glassy polymers has been modelled by Robertson [30] as the result of a thermally activated transition of a molecular chain from one conformation to another equivalently stable conformation. This model is successful for situations of negligible intermolecular barriers as arise at temperatures near the glass transition, Θ_g. Argon [31] suggested a molecular model for the initial yield in isotropic glassy polymers at low temperatures which accounts for the rate and temperature dependencies. His model for initial yield was later extended [37] to include pressure effects and strain softening. Haward and Thackray [21] and also Argon [31] proposed that the strain hardening resulted from the decreasing entropy of a network of orienting chains thereby citing an additional barrier to continued plastic flow in the first dual barrier representations. In a one-dimensional model, Haward and Thackray [21] represented the yield process by an Eyring dashpot for rate dependent yield in parallel with a Langevin spring for strain hardening. Parks, Argon and Bagepalli [38] extended spring and dashpot systems to three dimensions using the Wang and Guth [10] statistical mechanics of rubber elasticity model as the strain hardening spring element in parallel with an ideally plastic element. Boyce, Parks and Argon [37] extended this constitutive framework taking the Wang and Guth [10] spring element in parallel with the rate and temperature dependent Argon model. Boyce et. al. [37] also included pressure effects and strain softening in their model. Lee and Luken [39] have modified the Haward and Thackray [21] model by replacing the Langevin spring strain hardening element with the Mooney-Rivlin [6,5] rubber elasticity element.

In the parallel spring and dashpot systems the strong Bauschinger effect exhibited by these materials is provided for by taking the driving stress on the dashpot element

to be the total stress minus the internal back stress on the Langevin spring element; this requires a scalar difference in one dimensional models and a tensorial subtraction in three dimensional representations. The Bauschinger effect has also been modelled by modifying the anisotropic yield criterion of Hill [40] for pre-oriented polymers. In these modifications a scalar parameter monitors the internal stress accumulation as the result of an aligning network structure [35,41,42]. The actual presence and build-up of an internal stored stress has been experimentally documented in the deformation calorimetry experiments of Adams and Farris [43].

The proposed model retains the Boyce, Parks and Argon [37] framework for network deformation of a glassy polymer which uses a spring in parallel with a dashpot. The eight chain model developed in the previous Chapter provides a substantial modification to the strain hardening component by replacing the Wang and Guth [10] rubber elasticity model. In this way we account for the state of deformation dependence in glassy polymers PC and PMMA as observed in the experimental section of this Chapter using a physical basis for describing the orientation process in macromolecular networks.

3.3 Experiments

3.3.1 Specimen preparation

Test specimens were machined from commercially available grades of PMMA and PC bar stock. Uniaxial compression cube specimens of length $11.1mm$ and plane strain compression specimens measuring $9.5mm \times 9.5mm \times 12.7mm$ were cut from PMMA and PC bars. All specimens were annealed for several hours above the glass transition temperatures of the materials and allowed to slowly cool to room temperature. Specimens were lightly sanded on silicon carbide paper to smooth burrs left from the machining operation.

The geometry of the axisymmetric PC tensile specimen used in the cold drawing experiment is sketched in Figure 3.3. The tapered gage section was designed to remove any ambiguity over the location of formation of the necked region.

Preparation of birefringence specimens consisted of slicing thin sections from the as-tested compression specimens. The slices were oriented along the directions of principal stretch in the specimens. PMMA slices approximately $0.6mm$ thick were cut using an Isomet cut-off wheel equipped with a silicon carbide wafer blade and an oil based cutting fluid. This procedure was checked to determine whether the slicing operation alters the birefringence and to assess whether polishing the sliced faces after cutting was necessary for obtaining sound measurements of the birefringence. Isotropic specimens were sliced or sliced and polished and their birefringences were measured to determine whether the slicing and/or polishing produced any residual birefringence. Anisotropic specimen birefringences were measured then the specimens

were lightly polished on a polishing wheel using a $1.0\mu m$ alumina suspension as the abrasive. Specimen birefringences were measured after polishing to check whether polishing altered the birefringence. The optimal thickness of the birefringence specimen was also determined by successive polishing and measurements. These checks affirmed that the $0.6mm$ thick specimen in the as-cut condition produced reproducible birefringence measurements of sufficient accuracy.

3.3.2 Apparatus and test methods

Constant strain rate uniaxial compression and plane strain compression tests were conducted on an Instron 1350 servo-hydraulic testing machine. The constant strain rate condition was achieved by sending an exponentially decaying voltage waveform from a Macintosh personal computer to the Instron actuator by way of a Keithley digital to analog interface board. The voltages were scaled by the specimen initial height. The Macintosh computer was also used to collect the raw load and displacement data from the feedback circuitry of the testing machine. The actuator compliance was subtracted from the raw data then the information was converted to stress-strain curves.

The uniaxial compression test required that the specimen faces placed in contact with flat platens on the actuator and axially aligned with it were sufficiently lubricated to prevent barrelling of the specimen during deformation. A graphite particle suspension (DAG 41) was used to lubricate the uniaxial compression specimens.

The plane strain compression testing procedure utilized a stiff restraining die machined in sections from air hardenable steel, the sections were then properly heat-treated to attain the sufficient hardness. The die sections were bolted together to form the die. This sectional construction greatly facilitated specimen removal after deformation without sacrificing die stiffness. The interior of the die measured $63.5mm \times 31.8mm \times 9.5mm$ and was fitted with a punch of matching dimensions. This die was described in the previous Chapter, a sketch of it appeared in Figure 2.12. Plane strain specimens which measured $9.5mm$ in the Z direction of Figure 2.12 were coated with the DAG lubricant or a thin PTFE (teflon) foil then placed between the walls of the die. A final tightening of the apparatus brought the specimen and die in tight contact, usually deforming the teflon foil separating them, but did not deform the specimen prior to testing. The die restrained the specimen from deforming in the Z direction of Figure 2.12 thereby providing the plane strain condition. The punch compressed the specimen in the Y direction while the material flowed laterally in the X direction only.

Birefringence measurements were conducted using a Leitz microscope to transmit polarized light through the thin polymer slices of deformed specimens. A Berek S-N 3311 compensator provided a measure of the specimen retardation of light in nanometers using the known optics of the compensator [44]. Birefringence relates to

retardation in the following manner:

$$\Delta\eta = \frac{\Gamma}{t}, \tag{3.1}$$

where $\Delta\eta$ is the birefringence (or relative retardation), Γ is the retardation in nanometers calculated from the compensator reading and t is the specimen thickness.

The cold drawing experiment was conducted at 23°C using an Instron Model 1125 screw machine at a constant displacement rate of 2.54 *mm/minute*. Measurement was made of the deforming specimen diameter size during testing at the location of the minimum diameter using an Instron diametral extensometer. The load versus diametral contraction data was converted to local true stress versus local true strain at the neck using the known crosshead displacement rate and assuming incompressibility. The local strain rate at the deforming neck region was also calculated with the local strain and crosshead speed information.

3.4 Mathematical Formulation of Constitutive Model

3.4.1 Discussion of model constituents

The model of Boyce, Parks and Argon [37] has been shown to be predictive of the uniaxial behavior of glassy polymers over a range of temperatures and strain rates. In their model, two resistances to plastic flow act in parallel to account for both isotropic chain segment rotation and anisotropic chain orientation observed for these materials. In all, the model requires three elements. These are illustrated schematically in Figure 3.4 for a one dimensional analog to the polymer deformation model as originally sketched out by Haward and Thackray [21]. The three elements are: A linear spring used to characterize the initial response as elastic and represented by the Young's modulus E; a viscous dashpot representing rate and temperature dependent yield which monitors an isotropic resistance to chain segment rotation; and a non-linear rubber elasticity spring element which accounts for an anisotropic resistance to chain alignment. The dashpot and non-linear spring operate in parallel to deliver the total response of the material, σ, given by $\sigma = \sigma_v + \sigma_b$, where σ_v and σ_b are the stresses on the elements as shown in Figure 3.4.

The contributions of these individual elements to the glassy polymer response may be seen from the typical isothermal stress-strain response of glassy PC sketched in Figure 3.5. The viscoplastic element is that given by the Argon [31] model for the isotropic intermolecular barrier to chain segment rotation, as modified by Boyce, Parks and Argon [37] to evolve with pressure and strain softening. This barrier represents the driving stress for continued plastic deformation. The stress on the non-linear spring element is deemed the back stress and has been modelled by Boyce et. al. using the three chain rubber elasticity model of Wang and Guth [10]. The back stress is considered here to be an internal, non-dissipated stress. In the present

paper, three models of rubber elastic deformation will be considered individually as candidates for the strain hardening element. These will be compared on the basis of their abilities to predict the state of deformation dependence of strain hardening in PC and PMMA. The candidate models include that of Wang and Guth used in the Boyce, et. al. model, the tetrahedron model of Flory and Rehner [11] and the eight chain model developed in Chapter 2.

3.4.2 Kinematics of finite strain deformation

The mechanics of fully three dimensional large strain deformation involve the deformation gradient tensor, $\mathbf{F}$, which maps a material point of the reference configuration into the current configuration

$$\mathbf{F} = \nabla_P \mathbf{x}. \tag{3.2}$$

As in Lee [45], the deformation gradient is multiplicatively decomposed as follows

$$\mathbf{F} = \mathbf{F}^e\mathbf{F}^p, \tag{3.3}$$

where $\mathbf{F}^e$ is the elastic component of the deformation gradient and $\mathbf{F}^p$ is the deformation gradient of the relaxed configuration obtained by elastically unloading to a stress free state. The deformation gradient of the relaxed configuration in general consists of both a stretch and a rotation, thus using polar decomposition on the relaxed configuration, $\mathbf{F}^p$, the stretch of the relaxed configuration may be represented in terms of the left stretch tensor, $\mathbf{V}^p$

$$\mathbf{F}^p = \mathbf{V}^p\mathbf{R}^p, \tag{3.4}$$

or the right stretch tensor, $\mathbf{U}^p$

$$\mathbf{F}^p = \mathbf{R}^p\mathbf{U}^p. \tag{3.5}$$

The eigenvalues of the left plastic stretch tensor, $\mathbf{V}^p$, are denoted $\Lambda^P{}_i$, for $i = 1, 2, 3$. Additionally, in the representation followed here, the elastic component of the deformation gradient, $\mathbf{F}^e$, is restricted to be the result of stretching, $\mathbf{F}^e = \mathbf{V}^e = \mathbf{U}^e$.

The velocity gradient,

$$\mathbf{L} = \dot{\mathbf{F}}\mathbf{F}^{-1} = \mathbf{D} + \mathbf{W} = \mathbf{L}^e + \mathbf{F}^e\mathbf{L}^p\mathbf{F}^{e-1}, \tag{3.6}$$

is the sum of a symmetric tensor, $\mathbf{D}$, the rate of deformation, and the skew-symmetric tensor, $\mathbf{W}$, the spin. As shown in Equation 3.6, the velocity gradient may be further decomposed into elastic and plastic velocity gradients.

The velocity gradient of the relaxed configuration, $\mathbf{L}^p = \dot{\mathbf{F}}^p\mathbf{F}^{p-1}$, may be represented as the sum of symmetric and skew-symmetric tensors,

$$\mathbf{L}^p = \mathbf{D}^p + \mathbf{W}^p \tag{3.7}$$

where $\mathbf{D}^p$ is the rate of shape change in the relaxed configuration and $\mathbf{W}^p$ is the spin in this configuration. It may be shown, as in Boyce, Weber and Parks [46], that $\mathbf{W}^p$ is algebraically prescribed without loss of generality as a result of the imposed symmetry on the elastic deformation gradient. The shape change, $\mathbf{D}^p$, is constitutively prescribed as described below.

3.4.3 Constitutive description of model

In the three dimensional representation of Figure 3.6 the spring and dashpot elements have been redrawn as in Figure 3.4, where a tensor now acts on each element. The linear spring element is characterized by the fourth order tensor operator of elastic constants, $\mathcal{L}$, and the constitutive relationship

$$\mathbf{T} = \frac{1}{J}\mathcal{L}\left[\ln \mathbf{U}^e\right], \tag{3.8}$$

where $\mathbf{T}$ is the Cauchy stress, $\ln \mathbf{U}^e$ is the Hencky strain and $J = \det \mathbf{U}^e$ [47].

The viscous element represents the Argon [31] scalar equation for the plastic shear strain rate, $\dot{\gamma}^P$, which ensues once isotropic barriers to chain segment rotation are overcome:

$$\dot{\gamma}^P = \dot{\gamma}_0 \exp\left[-\frac{A\,s}{k\Theta}\left\{1 - \left(\frac{\tau}{s}\right)^{5/6}\right\}\right]. \tag{3.9}$$

In Equation 3.9, $\dot{\gamma}_0$ is the pre-exponential factor proportional to the attempt frequency [48], $s \equiv \frac{0.077\mu}{1-\nu}$ is the athermal shear strength, μ is the elastic shear modulus, $A\,s$ is the zero stress level activation energy, τ is the effective equivalent shear strength, k is Boltzmann's constant and Θ is absolute temperature. Equation 3.9 may be rearranged as follows to give the shear flow stress as a function of strain rate and temperature:

$$\tau = s\left[1 - \frac{k\Theta}{A\,s}\ln\left(\frac{\dot{\gamma}^P}{\dot{\gamma}_0}\right)\right]^{6/5}. \tag{3.10}$$

Strain softening is modelled by taking the athermal shear stress s to evolve to a "preferred" state, s_{ss}, after Boyce et. al. [37]

$$\dot{s} = h\left(1 - \frac{s}{s_{ss}}\right)\dot{\gamma}^P, \tag{3.11}$$

where h is the softening slope.

The effective equivalent shear stress on this element is found from the tensorial difference between the total stress, or Cauchy stress, $\mathbf{T}$, and the convected back stress on the non-linear spring element, $\mathbf{B}$

$$\tau = \left[\frac{1}{2}\mathbf{T}^{*\prime}\cdot\mathbf{T}^{*\prime}\right]^{1/2} \tag{3.12}$$

$$\mathbf{T}^* = \mathbf{T} - \frac{1}{J}\mathbf{F}^e\mathbf{B}\mathbf{F}^{eT}. \tag{3.13}$$

$\mathbf{T}^*$ is the driving stress state; that portion of the total stress which continues to activate plastic flow. The deviatoric tensor of the driving stress state is denoted $\mathbf{T}^{*\prime}$. Thus the rate of shape change, $\mathbf{D}^p$, is constitutively prescribed with Equations 7 through 11. The magnitude of $\mathbf{D}^p$ is $\dot{\gamma^p}$ and the tensorial direction of shape change is $\mathbf{N}$

$$\mathbf{D}^p = \dot{\gamma^p}\mathbf{N}. \tag{3.14}$$

$\mathbf{N}$ is a normalized tensor aligned with the deviatoric driving stress state

$$\mathbf{N} = \frac{1}{\sqrt{2\tau}}\mathbf{T}^{*\prime}. \tag{3.15}$$

This thesis is concerned with the modelling of the orientation induced backstress element, $\mathbf{B}$ [10,49,11]. The strain hardening response and its state of deformation dependence should be captured with this element. Three of the network models discussed in Chapter 2 have been considered as candidates for the backstress characterization. These are: the three chain model of Wang and Guth [10] which was originally considered for the strain hardening application by Boyce, et. al. [37] and also by Parks, Argon and Bagepalli [38]; the tetrahedron model proposed by Flory and Rehner [11] modified with a floating junction point capability; and the eight chain model proposed and developed in this thesis. The hardening models differ in the network response to principal stretch states but each requires two material properties and all are similarly implemented as the strain hardening element. The details of implementation of a rubber elasticity model as a backstress element are described below for the eight chain model of the large stretch behavior of rubber materials from Chapter 2.

The network response to the principal stretches λ_i, has been given in terms of the difference in two principal stresses in Chapter 2. An arbitrary pressure term which arises from the condition of incompressibility is then eliminated

$$\sigma_1 - \sigma_2 = \frac{nk\Theta}{3}\sqrt{N}\,\mathcal{L}^{-1}\left[\frac{\lambda_{chain}}{\sqrt{N}}\right]\frac{(\lambda_1^2 - \lambda_2^2)}{\lambda_{chain}} \tag{3.16}$$

where

$$\lambda_{chain} = \frac{1}{\sqrt{3}}(\lambda_1^2 + \lambda_2^2 + \lambda_3^2)^{\frac{1}{2}} = \frac{1}{\sqrt{3}}I_1^{\frac{1}{2}} \tag{3.17}$$

The principal values of the backstress element are taken to be colinear with the principal values of the left stretch tensor in the relaxed configuration. The stretch tensor in this configuration is denoted $\mathbf{V}^p$, its principal values are extracted by first a polar decomposition of the "relaxed" deformation gradient

$$\mathbf{F}^p = \mathbf{V}^p\mathbf{R}^p \tag{3.18}$$

which obtains $\mathbf{V}^p$, than an eigenvalue decomposition of $\mathbf{V}^p$ which yields the principal values of $\mathbf{V}^p$, denoted ${\Lambda_i}^P$

$$\mathbf{V}^p = \mathbf{Q}^T\Lambda^P\mathbf{Q} \tag{3.19}$$

The principal values of the deviatoric backstress tansor are denoted $\bar{B}_i$. These are colinear with the ${\Lambda_i}^P$ and are written as

$$\bar{B}_i = \frac{nk\Theta}{3}\sqrt{N}\mathcal{L}^{-1}\left\{\frac{{\Lambda^P}_{chain}}{\sqrt{N}}\right\}\frac{{\Lambda^P}_i^2 - \frac{1}{3}I_1}{{\Lambda^P}_{chain}} \tag{3.20}$$

In Equation 3.20 $I_1 = \left({\Lambda^P}_1^2 + {\Lambda^P}_2^2 + {\Lambda^P}_3^2\right)$ and ${\Lambda^P}_{chain} = \frac{1}{\sqrt{3}}{I_1}^{\frac{1}{2}}$. The backstress tensor is rotated from the principal frame of the ${\Lambda^P}_i$ to the general relaxed configuration containing $\mathbf{V}^p$ by

$$\mathbf{B} = \mathbf{Q}^T\bar{\mathbf{B}}\mathbf{Q} \tag{3.21}$$

The Boyce et. al. model [37] incorporated the three chain model of Wang and Guth as the strain hardening element and showed its usefulness in capturing the strain hardening response of PMMA in an extrusion process, as well as the general trend of the effect of initial orientation on shear banding in preoriented polymers [37,50]. The back stress components given by the three chain model are of the form

$$B_i = \frac{nk\Theta}{3}\sqrt{N}\left[{\Lambda^P}_i\mathcal{L}^{-1}\left\{\frac{{\Lambda^P}_i}{\sqrt{N}}\right\} - \frac{1}{3}\sum_{j=1}^{3}{\Lambda^P}_j\mathcal{L}^{-1}\left\{\frac{{\Lambda^P}_j}{\sqrt{N}}\right\}\right] \tag{3.22}$$

where the terms have the same meaning as in Equation 3.20.

The tetrahedron model was originally proposed by Flory and Rehner [11] to have a stationary junction point at the center of the deforming tetrahedron of Gaussian chains as in Figure 2.2. Treloar [12,13] modified the model by using non-Gaussian chains and allowing the junction point to seek an equilibrium position under the forces on the stretched chains in the network. The location of the junction point position at a given stretch state was found from an iterative procedure. In this Chapter we implement the tetrahedron model using Langevin chains whose junction point seeks out an equilibrium position under the applied principal stretches, after Treloar [13]. The position of the junction point is solved for using a Newton-Raphson scheme to find zero net force on the junction point as a function of principal stretches and junction point coordinates.

3.5 Results

3.5.1 Experimental results

The uniaxial compression and plane strain compression experimental stress-strain curves are shown in Figure 3.7 for PMMA at a strain rate of -0.001/s and in Figure 3.8 for PC at -0.01/s.[1] The strain rates were chosen such that nearly isothermal conditions prevailed throughout the deformation for each of the materials as confirmed by the temperature measurement techniques described in detail in Chapter 5. The stress-strain behavior for both materials was found to strongly depend upon the state of deformation. The observed yield stress in plane strain compression is higher than in uniaxial compression due to the plane strain constraint; the effect is further amplified because of the pressure dependence of yield in these materials. Following initial yield, both materials are observed to strain soften under uniaxial and plane strain compression conditions and to subsequently strain harden. The strain hardening is found to strongly depend on the state of deformation, progressing more rapidly with inelastic straining under plane strain compression than under uniaxial compression conditions. The contrast in hardening is due to the uniaxial orientation of chains which occurs in plane strain compression deformation versus the planar orientation which occurs under uniaxial compression. The additional paths for chain orientation in uniaxial compression permit larger strains thus "delaying" the orientation dependent strain hardening and extending the "locking" or limiting strain achieved in uniaxial compression beyond that achieved in plane strain compression. This will become more evident in the expanded discussion of the modelling versus experimental results. The dramatic state of deformation dependence emphasizes the need for an accurate tensorial description of material state to describe the large deformation behavior of polymers.

The results of birefringence measurements on the inelastically deformed specimens are plotted in Figure 3.9 as a function of inelastic strain for uniaxial compression PMMA specimens. These birefringence measurements were made on slices cut perpendicular to the uniaxial compression direction. Specimen birefringence is a measure of the optical anisotropy in a plane obtained from the relative retardation of light travelling perpendicular to the plane. Birefringence results from the anisotropic alignment of molecular dipoles within the material along principal strain directions in the plane of the specimen.

Our basis for modelling the strain hardening response of glassy polymers such as PMMA has been the capture and characterization of the three dimensional nature of

[1]The testing machine compliance has been subtracted from the raw data, yielding the results of Figures 3.7 and 3.8. Machine compliance was determined from the uniaxial compression apparatus and applied to the data of both uniaxial and plane strain compression tests. Plane strain testing required the additional apparatus sketched in Figure 2.12, this may have introduced an error in the experimentally determined plane strain stiffness.

molecular chain orientation during inelastic deformation. Measurements were made on each plane as described by the unit normal to the face and also at different magnitudes of strain. Table 3.1 compares results of birefringence measurements on plane strain compression and uniaxial compression specimens.

face	birefringence	strain
uniaxial		
1: $\frac{1}{\sqrt{\lambda}} - \frac{1}{\sqrt{\lambda}}$	0.00	-20%
2: $\lambda - \frac{1}{\sqrt{\lambda}}$	0.000640	-20%
3: $\lambda - \frac{1}{\sqrt{\lambda}}$	0.000640	-20%
1: $\frac{1}{\sqrt{\lambda}} - \frac{1}{\sqrt{\lambda}}$	0.00	-65%
2: $\lambda - \frac{1}{\sqrt{\lambda}}$	0.000897	-65%
3: $\lambda - \frac{1}{\sqrt{\lambda}}$	0.000897	-65%
plane strain		
1: $\lambda - \frac{1}{\lambda}$	0.001051	-43%
2: $1 - \lambda$	0.000425	-43%
3: $\frac{1}{\lambda} - 1$	0.000597	-43%

Table 3.1: Uniaxial and plane strain compression birefringence results.

In uniaxial compression the principal stretches are λ, $\frac{1}{\sqrt{\lambda}}$ and $\frac{1}{\sqrt{\lambda}}$ where λ is the stretch along the compression direction. For the uniaxial compression specimens the material is isotropic through the thickness direction parallel to the compression direction (ie. in the $\frac{1}{\sqrt{\lambda}}$, $\frac{1}{\sqrt{\lambda}}$ plane). As a result of this axisymmetric deformation the birefringence measured through a thickness along the compression direction is zero. The birefringence through any plane perpendicular to the compression direction, ie. through any λ, $\frac{1}{\sqrt{\lambda}}$ plane, is constant for a given amount of residual plastic strain. As the magnitude of residual strain increases the birefringence perpendicular to the uniaxial compression direction increases as shown in Table 3.1, illustrating the evolution of birefringence and hence, orientation, with inelastic strain. During plane strain compression the principal stretches are λ, 1 and $\frac{1}{\lambda}$. Measurements of birefringence made through thicknesses parallel to the three principal stretch directions are found to be non-zero in all three directions and to depend on the relative anisotropy in the planes of the specimens. These measurements confirm and further emphasize the tensorial nature of molecular chain orientation and developing anisotropy during large stretch deformations of glassy polymers. We further note that the birefringence of the $\lambda - \frac{1}{\lambda}$

plane at -43% strain under plane strain conditions is significantly higher than that at -65% strain under uniaxial conditions, again demonstrating a dramatic difference between both the state and the degree of orientation imposed under different conditions of straining.

The normalized load versus diametral contraction results from the cold drawing of PC as a function of constant displacement rate are presented in Figure 3.10. The data at $2.54mm/minute$ registered a peak load of $2349N$; the initial diameter of the measured contracting region was $6.35mm$ in all specimens. The effect of rate on the maximum load is to increase the peak load with increasing rate. The amount of strain softening is not strongly affected by the applied displacement rate, and at large values of cross-section contractions the data converge, showing little rate dependence in this regime. At yielding the specimen necks down in the immediate vicinity of the minimum cross-section and, upon yielding and softening, a very rapid decrease in diameter is recorded by the lateral extensometer. Once the neck stabilizes locally drawing ensues as material is pulled from increasingly wider diameters adjacent to the extensometer. During this process the load cell records very little increase in stress. Continued drawing eventually becomes increasingly more difficult as the undrawn region from which material is being pulled increases in size and hardening of the drawn material occurs. Eventually the phenomenon of locking is recorded as a sharp upturn in the load versus displacement curve reflecting the increased difficulty in further deforming the material. The specimen fractures at the advent of locking.

The data in Figure 3.10 have been converted to true local stress versus true local strain and plotted in Figure 3.11A. Included with this data are the results of a uniaxial compression test on PC at a strain rate of -0.01/second. In Figure 3.11B the strain rate versus strain results of the cold drawing experiment are included which illustrate that the local strain rate increases by an order of magnitude during yielding, but that the nominal strain rate is close to that of the compression test included in Figure 3.11A. All aspects of the cold drawing response have been affected by the changing strain rate during deformation which occurred in the tension experiment, resulting in a yield point for the tension test which is responding to a higher rate than is the compression result. The affects of strain rate on the yield and subsequent response of PC is discussed in more detail in Chapter 5. Here it suffices to say that the rate effects on the strain hardening response of PC are small enough as to be overwhelmed by the state of deformation dependence observed in the cold drawing versus compression results in Figure 3.11A. The strain hardening response in the tensile deformation experiment results from a uniaxial alignment of the polymer chains in a manner which is similar to the plane strain results of Figure 3.8. The uniaxial compression deformation results in a planar orientation of chains as discussed earlier, thus delaying "locking" in uniaxial compression beyond the failure strain in the cold drawing experiment.

3.5.2 Model results and comparison with experiments

In Chapter 5 we discuss constant strain rate uniaxial tests over a range of strain rates and temperatures on PC and PMMA. Results from these tests provide the material properties which capture the rate, temperature, and strain softening behavior of the material, the procedure for determining these properties for PMMA are discussed in [33]. The material properties for both materials are tabulated below in Table 3.2:

	PC	PMMA
Elastic		
E(MPa)	2300	3250
ν	0.30	0.30
Yield		
$\dot{\gamma}_0(s^{-1})$	$2(10^{15})$	$2.8(10^{7})$
$A(m^3)$	$3.31(10^{-27})$	$1.39(10^{-27})$
Softening		
h(MPa)	500	315
$\frac{s_{ss}}{s_0}$	0.79	0.82

Table 3.2: Material properties required by the model.

The strain hardening properties required by each of the rubber elasticity models considered here need to be determined. Three network models of rubber elastic deformation have been individually considered as the strain hardening element, each of these requires two material properties. The strain hardening properties are a hardening modulus, $C_R = nk\Theta$, and limiting chain stretch, $\sqrt{N}$. These were obtained for each of the three models by fitting the uniaxial compression data, providing the following:

	PC	PMMA
three chain		
C_R(MPa)	17.0	12.0
N	3.5	3.8
four chain		
C_R(MPa)	200.0	100.0
N	2.95	2.75
eight chain		
C_R(MPa)	12.7	10.5
N	2.25	2.5

Table 3.3: Strain hardening material properties required by the rubber elasticity models.

Since the uniaxial compression response was used to fit the hardening behavior, the corresponding behavior using the three chain, tetrahedron and eight chain models of the strain hardening response is expected to be well characterized in all cases. The plane strain simulations used the properties determined in the uniaxial compression tests and therefore provide a true test of the ability of each model to predict the state of deformation dependence of the strain hardening response.

Figure 3.12 depicts the three chain model simulations in uniaxial and plane strain compression for PC at a strain rates of $-.01/s$, superposed with the experimental results at the same strain rate presented earlier in Figure 3.8. Figure 3.13 similarly presents the three chain model simulations for PMMA at $-.001/s$ and corresponding experimental data. In both cases the uniaxial compression data is well modelled as anticipated. The three chain model of Wang and Guth [10] does predict a state of deformation dependence, albeit incorrectly, to the strain hardening response of PC and PMMA. The predicted dependence grossly underpredicts the limiting extensibility in plane strain compression based on the uniaxial compression locking stretch. The three chain model fails to correctly capture the tensorial nature of the orientation process. Insight as to why this is so is provided by the schematic of the three chain model given earlier in Figure 2.1 for two deformation states. In the three chain model the limit in extensibility is always achieved for the single chain locking stretch, $\sqrt{N}$. In plane strain compression one chain stretches to its locking stretch value, the two remaining chains in the network deform subject to the incompressibility constraint on the entire model. The model predicts limiting extensibility when the dimension change in the direction of principal chain extension, $\frac{1}{\lambda}$, equals the chain locking stretch, $\sqrt{N}$. In uniaxial compression two chains stretch equivalently albeit independently, while the

third must compress according to incompressibility of the network. The stretching chains reach their locking stretch value together, but the applied stretch at which this occurs differs from that in plane strain. Locking is predicted when $\frac{1}{\sqrt{\lambda}} = \sqrt{N}$ in uniaxial compression. Thus a state of deformation dependence on the strain hardening response is predicted by the model. But as the comparisons with the data in Figures 3.12 and 3.13 show, the correct tensorial nature of the strain hardening response is not captured. This model responds without any cooperative network stretch save the incompressibility constraint. In the actual material a stretching chain is linked to a network by entanglements influencing other chains to stretch and providing a network response.

The results of simulations with the four chain model are compared with the experimental data in Figures 3.14 and 3.15 for PC and PMMA, respectively. Although it was assumed that each model could reproduce the uniaxial compression curve of either material, the tetrahedron model was found to lack the correct curvature needed to capture the PMMA data, regardless of material property selection. The best fit to the uniaxial compression PMMA curve is presented; material parameters corresponding to this curve were used to predict the plane strain response. Two sets of simulations were performed for the tetrahedron model, these differed only in the orientation of the chains in the tetrahedron with respect to principal stretch space. One orientation used appears in the sketch of Figure 2.2, the other is rotated 90° from this orientation. As the results in Figures 3.14 and 3.15 show, the tetrahedron model does predict a state of deformation dependent strain hardening behavior, but fails to adequately capture this aspect of the response. In addition, the tetrahedron model does not possess symmetry with respect to principal stretch space. The lack of orthogonal symmetry in this model results in plane strain simulations which depend on the spatial orientation of the tetrahedron. The tetrahedron model fares somewhat better than the three chain model in its prediction of the plane strain response. The chains in this model undergo stretches cooperatively so that the network limiting extensibility rather than a single chain extensibility determines the locking stretch value. The network extensibility changes with deformation state for the tetrahedron model.

Simulations with the eight chain model developed in Chapter 2 are compared with the experimental data of PC in Figure 3.16 and PMMA in Figure 3.17. As was the case for the three chain and tetrahedron models, the strain hardening response predicted by the eight chain model is based entirely on the two material properties in Table 3.3 determined from the uniaxial compression test, and the model geometry and functionality. Unlike the earlier models presented, the eight chain model is found to capture the strong state of deformation dependence of both polymers with remarkable accuracy. All chains in the eight chain model stretch equally under any deformation state, the chain deformation for two such states was sketched in Figure 2.3. The stretch in each chain is that given earlier in Equation 3.23,

$$\lambda_{chain} = \frac{1}{\sqrt{3}}\left(\lambda_1^2 + \lambda_2^2 + \lambda_3^2\right)^{1/2} = \frac{1}{\sqrt{3}} I_1^{1/2} \tag{3.23}$$

this stretch is simply the root mean square of the applied plastic stretches. Because eight chains undergo this stretch, the model essentially averages contributions from eight orientations of a single chain in space. The root mean square of the stretches apparently governs the state of deformation dependence of the strain hardening response, as evidenced by the success of this model in predicting this response for the materials studied here.

The cold drawing experiment was simulated using the eight chain strain hardening element and the material properties determined from the uniaxial compression test. The finite element model used in the simulation appears in Figure 3.18. One quarter of the axisymmetric geometry is modelled using ABAQUS type CAX8R elements. The nodes at the top of the model (the specimen grip section) are constrained in the axial direction. The nodes at the bottom of the model (the specimen center) are prescribed to displace axially at $2.54mm/minute$ in accordance with the experiment. The nodes at the symmetry axis are constrained radially.

The results of the simulation at $2.54mm/minute$ are plotted as normalized load versus diametral contraction in Figure 3.19 and compared with the experimental results. Figure 3.20 contains the local stress versus local strain results of the simulation and experiment at $2.54mm/minute$. All aspects of the material response are accurately predicted including the peak load, percent load drop and natural draw ratio in the load versus contraction data and the yield stress, strain softening and strain hardening characteristics of the stress-strain response. The applicability of the present polymer deformation model to problems of glassy polymer deformation processing is strongly evident from the results of Figures 3.19 and 3.20. The cold drawing process, which includes time-varying, non-uniform deformation, is very accurately captured by the model presented in this Chapter using material properties determined from characterization of the uniaxial compression tests.

The results of implementing the rubber elasticity network models described in Chapter 2 into the strain hardening element of the glassy polymer models follow analagously from the results of the simulations on rubbery materials in Chapter 2. The three and four chain models are seen to fail to accurately predict the state of deformation dependence on strain hardening in glassy polymers for the same reasons they failed to accurately capture the three dimensional rubber deformation. Conversely, the eight chain model universally describes the state of deformation dependence of networks both above and below the glass transition temperatures of polymer solids.

3.6 Summary

In this Chapter the large strain deformation response of two glassy polymers, PC and PMMA, has been examined. Constant strain rate tests in uniaxial compression and

plane strain compression were performed on these materials which have revealed a tensorial nature to the strain hardening response of these materials that is strongly a function of the state of deformation. Birefringence measurements of oriented polymers reveal that the observed strain hardening in the mechanical response evolves with an increase in optical anisotropy that arises from molecular network orientation. The anisotropy evolves with magnitude of strain and state of strain as confirmed by birefringence results in uniaxial compression and plane strain compression. This strain induced orientation has been modelled using network representations from the rubber elasticity literature [10,11] and by the eight chain model of rubber elasticity developed in Chapter 2. The earlier models fail to truly capture the tensorial nature of the orientation processes during large strain deformation and cannot predict the correct state of deformation dependence of the strain hardening response of PC or PMMA. The eight chain model has been shown to fully capture the state of deformation dependence of the glassy polymer strain hardening response through its ability to physically mimic the cooperative nature of network deformation. The model requires one test to determine two physically based material properties describing anisotropic strain hardening, an initial modulus and a limiting network extensibility, then uses the information to predict the response of the material to other deformation states.

A cold drawing experiment was conducted on PC. The eight chain model was used in the simulation of the cold drawing experiment and found to accurately capture all aspects of this polymer forming operation. In Chapter 4 the glassy polymer model described here is used to predict effects of initial orientation in glassy polymers on flow stresses, deformation patterns and finite extensibilities.

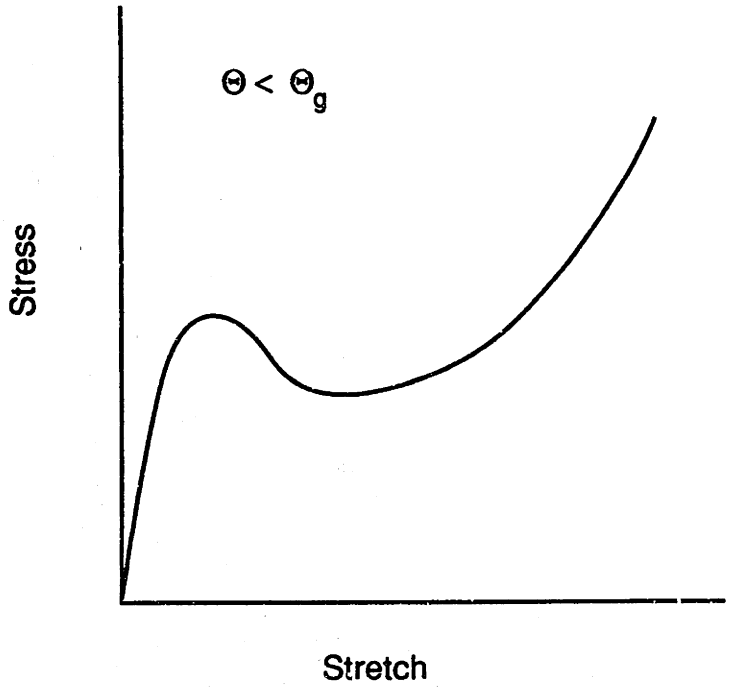

Figure 3.1: Sketch of glassy polymer stress versus stretch response showing yield, strain softening and orientation induced strain hardening.

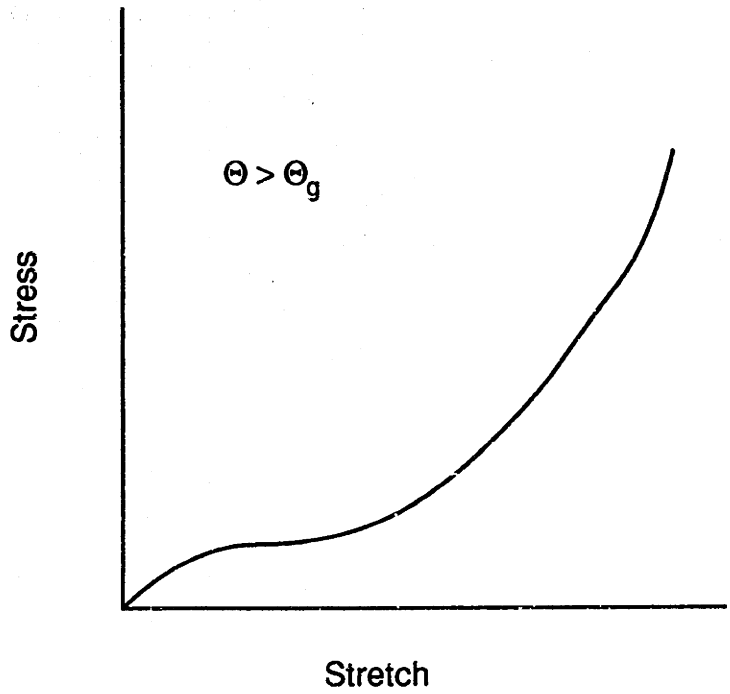

Figure 3.2: Sketch of rubbery polymer stress versus stretch response showing extensive elastic strain hardening.

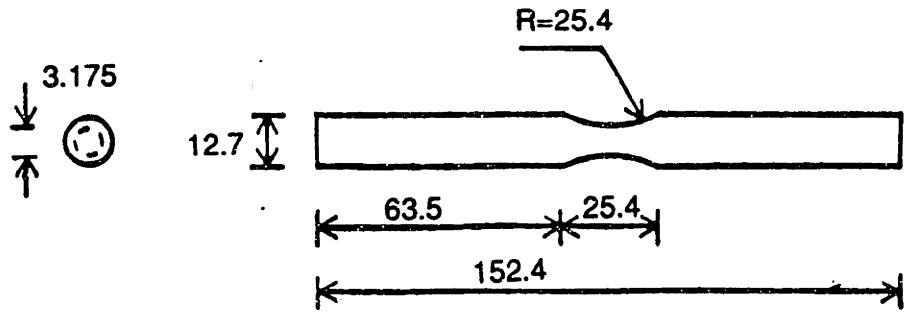

Figure 3.3: Sketch of the axisymmetric specimen used in the cold drawing of PC, all dimensions are in mm.

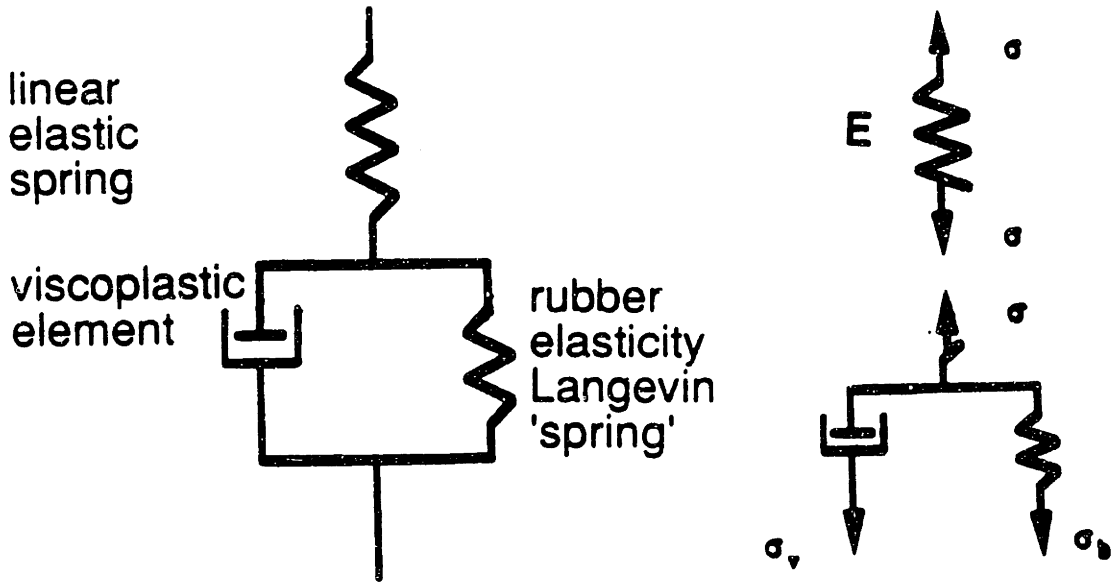

Figure 3.4: One dimensional analog to the spring and dashpot model of polymer deformation containing an elastic spring in series with a viscous dashpot and non-linear spring.

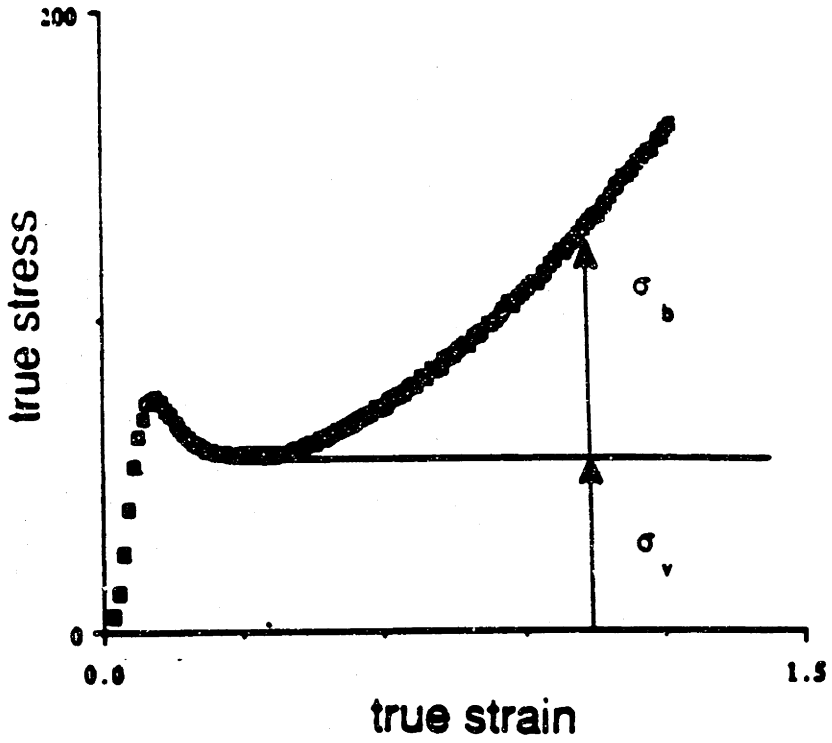

Figure 3.5: Stress-strain response of glassy polycarbonate showing contributions of all model elements to the total deformation response.

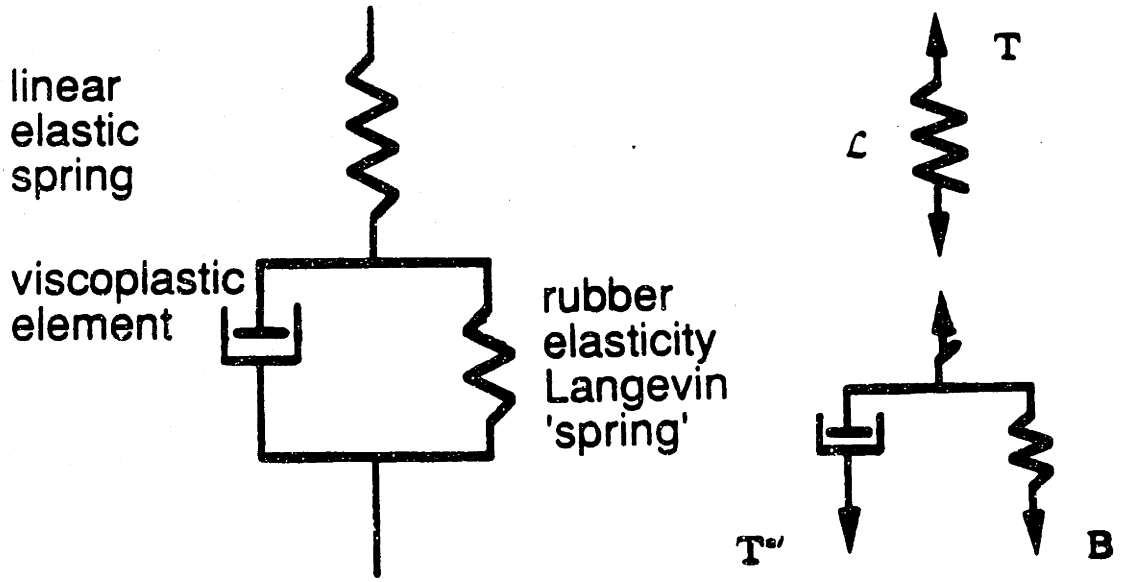

Figure 3.6: Three dimensional representation of the polymer deformation model which includes the tensor of elastic constants, the Argon model of rate and temperature dependent yield and the non-linear rubber elasticity spring element.

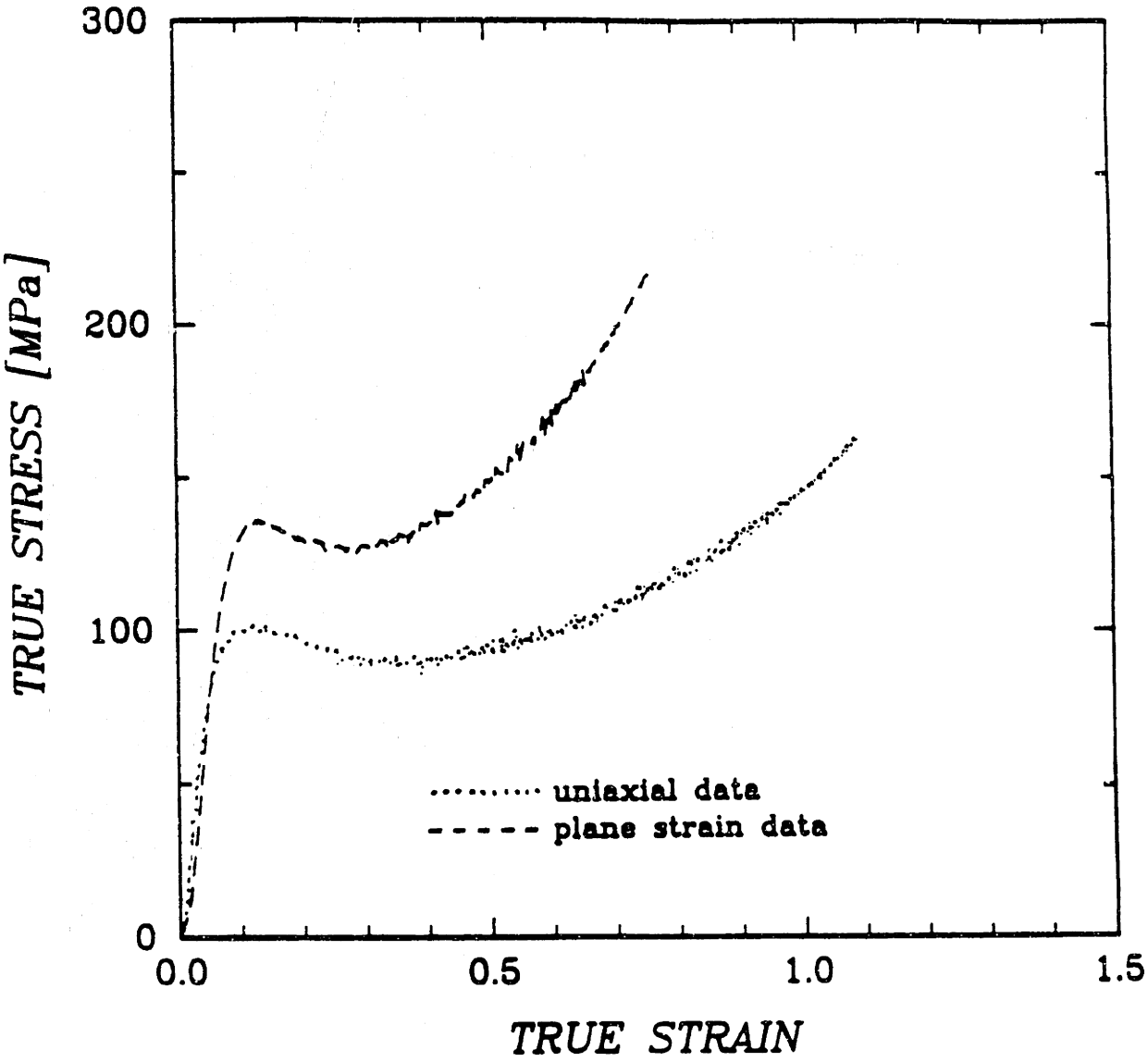

Figure 3.7: Experimentally determined uniaxial compression and plane strain compression stress-strain curves for PMMA at $\dot{\epsilon} = -0.001/s$ and room temperature.

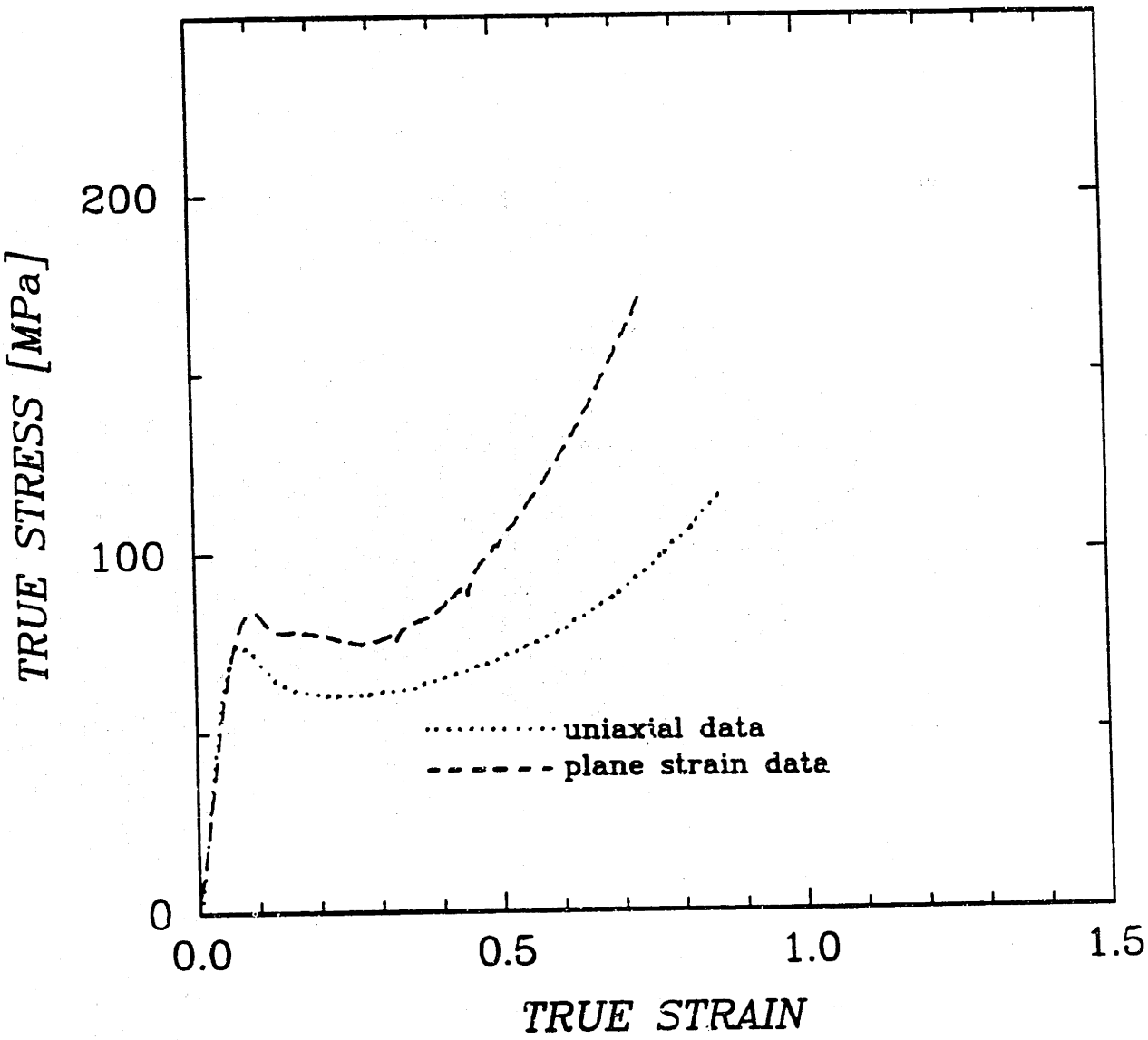

Figure 3.8: Experimentally determined uniaxial compression and plane strain compression stress-strain curves for PC at $\dot{\epsilon} = -0.01/s$ and room temperature.

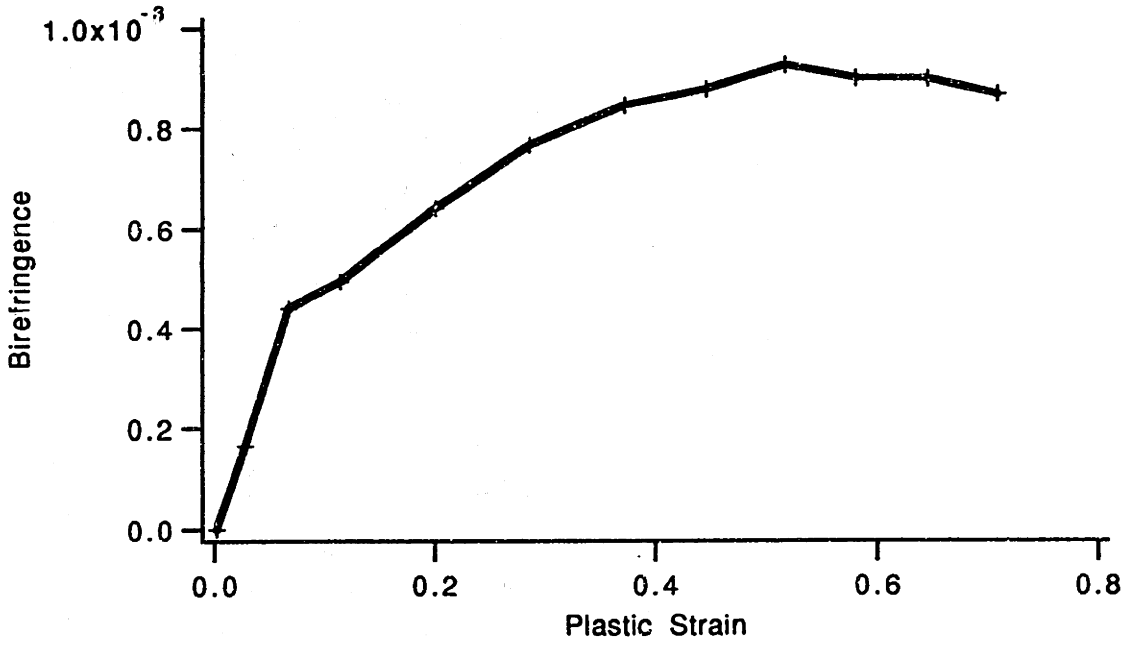

Figure 3.9: Evolution of birefringence with plastic strain in PMMA from uniaxial compression tests to various amounts of plastic strain.

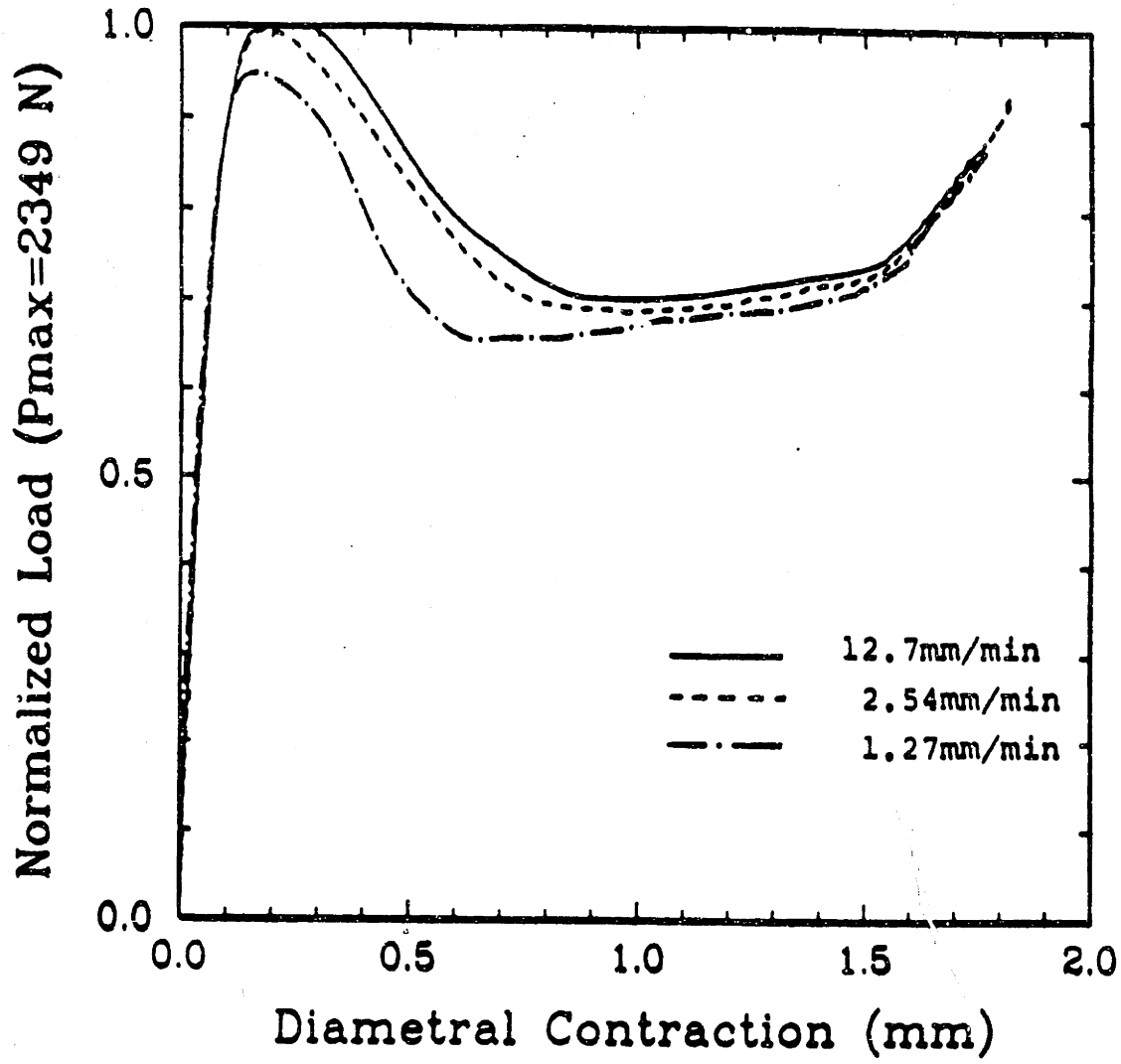

Figure 3.10: Normalized load versus diametral contraction response for the cold drawing test on PC as a function of constant displacement rate and at 23°C. The peak load at yield is 2349 N.

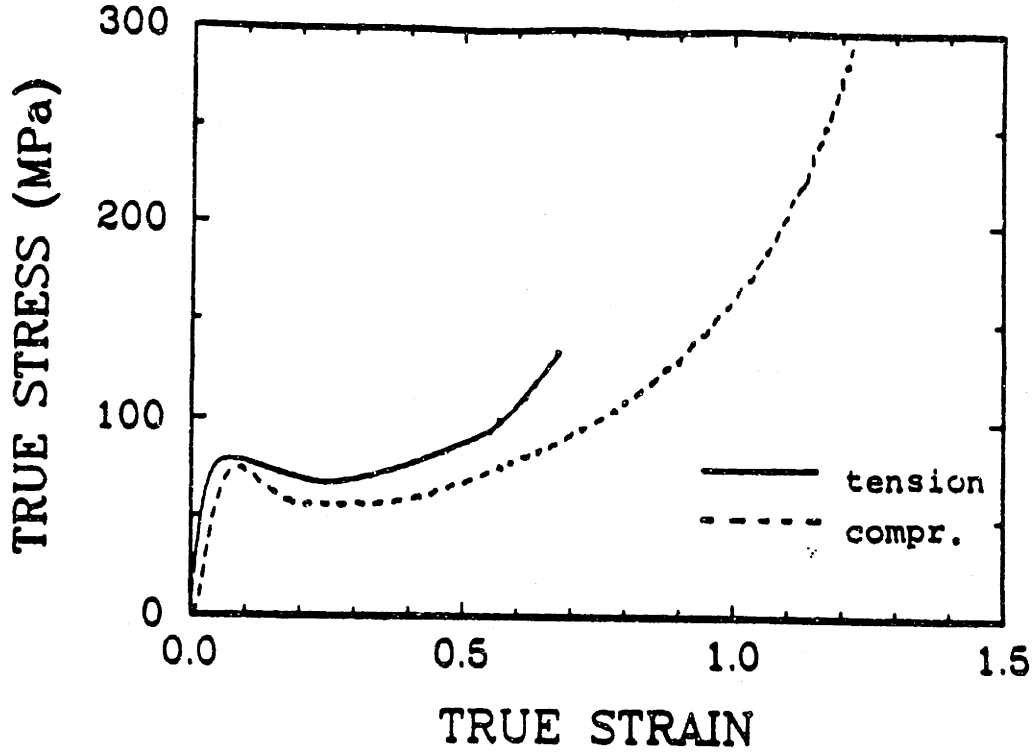

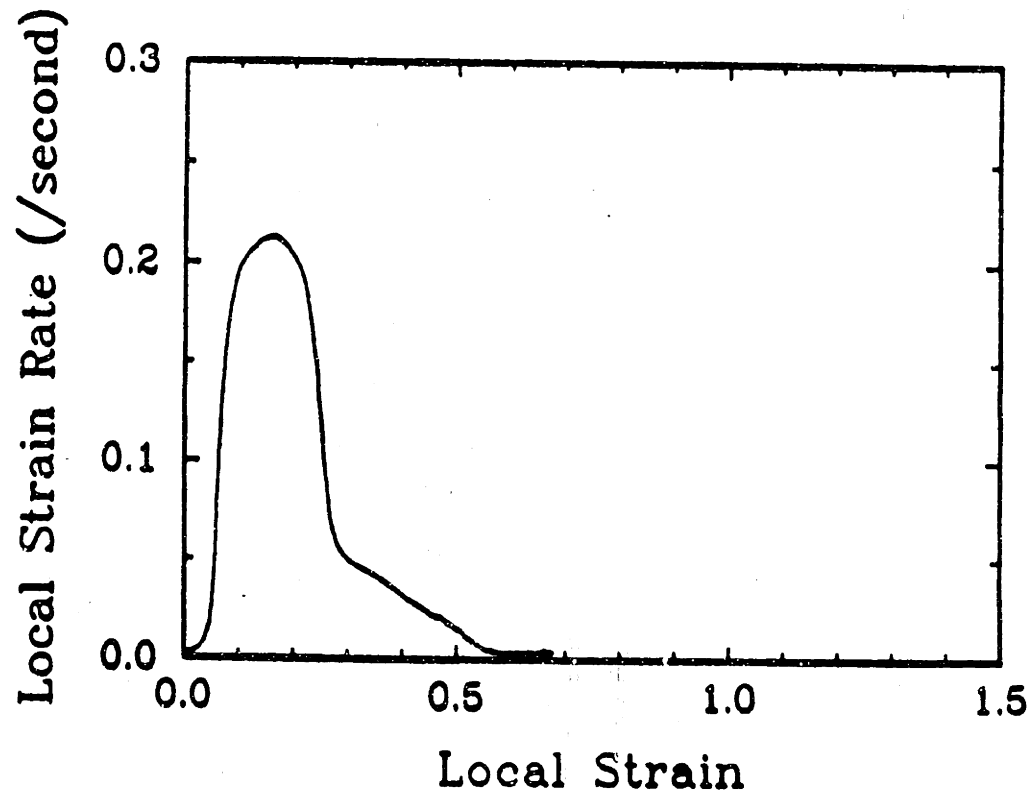

Figure 3.11: (A) True stress versus true strain response for PC during cold drawing at 2.54*mm/minute* and uniaxial compression at -0.01/second deformations. (B) Local strain rate versus strain for the cold drawing experiment calculated for the region of the neck.

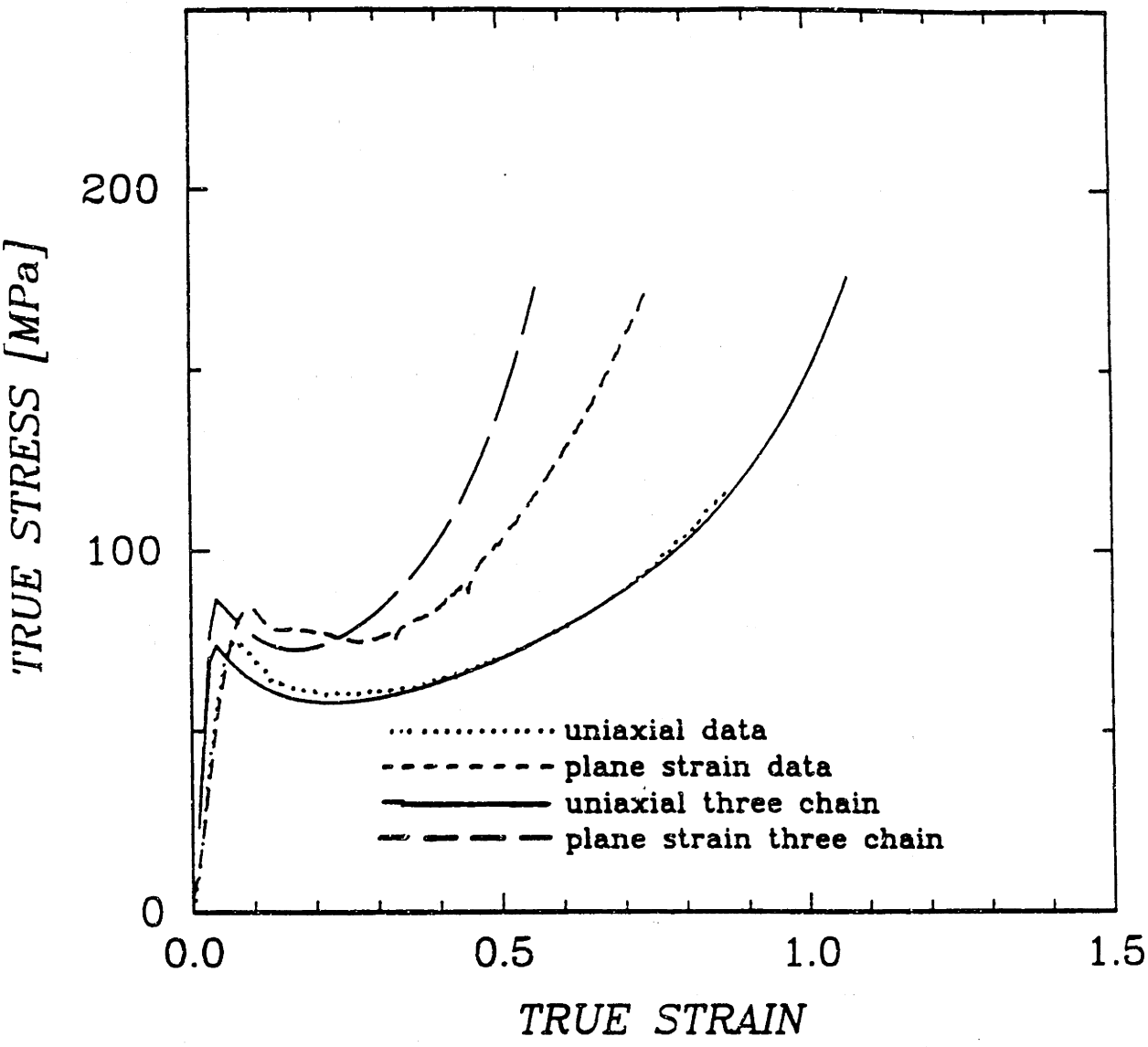

Figure 3.12: Three chain model simulations and experimental curves of the uniaxial compression and plane strain compression responses of PC at $\dot{\epsilon} = -0.01/s$. The model was fitted to the uniaxial response, then the plane strain response was predicted based on uniaxial properties.

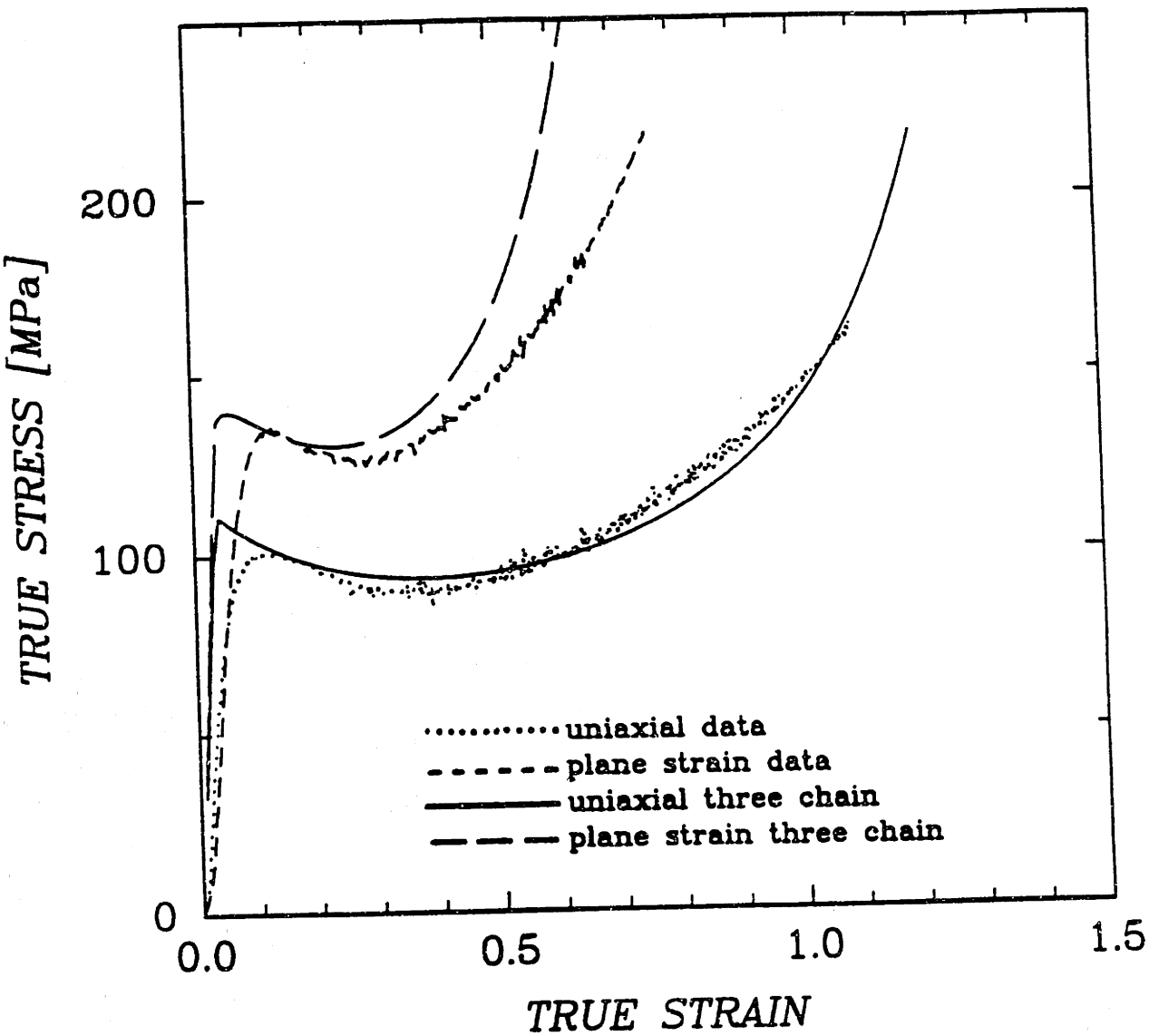

Figure 3.13: Three chain model simulations and experimental curves of the uniaxial compression and plane strain compression responses of PMMA at $\dot{\epsilon} = -0.001/s$. The model was fitted to the uniaxial response, then the plane strain response was predicted based on uniaxial properties.

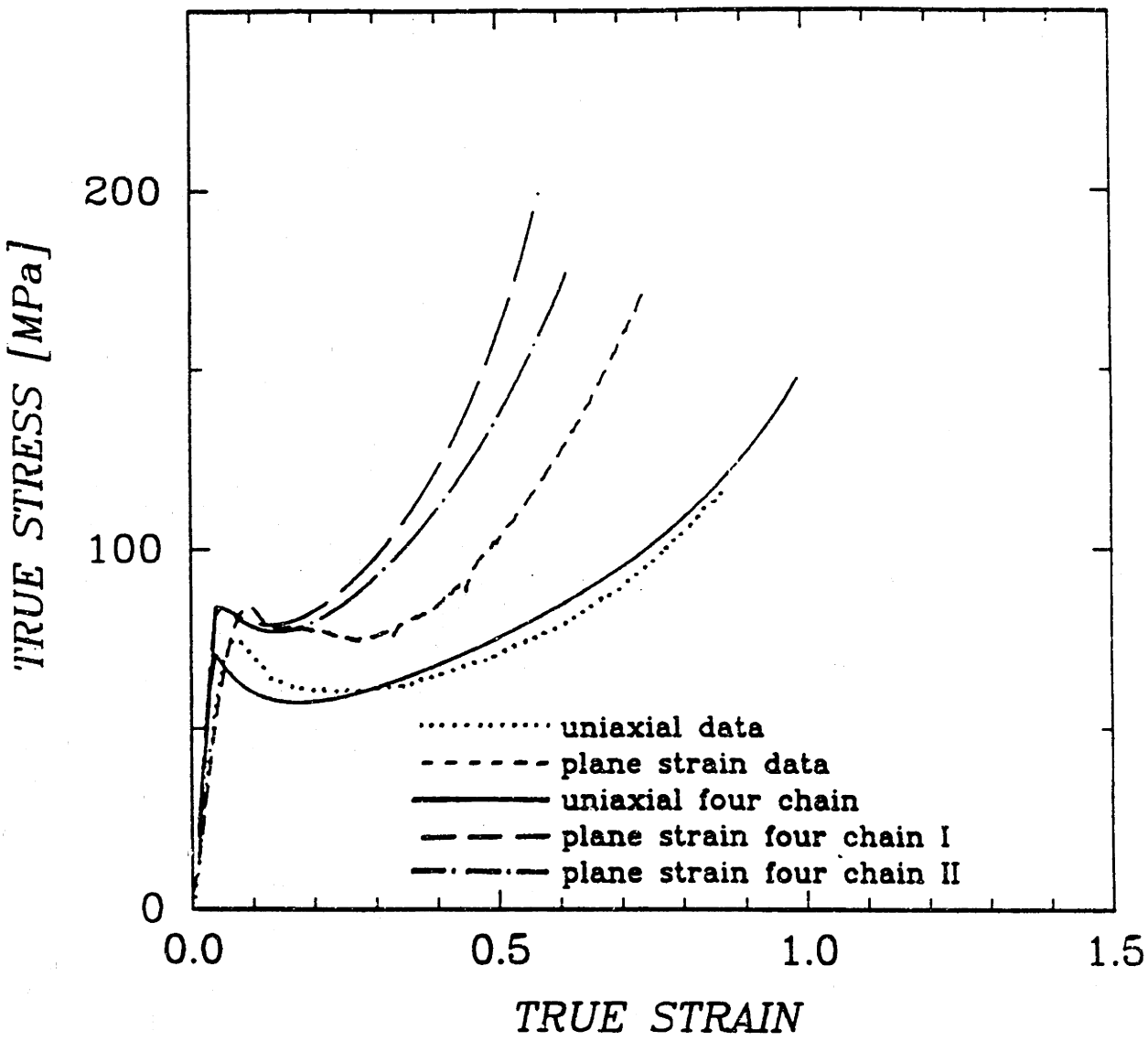

Figure 3.14: Four chain model simulations and experimental curves of the uniaxial compression and plane strain compression responses of PC at $\dot{\epsilon} = -0.01/s$. The model was fitted to the uniaxial response, then the plane strain response was predicted based on uniaxial properties. Two orientations of the four chain model were implemented as discussed in the text.

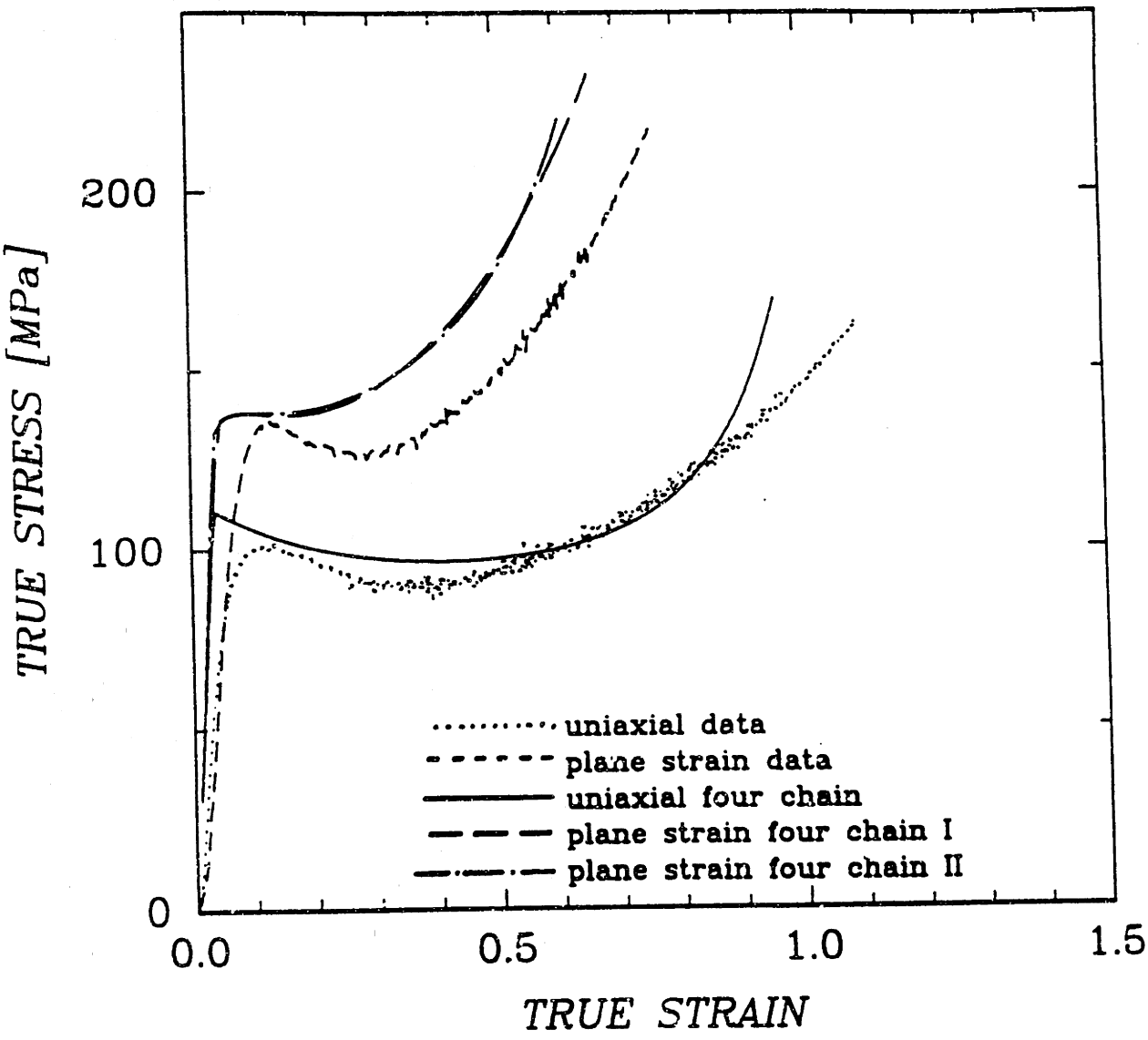

Figure 3.15: Four chain model simulations and experimental curves of the uniaxial compression and plane strain compression responses of PMMA at $\dot{\epsilon} = -0.001/s$. The model was fitted to the uniaxial response, then the plane strain response was predicted based on uniaxial properties. Two orientations of the four chain model were implemented as discussed in the text.

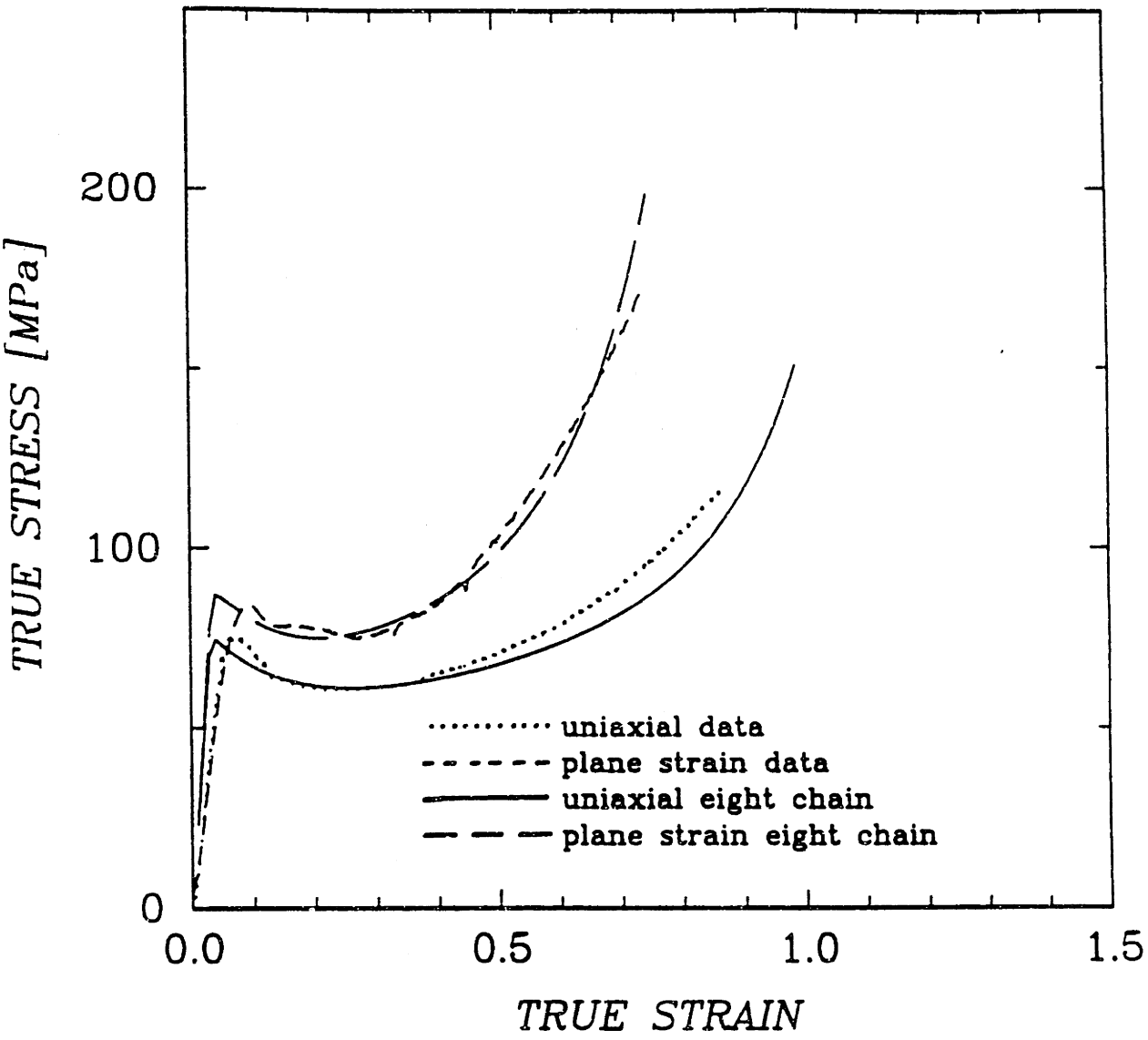

Figure 3.16: Eight chain model simulations and experimental curves of the uniaxial compression and plane strain compression responses of PC at $\dot{\epsilon} = -0.01/s$. The model was fitted to the uniaxial response, then the plane strain response was predicted based on uniaxial properties.

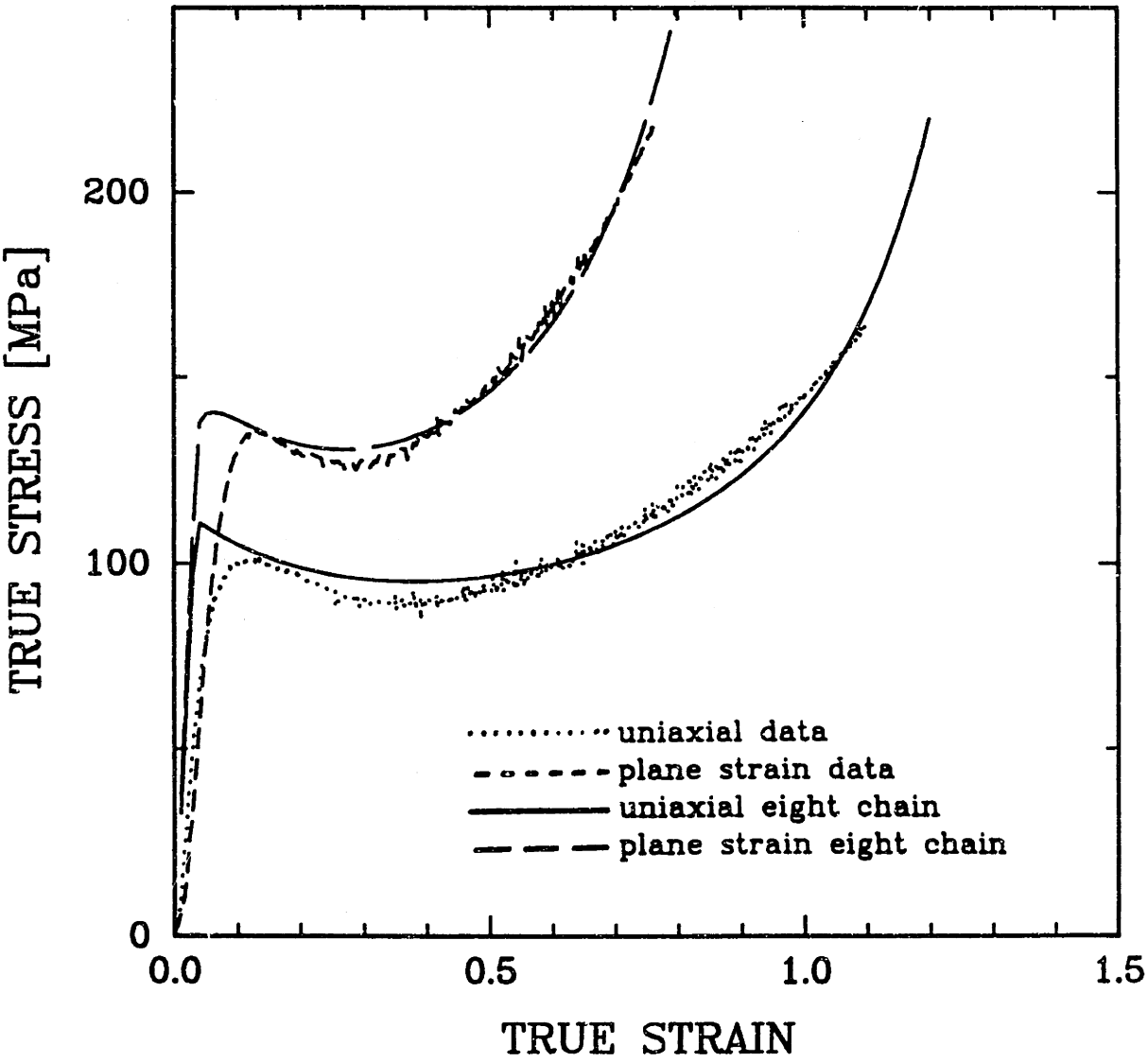

Figure 3.17: Eight chain model simulations and experimental curves of the uniaxial compression and plane strain compression responses of PMMA at $\dot{\epsilon} = -0.001/s$. The model was fitted to the uniaxial response, then the plane strain response was predicted based on uniaxial properties.

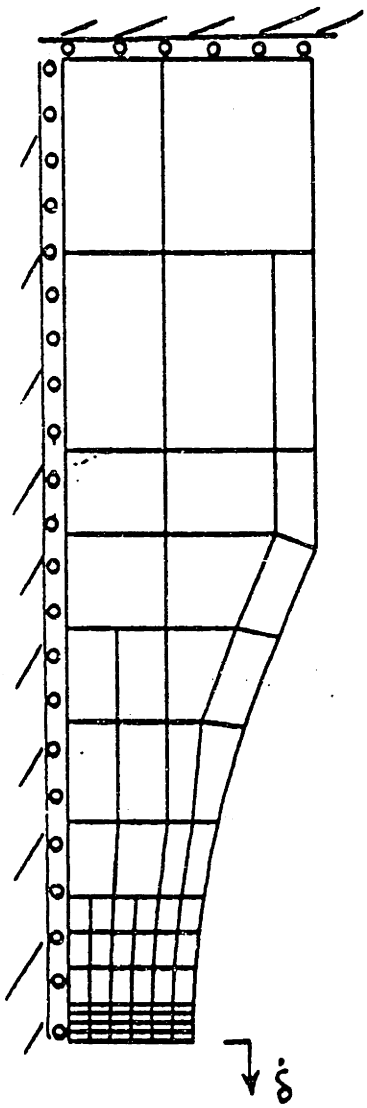

Figure 3.18: Finite element model of the cold drawing experiment using eight node reduced integration axisymmetric elements.

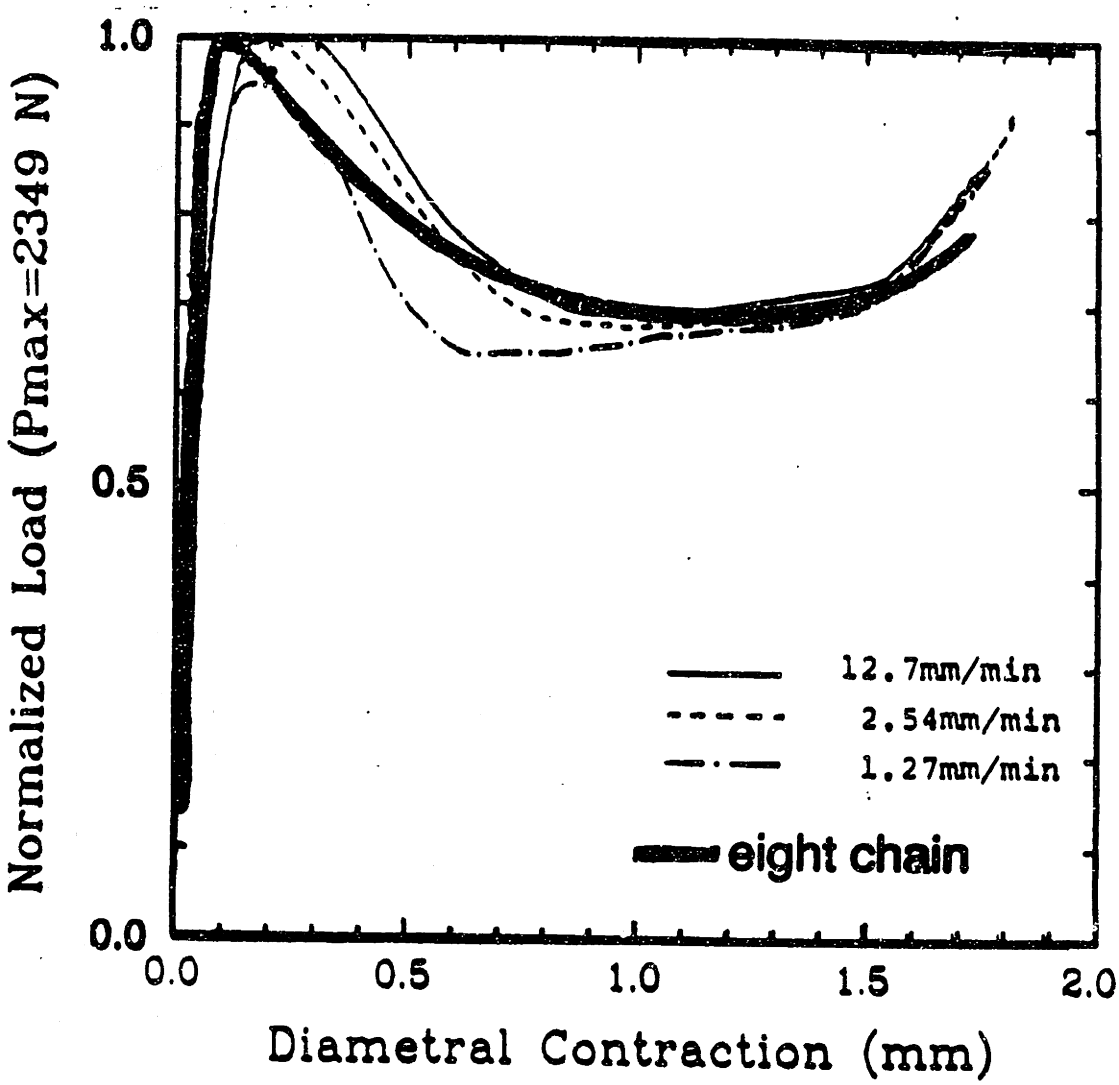

Figure 3.19: Comparison of experiment and simulation at $2.54mm/min$ for the load versus contraction of the cold drawing of PC using the eight chain strain hardening element.

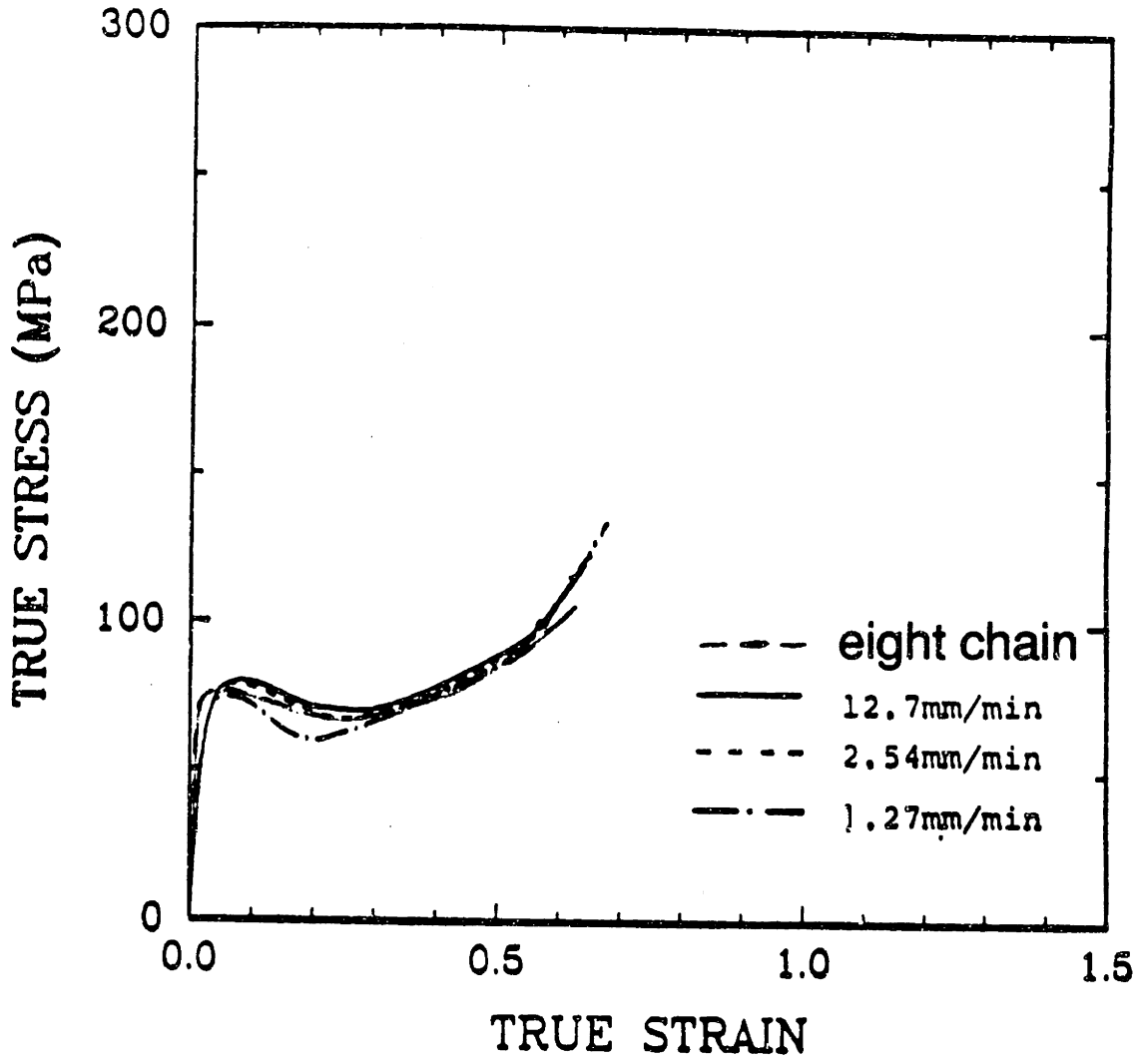

Figure 3.20: Comparison of experiment and simulation at $2.54mm/min$ for the true stress versus true strain of the cold drawing of PC using the eight chain model as the strain hardening element.

Chapter 4

Effects of Initial Anisotropy on the Finite Strain Deformation Behavior of Glassy Polymers

In the previous Chapter a model was developed for the large strain deformation response of glassy polymers. We have shown that the model captures the tensorial evolution of anisotropy in initially isotropic materials by virtue of its ability to predict the strongly state of deformation dependent strain hardening behavior of PC and PMMA. We now discuss our investigation of the effects of initial anisotropy on the response of glassy polymers. The issue of existing anisotropy in glassy polymers is raised as it concerns the solid phase deformation processing of these materials. Highly anisotropic polymer components are produced during solid phase processing as a result of the massive reorientation of molecular chains during the large strain forming operation. Indeed the polymer preform used as the starting material is usually anisotropic owing to its prior deformation history. The process end product has often been fashioned for a particular application, i. e. to possess an increased flow strength along a particular axis, thereby exploiting the orientation induced anisotropy effects. The fully three dimensional issues involved in the use of glassy polymer components include anisotropic flow strengths, limiting extensibilities and deformation patterns. These characteristics have been altered by the initial forming operation but are obviously not expected to be enhanced in all directions. It is imperative that all aspects of existing anisotropy in polymer components be understood prior to service as the presence of anisotropy in structural components may also lead to premature failure or unexpected shear localization.

In this Chapter the effects of initial deformation and the associated anisotropies are investigated through uniaxial compression tests on preoriented polycarbonate (PC) and polymethylmethacrylate (PMMA) specimens. The evolving anisotropy is monitored by testing materials preoriented by various amounts of strain and under different states of deformation. The tensorial nature of the anisotropic material is

characterized by examining the preoriented material response in three orthogonal directions.

The universality of the polymer deformation model developed in the preceeding Chapters is evaluated based on its ability to predict, through full, three dimensional consideration, the anisotropies manifested in the compression results contained in this Chapter. All aspects of the anisotropic response of glassy PC are shown to be accurately captured based on the characterized isotropic response and a knowledge of the anisotropic state of the material.

Although anisotropy evolves with temperature and strain rate, which will be discussed in further detail in Chapter 5, we submit an experimental observation that the subsequent deformation response of preoriented polymers may be predicted using only a measure of optical anisotropy, and not the prior strain or thermal history. Optical anisotropy, as measured for example by birefringence, therefore represents a true internal variable indicative of the evolution of anisotropy with inelastic strain, state of strain and temperature.

4.1 Introduction

Polymer components are often manufactured by any of a number of processes such as forging, stamping or extruding, known collectively as solid phase deformation processes. In such processing operations a glassy polymer preform is subjected to large strains while exposed to spatially and time varying temperatures, pressures and strain rates. The intended deformation of the preform is not homogeneous in general. For instance, during forging some regions of the material undergo large deformations while neighboring regions deform very little. The preform is usually anisotropic in the as-received condition because of the rolling or extruding associated with the initial forming of solid polymer sheet or bar stock. Processing of an anisotropic material under the conditions described above for solid phase deformation must not only account for the direction dependent properties of the anisotropic polymer preform but should also anticipate undesirable features of anisotropic behavior such as premature fracture and shear banding. The component produced from a solid phase deformation processing operation is invariably anisotropic, exhibiting direction dependent flow strengths, limiting extensibilities, deformation patterns and strain hardening characteristics. While assessment of short term performance may simply require testing of the anisotropic nature of the polymer end product, design of processing operations to predict dimensional stability, meet net shape specifications and address structural integrity considerations requires accurate, three dimensional characterization of the effects of anisotropy on the behavior of glassy polymers during finite straining.

Previous experimental work on preoriented polymers include studies of the effect of preorientation on the elastic constants and yield in glassy polymers [51,41,42,35,52]. Rider and Hargreaves [35] oriented PVC by hot rolling then tested in uniaxial tension

at various angles to the rolling direction. They found the onset of yielding to occur in localized shear bands when testing off-axis from a principal orientation direction. Studies on oriented PET tested in tension describe observations of deformation bands in terms of the structure of oriented polymers [41]. For oriented PET sheet in which the material was tested in tension and in simple shear at different angles to the draw direction, shear localizations were found to always occur upon off-axis tensile testing but not always in shear [51]. Ward [34] measured the change in natural draw ratio as a function of preorientation in polyethylene terephthalate (PET) where he found the draw ratio of the material to reduce with increasing axial preorientation. In the shear band studies [41,42,35] the strong Bauschinger effect exhibited by these materials has been modelled by a scalar parameter which monitors the accumulation of an internal stress, this scalar parameter was used in a modified form of Hill's anisotropic yield criterion [40]. The buildup of an internal stored stress has been experimentally verified by Adams and Farris [43] using a deformation calorimeter and also by the calorimetry and DSC experiments of Oleynik [53].

Lee and coworkers have modelled both the tensile behavior and the solid phase cup forming of polycarbonate using an elastic-viscoplastic constitutive relationship [54,39]. Their model uses as the strain hardening element the Mooney-Rivlin rubber elasticity formulation which has been shown in Chapter 2 to not be capable of capturing the three dimensionality of the strain hardening response of rubber materials at large strains. Lee et. al. similarly find this representation not suitable for capturing strain hardening in glassy PC [39]. The model developed in the preceeding chapters has been shown to capture the tensorial nature of strain hardening in macromolecular networks. It is expected that this model can predict the response of anisotropic polymers as well. This Chapter is concerned with investigation of the three dimensional yield and post yield characteristics of preoriented materials. Highly anisotropic materials were produced by an initial orientation process and both the magnitude of initial strain and the deformation process used to preorient the materials were varied. Several specimens were cut from each preoriented sample to allow for testing of the anisotropic response by uniaxial compression in three directions. The preoriented specimens varied strongly in the amounts of strain endured prior to failure (limiting extensibilities), flow strengths, deformation patterns and strain hardening characteristics.

The three dimensional nature of the anisotropy in these materials warrants characterization in terms of a tensorial representation of the stored internal stress rather than a scalar parameter used in earlier studies [41,42,35]. The previous chapter showed the evolution of anisotropy with state of deformation and magnitude of strain to be the result of three dimensional orientation of the glassy polymer molecular network in response to plastic straining for PC and PMMA. The orientation induced anisotropy has been modelled as an internally stored backstress tensor which correctly accounts for the strong state of deformation dependence exhibited by two initially isotropic

glassy polymers, PC and PMMA.

It is desirable to determine whether the newly developed model of orientation induced anisotropy in initially isotropic materials has accurately captured the three dimensional aspects of the polymer response, and therefore represents a true constitutive relationship of glassy polymer deformation. Such a model can then be used in the design of solid phase processing operations to assess dimensional stability requirements and to meet net shape specifications and flow stress requirements. Using material properties identified for the isotropic polymer in the previous study, and a knowledge of the orientation state in the anisotropic specimen, uniaxial compression simulations are performed on anisotropic polymers. Comparisons are made of the flow strengths, extensibilities, cross sectional deformation patterns and strain hardening characteristics exhibited by the experimental results and predicted in the simulations.

4.2 Experiments

The experimental procedures outlined in the previous Chapter have been followed in obtaining the results of this Chapter as well. Specifically, the uniaxial compression and plane strain compression tests described earlier are used again as the processes by which specimens are preoriented. The anisotropic materials which resulted from either uniaxial compression or plane strain compression preorientation described above were cut into cubes for retesting using a Buehler Isomet low speed saw equipped with a silicon carbide wafer blade. Care was taken to insure the cutting operation produced no additional deformation sufficient to affect the material response. The isomet cutting operation was evaluated based on birefringence measurements of isotropic materials which were sliced using this same procedure. Since the cutting operation did not impart a birefringence to the isotropic material the operation was considered to not affect the deformation response of the preoriented specimens.

All tests on preoriented specimens were conducted in uniaxial compression; the compression direction, state of initial orientation and magnitude of initial orientation were variables in this study. The current strain in the preoriented material was measured at the time of recompression. The expected amount of extensibility was approximated for each individual preoriented specimen based on the magnitude and direction of the major orientation axis with respect to the subsequent compression axis, and each specimen was deformed to that estimate of its limiting strain. In this way the full range of the anisotropic response of the material could be captured during the recompression tests.

Recompression testing also included some interrupted tests for which the deforming cross section of the anisotropic specimens could be measured as a function of plastic strain. All three specimen directions were measured with a micrometer to give the current plastic strain with respect to the initial anisotropy in the material along the compression axis, and the cross section dimensions.

4.3 Modelling

The kinematics and constitutive relationships used in the modelling of the large strain deformation of initially isotropic glassy polymers was described in Chapter 3. Incorporation of the effects of initial anisotropy is acheived through an initial plastic deformation gradient which enters the formulation for anisotropic polymers [50]. The magnitude and state of strain resulting from the preorientation process are described by an initial deformation gradient $\mathbf{F}^i$. The relaxed configuration is achieved by elastically unloading, and the deformation gradient $\mathbf{F}$ is a product of the initial deformation gradient tensor, the additional plastic gradient of the current deformation process, $\mathbf{F}^{p*}$, and the elastic deformation gradient, $\mathbf{F}^e$:

$$\mathbf{F} = \mathbf{F}^e\mathbf{F}^p \tag{4.1}$$

$$\mathbf{F}^p = \mathbf{F}^{p*}\mathbf{F}^i \tag{4.2}$$

The relationships among the various configurations are shown in the schematic representation of Figure 4.1. The preorientation affects the total backstress tensor, the principal components of which depend on both the preorientation tensor and the reloading orientation. The backstress tensor of the total plastic deformation gradient in the relaxed configuration is coaxial with the left plastic stretch tensor,

$$\mathbf{F}^p = \mathbf{V}^p\mathbf{R}^p\,. \tag{4.3}$$

4.4 Results

4.4.1 Experimental results

Results of uniaxial compression and plane strain compression tests on isotropic PC are plotted in Figure 4.2. The strong state of deformation dependence exhibited in Figure 4.2 was described in Chapter 3 for PC and PMMA as being the result of a very anisotropic molecular orientation process which occurs in glassy polymers during plastic deformation. This evolution of anisotropy has been characterized in terms of the birefringence properties of oriented glassy polymers in Chapter 3; birefringence measurements confirmed that the three dimensional structures of specimens oriented under different states of deformation varied significantly with deformation state. Specifically, birefringence measurements establish that under uniaxial compression deformation the material develops axisymmetric anisotropy whereas the state of orientation developed during plane strain compression is fully three dimensional. Testing of materials preoriented by either uniaxial or plane strain compression with the constraint of a constant state of deformation during recompression serves to further illustrate and investigate the highly anisotropic nature of the oriented glassy polymer.

Figures 4.3 to 4.9 contain results of recompression tests on preoriented PC specimens. All recompression tests were conducted in uniaxial compression. Results include stress-strain responses and cross-sectional deformation maps for PC specimens initially loaded to various amounts of strain[1] in either uniaxial or plane strain compression thereby providing a number of specimens with different initial states of orientation. Each figure of anisotropic stress-strain results includes the response to the initial deformation procedure used to preorient the material.

Table 4.1 contains the principal stretch state for each of the preoriented specimens and is provided to aid in the descriptions of the experimental results and comparisons with simulations . All results for preoriented materials will be discussed in terms of the convention established in this table. Chains are oriented along directions for which the stretch is $\lambda > 1.0$ and coiled along directions having a stretch $\lambda < 1.0$.

Uniaxial Compression Prestrain
(transverse isotropy)

	Recompression Axes	λ_X	λ_Y	λ_Z
Figure 4.3	X(=Z), Y	1.3298	0.5655	1.3298
Figure 4.4	X(=Z), Y	1.4514	0.4747	1.4514
Figure 4.5	X(=Z)	1.2905	0.6005	1.2905
Figure 4.6	Y'	1.3962	0.5130	1.3962
	the Y axis is rotated 45° cw about the Z axis to the Y' axis			

Plane Strain Prestrain
(three dimensional anisotropy)

	Recompression Axis	λ_X	λ_Y	λ_Z
Figure 4.7	X, Y, Z	1.4191	0.7047	1.0000
Figure 4.8	X, Y, Z	1.6487	0.6065	1.0000
Figure 4.9	X, Y, Z	1.6487	0.6065	1.0000

Table 4.1: Summary of anisotropic cases considered in this paper, including convention used to describe the directions in the preoriented materials.

[1]This material recovers on the order of 25% of the total strain upon unloading and prior to redeforming the specimens. Strains reported in the following sections are the values of current plastic strain at the time of recompressing the materials unless otherwise noted.

initial transversely isotropic orientation

Figure 4.3 shows the strongly anisotropic response of PC preoriented in uniaxial compression to a current plastic strain of $\epsilon = -0.57$. The specimen is biaxially oriented as a result of the initial compression, the material possesses transverse isotropy with respect to the original compression axis. Birefringence measurements from Chapter 3 confirm the chains are preferentially oriented in the plane normal to the compression axis as a result of uniaxial compression. The data in Figure 4.3 include the recompression responses along the original compression direction (Y) and perpendicular to the initial compression axis (along the Z axis). The anisotropic effects include direction dependent flow strengths, extensibilities and strain hardening characteristics. Comparisons of the preoriented material responses with the isotropic behavior also included in Figure 4.3 show that the anisotropic flow strength is increased for recompression normal to the plane of chain orientation and reduced for recompression along a direction of chain orientation. The isotropic response includes a significant amount of strain softening from the initial yield stress level. Enhancing the yield strength of preoriented materials beyond the original isotropic value requires a significant amount of prestrain to orient the chains and combat the softening effect. The result of preorienting to small amounts of strain on the order of 20% to 35% is to actually decrease the flow stress in all directions.

It is perhaps useful to point out that the resistance to plastic flow in compression deformation experiments is always due to the presence or absence of preferential alignment of molecular chains in the plane normal to the current compression axis. The increased flow strength exhibited during recompression along the Y axis is the response of the material continuing to align chains in the XZ plane which had been partially oriented during the original compression. When the material is recompressed along the Z axis, the plane normal to the compression axis is the XY plane which is in a state of anisotropic alignment; one principal direction is a direction of preferential alignment and the other is the original compression axis in which chains are not stretched. The compression response in this case reflects the recoiling of the chains in the Z direction to a less oriented state, a process which overcomes a resistance to flow which is lower than the original isotropic resistance.

The other manifestations of the oriented molecular network include the post-yield strain hardening characteristics and direction dependent extensibilities. The extensibility of the material is greatly reduced for recompression along the Y axis because such a procedure attempts to further orient chains in the XZ plane. The rapidly accumulating strain hardening response of the material during this process reflects a rapid approach to locking of the chains at the extensibility limit. In contrast, compression along the Z axis recoils the oriented chains along the Z direction while forcing alignment in the XZ plane of the cross section. The process of initially reversing the effects of the initial orientation prior to reorienting the polymer chains increases the observed extensibility of the anisotropic material during recompression along the Z direction. The chains in this configuration offer less resistance to the compressive load as they return to a recoiled state; the stress-strain response to this process shows little strain hardening for most of the recompression deformation until the recoiling process

is complete and orientation perpendicular to the load axis begins.

The level of uniaxial prestrain is increased to 75% for the anisotropic responses of Figure 4.4. Recompression normal to the oriented chains is again characterized by an enhanced flow stress, more rapid strain hardening and greatly reduced extensibility compared to the isotropic response. As the level of prestrain is increased from 57% in Figure 4.3 to 75% in Figure 4.4 the flow stress is increased and the extensibility is reduced for loading along the Y axis because the increased Y prestrain has increased chain orientation in the XZ plane. For the anisotropic response along a direction of prior chain alignment such as the Z axis as seen in Figure 4.4, the flow stress is reduced, the strain hardening is delayed and the extensibility is enhanced as compared to the isotropic response. The increase in prestrain has increased the magnitude of each of these effects in the Z direction which can be seen from a comparison of Figures 4.3 and 4.4.

The uniaxial recompression along the Z direction of a specimen uniaxially preoriented to a current plastic strain of 51% was performed by incrementally loading the specimen. After each loading and unloading cycle the dimensions of the specimen were measured with a micrometer giving information on the current level of recompressive plastic strain and the cross sectional dimensions. The evolving cross section which was initially square has been drawn as a function of recompressive strain in the deformation maps of Figure 4.5. The highly anisotropic flow pattern of this material is further evidence of the effects of preorientation on the glassy polymer response. The X direction in Figure 4.5, for which very little deformation occurs, is a direction of prior chain orientation whereas the direction of primary material flow is the original compression direction, Y. Obviously chain orientation serves as a strong barrier to continued plastic deformation. The material flows very freely along the initial compression direction, and although it is not externally constrained from doing so, material flow is restricted in the oriented direction. The Y direction offers a path of low resistance for chains seeking to stretch and orient in the plane of the cross section. The previous discussion on the anisotropic strain hardening characteristics described the compression of oriented chains as an easy process when compared to either compressing the isotropic material or compressing the anisotropic material normal to a plane in which chains are oriented. The deformation maps illustrate that it is the combination of compressing oriented chains in the direction of loading and stretching of chains in a direction of low resistance normal to the compression axis that accounts for the very soft response of the anisotropic material in the Z direction.

Figure 4.6 contains the results of recompression on a specimen possessing axisymmetric orientation as was the case for the specimens tested in Figures 4.3 to 4.5. In the current case the recompression specimen was machined at 45° to the plane of transverse isotropy, and therefore recompressed at 45° to the original compression axis. The isotropic response is included in Figure 4.6 for comparison. The response of the material to a very high barrier to continued chain alignment at 45° to the compression axis included extensive specimen shear. This experiment was repeated for the purpose of measuring the deforming specimen cross section during the recompression. The current height and thickness were determined by micrometer measurement and recorded as a function of plastic strain. The width was calculated assuming

incompressibility.[2]

initial three dimensional orientation

Results of uniaxial recompression on specimens preoriented to 35% strain in plane strain compression appear in Figure 4.7 with the isotropic response included for comparison. Plane strain deformation produces a fully three dimensional anisotropic state as confirmed by the birefringence measurements of Chapter 3 which yielded different levels of optical anisotropy in the three planes of principal stretch. The amount of plane strain prestrain is increased to 50% in the recompression responses of Figure 4.8. The three dimensional anisotropy of the plane strain orientation process is evident from the very different responses of the material in three different directions. The effects of initial anisotropy, seen for the uniaxial preorientation results in Figures 4.3 and 4.4, accumulate more rapidly for preorientation in plane strain compression because plane strain deformation provides a one dimensional path for chain extension. Bearing in mind that the anisotropic responses are all due to uniaxial recompression, it is of interest to compare the anisotropic responses in Figures 4.7 and 4.8 to the results of Figures 4.3 and 4.4, the variables being magnitude of prestrain and state of prestrain. The strain hardening characteristics for recompression after plane strain preorientation all occur in response to a non-axisymmetric barrier to continued plastic flow whereas this was not true for Y recompression in uniaxially preoriented specimens. Each such recompression after plane strain compression initial orientation offers a preferential path for material flow; the rate at which strain hardening evolves is dependent on the strength of the weaker barrier, with the result of the weakest combination of barriers yielding the softest response.

The deformation maps in Figure 4.9 further illustrate the effects of a three dimensionally anisotropic barrier to plastic flow. The evolving cross section dimensions have been plotted versus recompressive plastic strain in Figure 4.9 for all three orientations of recompression specimens prestrained to 50% in plane strain. Because all three cross sections are in no way externally impeded from expanding, the effects of the anisotropic resistance to plastic flow are clearly seen to be responsible for the direction dependent flow patterns presented. The degree of the existing anisotropy in the plane of the cross section is directly apparent from the deformed shape of the cross section. The magnitudes of the individual barriers to plastic flow can be inferred by comparison of deformation maps and corresponding stress-strain curves. The material is strongest in recompression along the Y direction for which continued plastic flow requires the further orientation of chains in two previously oriented directions. Extensibility is greatly reduced in this direction owing to the existing chain orientation in the XZ plane. These results are similar to those found for the transversely isotropic material in that the response of the anisotropic material is a function of the three dimensional nature of anisotropy, depending on the level of chain orientation

[2]The size of the preoriented specimen prior to recompression was $2.15mm \times 5.20mm \times 4.55mm$. No accurate measure of the angle of shear during the recompression deformation could be obtained for this size specimen. The width dimension was similarly difficult to obtain directly owing to the shear in the width direction.

both in the direction of loading and in the plane normal to the compressive load.

The anisotropic effects illustrated here have implications for both the processing of solid polymer components from anisotropic preforms and the predicting of the structural integrity of anisotropic polymer components. Materials containing anisotropy can have very different responses from those expected for isotropic materials even if the anisotropy is not extensive. The initial yield response is greatly changed during strain softening, before any appreciable anisotropy develops due to chain orientation. The presence of substantial anisotropy results in vastly different strain hardening characteristics, flow strengths, deformation patterns and extensibilities from those expected for the isotropic polymer. Birefringence measurements from Chapter 3 confirm that the locked in polymer chain network orientation is responsible for the observed anisotropy of the large strain deformation responses.

effects of thermal and strain history

The ability to characterize the orientation induced mechanical anisotropy in glassy polymers by the measurement of optical anisotropy was investigated by the results of Figure 4.10 for two PMMA specimens subjected to different strain and thermal histories. Both specimens were preoriented in uniaxial compression; the *temperature* during deformation and magnitude of prestrain were variables. The stress-strain responses of two tests, one conducted at 23°C to a final strain of 89% the other tested at 75°C to 104% strain, are presented in Figure 4.10A. Upon unloading, and also cooling in the case of the 75°C test, the materials recovered to 66% and 83% respectively, these strains are marked on Figure 4.10A and represent the strains in the materials at the time of recompression. The two tests obviously represent two different strain and thermal histories. Residual birefringence measurements made on the specimens after recovery verify that these two specimens contain the same level of optical anisotropy. The birefringence versus current plastic strain results for these specimens are given in Figure 4.10B.

The preoriented materials were machined to supply two anisotropic specimens each for retesting under identical conditions at 23°C both parallel and perpendicular to the plane of chain orientation. Results of these recompression tests are given in Figure 4.11 and show that the highly anisotropic response of these materials, characterized by flow strength, strain hardening slopes and limiting extensibilities, are remarkably similar. The material property common to each of these specimens is the optical anisotropy measured by birefringence. Characterization of anisotropy in terms of the measure of birefringence shows great promise as a predictor of highly anisotropic mechanical behavior because of the similarity of results in Figure 4.11. The authors submit this experimental result as evidence for the use of optical anisotropy as a state variable, indicative of the three dimensional orientation state of polymers, and capable of a measurable amount of evolution with temperature as well as magnitude of strain and state of strain. Knowledge of the prior strain or thermal history of an anisotropic polymer preform or component is not necessary for predicting its response to a processing operation or service loads, provided the effects of anisotropy such as direction dependent flow strengths, strain hardening characteristics, limiting exten-

sibilities and deformation patterns presented here can be well characterized. In the section which follows the successful characterization of the isotropic state in terms of the three dimensional backstress tensor is shown to fully predict the anisotropic behavior. A basis is established by this work for incorporating the measurable evolution of birefringence into the existing framework of a model for an evolving molecular network.

4.4.2 Comparisons with simulations

The procedure used to characterize the evolution of anisotropy during large strain deformation of glassy polymers has been described in detail in Chapter 3 and will only be summarized here. The rate and temperature dependence of initial yield, described by the Argon expression in Equation 3.9, requires two tests to characterize the rate and temperature dependencies of the material. Characterization of the strain hardening response requires one test to determine the two physically based parameters of the tensor resistance in Equation 3.20. One of the tests required for the rate and temperature dependent characteristics serves also as the test required for obtaining the additional information on strain hardening, thus the total number of required tests is two. The properties required of the strain hardening response are the limiting chain extensibility, $\sqrt{N}$, and the rubbery modulus, $C_R = nk\Theta$, these are determined by fitting values to the uniaxial compression curve shown in Figure 4.2. Characterization of the evolution of anisotropy in the initially isotropic polymer is complete for isothermal responses with this process. The large strain response of the isotropic polymer to any state of deformation can be predicted based on the characterization of the original uniaxial compression response *without changing the material properties determined from the uniaxial compression response.* The plane strain compression response of PC is simulated in this manner.

The results in Figure 4.12 illustrate the ability of the model to predict the strong state of deformation dependence of glassy polymers using the procedure just outlined. As in the procedure described in Chapter 3, the model has been fit to the uniaxial compression data in Figure 4.12 and used to predict the plane strain compression data, also in the figure. The current theory models the initial response of the glassy polymer as linear elastic to the point of the yield stress. Yield is itself modelled as an instantaneous process, resulting in immediate strain softening of the simulated response. In contrast the actual material undergoes a viscoplastic response after approximately -0.05% strain and the actual yield event is the result of a thermally activated and rate sensitive number of transformations which occur over a range of straining [48]. The simulations of the anisotropic responses continue to predict linear elastic behavior followed by a sudden imposition of inelastic deformation whereas the experimental results which follow will show a more gradual transition to inelastic deformation.

predicting the effects of initial axisymmetric anisotropy

The incorporation of the initial orientation into the model is achieved in terms of an initial deformation gradient, $\mathbf{F}^i$, which produces an initial backstress tensor, as described in Section 4.3. No additional parameters are introduced to simulate the anisotropic effects presented earlier. Complete characterization of the evolving backstress tensor is achieved by the single uniaxial compression test in Figure 4.12 and the knowledge of the anisotropic state of the material described by $\mathbf{F}^i$.

The comparison of theory with experiment begins with the anisotropic response of a material preoriented to 57% strain in uniaxial compression which was described in Figure 4.3 and is reproduced along with the results of the simulations in Figure 4.13. The strongly direction dependent responses of preoriented PC are very accurately predicted with the model. The theory captures the anisotropic flow stresses, the strain hardening behaviors and the limiting extensibilities as they have been described. In particular, the simulation of the recompression along the Z axis predicts the extensive softening effect owing to the compression of coiled chains during this deformation. The simulation matches the highly anisotropic experimental result for the entire recompressive strain, capturing the enhanced extensibility of the material in this direction. The anisotropic response along the Y axis appears in stark contrast to the Z direction recompression. The true usefulness of the theory is its ability to very accurately characterize this highly anisotropic behavior, capturing the rapid accumulation of orientation induced strain hardening which leads to reduced extensibility in this direction.

Increasing the level of prestrain in the anisotropic material was shown earlier to intensify the differences in the direction dependent responses. As the results in Figure 4.14 show, the model continues to capture the effects of initial anisotropy as the level of anisotropy increases.

The size of the deforming anisotropic cross section was monitored during the Z axis recompression simulation of a material preoriented by -51% strain. The predicted deformation map has been plotted versus recompressive strain in Figure 4.15 for comparison with Figure 4.5. Agreement between theory and experiment is extremely good, the deforming cross section simulation results from an accurate characterization of the relative strengths of the barriers to plastic flow which exist in the cross section. The simulations predict that virtually no plastic flow occurs along the X direction after -97.5% recompressive plastic strain, a remarkable testimony to the relative strength of the barrier to continued plastic flow along the X axis which is the result of highly oriented chains in this direction.

Figure 4.16 contains the comparison of theory with experiment for the transversely isotropic material recompressed along the Y' axis such that the plane of principal chain orientation was at 45^o to the recompression axis. The figure shows how remarkably well the theory predicts the stress-strain response of the specimen which undergoes extensive shear as part of its anisotropic response to the recompression. The strain hardening response of this specimen is linear to -60% strain at which point an increase in the slope of the stress-strain response can be detected. The theory accurately captures this effect, predicting an initially linear strain hardening response, albeit at

a slightly higher slope than that of the data, then capturing the onset of an increasing strain hardening slope at 60% strain. The prediction lies within 5 MPa of the actual response throughout the strain hardening portion of the stress-strain curve. The simulated deformation maps actually predict specimen shear during the recompression, but because an accurate measure of the actual experimentally observed specimen shear could not be obtained, the experimental and simulated deformation maps can not be included for comparison. A comparison has been made in Table 4.2 of the size of the deformed specimen as determined from micrometer measurements[3] and predicted in the simulations versus current plastic strain. The size of the deforming anisotropic specimen is well predicted in addition to the stress-strain response, verifying that this model accurately accounts for the effects of initial anisotropy in glassy polymers. This recompression of an anisotropic specimen at 45° to the plane of transverse isotropy, which involves considerable specimen shear, provides a test of the ability of the model to capture the behavior of the preoriented glassy polymer when the principal axes of network stretch change during deformation. Our finite deformation decomposition for an anisotropic material described in Section 4.3 accounts for the response during lagre rotations of the principal network stretch space by prescribing the backstress tensor to be colinear with the left plastic stretch tensor. As the results in Figure 4.16 show, this formulation provides a very accurate characterization of the response during a deformation with boundary conditions involving changing directions of the principal network stretches.

Experiment	**Simulation**
ϵ=-25.9%	ϵ=-28.9%
t=1.0442	t=1.0440
w=1.2395	w=1.2400
ϵ=-55.8%	ϵ=-53.8%
t=1.1190	t=1.0890
w=1.5610	w=1.5670
ϵ=-69.3%	ϵ=-66.4%
t=1.1760	t=1.1200
w=1.7000	w=1.7160

Table 4.2: Comparison of the experimentally determined and predicted normalized sizes of the cross section of the deforming specimen described in Figures 4.6 and 4.16 at various levels of recompressive strain.

[3]The width dimension of the specimen was calculated from incompressibility as described in Section 4.4.1

predicting the effects of initial three dimensional anisotropy

Results of simulations on the anisotropic response of materials containing three dimensional anisotropy as a result of initial deformation in plane strain compression are shown with the experimental data in Figures 4.17 to 4.19. The stress-strain responses, which vary significantly in all three directions, are again very accurately captured by the model. The simulations required the characterization of the isotropic response in uniaxial compression and the knowledge of the anisotropic state of the material to accurately account for the three dimensional nature of changes in flow stresses, extensibilities, strain hardening characteristics, and deformation patterns. The simulations are particularly accurate in capturing the shapes of the strain hardening curves, matching slopes and extension limits with the experimental data in all three directions. The predictive capabilities of the theory are perhaps best represented in the three recompression deformation maps of Figure 4.19 which are almost exact replicas of the experimentally determined counterparts in Figure 4.9. The relative strengths of the barriers to continued plastic flow in directions X, Y and Z can be directly determined from these deformation maps. The implications these results have for the problems of processing of anisotropic polymers and using processed polymer components in structural applications are astounding. Never before has such anisotropic behavior been so readily predicted as in this study.

Clearly the isothermal response of these materials has been fully and accurately described by the model developed and verified in this thesis. To the author's knowledge, no other existing theory of the large strain response of anisotropic materials comes close to either monitoring the evolving anisotropy or capturing the effects of initial anisotropy based on the initial isotropic simple compression behavior. In Chapter 5 where the effects of temperature and strain rate are examined, we will present a model for the temperature dependent strain hardening response and show that this model predicts the same backstress tensor for the two anisotropic specimens tested in Figure 4.11. The identical responses of these specimens, preoriented under the different histories in Figure 4.10A and found to possess the same amount of anisotropy by the birefringence results of Figure 4.10B, result from the identical anisotropic states in the two specimens. This anisotropy is measured by the backstress tensor in our model, a measure of anisotropy which is in agreement with the birefringence measure in that both methods predict identical anisotropic states for the specimens in Figure 4.11.

4.5 Summary

The effects of initial anisotropy have been experimentally observed to include direction dependent flow stresses, strain hardening characteristics, limiting extensibilities and deformation patterns. The existing anisotropy is a strong function of the deformation state used to preorient the material. Two anisotropic states were examined here, the transversely isotropic state developed during preorientation in uniaxial compression and the fully three dimensional state of anisotropy produced during plane strain deformation. These remarkably direction dependent responses of anisotropic glassy

polymers warrant thorough characterization for applications involving processing of anisotropic materials or the use of anisotropic polymer components in service.

The model for the evolution of anisotropy during large strain deformations in glassy polymers from Chapter 3 was used here to predict the anisotropic effects in preoriented materials. The model requires one test to characterize the evolving anisotropy and the knowledge of the current state of anisotropy in the preoriented materials. All aspects of the anisotropy were well predicted with the model confirming for the first time in any material the ability to completely capture the essence of three dimensional anisotropy under large strain deformations.

An experimental observation that the anisotropic response of glassy polymers can be characterized by the current level and three dimensional nature of anisotropy, regardless of the strain or thermal history which produced the anisotropy, was included. Birefringence has been targeted as a basis for directly incorporating the material characterization of anisotropy into the anisotropic backstress element of the existing model.

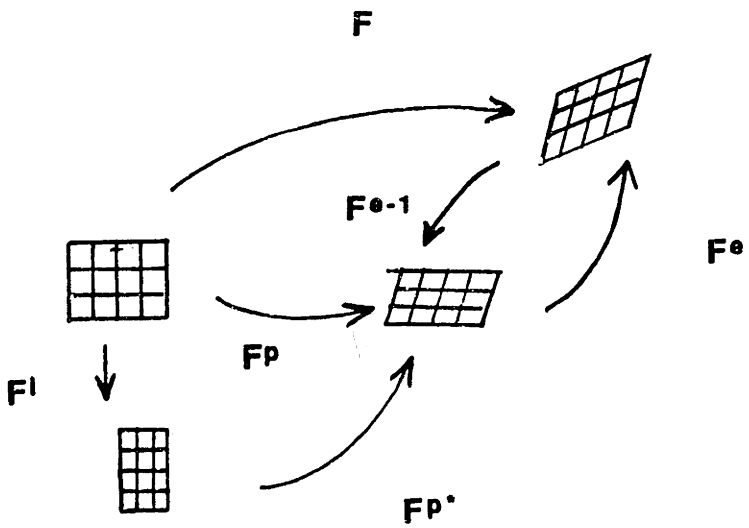

Figure 4.1: Schematic representation of the kinematic configurations required for the description of anisotropic glassy polymers, and their relationships to various deformation quantities.

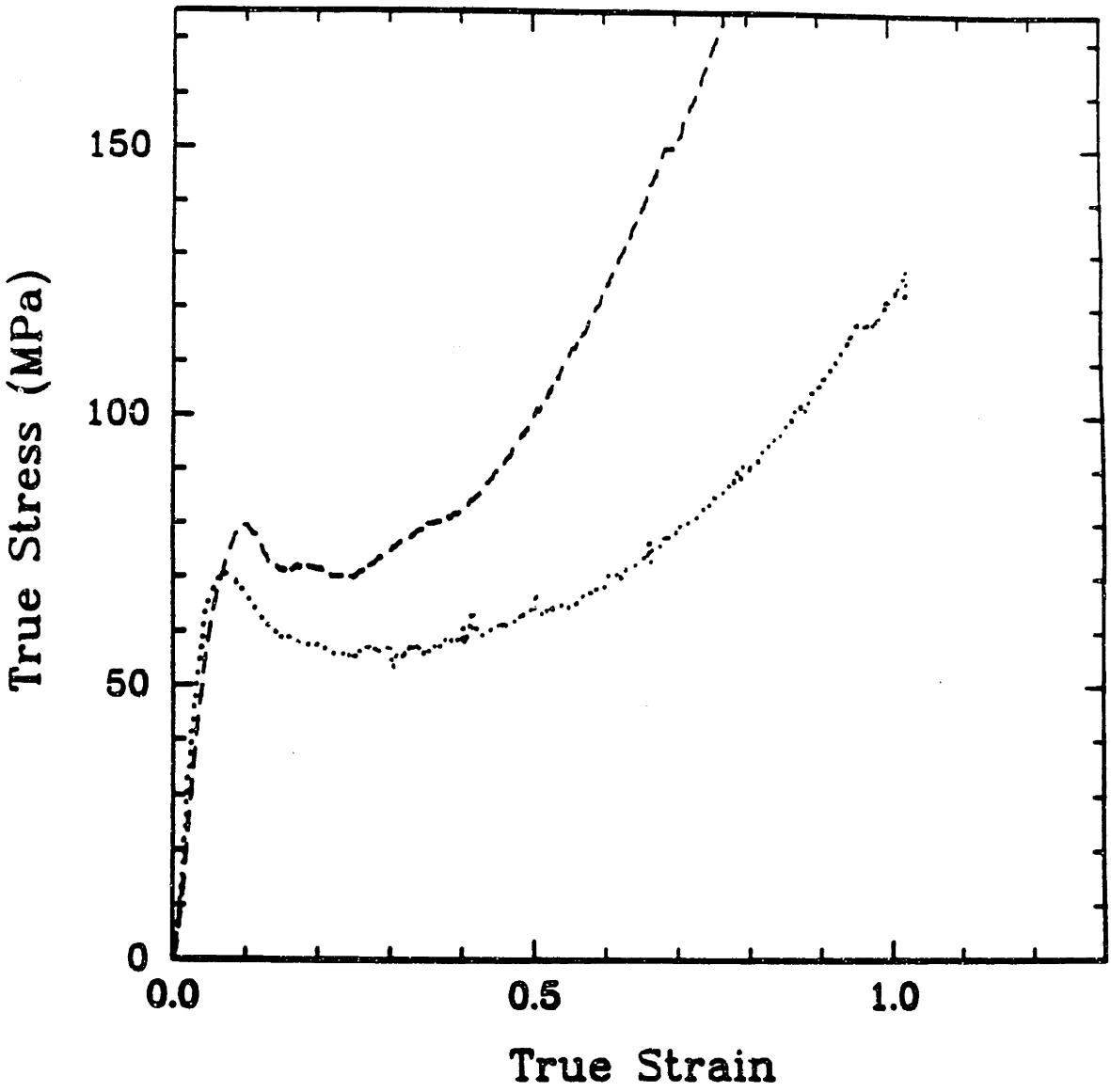

Figure 4.2: Experimentally determined uniaxial compression and plane strain compression stress-strain curves for PC at $\dot{\epsilon} = -0.001/s$ and room temperature.

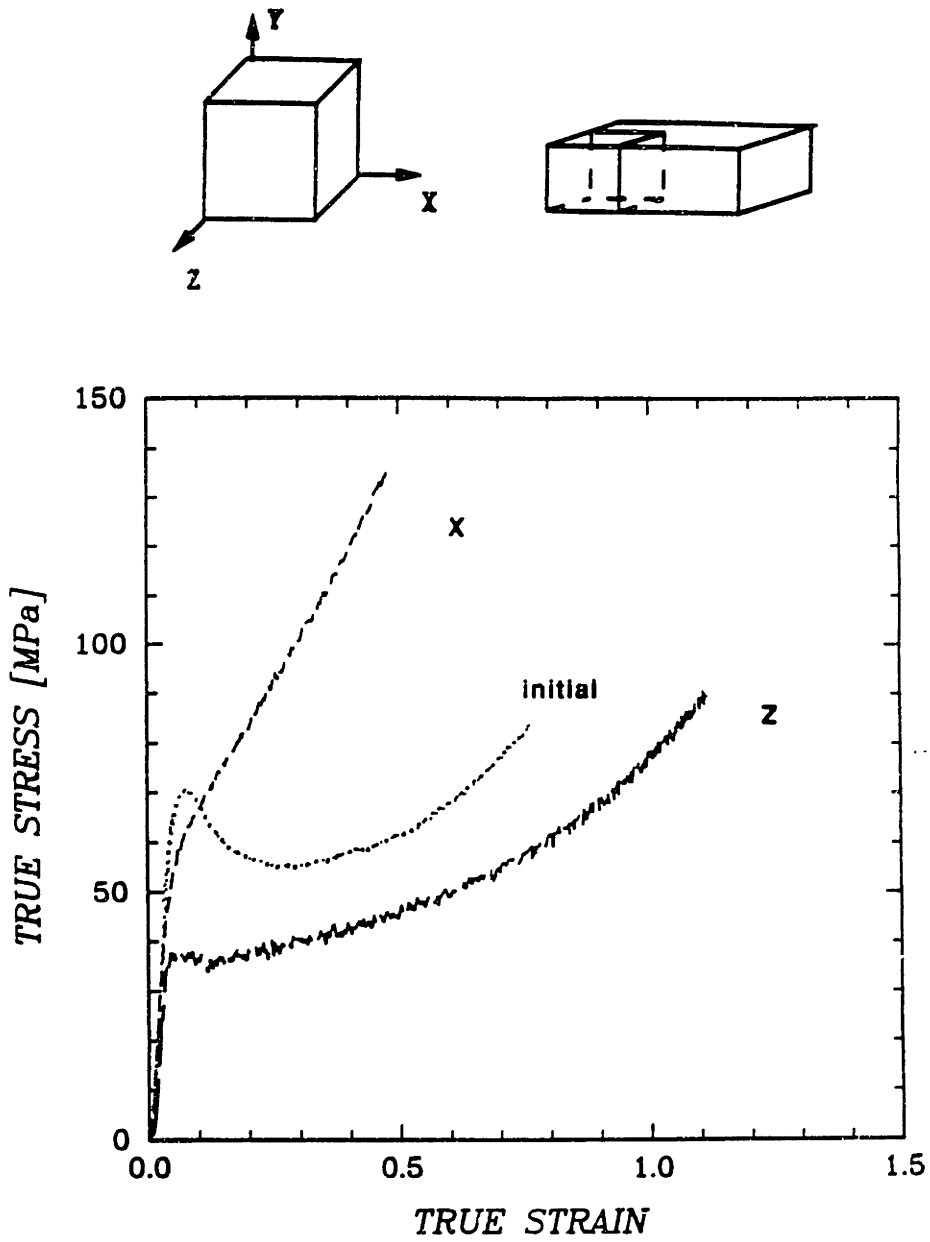

Figure 4.3: Experimentally determined uniaxial compression stress-strain curves of the isotropic response of PC and anisotropic response as a result of transverse isotropy in PC prestrained by $\epsilon = -0.57$ at $\dot{\epsilon} = -0.001/s$ and room temperature.

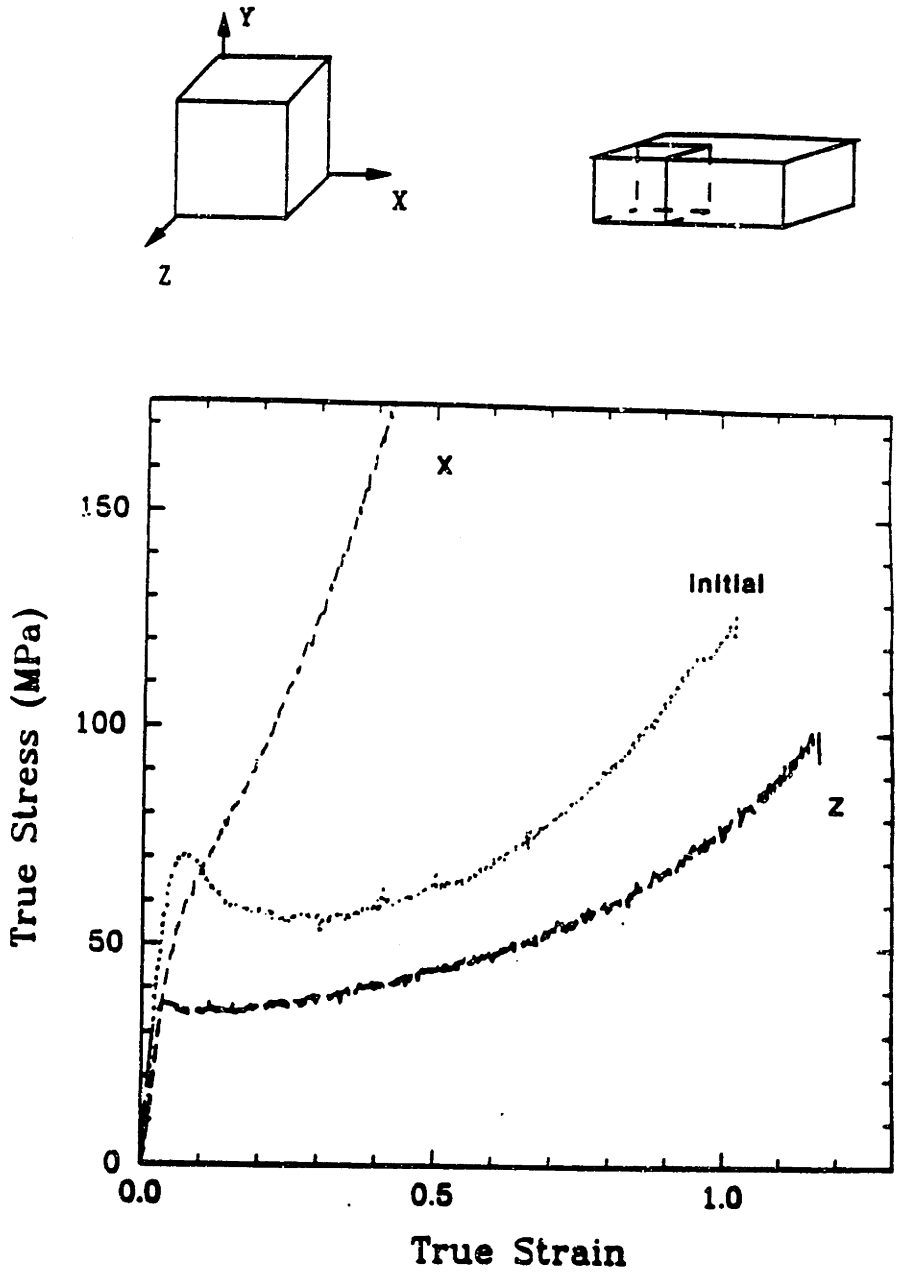

Figure 4.4: Experimentally determined uniaxial compression stress-strain curves of the isotropic response of PC and anisotropic response as a result of transverse isotropy in PC prestrained by $\epsilon = -0.75$ at $\dot{\epsilon} = -0.001/s$ and room temperature.

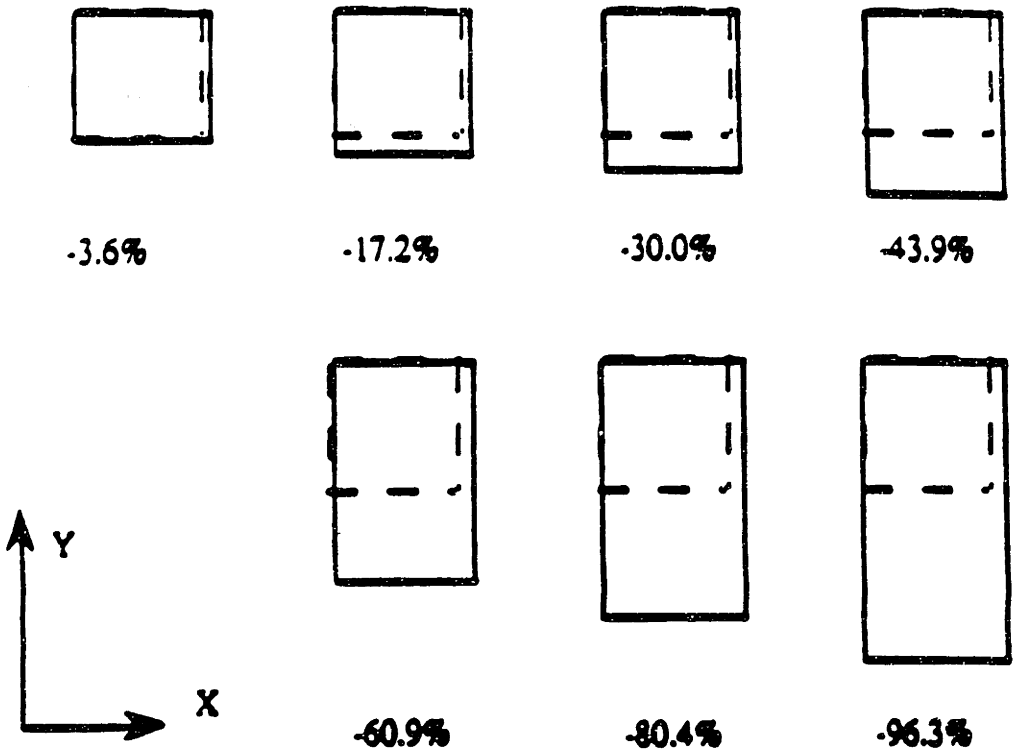

Figure 4.5: Experimentally determined deformation maps from micrometer measurements of the anisotropic evolving cross section versus plastic strain in anisotropic PC prestrained in uniaxial compression by $\epsilon = -0.51$ at $\dot{\epsilon} = -0.001/s$ and room temperature.

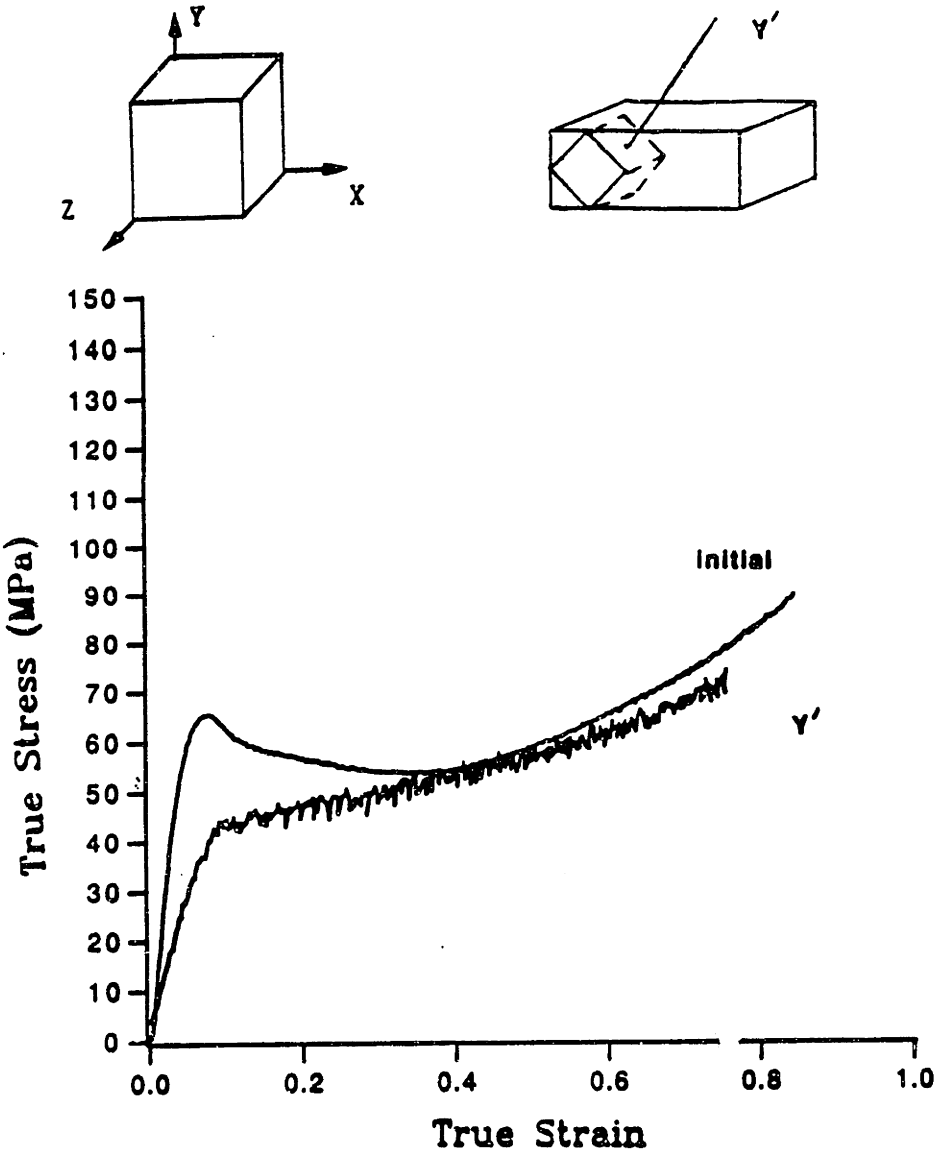

Figure 4.6: Experimentally determined uniaxial compression stress-strain curves of the isotropic response of PC and anisotropic response as a result of principal chain alignment in a plane at 45° to the recompression axis in PC prestrained by $\epsilon = -0.67$ at $\dot{\epsilon} = -0.001/s$ and room temperature.

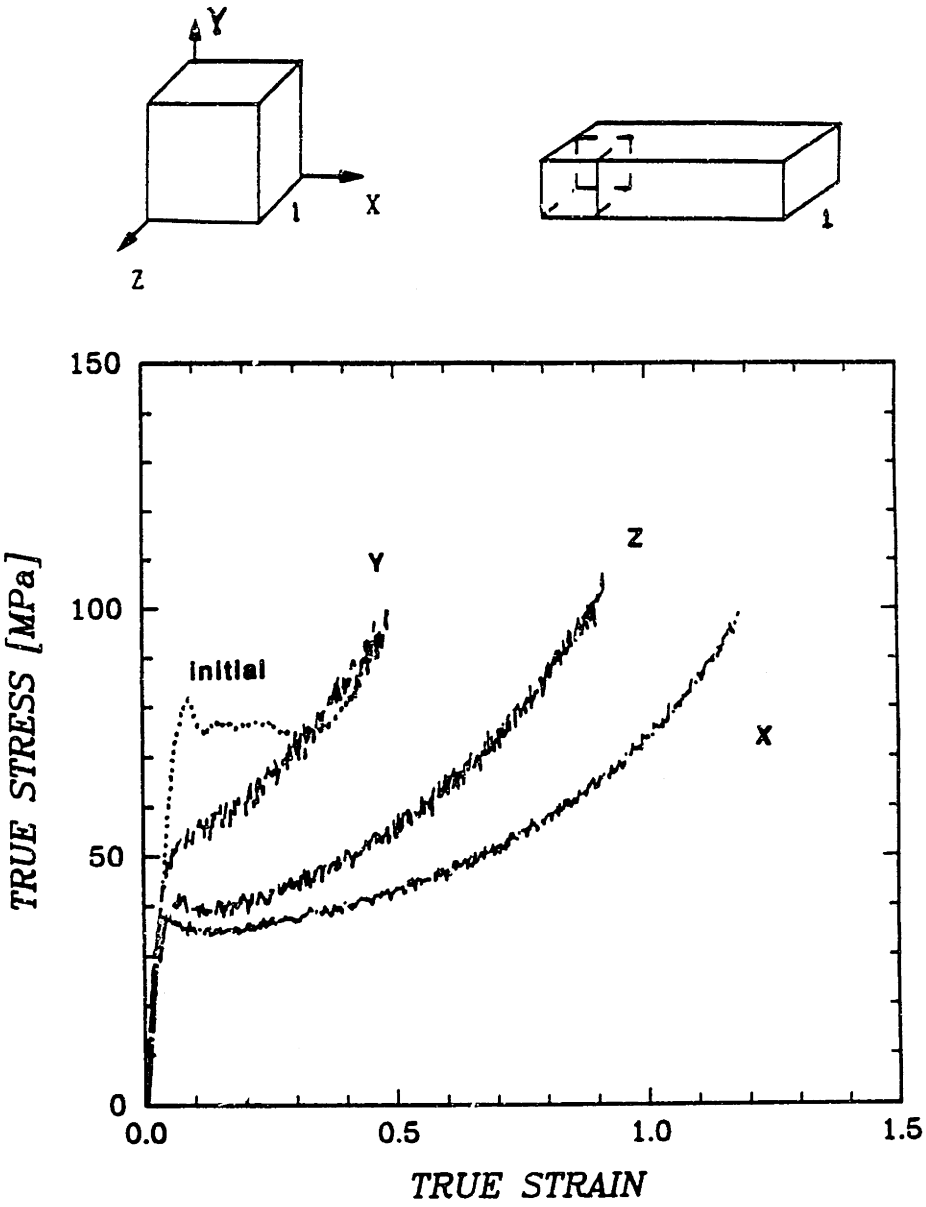

Figure 4.7: Experimentally determined plane strain compression stress-strain curves of the isotropic response of PC and anisotropic response as a result of three dimensional anisotropy in PC prestrained by $\epsilon = -0.35$ at $\dot{\epsilon} = -0.001/s$ and room temperature.

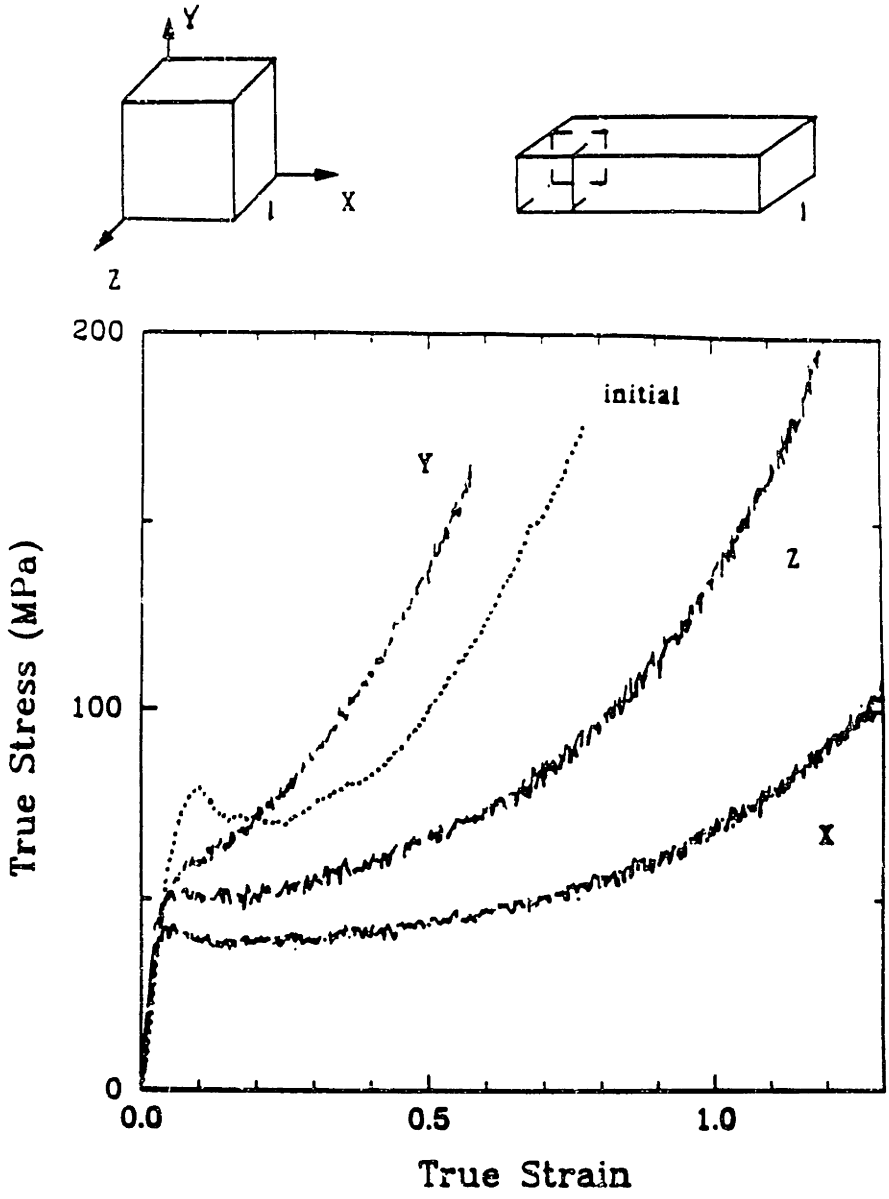

Figure 4.8: Experimentally determined plane strain compression stress-strain curves of the isotropic response of PC and anisotropic response as a result of three dimensional anisotropy in PC prestrained by $\epsilon = -0.50$ at $\dot{\epsilon} = -0.001/s$ and room temperature.

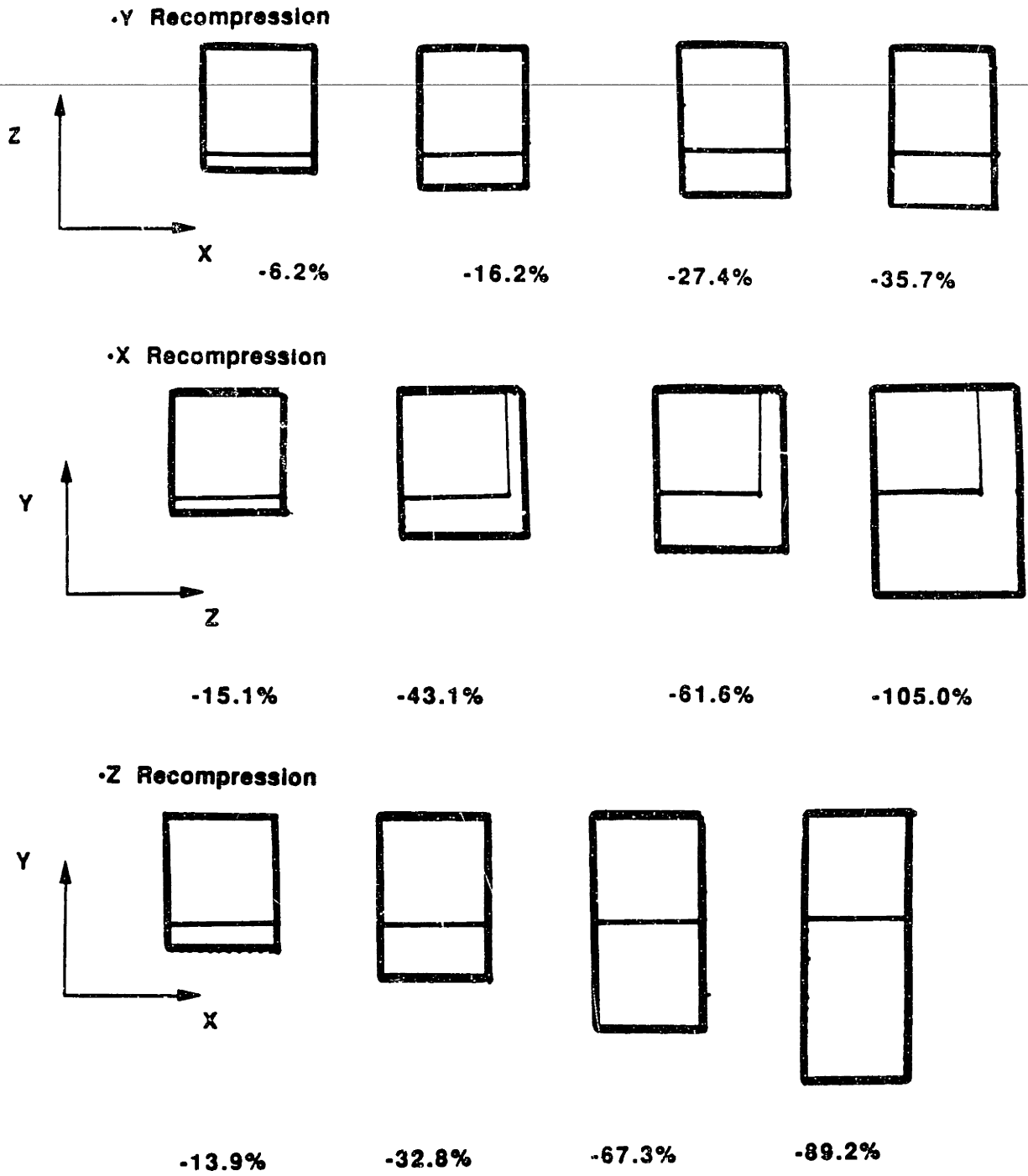

Figure 4.9: Experimentally determined deformation maps from micrometer measurements of the anisotropic evolving cross section versus plastic strain in anisotropic PC prestrained in plane strain compression by $\epsilon = -0.50$ at $\dot{\epsilon} = -0.001/s$ and room temperature.

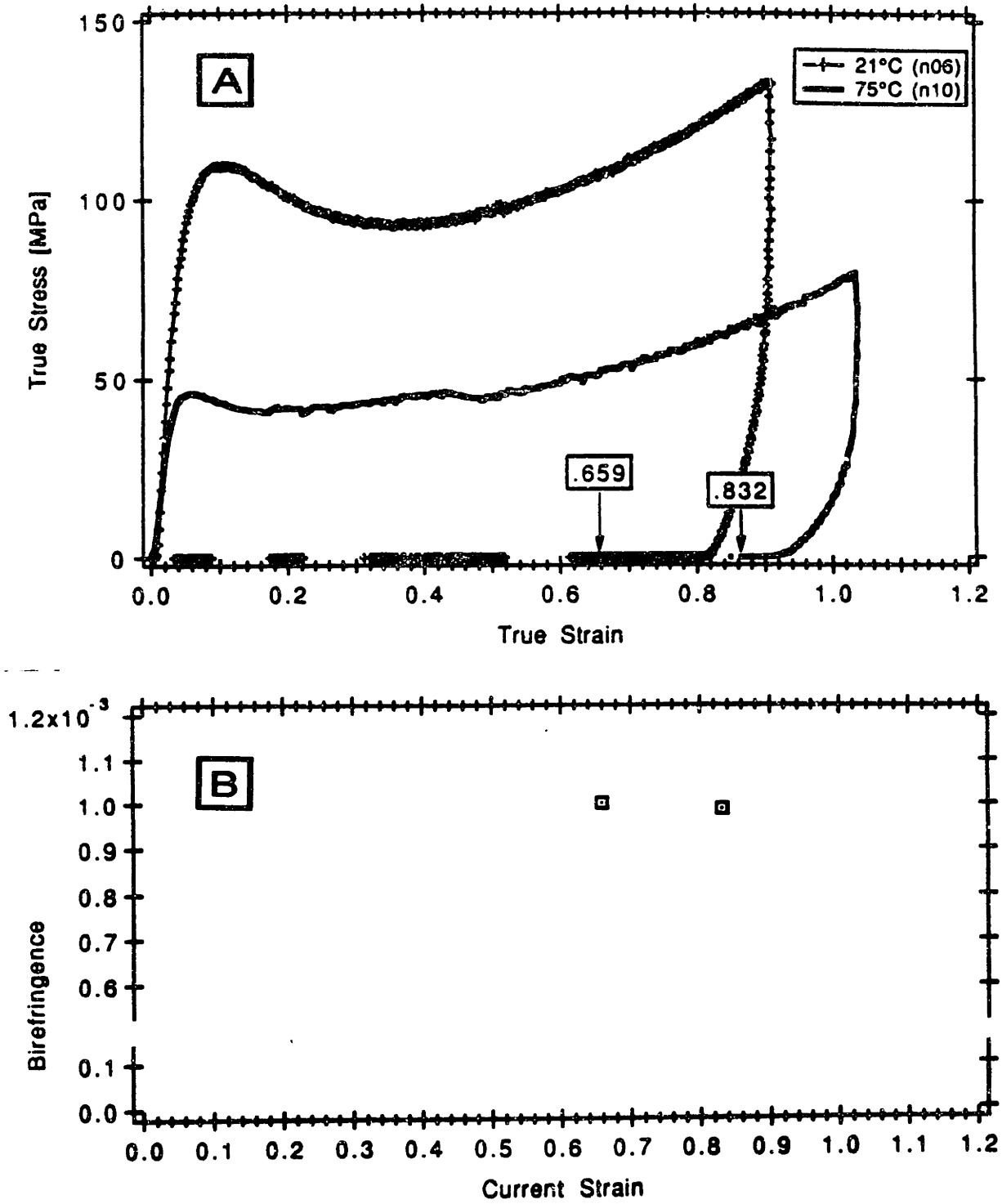

Figure 4.10: (A) Experimentally determined uniaxial compression stress-strain curves of isotropic PMMA under different thermal and strain histories; one tested at room temperature to a final strain under load of $\epsilon = -0.89$ at $\dot{\epsilon} = -0.001/s$, the other subjected to a strain of $\epsilon = -1.04$ at $\dot{\epsilon} = -0.001/s$ and 75°C. (B) Birefringence versus strain for the specimens tested in (A) confirming that the specimens contain the same level of anisotropy as measured by birefringence.

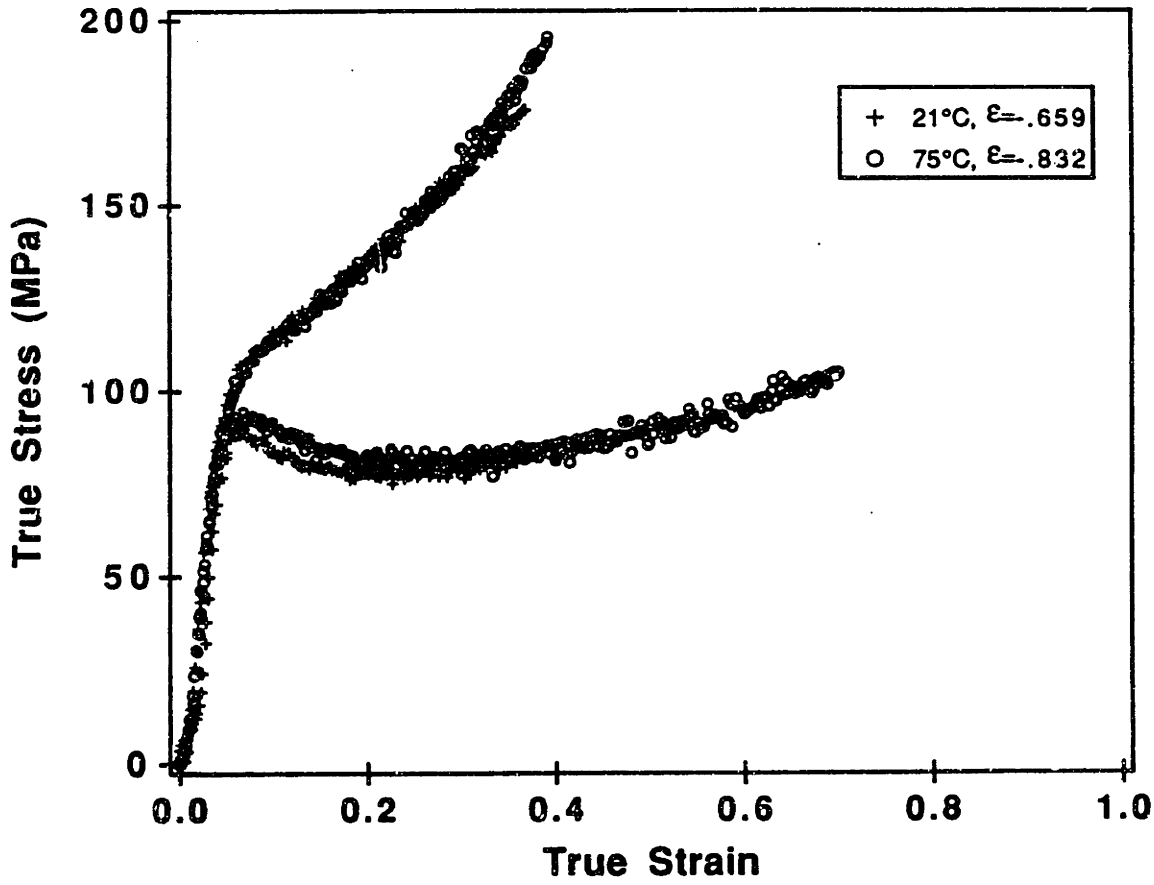

Figure 4.11: Experimentally determined uniaxial compression stress-strain curves of the anisotropic response of PMMA as a result of transverse isotropy in materials subjected to the different thermal and strain histories shown in Figure 9A; one prestrained by $\epsilon = -0.66$ at $\dot{\epsilon} = -0.001/s$ and room temperature, the other prestrained by $\epsilon = -0.83$ at $\dot{\epsilon} = -0.001/s$ and 75°C.

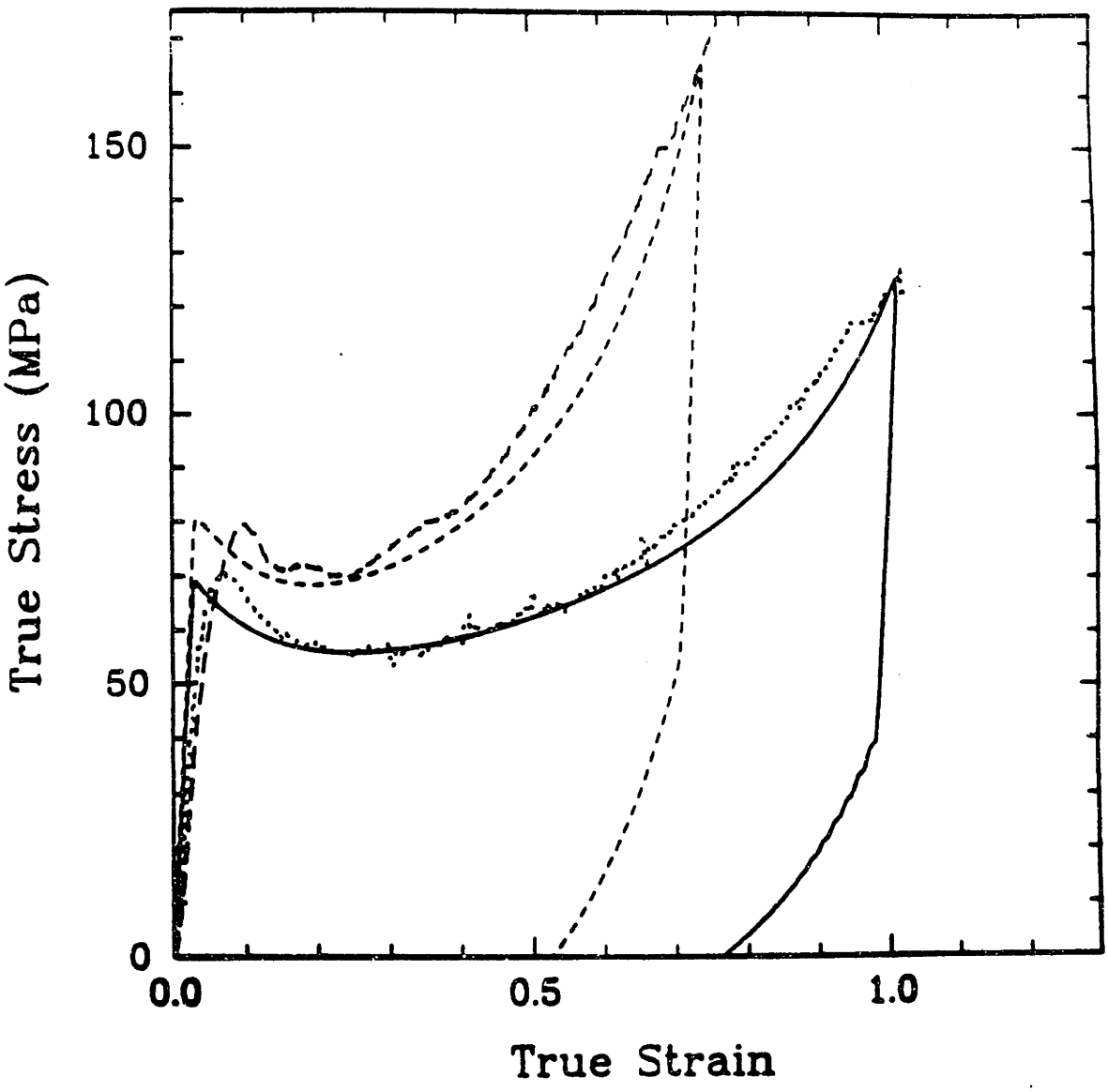

Figure 4.12: Eight chain model simulations and experimental curves of the uniaxial compression and plane strain compression responses of PC at $\dot{\epsilon} = -0.001/s$. The model was fitted to the uniaxial response, then the plane strain response was predicted based on uniaxial properties.

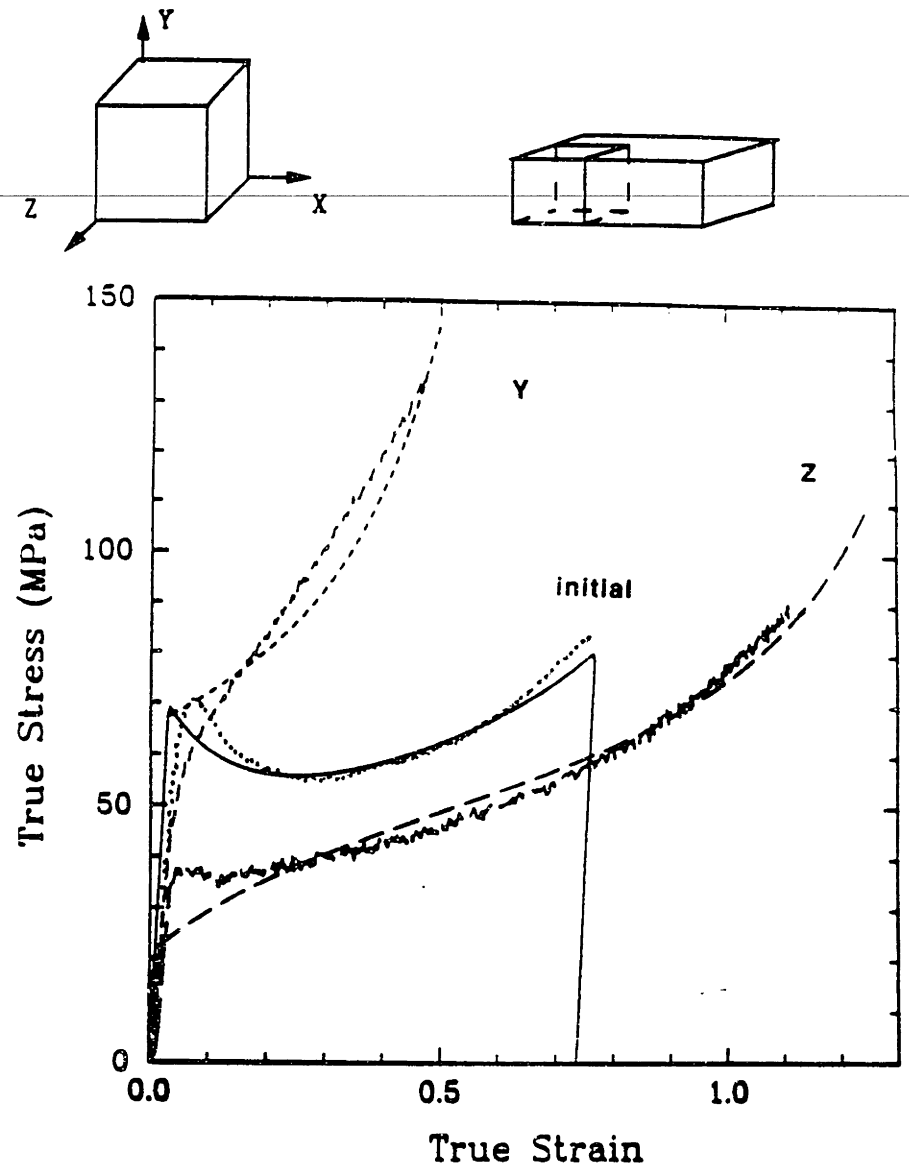

Figure 4.13: Comparison of theory with experiments described in Figure 4.3 for the anisotropic response of transversely isotropic PC prestrained by $\epsilon = -0.57$ at $\dot{\epsilon} = -0.001/s$ and room temperature.

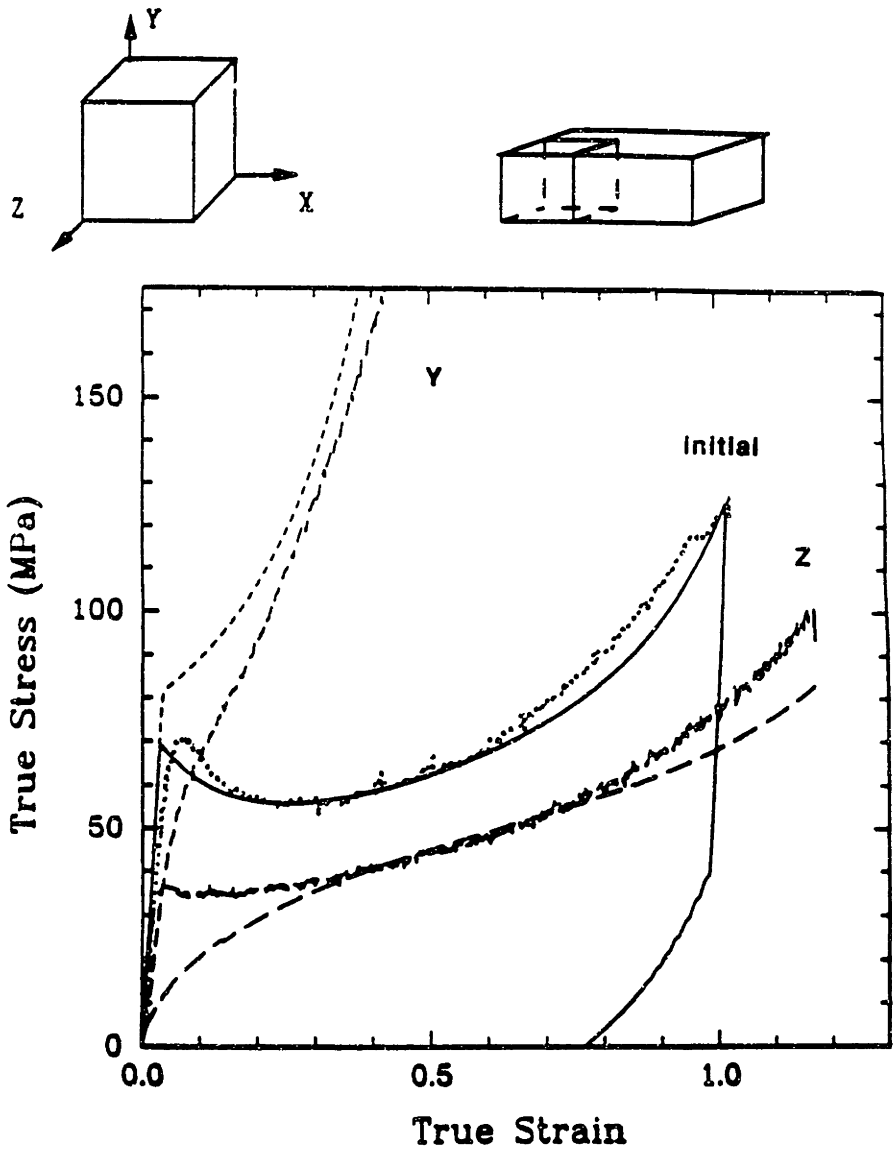

Figure 4.14: Comparison of theory with experiments described in Figure 4.4 for the anisotropic response of transversely isotropic PC prestrained by $\epsilon = -0.75$ at $\dot{\epsilon} = -0.001/s$ and room temperature.

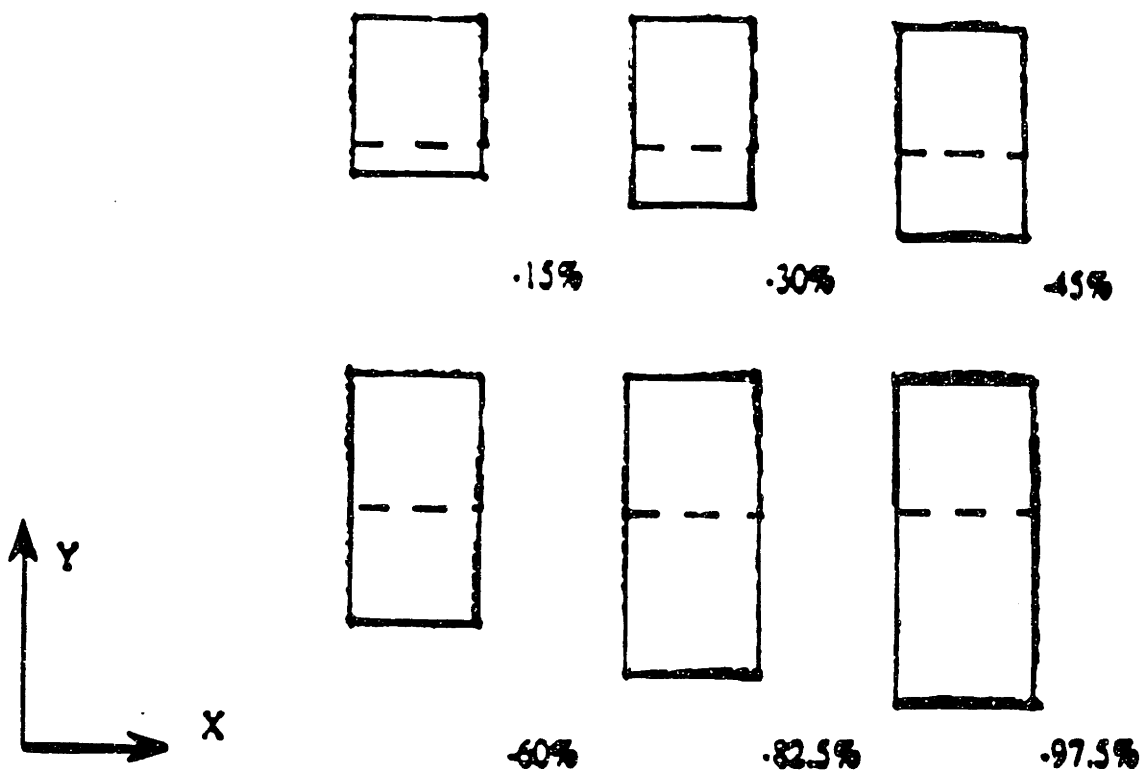

Figure 4.15: Simulations of the anisotropic response of the evolving cross section during recompression versus plastic strain in anisotropic PC prestrained in uniaxial compression by $\epsilon = -0.51$ at $\dot{\epsilon} = -0.001/s$ and room temperature. Compare with experiments described in Figure 4.5.

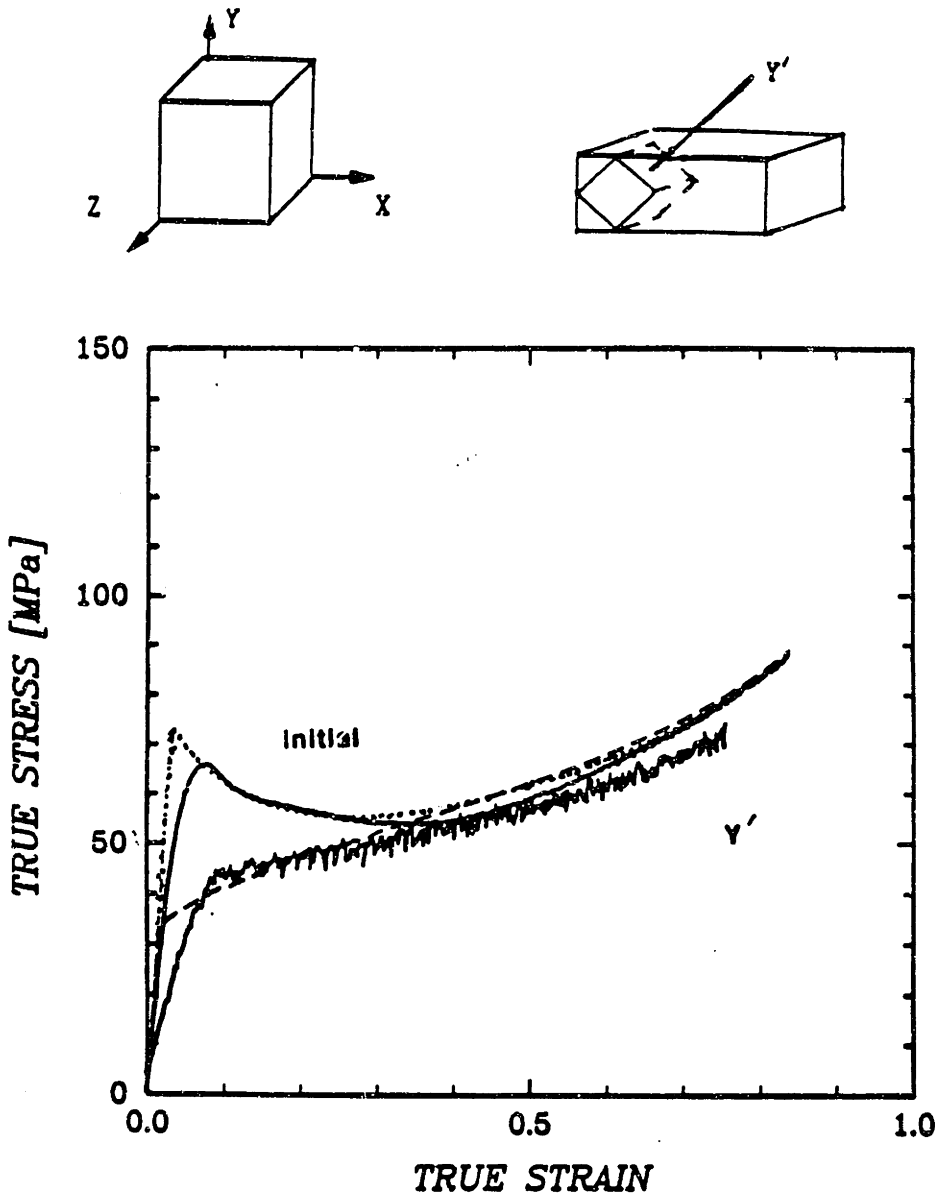

Figure 4.16: Comparison of theory with experiments described in Figure 4.6 for the anisotropic response of PC prestrained by $\epsilon = -0.67$ at $\dot{\epsilon} = -0.001/s$ and room temperature. The plane of principal chain orientation is oriented at 45^o to the recompression direction, resulting in extensive specimen shear during the recompression.

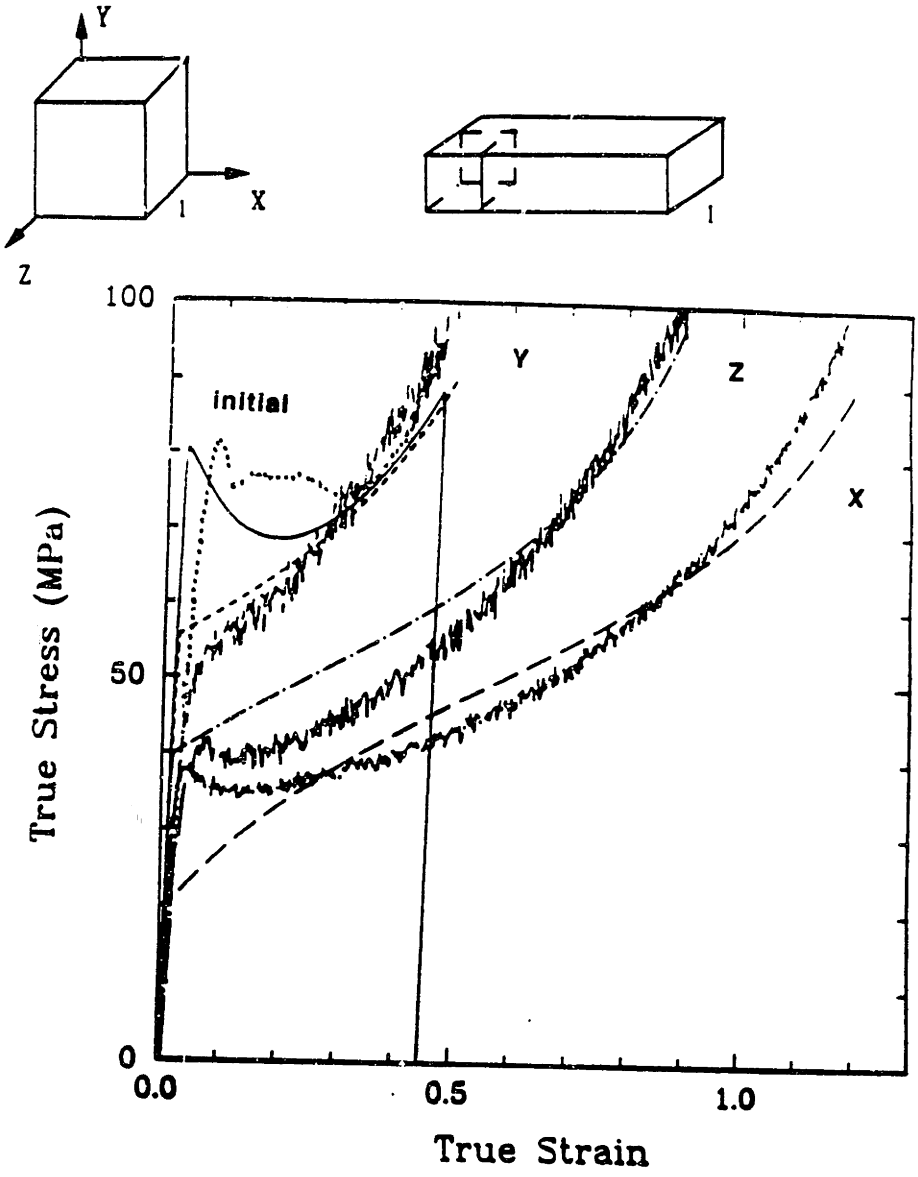

Figure 4.17: Comparison of theory with experiments described in Figure 4.7 for the anisotropic response of three dimensionally anisotropic PC prestrained by $\epsilon = -0.35$ at $\dot{\epsilon} = -0.001/s$ and room temperature.

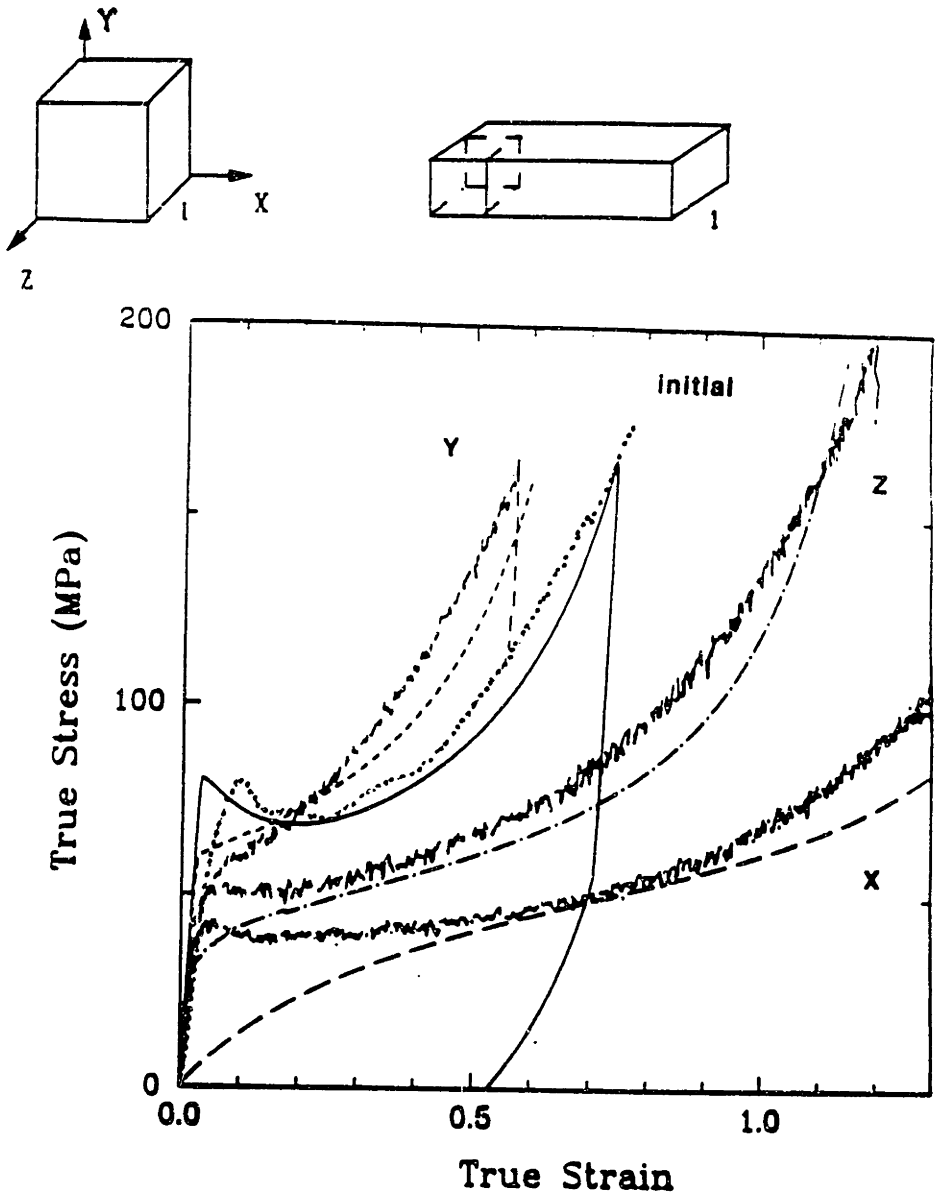

Figure 4.18: Comparison of theory with experiments described in Figure 4.8 for the anisotropic response of three dimensionally anisotropic PC prestrained by $\epsilon = -0.50$ at $\dot{\epsilon} = -0.001/s$ and room temperature.

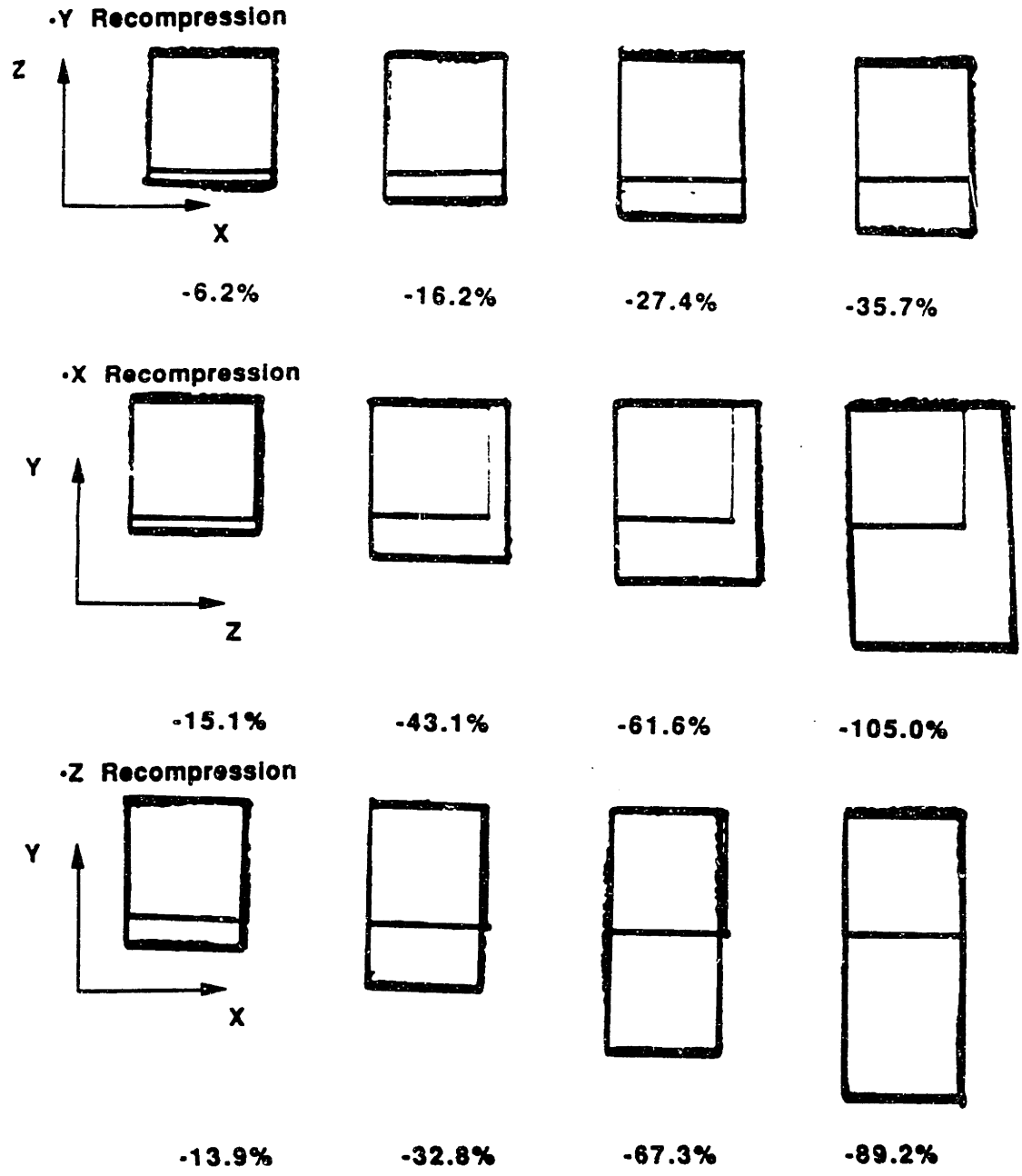

Figure 4.19: Simulations of the anisotropic response of the evolving cross section during recompression versus plastic strain in anisotropic PC prestrained in plane strain compression by $\epsilon = -0.50$ at $\dot{\epsilon} = -0.001/s$ and room temperature. Compare with experiments described in Figure 4.9.

Chapter 5

Effects of Strain Rate and Temperature on the Glassy Polymer Response

5.1 Introduction

The focus of the discussion to this point has been on the isothermal response of amorphous polymers with particular emphasis on the room temperature response of glassy polymers, PC and PMMA in Chapters 3 and 4, and of several rubbery polymers in Chapter 2. Through careful study of the isothermal responses of these materials theories for the evolution of anisotropy have been developed for both rubbery and glassy polymers. These theories have been shown to predict the state of deformation dependence seen in the isothermal responses reported in this thesis. Furthermore, the theory for the evolution of anisotropy in glassy polymers has been used to predict the effects of initial anisotropy in these materials. The addition of temperature and strain rate effects on the evolution of anisotropy in glassy polymers during strain hardening can now be isolated through a matrix of (a) constant strain rate compression tests over a range of temperatures and (b) constant strain rate compression tests at constant temperature over a range of strain rates.

Also in this Chapter a theory for the temperature dependent strain hardening response of glassy polymers is discussed and implemented into the constitutive model described in this thesis. Results of experimental data collected under both isothermal and adiabatic conditions are compared with the theory for both PC and PMMA.

5.2 Strain Rate and Temperature Effects

Polymers continue to be used with increased frequency in applications where they are subjected to rapid strain rates. The processing of glassy polymer components usually involves large strain deformations at elevated temperatures and rapid strain rates. End product applications where high strain rate deformations are expected to occur include thin layer polymer coatings and substitutes for silicate glasses in lenses,

windows, or goggles where toughness and impact resistance are of primary concern. Polycarbonate is one such polymer which possesses high toughness over a relatively large temperature range and is used in these applications. Yet the effects of temperature and strain rate on the response of glassy polymers during large deformations have been relatively uncharacterized to date.

The effects of strain rate and temperature on the strain hardening response of glassy polymers have been studied by other investigators [24,43,55,56]. G'Sell and Jonas monitored a constant local strain rate during tensile testing by way of feedback control of the deforming polymer cross section. They modelled the rate effects on PVC and HDPE using a non-linear viscoelastic representation of strain hardening of the form:

$$\sigma = K \exp\left(\frac{\gamma\epsilon}{2}\epsilon^2\right)\dot{\epsilon}^m \tag{5.1}$$

G'Sell and Jonas found that strain hardening in both materials could be characterized by a strain rate sensitivity of $m \leq 0.06$ and a strain hardening coefficient which evolves with strain: $\gamma = \gamma_e\,\epsilon_e$. Adams and Farris measured the heat, work and internal energy changes during deformation for PC using a deformation calorimeter [43]. They found that a substantial portion of the work required to cold draw PC was stored as a latent internal energy change; the percent of internal energy change was found to depend inversely on strain rate in the range of $0.03/second$ to $0.003/second$. Adams and Farris found no strong dependence of stored energy on temperature in the range 20°C to 65°C. Machida and Lee studied the deep drawing of polypropylene sheets with various temperature boundary conditions [55]. Drawability of the polymer during cup forming was increased with increasing temperature. A positive temperature gradient from the punch section to the flange region was also found to improve drawability and produce uniformly thick cup edges. The deformation behavior of a number of polymers was studied over a range of strain rates by Walley et. al. who showed the effects of strain rate on the strain hardening response of several materials [56]. Among their conclusions was the assertion that some materials such as polyvinylidene difluoride (PDVE) show no strain hardening but rather strain softening at rapid strain rates because of adiabatic heating effects concomitant with the high strain rate test. One thing that is clear from these studies is that both temperature and strain rate affect the strain hardening reponse of glassy polymers, and that these effects are often coupled during deformation studies. The series of experiments presented in this Chapter isolates the temperature effect so that each effect may be investigated separately.

Raha and Bowden [57] proposed a model for the temperature dependent birefringence response of glassy PMMA which was observed experimentally in their plastically deformed plane strain compression specimens. They proposed that the glassy polymer, which forms a network by virtue of physically entangled chains, evolves during deformation as secondary valance interactions which are essentially weak entanglements dissociate with plastic strain. A thermally equilibrated number of secondary interactions was thought to exist as well which accounts for the observed temperature dependent birefringence. The thermally equilibrated interaction number and its

dissociation was modelled by Raha and Bowden in terms of an evolving chain density with temperature as follows

$$n_o(\Theta) = A' + B' \left[1 - \exp\left(\frac{-E_a}{R\Theta}\right)\right] \tag{5.2}$$

where A' represents a strong network which does not undergo thermal dissociation, the term containing B' represents the thermally evolving chain density, E_a is the thermal dissociation energy, R is the universal gas constant and Θ is temperature. Raha and Bowden determine $E_a = 5.9(\pm 0.5) kcal/mol$ by reduction of their birefringence data; they quote a value for the thermal dissociation of a $-COOCH_3$ interaction detemined independently of their theory for PMMA of $5.6 kcal/mol$. Their model was well predictive of their plane strain compression data.

Kahar et. al. [25] similarly observed temperature dependent birefringence in PMMA. They proposed that the effect was due to a temperature dependent value of the optical anisotropy, α_{op}, of a rigid link. Their temperature dependent birefringence versus stretch model based on this theory was able to capture the temperature dependent birefringence data they generated under hydrostatic extrusion.

Boyce [58] noted that in the glassy polymer the evolving chain density, n, for which a chain is defined as that segment between physical entanglements, must result in an evolution of the number of rigid links per chain, N, according to

$$n(\Theta)N(\Theta) = constant \tag{5.3}$$

in order that the total number of rigid links and hence, mass, is conserved. In this Chapter the suggestion of a dissociating network is followed in incorporating temperature dependence into the glassy polymer model using the evolution of $n(\Theta)$ and $N(\Theta)$ in accordance with Equation 5.3.

5.2.1 experimental procedure

Constant strain rate uniaxial compression tests were performed on PC and PMMA specimens according to the procedure outlined in Chapter 3 with the following modifications and additions. The surface temperature was measured during deformation for the room temperature tests at various strain rates. A Mikron M67S infrared detector was employed for this purpose. Operation of the infrared detector requires calibration of the specimen radiant energy by using either the known target temperature or emissivity. The highest signal to noise ratio of the infrared detector is achieved for targets of emissivity close to 1.00. A black paint with a known emissivity close to 1.00 was used to coat the polymer surface to achieve the cleanest temperature results. The infrared detector was positioned near the specimen during compression testing to collect the surface temperature rise. This information was collected together with the load and stroke information thus the temperature versus strain information was readily extracted. The infrared detector set up is sketched in Figure 5.1. In order that the infrared detector be afforded a sufficient target size throughout the duration of the large strain deformation experiment, the specimen size was increased from that reported in Chapter 3 to cubes of length 0.5 inches.

The elevated temperature tests were conducted under isothermal conditions inside a radiant furnace which surrounded the Instron load train. A RESEARCH INC Model E4-5 radiant furnace was used, the temperature environment within the furnace was controlled manually.

5.2.2 experimental results

The isothermal response of PMMA at a strain rate of $\dot{\epsilon} = -0.001/second$ as a function of temperature below the glass transition temperature is given in Figure 5.2. The test temperature affects the initial yield response by lowering the flow stress with increasing test temperature. In addition the strain hardening characteristics are affected by the environment temperature. The arrows on Figure 5.2 measure the amount of strain hardening from the strain softened stress at a given magnitude of strain for each temperature curve. One effect of temperature on strain hardening is to decrease the rate of strain hardening with increasing temperature. Increasing temperature thus serves to increase the limiting extensibility as evidenced in the divergence of the strain hardening responses at high strains.

Figure 5.3 contains similar results for PC over a broader range of temperatures which fall within the glassy regime for this material. The temperature dependent yield is followed by strain softening and then by strain hardening which is temperature dependent for PC as well. The arrows measuring the amount of strain hardening from the strain softened value of each curve verify that the amount of strain hardening decreases at a given strain with increasing temperature. The limiting extensibility increases with increasing temperature for PC; the 25°C response is very close to locking at a strain of −120% while the 75°C response is able to sustain a strain of −130%.

The effect of strain rate on the room temperature response of PMMA has been investigated over the range of $\dot{\epsilon} = -0.001/second$ to $\dot{\epsilon} = -0.5/second$. The stress-strain and surface temperature versus strain results are recorded in Figure 5.4. The test at $\dot{\epsilon} = -0.001/second$ resulted in isothermal deformation conditions as verified by the flat temperature response associated with this strain rate. This familiar isothermal response is characterized by yield, strain softening and extensive strain hardening. As the strain rate is increased the temperature versus strain response indicates that the temperature at the specimen surface is increasing during deformation. The expected rate dependent yield response of the flow stress increasing with increasing strain rate is observed. At a strain rate of $\dot{\epsilon} = -0.1/second$ approximately adiabatic conditions exist. Once plastic deformation ensues the material surface temperature begins to rise. The result of the plastic work going into heating the specimen is to affect the response of the material in a manner which is consistent with its temperature dependent response seen in Figure 5.2. With increasing temperature both the flow stress and strain hardening rates decrease as was seen in Figure 5.2. For the PMMA response at initially 25°C and at $\dot{\epsilon} = -0.1/second$, substantial specimen heating is occurring during the softening portion of the response. The material responds to its current temperature by continuing to soften beyond the percent drop which occurs during strain softening under isothermal conditions. The additional softening is due

to thermal softening. The softening response does eventually cease and the stress-strain response levels off even though the temperature in the specimen continues to rise. This aspect of the observed behavior is the result of the additional effect of strain hardening occurring due to the evolution of chain alignment with plastic stretch. Note that as discussed earlier, this strain hardening is also temperature dependent and is therefore also affected by the temperature rise during deformation. At moderate and high levels of strain the specimen simultaneously continues to thermally soften and strain harden as it is deformed and continues to heat up. The actual effect of the increased strain rate on the post yield response of PMMA is therefore attributed to the temperature effects associated with the adiabatic heating of the material at $\dot{\epsilon} = -0.1/second$.

Figure 5.5 contains the room temperature rate dependent response of PC together with the specimen surface temperature versus strain data at each strain rate. For PC at room temperature and $\dot{\epsilon} = -0.001/second$ isothermal conditions exist. The material shows the expected yield, strain softening and strain hardening responses. As the strain rate is increased the data shows the expected rate dependent yield response of increased yield strength at increased strain rate although the strain rate dependence of PC is not very large. At $\dot{\epsilon} = -0.1/second$ approximately adiabatic conditions exist which result in the superposed temperature responses to the stress-strain result at this strain rate. The material softens by a slightly larger amount than does the isothermal material in response to the current temperature during adiabatic conditions which is decreasing throughout the strain softening process. Strain hardening commences to combat the softening effect in a manner which is temperature dependent and the strain hardening response is eventually observed for this material. In Figure 5.4 we showed that thermal softening and temperature dependent strain hardening combined to obscure the strain hardening associated with any chain alignment which occurred during the test at this rate for PMMA. In PC this is not so owing to the extensive strain hardening which occurs in PC relative to the small effect of the temperature rise in the material.

The results of the room temperature responses of PMMA as a function of strain rate were repeated to illustrate the extent to which thermal softening during adiabatic heating of PMMA obscures the hardening response of this material and to verify that strain hardening does indeed occur. The curves in Figure 5.6 again illustrate the increased strain softening and decreased strain hardening observed for PMMA during the approximately adiabatic conditions at $\dot{\epsilon} = -0.1/second$ as compared to the isothermal response at $\dot{\epsilon} = -0.001/second$. Each specimen was retested at the same strain rate of its initial compression condition; the specimen initially tested at $\dot{\epsilon} = -0.1/second$ was allowed to cool to room temperature prior to recompression at $\dot{\epsilon} = -0.1/second$. During the recompression testing of each specimen at different strain rates approximately isothermal conditions exist in each because of the reduced amount of plastic work being done during the recompression cycle. The recompression results serve to illustrate a very important point about the mechanisms of plastic deformation in glassy polymers: As we have discussed in Chapter 3 there are two distinct barriers to plastic deformation in the glassy polymer, each of which evolves with several parameters associated with the deformation process such as amount of strain,

state of deformation, temperature and strain rate. The barrier to chain segment rotation which is rate and temperature dependent responds to the current conditions of both strain rate and temperature. As the recompression of the initially isothermal response in Figure 5.6 shows, the material acknowledges this isotropic barrier at the level of the current strain softened stress which is 15MPa below the peak yield stress. The material then seeks out the strain hardening curve indicative of its current amount of orientation. The level of existing orientation is a function of the conditions present during the prior deformation; the current rate of strain hardening responds to the room temperature evolution of anisotropy. When the material initially tested under adiabatic conditions is first allowed to cool to room temperature then retested at $\dot{\epsilon} = -0.1/second$, it responds by acknowledging its current, room temperature barrier to chain segment rotation which is 15MPa below the peak yield value for this strain rate. The material then seeks out its prior orientation induced strain hardened state, responding with the amount of orientation which was produced under the preorientation conditions, and currently strain hardening according to the room temperature rate of evolution of anisotropy. Had this material not undergone any orientation induced strain hardening during the initial compression, the curvature of the strain hardening response upon reloading would have been concave up, indicative of the commencement of strain hardening, as shown by the dashed line in Figure 5.6.

5.2.3 modelling the temperature dependent response

The glassy polymer model developed in the proceeding Chapters is modified for temperature dependence in the following manner. The elastic constants are temperature dependent; a typical result for the temperature dependent shear modulus is shown for PC in Figure 5.7 [59]. In this thesis it is assumed that such results provide the correct shape of the modulus versus temperature curve for a given polymer but that the specific batch of polymer may require a shift of the baseline, e. g. the room temperature value. The following temperature dependent shear moduli of PC and PMMA in units of MPa have been determined from such database curves

PC

$$\log \mu_1 = \log(884.61) - 0.00108\,/K\,(\Theta - 298\,K) \tag{5.4}$$

PMMA

$$\log \mu_1 = \log(1205.0) - 0.0018\,/K\,(\Theta - 298\,K) \tag{5.5}$$

The Argon model explicitly addresses rate and temperature effects on the yield stress; the modification of Boyce et. al. [37] allows for these effects during the softening response as temperature dependence also enters through the athermal shear strength, s, defined after Equation 3.9, because of its relation to the temperature dependent elastic constants.

Temperature dependent strain hardening is incorporated into the model using the proposed model in the following equation, which is based on the work of Raha and Bowden [57] for the thermally evolving chain density

$$n(\Theta) = A - B\exp\left(\frac{-E_a}{R\Theta}\right) \tag{5.6}$$

where A is a non-dissociating network, B is the dissociating portion of the network, R is the universal gas constant ($0.001695 kcal/mol\,K$), Θ is temperature and E_a is the thermal dissociation energy. Following Boyce [58], we take Equation 5.3 to hold, the constant required in Equation 5.3 may be determined from the isothermal room temperature test. This test also serves together with a high temperature isothermal test to determine A and B in Equation 5.6.

The value of $E_a = 5.6 kcal/mol$ was used for PMMA from the work reported in Raha and Bowden [57]. The total number of tests required to determine all the material properties used in the model is two for PMMA. No such value for a secondary dissociation energy could be found for PC; a third test was required to determine E_a for PC; our data yielded $E_a = 2.0 kcal/mol$ for PC and the following values for A and B in Equation 5.6

	PC	PMMA
A	$5.243(10^{27})m^{-3}$	$2.740(10^{27})m^{-3}$
B	$4.547(10^{27})m^{-3}$	$1.194(10^{27})m^{-3}$

Table 5.1: Temperature dependent constants for the model of Equation 5.6.

Isothermal tests were simulated by incorporating the constant temperature values of all properties directly into the model for the given temperature. Simulation of the adiabatic results requires the incorporation of thermal properties to determine the temperature rise as a function of the rate of dissipative plastic work. Under adiabatic conditions the energy balance equation is [60]

$$\rho c\dot{\Theta} = \dot{q} = [tr(\mathbf{T}^{*\prime}\mathbf{D}^p)] \tag{5.7}$$

where ρ is the density, c is the specific heat, $\dot{q}$ is the rate of heat generation and the tensor product represents the plastic work rate which is the trace of the product of the driving stress and the plastic strain rate. Note that only the driving stress state, $\mathbf{T}^{*\prime}$, is dissipative as the backstress, $\mathbf{B}$, is stored in the material.

5.2.4 results of simulations

Figure 5.8 contains the experimentally observed isothermal responses of PMMA at temperatures of 25°C, 50°C and 75°C, along with the model simulations of these test conditions. The 25°C data and 75°C data were used to determine the constants A and B in Equation 5.6. The 50°C data was predicted based on the temperature dependent strain hardening characterization provided by Equation 5.6. The model is found to be well predictive of the temperature dependent response of PMMA throughout the

full range of extensibility of the material. The temperature dependent yield stress is well characterized for the range of responses tested as are the isothermal softening and hardening responses. All material properties required of the constitutive model, which have been listed in Tables 3.2, 3.3 and 5.1, can be determined from two experimental tests for PMMA. The isothermal 25°C and 75°C uniaxial compression tests have been used here along with an independently determined [57] value of a particular interaction dissociation energy for PMMA side groups to determine the strain hardening temperature dependence. The temperature dependent strain hardening of the 50°C curve was predicted by the model of Equation 5.6, using the dissociation energy as the driving force, the model is validated by its ability to predict the 50°C strain hardening curve. The results indicate that the theory of a secondary interaction dissociation provides a plausible explanation for temperature dependent strain hardening in glassy polymers. Because an independently determined value for the dissociation energy was used, the physical basis for the theory has been validated by the PMMA results.

The results of the simulations presented in Figure 5.8 were used to determine the level of backstress predicted for the two specimens prior to testing in Figure 4.11, due to the initial deformation histories of Figure 4.10A. Recall that these specimens contained the same level and state of anisotropy as confirmed by the birefringence measurements in Figure 4.10B. The principal values of the backstress tensor for the two specimens prior to reloading are tabulated below along with their deformation prehistories.

	23°C deformation to $\epsilon = -66\%$	75°C deformation to $\epsilon = -83\%$
B_{11}	9.455 MPa	9.126 MPa
B_{22}	-18.909 MPa	-18.251 MPa
B_{33}	9.455 MPa	9.126 MPa

Table 5.2: Backstress tensor principal values for the preoriented specimens of Figure 4.10A prior to the recompression expermients of Figure 4.11.

Table 5.2 verifies that the model is capable of predicting the same anisotropic state for these two specimens. The backstress is clearly responsible for driving the anisotropic response of preoriented materials; identical backstress tensors yield the identical anisotropic responses of Figure 4.11. These results also establish the validity of using the birefringence measure of anisotropy as a state variable in preoriented glassy polymers as both the birefringence measurements of Figure 4.10B and the backstress values of Table 5.2 predict identical material states for the specimens subjected to the very different deformation and thermal histories of Figure 4.10A. We have established the ability to capture the evolution of anisotropy with state of strain, magnitude of

strain and now temperature with our model of the glassy polymer deformation response.

Figure 5.9 contains the results for the experimentally determined isothermal temperature dependent response of PC at 25°C, 75°C and 125°C and comparison with theory. Here because a value for the secondary valence dissociation energy could not be found for PC, all three simulations were used to characterize the temperature dependent strain hardening response by determining values of A and B listed in Table 5.1 and E_a in Equation 5.6. Once again the Argon model of initial yield is well predictive of the temperature dependent flow stress of PC for this wide temperature range. Although the temperature dependent strain hardening simulations are all the results of fits for this material, the results do provide the following verification of the theory proposed by Raha and Bowden [57] as modified in Equation 5.6: The consequence of prescribing an evolving chain density, $n(\Theta)$, and a corresponding evolution in the number of links per chain, $N(\Theta)$, is that the single chain limiting extensibility is also temperature dependent, and is given as

$$\lambda_L(\Theta) = \sqrt{N(\Theta)}. \tag{5.8}$$

A decrease in $n(\Theta)$ with temperature results in an increase in $N(\Theta)$ by Equation 5.3, and hence $\lambda_L(\Theta)$ by Equation 5.8, with temperature. The data and simulations both show that an increase in the network extensibility with increasing temperature does indeed occur. As the results of Figure 5.9 show, the limiting extensibility of the polymer increases with increasing temperature. This result is consistent with the evolution of chain density with temperature as proposed.

An isothermal response at $\dot{\epsilon} = -0.001/second$ and an adiabatic response at $\dot{\epsilon} = -0.1/second$ were each simulated for PMMA, the stress versus strain results appear with the room temperature experimental curves at those rates in Figure 5.10. The Argon model captures the rate dependent flow stress of PMMA. Extensive softening is predicted for the adiabatic response owing to the temperature rise in the material and its effect on the material properties. Temperature dependent strain hardening is predicted, the combination of excessive softening and decreased hardening which both result from the temperature rise in the material are modelled accurately as evidenced by the prediction of the adiabatic response at large strains. No orientation induced strain hardening is observed in the simulation by virtue of the excessive softening which obscures hardening in the prediction, and is in accordance with the data. The previous discussion of the results in Figures 5.4 to 5.6 argued that indeed orientation and strain hardening occur during this deformation which is evident upon reloading of the deformed specimen as was done for Figure 5.6.

The results of Figure 5.10 serve to illustrate the usefulness of the constitutive model in characterizing the large strain deformation response of polymers at moderately high strain rates for which material heating would be expected to affect the stress-strain response. Such conditions occur in solid phase deformation processing of polymers, the effects of processing conditions have previously not been well characterized by a true, predictive constitutive model.

The specimen surface temperatures during deformation for the PMMA experiments in Figure 5.10 have been given in Figure 5.11 along with the predictions of

the model based on isothermal conditions at $\dot{\epsilon} = -0.001/second$ and adiabatic conditions at $\dot{\epsilon} = -0.1/second$. A uniform temperature is maintained during straining at $\dot{\epsilon} = -0.001/second$ as the experimental results show, the isothermal simulation was therefore an obvious choice. The temperature rise at the surface of the specimen during straining at $\dot{\epsilon} = -0.1/second$ is not well predicted with the assumption of adiabatic conditions. One explanation of the result is that the onset of plastic deformation and the concomitant temperature rise during adiabatic heating is predicted to occur as the result of a singular yield event at a strain of $\epsilon = -0.05$. The experimental result requires a strain of $\epsilon = -0.15$ prior to any measurable temperature rise. The glassy polymer yield is currently thought to be the result of many localized transformation events which occur over a range of strains as the applied stresses drive the material to a preferred state [48]. The current model does not use this explanation of yield and therefore predicts viscoplastic deformation effects to ensue more rapidly with strain than are actually observed. Nevertheless, the predicted rate of temperature rise exceeds the experimentally observed response which may be the fault of an erroneous assumption on the part of the use of an adiabatic simulation. Clearly, an additional investigation into this result is needed.

Figures 5.12 and 5.13 give the theory versus experiment comparisons for PC in terms of stress-strain curves and temperature-strain curves, respectively. The effect of a roughly 20°C temperature rise at room temperature, which is still fully 100°C below the glass transition temperature for PC, is quite small. Yet these simulations provide a useful exercise in terms of evaluating the model capabilities.

The simulations predict the excessive softening and reduced hardening responses which were found experimentally to occur in PC during testing at $\dot{\epsilon} = -0.1/second$. These effects are once again the result of the temperature rise during deformation at this strain rate. The results of Figure 5.13 for the temperature versus strain profiles of the experimental results at $\dot{\epsilon} = -0.1/second$ and $\dot{\epsilon} = -0.001/second$ and adiabatic and isothermal simulations show good agreement. Isothermal conditions were found to exist at $\dot{\epsilon} = -0.001/second$. The adiabatic simulation predicts the onset of a measureable temperature rise at a premature strain level of $\epsilon = -0.05$, because of the way in which yield is modelled as a singular event. Work in progress [48] to improve this aspect of the model was described in the discussion of Figure 5.11. The data show a temperature rise commencing at $\epsilon = -0.20$ for PC. The rate of temperature rise predicted assuming adiabatic conditions for PC at $\dot{\epsilon} = -0.1/second$ is in very good agreement with the experimental result at that strain rate. Note that the results in Figure 5.13 indicate that adiabatic conditions are not necessarily characterized by a linear temperature rise with strain; both the experimental and adiabatic simulation curves level off at high strains. This behavior is the result of the excessive material softening during adiabatic heating which lowers the resistance to plastic flow in the material. This resistance is modelled as an evolving isotropic barrier to plastic flow which is one of two barriers to plastic flow in the glassy polymer model and which is the dissipative portion of plastic work, see Equation 3.13. As this term decreases the plastic work rate decreases, and by Equation 5.7 so does the rate of temperature rise. These results provide a very strong verification of the model by confirming that only part of the total stress activates plastic flow while the remainder of the stress

is stored. Our use of two distinct barriers to plastic flow in the model accounts for this result very concisely and accurately, and results in the ability to predict the very complicated response to deformation under adiabatic conditions in the glassy polymer.

5.3 Summary

In this Chapter the effects of strain rate and temperature on the response of PC and PMMA have been investigated. By simultaneous measurement of the surface temperature during the deformation experiment the effects of temperature were found to attribute to the observed rate dependent response. The initial yield in isotropic glassy polymers is found to be both rate and temperature dependent. The strain softening and strain hardening regimes have been observed to have a strain rate dependent response [56] for several polymers. Here the apparent strain rate effects on both strain softening and strain hardening are found to be due to the current temperature of the material. Under isothermal test conditions the specimen temperature remains constant, but during adiabatic testing which occurs at moderate strain rates, the specimen temperature rises throughout the strain softening and strain hardening deformation regimes. The effects of the temperature rise during adiabatic heating of the material are found to be consistent with the temperature dependence of both the initial yield and the strain hardening responses. The two distinct barriers to plastic flow which were described in the discussion of the glassy polymer model in Chapter 3 are found to evolve with various processing parameters such as strain rate and temperature in the current results, providing further justification for the current model of polymer deformation.

The temperature dependent constitutive model included the Argon model for rate and temperature dependent yield, and formulation of the temperature dependent elastic constants. A model for temperature dependent strain hardening was proposed using the work of Raha and Bowden [57] and of Boyce [58] which postulates that the weaker interactions forming part of the polymer structure break down with plastic strain and have a thermally equilibrated number. The model is found to be predictive of the temperature dependent responses of PMMA and PC during isothermal conditions at various temperatures, and for predicting isothermal and adiabatic stress-strain responses. The model over estimates the temperature rise under assumed adiabatic conditions in PMMA although the stress-strain prediction is in good agreement; suggestions for future work should address this issue. The model very accurately predicts the adiabatic response of PC at high strains including the stress-strain response as well as the temperature-strain response. These results indicate that the temperature dependent strain hardening response is well characterized by the model of Equation 5.6.

The optical birefringence of glassy polymers has been observed at various instances within this thesis to evolve with state of deformation, magnitude of strain and temperature. In particular the birefringence measure has been cited earlier as an internal state variable which may be capable of predicting the anisotropic response

of preoriented materials without regarding the prior strain or thermal history of the material (see the discussion of Figures 4.10 and 4.11). It may also be feasible to use the characterization of the evolution of optical birefringence with temperature to predict the strain hardening response of glassy polymers at different strain rates and temperatures. This proposal is very strongly motivated by the results of Table 5.2 for the backstress tensor predictions of the specimens tested in Figures 4.10 and 4.11 which serve to verify the birefringence results of Figure 4.10B. Both measures of anisotropy indicate that the materials are in identical anisotropic states prior to the recompressions of Figure 4.11, the recompression tests confirm that these anisotropic materials behave identically. Further work which includes a more detailed analysis of the evolution of birefringence with deformation state and temperature is needed to develop this direct use of birefringence as a state variable in polymer deformation models.

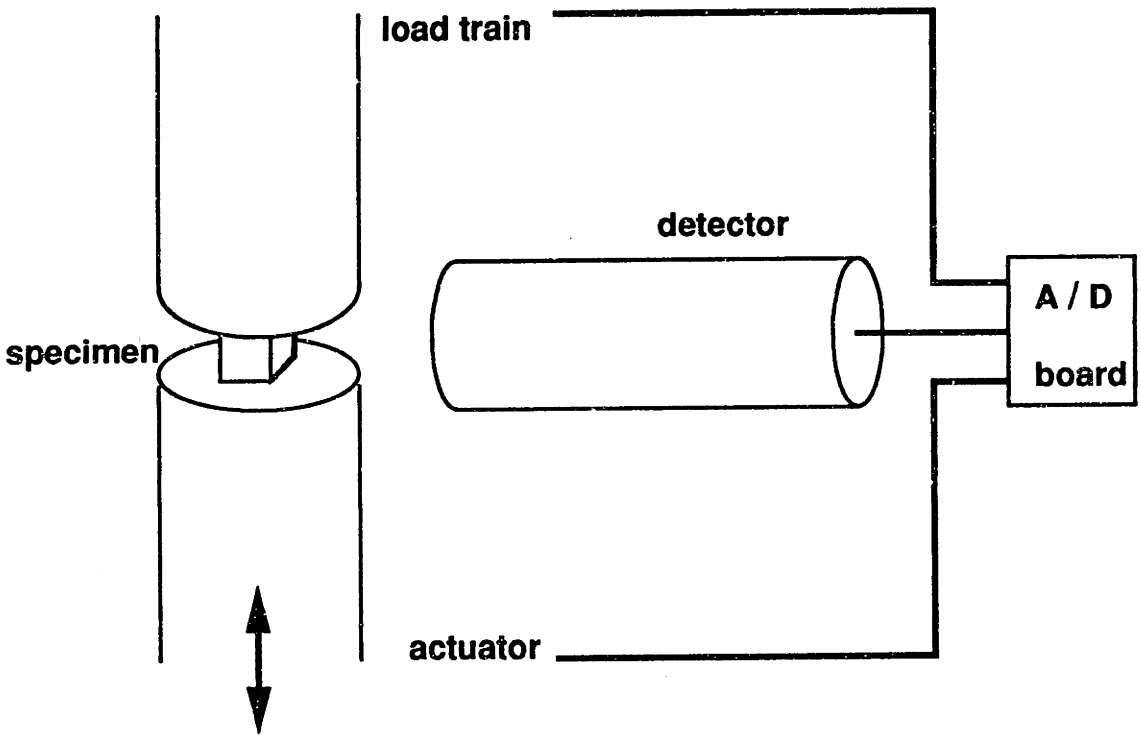

Figure 5.1: Sketch of the infrared detector and Instron load train apparatus.

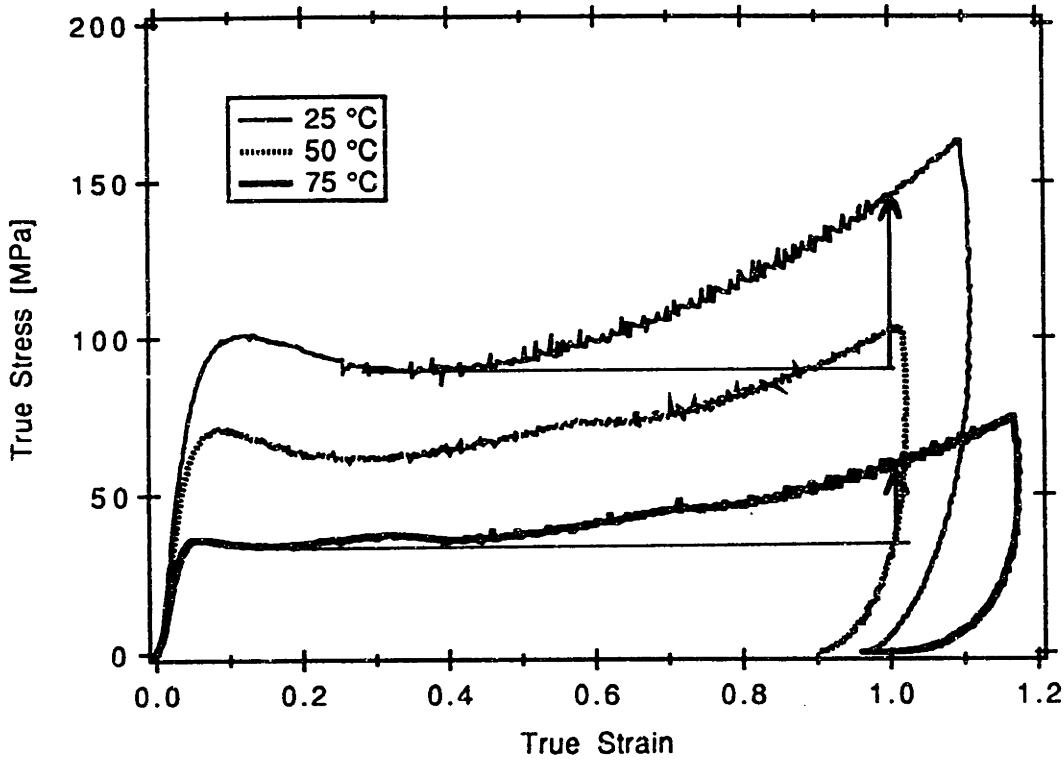

Figure 5.2: Experimentally determined uniaxial compression stress-strain curves for PMMA at $\dot{\epsilon} = -0.001/s$ over a range of temperatures.

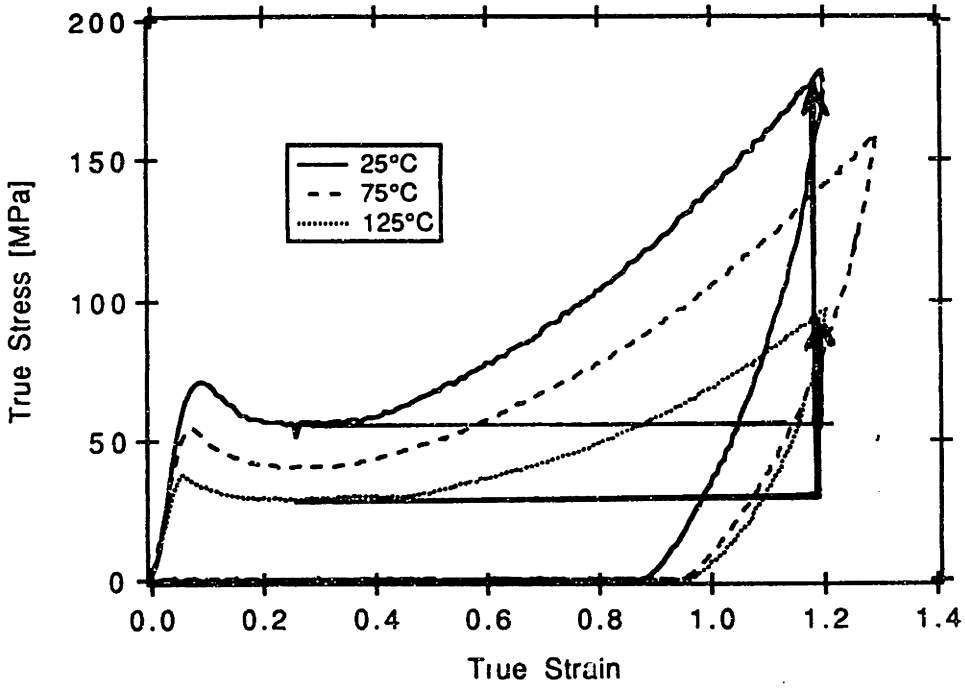

Figure 5.3: Experimentally determined uniaxial compression stress-strain curves for PC at $\dot{\epsilon} = -0.01/s$ over a range of temperatures.

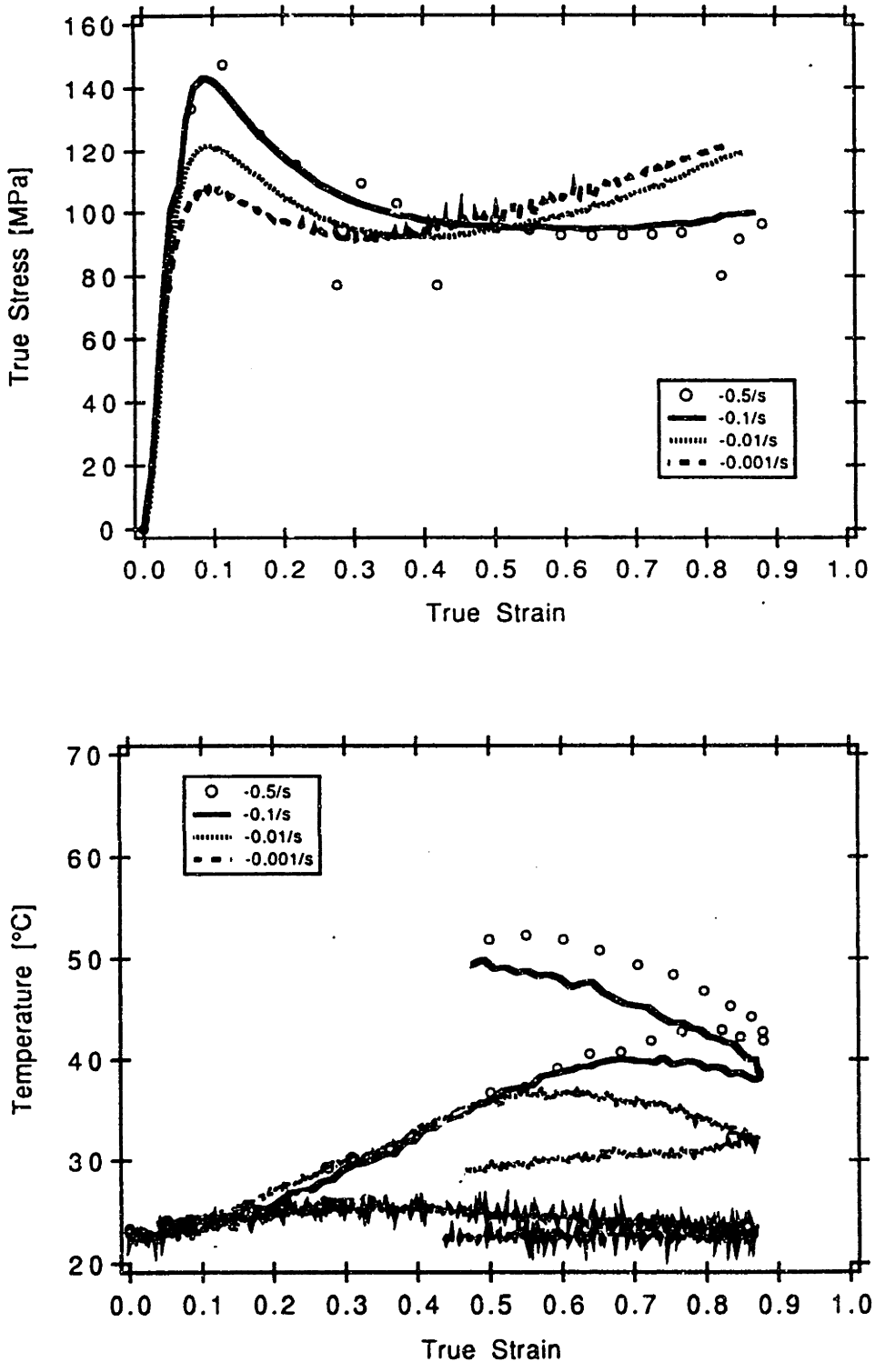

Figure 5.4: Experimentally determined uniaxial compression stress-strain curves and temperature-strain curves for PMMA over three decades of strain rate from $\dot{\epsilon} = -0.001/s$ to $\dot{\epsilon} = -0.5/s$.

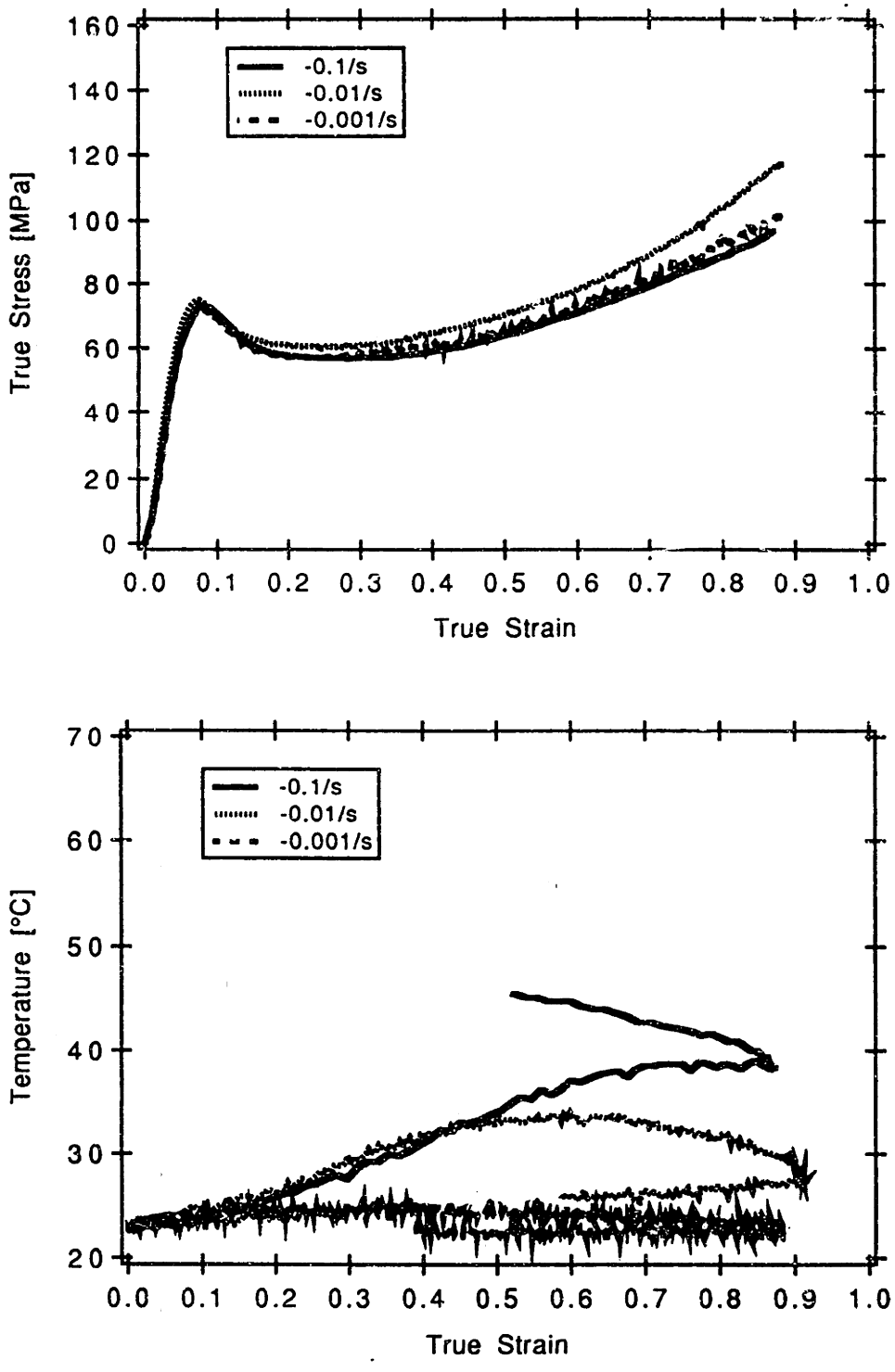

Figure 5.5: Experimentally determined uniaxial compression stress-strain curves and temperature-strain curves for PC over three decades of strain rate from $\dot{\epsilon} = -0.001/s$ to $\dot{\epsilon} = -0.1/s$.

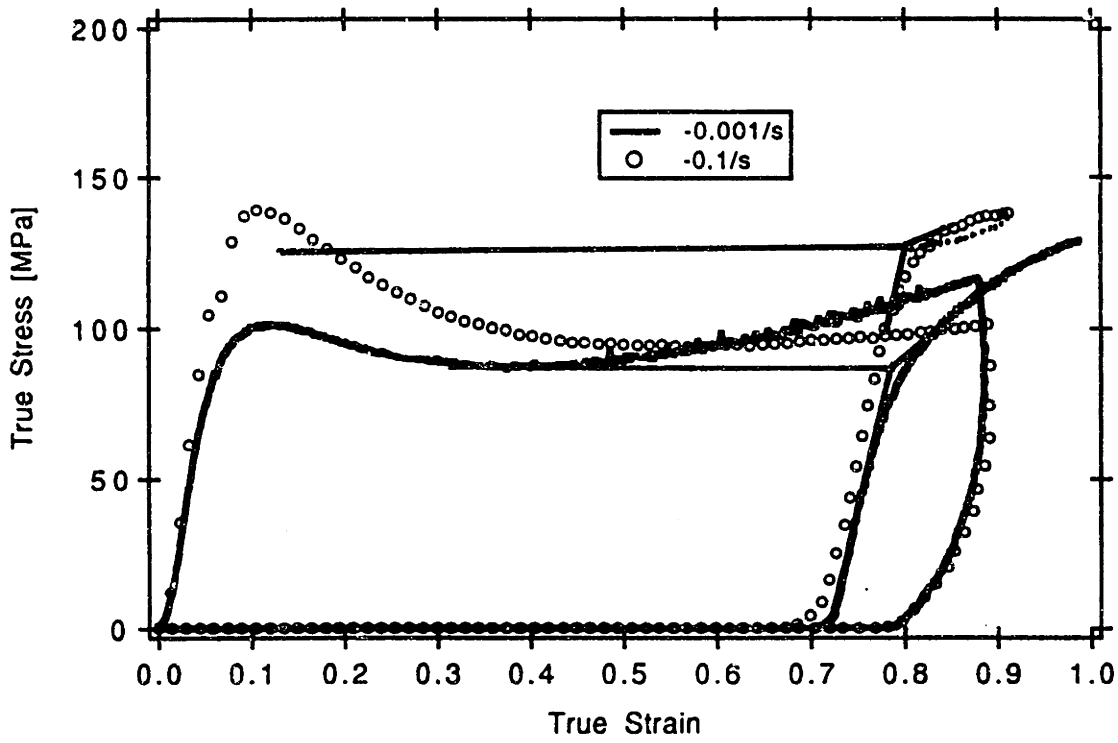

Figure 5.6: Experimentally determined initial uniaxial compression stress-strain curves and recompression curves for PMMA at strain rates of $\dot{\epsilon} = -0.001/s$ and $\dot{\epsilon} = -0.1/s$.

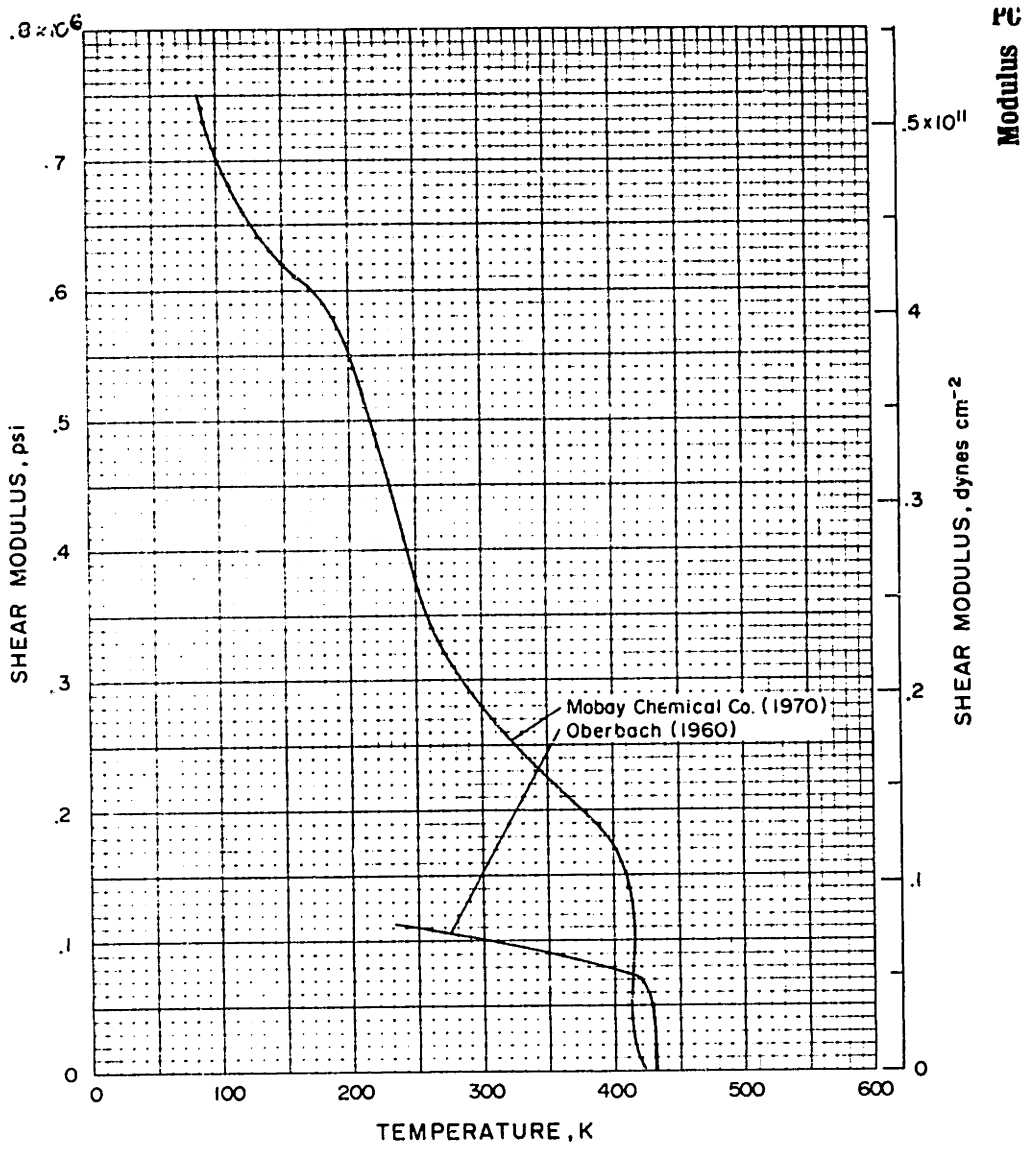

Figure 5.7: The temperature dependence of the shear modulus for polycarbonates below the glass transition temperatures [59].

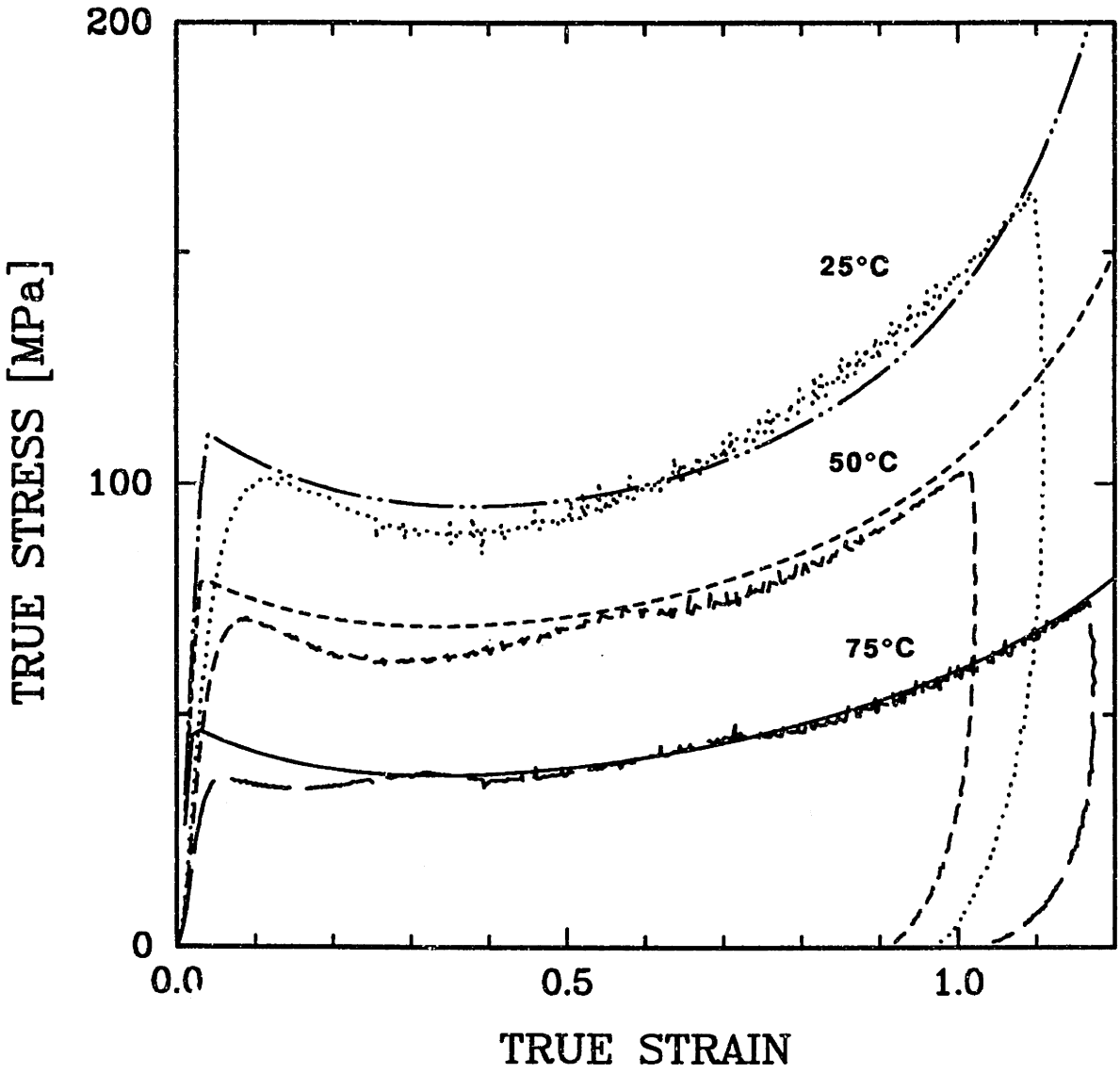

Figure 5.8: Comparison of theory versus experiment for the temperature dependent isothermal response of glassy PMMA.

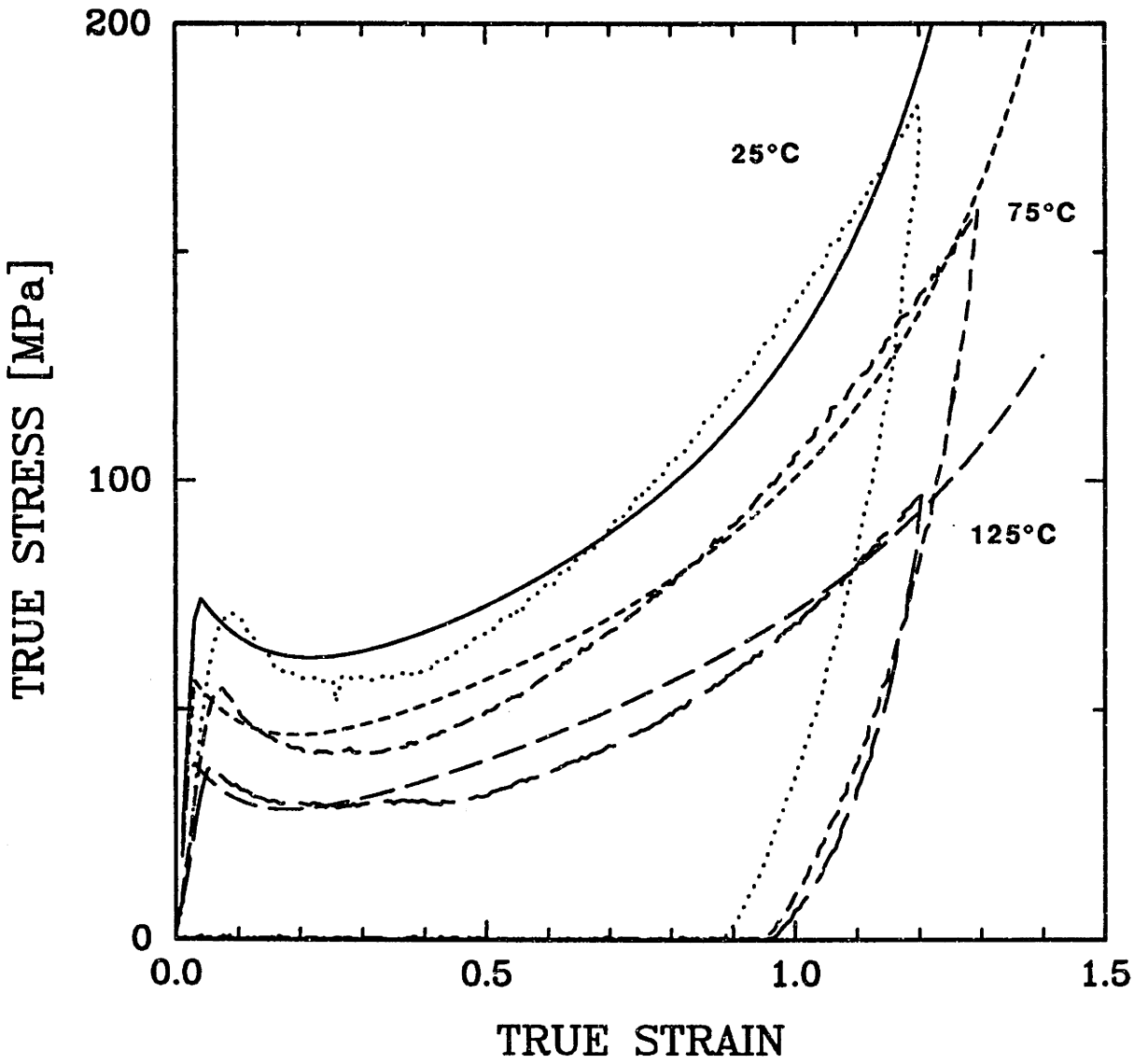

Figure 5.9: Comparison of theory versus experiment for the temperature dependent isothermal response of glassy PC.

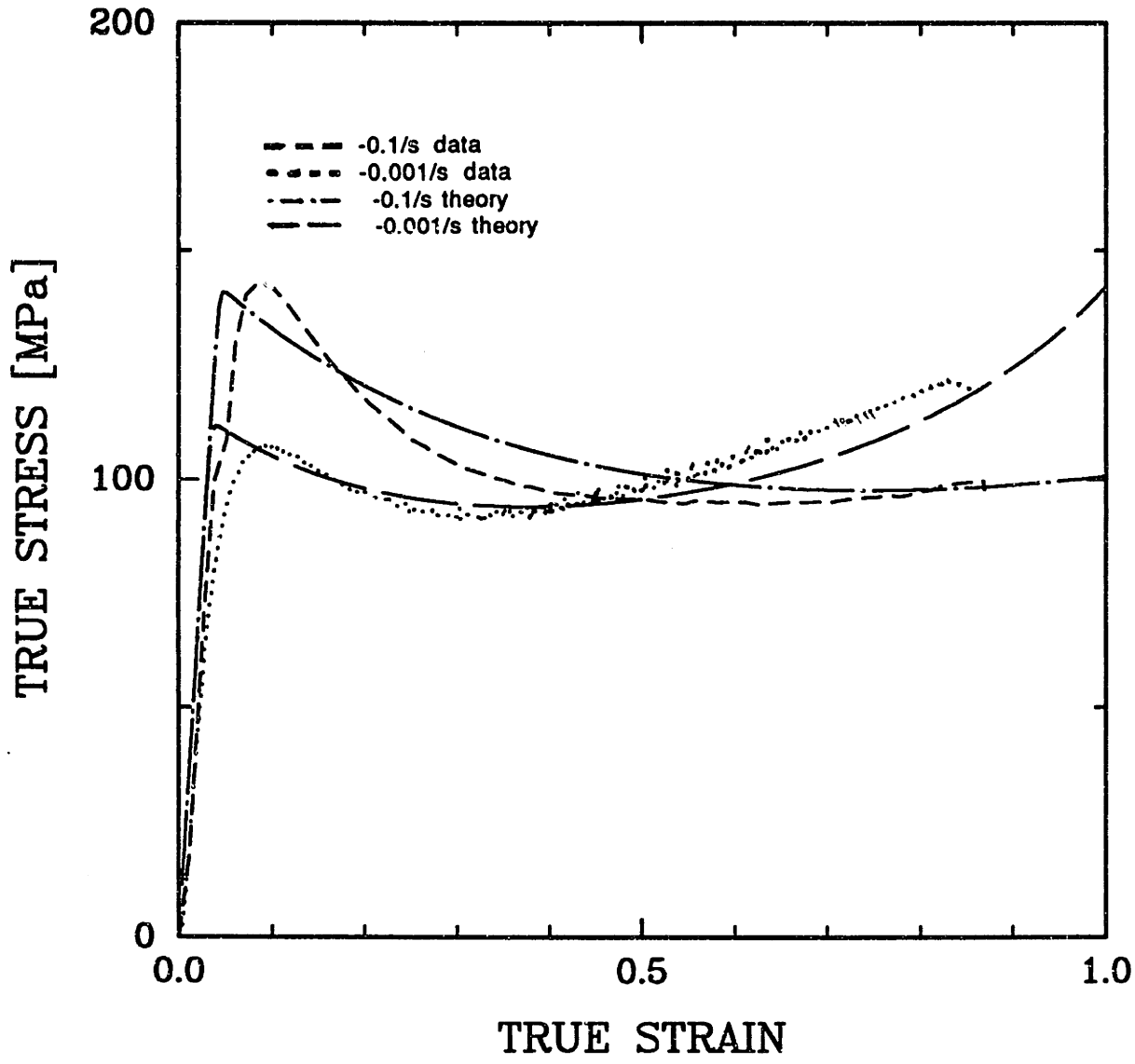

Figure 5.10: Comparison of theory and experiment for the responses of PMMA at a strain rate of $\dot{\epsilon} = -0.001/second$ which was simulated assuming isothermal conditions, and at a strain rate of $\dot{\epsilon} = -0.1/second$, simulated as an adiabatic response.

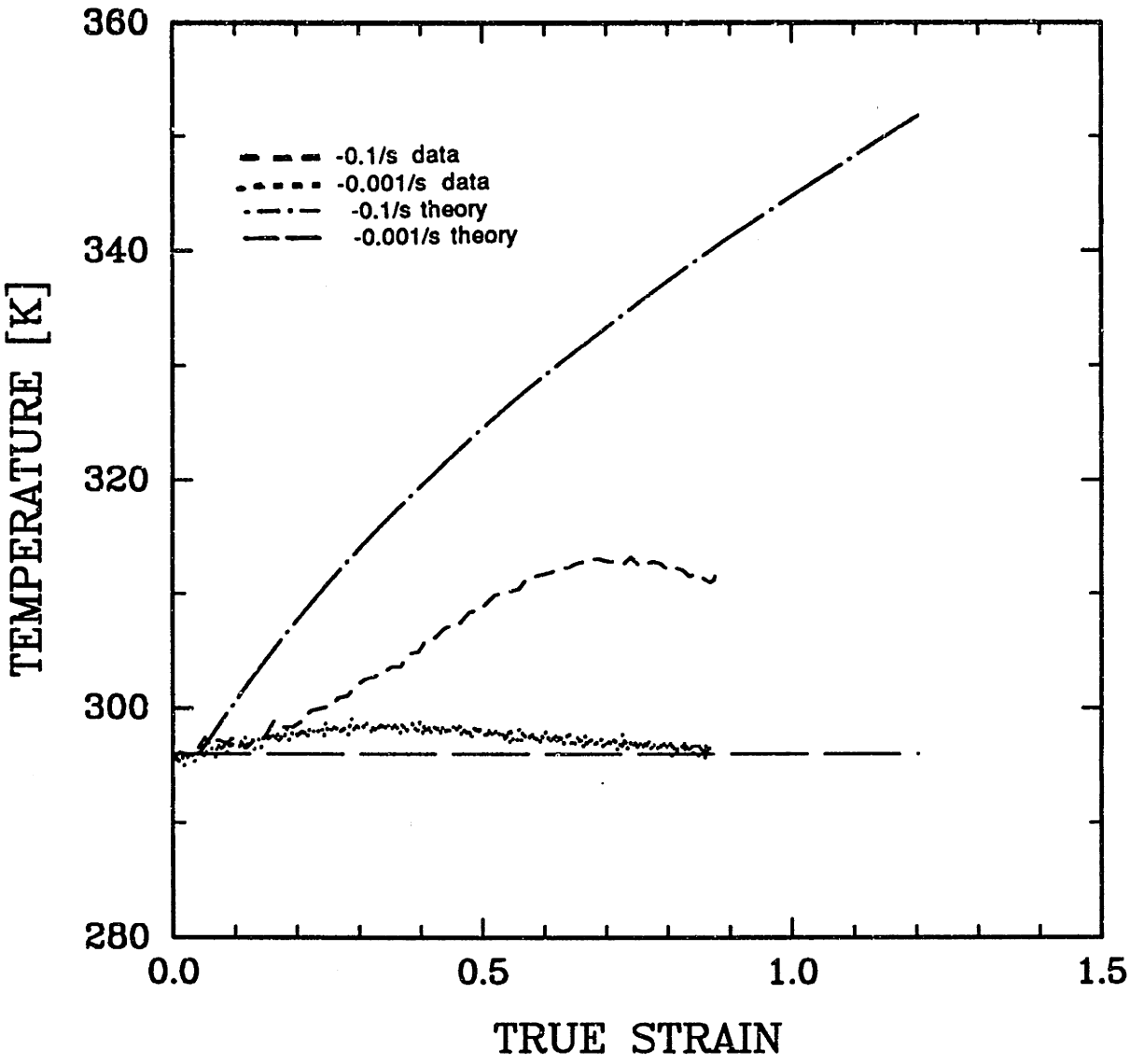

Figure 5.11: Comparison of theory and experiment for the surface temperature versus strain responses of PMMA at a strain rate of $\dot{\epsilon} = -0.001/second$ which was simulated assuming isothermal conditions, and at a strain rate of $\dot{\epsilon} = -0.1/second$, simulated as an adiabatic response.

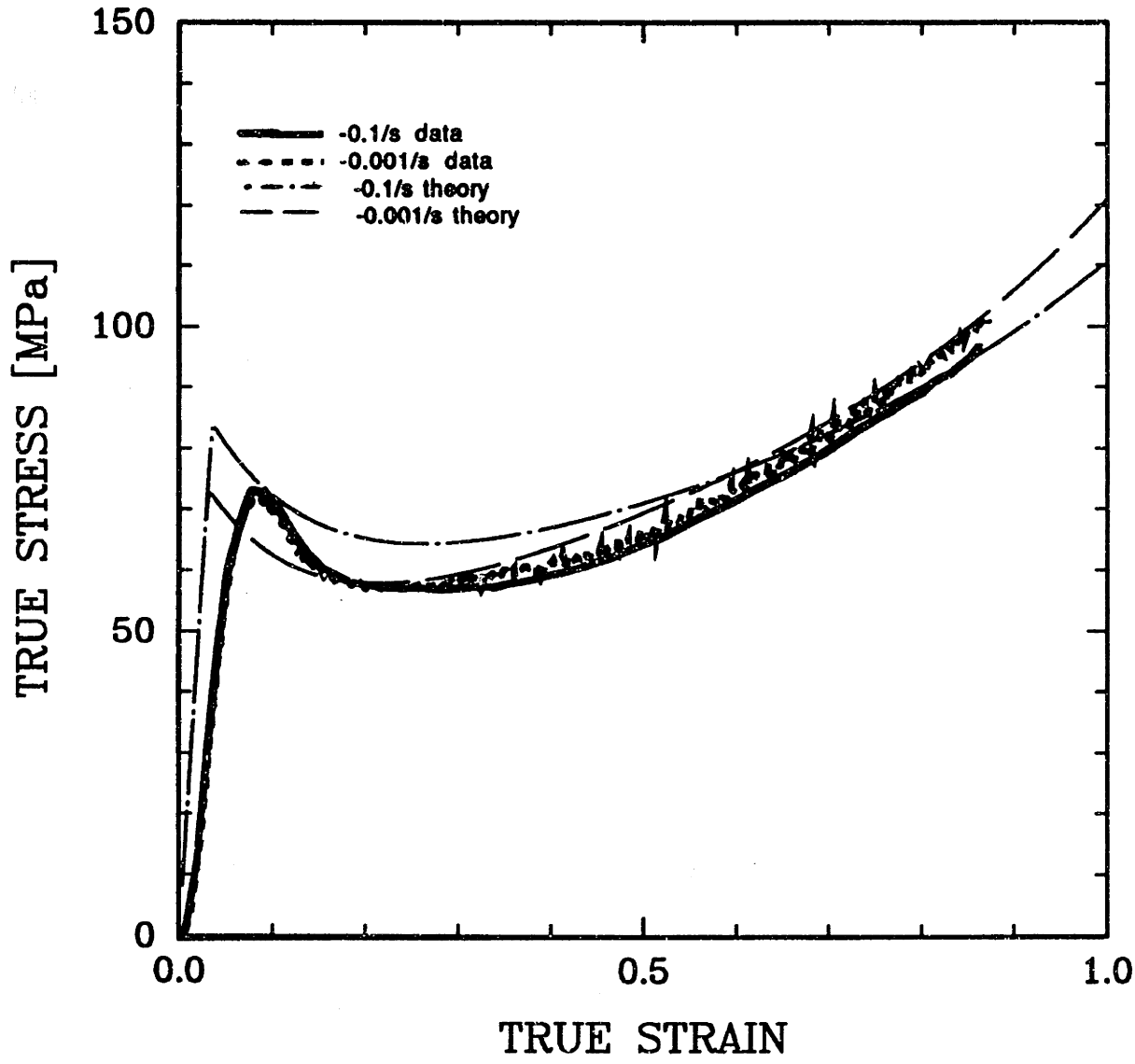

Figure 5.12: Comparison of theory and experiment for the responses of PC at a strain rate of $\dot{\epsilon} = -0.001/second$ which was simulated assuming isothermal conditions, and at a strain rate of $\dot{\epsilon} = -0.1/second$, simulated as an adiabatic response.

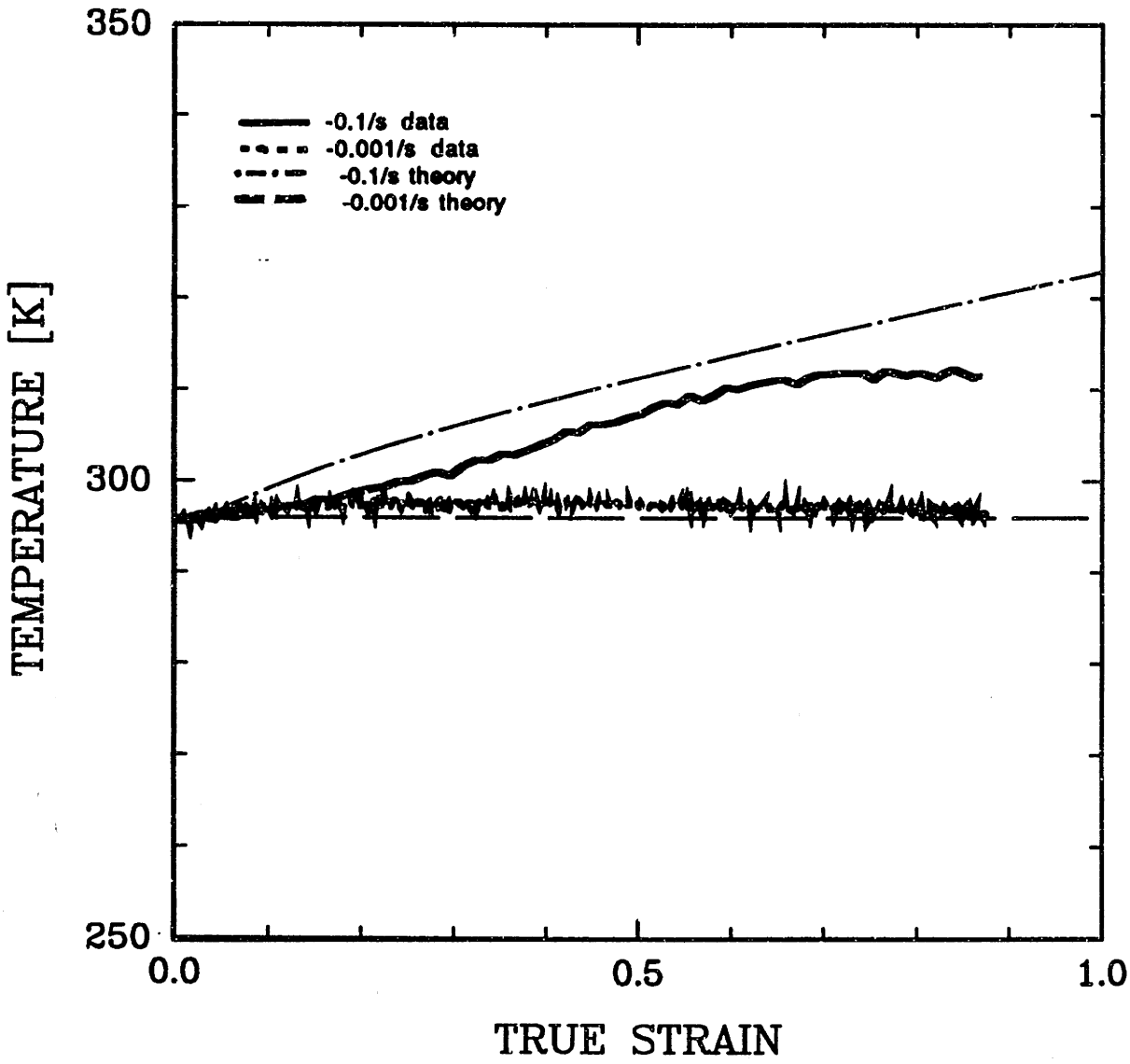

Figure 5.13: Comparison of theory and experiment for the surface temperature versus strain responses of PC at a strain rate of $\dot{\epsilon} = -0.001/second$ which was simulated assuming isothermal conditions, and at a strain rate of $\dot{\epsilon} = -0.1/second$, simulated as an adiabatic response.

Chapter 6

Summary

Although glassy polymers continue to be used extensively in engineering applications, very little has previously been understood in more than a qualitative sense about the large strain deformation response of these materials. The absence of this information has heretofore hindered the glassy polymer processing industry which resorts to trial and error forming operation designs to substitute for the lack of quantitative modelling of the polymer deformation response. This thesis has served to further the knowledge of the polymer deformation procedure in amorphous materials both above and below their glass transition temperatures.

A new constitutive model of rubber deformation has been developed in this thesis. This physically based treatment which follows the statistical mechanics of rubber elasticity framework provides for characterization of the three dimensional effects of rubber deformation. With one test to determine two material constants related to the rubbery polymer deformation process the state of deformation dependence of a rubbery material is completely characterized. The eight chain rubber elasticity model mimics the actual deformation process in a physical material. We find eight chains spanning the diagonals of a cube to be necessary and sufficient to capture the principal stretch state of the rubbery material in any state of deformation. The eight chain rubber deformation model of Chapter 2 was shown to "predict" the state of deformation dependence in three materials we tested ourselves and in another set of published data in the literature. This model was found to be superior to several rubber elasticity models in the literature which ranged in their mathematical and physical complexities.

The glassy polymer response has been investigated in the remaining chapters of this work. The first aspect considered was the state of deformation dependence of the strain hardening response of glassy polymers. Compression tests were conducted on initially isotropic polycarbonate and polymethylmethacrylate specimens to characterize the evolution of anisotropy during strain hardening. Measurements of optical anisotropy were obtained from the deformed specimen birefringence properties. Birefringence was found to evolve with magnitude of strain and state of deformation. These results confirmed that the state of anisotropy developed in uniaxial compression was one of transverse anisotropy whereas plane strain compression deformation resulted in a fully three dimensional state of anisotropy. Birefringence provides a

means of direct structural measurement of the three dimensional state of anisotropy in glassy polymers.

An existing model of the large strain deformation response of glassy polymers was found to fully capture many aspects of the observed response of PC and PMMA, but not the state of deformation dependent strain hardening response. The rubber deformation model of Chapter 2 was incorporated into the existing kinematic framework of [37] and shown to predict anisotropic strain hardening in glassy PMMA and PC requiring one test to characterize the strain hardening properties. The advent of the eight chain element to the already strong representation of polymer deformation of Boyce et. al. [37] resulted in a model of polymer deformation unparallelled in its ability to characterize the large strain elastic-viscoplastic response of polymer materials.

The effects of initial anisotropy in glassy polymers were investigated through constant strain rate tests on preoriented materials. Highly anisotropic responses of preoriented materials included direction dependent flow strengths, strain hardening characteristics, limiting extensibilities and deformation patterns. The extent to which the existing anisotropy is manifested in the subsequent deformation response of glassy polymers is astounding. Even without the complications associated with shear banding effects, the implications for processing of anisotropic polymers are clearly evident in the three dimensional responses of materials containing anisotropy. Predictions of the anisotropic response based on the isotropic behavior would clearly result in erroneous assessments of formability and structural integrity of such materials. The polymer deformation model presented in this thesis has been shown to be successfully predictive of the effects of initial anisotropy in glassy PC. All aspects of the anisotropic response of the material were captured by the model which used the characterized initially isotropic response and the anisotropic state of the polymer. The model was shown to be fully predictive of the three dimensional effects of polymer deformation.

The strain rate and temperature effects on the strain hardening response of glassy polymers were investigated through constant strain rate tests over a range of strain rates and temperatures. By systematically isolating the effects of both strain rate and temperature, much insight into the nature of these effects has been gained. Our polymer deformation model which uses two barriers to plastic flow has been further validated by the rate and temperature tests which illustrate that two barriers to continued plastic flow do exist in the glassy polymer. The strain rate and temperature effects on the overall polymer response have been separated into effects on the individual barriers. In particular the barrier to initial yield resulting from chain segment rotation has been verified to be both rate and temperature dependent. The strain hardening response to chain alignment was found to depend on temperature but not on strain rate for the range of rates considered here. Rate effects which appear to affect the strain hardening characteristics have been shown to be the result of the temperature dependence of the polymers.

The model was modified to assess the rate and temperature effects. Temperature dependent elastic constants were added as was a model for the temperature dependent strain hardening response which is due to an evolving network structure with

temperature. The model predicts the stress-strain curves for isothermal conditions at different temperatures and for isothermal versus adiabatic responses. The model overpredicts the specimen temperature rise during an adiabatic simulation on PMMA when compared to an experiment conducted at $\dot{\epsilon} = -0.1/second$, probably because the adiabatic condition was not met experimentally under these conditions. The model performs excellently in simulating the adiabatic response of PC as compared to the experimental results at $\dot{\epsilon} = -0.1/second$. The very complicated adiabatic response, which involves the evolution of two barriers to plastic flow with strain and temperature, is shown to be well modelled by our taking two barriers to plastic flow, one of which is stored and the other dissipative, and correctly characterizing their evolution with temperature and strain during deformation.

Several of the deformation processing parameters investigated here were found to affect the evolution of optical anisotropy in PMMA as measured by birefringence. The specimen birefringence has been shown to evolve with magnitude of strain, state of deformation and temperature. That this evolution may find use as a measure of the anisotropic state of the glassy polymer was evidenced in the recompression tests of two PMMA specimens which were preoriented under vastly different strain and thermal histories. The birefringence of these two specimens was the same and the anisotropic recompression response of both specimens was virtually identical. Knowledge of the prior strain and thermal history of anisotropic glassy polymers is often inaccessible to the polymer processor and indeed may not be necessary to the polymer designer, provided accurate characterization of the anisotropy through birefringence measurements may be accomplished. Our initial studies indicate that such a procedure warrants further investigation including experimental work to characterize the evolution of birefringence with state of strain, magnitude of strain and temperature.

This thesis has investigated the important effects in processing of glassy polymers, aspects of the large strain deformation response of these materials which were studied include the state of deformation dependence, strain rate dependence and temperature dependence. We have presented a glassy polymer deformation model which not only accounts for the observed effects in isotropic polymers but has been shown in this thesis to be able to accurately predict the response of preoriented materials to various deformation states and temperatures. The extensive experimental results which have been accurately captured offer strong support for this model as a sound constitutive relationship for glassy polymers which possesses the unrivaled ability to predict the highly anisotropic three dimensional aspects of large strain deformations of these materials.

Future work in the processing of glassy polymer components includes the design of solid phase forming operation procedures for specific polymer component output properties using the well characterized polymer deformation process which our model provides. Such a design methodology eliminates the current iterative design and implementation practices which have been required in the past to achieve the desired component properties in the absence of an understanding of the effects of large strain deformation processing of these materials. The work presented in this thesis allows for the design of process parameters using finite element simulations of the material response to such variables as die shape, temperature, strain rate and polymer pre-

form initial state. These parameters can now be optimized before any component is ever produced. The understanding of polymer deformation which has been provided herein is invaluable to the efficient, accurate design of solid phase polymer forming operations.

Additional work on characterizing the evolution of birefringence with plastic strain and temperature would provide for the possibility of real time process control of polymer forming operations. We have shown in this thesis that polymer birefringence is capable of detecting anisotropy in preoriented polymers, that the birefringence evolves measurably with temperature, magnitude of strain and state of strain and that specimens which have been subjected to different strain and thermal histories such that they possess the same level and state of anisotropy as measured by birefringence will respond identically to subsequent deformations. Through a thorough characterization of the evolution of birefringence in glassy polymers the stress-strain response of anisotropic materials may be predicted directly from the birefringence measure. This procedure may be implemented directly into the solid phase processing operation to provide real time feedback of the orientation induced anisotropy of the deforming polymer, which in turn provides a prediction of the mechanical behavior of the finished polymer component. The anisotropic responses of preoriented glassy polymers, all of which were investigated in this thesis including direction dependent flow stresses, strain hardening characteristics, limiting extensibilities and deformation patterns, could all be predicted and controlled using the birefringence feedback for detection and measurement of anisotropy during processing.

Bibliography

[1] L. R. G. Treloar. The Mechanics of Rubber Elasticity. *Proceedings of the Royal Society of London, Series A*, 351:301–330, 1976.

[2] L. R. G. Treloar. Stress-Strain Data for Vulcanized Rubber under Various Types of Deformation. *Transactions of the Faraday Society*, 40:59–70, 1944.

[3] R. W. Ogden. Large Deformation Isotropic Elasticity: On the Correlation of Theory and Experiment for Incompressible Rubberlike Solids. *Proceedings of the Royal Society of London Series A*, 326:565–584, 1972.

[4] L. R. G. Treloar. *The Physics of Rubber Elasticity.* Oxford University Press, Oxford, 1975.

[5] R. S. Rivlin. Large Elastic Deformations of Isotropic Materials, IV. Further Developments of the General Theory. *Philosophical Transactions of the Royal Society of London, Series A*, 241:379–397, 1948.

[6] M. J. Mooney. A Theory of Large Elastic Deformation. *Journal of Applied Physics*, 11:582–592, 1940.

[7] Y. Obata, S. Kawabata, and H. Kawai. Mechanical Properties of Natural Rubber Vulcanites in Finite Deformation. *Journal of Polymer Science, Series A-2*, 8:903–919, 1970.

[8] K. C. Valanis and R. F. Landel. The Strain-Energy Function of a Hyperelastic Material in Terms of the Extension Ratios. *Journal of Applied Physics*, 38:2997–3002, 1967.

[9] J. E. Mark and B. Erman. *Rubberlike Elasticity A Molecular Primer.* John Wiley and Sons, New York, 1988.

[10] M. C. Wang and E. J. Guth. Statistical Theory of Networks of Non-Gaussian Flexible Chains. *Journal of Chemical Physics*, 20:1144–1157, 1952.

[11] P. J. Flory and J. Rehner Jr. Statistical Mechanics of Cross-Linked Polymer Networks. *Journal of Chemical Physics*, 11:512–520, 1943.

[12] L. R. G. Treloar. The Elasticity of a Network of Long-Chain Molecules: Part III. *Transactions of the Faraday Society*, 42:83–94, 1946.

[13] L. R. G. Treloar. The Photoelastic Properties of Short-Chain Molecular Networks. *Transactions of the Faraday Society*, 50:881–896, 1954.

[14] P. J. Flory and B. Erman. Theory of Elasticity of Polymer Networks. 3. *Macromolecules*, 15:800–806, 1982.

[15] S. F. Edwards and Th. Vilgis. The Effect of Entanglements in Rubber Elasticity. *Polymer*, 27:483–492, 1986.

[16] D. F. Jones and L. R. G. Treloar. The Properties of Rubber in Pure Homogeneous Strain. *Journal of Physics Series D: Applied Physics*, 8:1285–1304, 1975.

[17] W. Kuhn and F. Grun. Beziehungen Zwischen Elastischen Konstanten und Dehnungsdoppelbrechung Hochelastischer Stoffe. *Kolloid Zeitschrift.*, 101:248–271, 1942.

[18] L. R. G. Treloar and G. Riding. A Non-Gaussian Theory for Rubber in Biaxial Strain I. Mechanical Properties. *Proceedings of the Royal Society of London, Series A*, 369:261–280, 1979.

[19] F. Fardshisheh and E. T. Onat. . In A Sawczuk, editor, *Problems in Plasticity*, page 89. Noordhoff, Leyden, 1972.

[20] M. E. Gurtin. *An Introduction to Continuum Mechanics.* Academic Press, New York, 1981.

[21] R. N. Haward and G. Thackray. The Use of a Mathematical Model to Describe Isothermal Stress-Strain Curves in Glassy Thermoplastics. *Proceedings of the Royal Society of London, Series A*, 302:453–472, 1968.

[22] P. S. Hope, I. M. Ward, and A. G. Gibson. The Hydrostatic Extrusion of PMMA. *Journal of Materials Science*, 15:2207–2220, 1980.

[23] V. K. Stokes and H. F. Nied. Solid Phase Sheet Forming of Thermoplastics, Parts I and II. *Transactions of the ASME Journal of Engineering Materials and Technology*, 108:107–117, 1986.

[24] C. G'Sell and J. J. Jonas. Determination of the Plastic Behavior of Solid Polymers at Constant True Strain Rate. *Journal of Materials Science*, 14:583–591, 1979.

[25] N. Kahar, R. A. Duckett, and I. M. Ward. Stress Optical Studies of Oriented Polymethylmethacrylate. *Polymer*, 19:136–144, 1978.

[26] N. Heymans. Development of Orientation in Glassy Polycarbonate at High Strains. *Polymer*, 28:2009–2017, 1987.

[27] P. B. Bowden and S. Raha. The Formation of Micro Shear Bands in Polystyrene and Polymethylmethacrylate. *Philosophical Magazine*, 22:463–482, 1970.

[28] C. G'Sell, S. Boni, and S. Shrivastava. Application of the Plane Simple Shear Tests for Determination of the Plastic Behavior of Solid Polymers at Large Strains. *Journal of Materials Science*, 18:903–918, 1983.

[29] Y. Y. Wang and D. M. Parks. unpublished experimental results.

[30] R. E. Robertson. Theory for the Plasticity of Glassy Polymers. *Journal of Chemical Physics*, 44:3950–3956, 1966.

[31] A. S. Argon. A Theory for the Low-Temperature Plastic Deformation of Glassy Polymers. *Philosophical Magazine*, 28:839–865, 1973.

[32] I. V. Yannas and R. R. Luise. The Strophon Theory of Deformation of Glassy Amorphous Polymers: Application to Small Deformations. In R. E. Zachariades and R. S. Porter, editors, *The Strength and Stiffness of Polymers*, pages 255–292. Marcel Dekker, 1983.

[33] M. C. Boyce and E. M. Arruda. An Experimental and Analytical Investigation of the Large Strain Compressive and Tensile Response of Glassy Polymers. *Polymer Engineering and Science*, 30:1288–1298, 1990.

[34] I. M. Ward. The Role of Molecular Networks and Thermally Activaled Processes in the Deformation Behavior of Polymers. *Polymer Engineering and Science*, 24:724–736, 1984.

[35] J. G. Rider and E. Hargreaves. Yielding of Oriented Polyvinylchloride. *Journal of Polymer Science, Series A-2*, 7:829–844, 1969.

[36] D. J. Brown and A. H. Windle. Stress-Orientation-Strain Relationships in Non-Crystalline Polymers. *Journal of Material Science*, 19:1997–2012, 1984.

[37] M. C. Boyce, D. M. Parks, and A. S. Argon. Large Inelastic Deformation of Glassy Polymers, Part I: Rate Dependent Constitutive Model. *Mechanics of Materials*, 7:15–33, 1988.

[38] D. M. Parks, A. S. Argon, and B. Bagepalli. Large Elastic-Plastic Deformation of Glassy Polymers. Technical report, M.I.T. Program in Polymer Science and Technology, 1984.

[39] D. Lee and P. C. Luken. Material Modelling and Solid Phase Forming of Polycarbonate Sheet. *Polymer Engineering and Science*, 26:612–619, 1986.

[40] R. Hill. *The Mathematical Theory of Plasticity.* Oxford University Press, Oxford, 1950.

[41] N. Brown and I. M. Ward. Deformation Bands in Oriented PET. *Philosophical Magazine*, 17:961–981, 1968.

[42] F. F. Rawson and J. G. Rider. Effects of Internal Stress on the Yielding of Oriented PVC. *Journal of Polymer Science, Series C*, 33:87–99, 1971.

[43] G. W. Adams and R. J. Farris. Latent Energy of Deformation of Bisphenol A Polycarbonate. *Journal of Polymer Science*, 26:433–445, 1988.

[44] M. D. Graham. Retardation in *nm*, for Plate Angle *i* in Degrees, for Berek Compensator S-N 3311. M.I.T. internal document.

[45] E. H. Lee. Elastic-Plastic Deformation at Finite Strains. *ASME Journal of Applied Mechanics*, 56:1–6, 1969.

[46] M. C. Boyce, G. G. Weber, and D. M. Parks. On the Kinematics of Finite Strain Plasticity. *Journal of the Mechanics and Physics of Solids*, 37:647–665, 1989.

[47] L. Anand. On H. Hencky's Approximate Strain Energy Function for Modelling Deformations. *ASME Journal of Applied Mechanics*, 46:78–82, 1979.

[48] O. A. Hasan, M. C. Boyce, X. S. Li, and S. Berko. An Investigation of the Yield and Post-Yield Behavior and Corresponding Structure of Glassy Polymers. Accepted for publication in *Journal of Polymer Science, Polymer Physics Edition*.

[49] E. M. Arruda and M. C. Boyce. A Three-Dimensional Constitutive Model for the Large Stretch Behavior of Rubber Elastic Materials. Accepted for publication in *Journal of the Mechanics and Physics of Solids*.

[50] M. C. Boyce, D. M. Parks, and A. S. Argon. Plastic Flow in Oriented Polymers. *International Journal of Plasticity*, 5:593–615, 1989.

[51] N. Brown, R.A. Duckett, and I. M. Ward. The Yield Behavior of Oriented PET. *Philosophical Magazine*, 18:483–502, 1968.

[52] E. M. Berg, D. C. Sun, and J. H. Magill. 3-D Structure-Property Relationships in Rolltruded Polymers, Part I: Mechanical Property Enhancement in Three Directions. *Polymer Engineering and Science*, 29:715–721, 1989.

[53] E. Oleynik. Distortional Plasticity of Organic Glassy Polymers. In E. Baer and A. Moet, editors, *High Performance Polymers*, page 79. Hanser, Munich, 1991.

[54] T.A. Vest, J. Amoedo, and D. Lee. Modeling of Tensile Stress Strain Behavior in Semi-Crystalline and Amorphous Polymers. pages 71–86.

[55] T. Machida and D. Lee. Deep Drawing of Polypropylene Sheets Under Differential Heating Conditions. *Polymer Engineering and Science*, 28:405–412, 1988.

[56] S. M. Walley, J. E. Field, P. H. Pope, and N. A. Stafford. A Study of the Rapid Deformation Behavior of a Range of Polymers. *Philosophical Transactions of the Royal Society of London, Series A*, 328:1–33, 1989.

[57] S. Raha and P. B. Bowden. Birefringence of Plastically Deformed Polymethylmethacrylate. *Polymer*, 13:174–183, 1972.

[58] M. C. Boyce. *Large Inelastic Deformation in Glassy Polymers.* PhD thesis, The Massachusetts Institute of Technology, 1986.

[59] R. E. Schramm, A. F. Clark, and R. P. Reed. *A Compilation and Evaluation of Mechanical, Thermal and Electrical Properties of Selected Polymers.* National Bureau of Standards, Monograph 132, 1973.

[60] M. C. Boyce, E. L. Montagut, and A. S. Argon. The Effects of Thermomechanical Coupling on the Cold Drawing Process of Glassy Polymers. In *ASME Winter Annual Meeting Proceedings: Symposium on Mechanics of Plastics and Plastic Composites*, 1991.

Appendix A

Force-stretch relations

The force versus stretch relations may be explicitly written in terms of the various model parameters for each of the models discussed in the text with the exception of the four chain model. For the four chain model, considered here to contain a junction point that seeks an equilibrium position for each increment in stretch, the force-stretch relations involve the coordinates of this position which must be solved for numerically. The expressions given here for the four chain model are for the case of a *stationary* junction point, and represent a situation for which the junction point is not in equilibrium.

The force-deformation expressions in uniaxial extension, biaxial extension and pure shear for the models are determined by directly differentiating the strain energy. The strain energies given in Equations 2.14 and 2.35 of Chapter 2 are truncated expressions of infinite series for the inverse Langevin function in the three and eight chain models, respectively. Approximate force-stretch relations may be found from differentiation of the strain energy terms given in each of these cases. The exact expressions are obtained in the three and eight chain models using the equations which relate the differences in principal stresses. To illustrate, Equation 2.12 in Chapter 2 for the three chain model has been reprinted below along with the corresponding equations for the remaining principal stress differences.

$$\sigma_1 - \sigma_2 = \frac{nk\Theta}{3}\sqrt{N}\left(\lambda_1\mathcal{L}^{-1}\left\{\frac{\lambda_1}{\sqrt{N}}\right\} - \lambda_2\mathcal{L}^{-1}\left\{\frac{\lambda_2}{\sqrt{N}}\right\}\right) \tag{A.1}$$

$$\sigma_2 - \sigma_3 = \frac{nk\Theta}{3}\sqrt{N}\left(\lambda_2\mathcal{L}^{-1}\left\{\frac{\lambda_2}{\sqrt{N}}\right\} - \lambda_3\mathcal{L}^{-1}\left\{\frac{\lambda_3}{\sqrt{N}}\right\}\right) \tag{A.2}$$

$$\sigma_3 - \sigma_1 = \frac{nk\Theta}{3}\sqrt{N}\left(\lambda_3\mathcal{L}^{-1}\left\{\frac{\lambda_3}{\sqrt{N}}\right\} - \lambda_1\mathcal{L}^{-1}\left\{\frac{\lambda_1}{\sqrt{N}}\right\}\right) \tag{A.3}$$

Incompressibility is imposed in the form

$$\lambda_1\lambda_2\lambda_3 = 1 \tag{A.4}$$

along with the boundary conditions associated with each state of deformation to determine each load versus stretch expression. This is illustrated below for the three deformation states examined in this manuscript.

1. uniaxial extension

   boundary condition: $\sigma_2 = \sigma_3 = 0$

   incompressibility: $\lambda_1 = \lambda$, $\lambda_2 = \lambda_3 = \lambda^{-\frac{1}{2}}$

   Equation A.1 becomes

$$\sigma_1 = \frac{nk\Theta}{3}\sqrt{N}\left(\lambda\mathcal{L}^{-1}\left\{\frac{\lambda}{\sqrt{N}}\right\} - \lambda^{-\frac{1}{2}}\mathcal{L}^{-1}\left\{\frac{1}{\sqrt{\lambda N}}\right\}\right) \tag{A.5}$$

   If the initial material dimension is assumed to be unity then incompressibility enters again in the conversion to a force versus stretch relation:

$$f_1 = \sigma_1 A_1 = \sigma_1 \lambda_2 \lambda_3 = \frac{\sigma_1}{\lambda_1} \tag{A.6}$$

   The uniaxial extension force-stretch relations are

$$f_1 = \frac{nk\Theta}{3}\sqrt{N}\left(\mathcal{L}^{-1}\left\{\frac{\lambda}{\sqrt{N}}\right\} - \lambda^{-\frac{3}{2}}\mathcal{L}^{-1}\left\{\frac{1}{\sqrt{\lambda N}}\right\}\right) \tag{A.7}$$

$$f_2 = 0 \tag{A.8}$$

$$f_3 = 0 \tag{A.9}$$

2. equi-biaxial extension

   boundary condition: $\sigma_1 = \sigma_2$, $\sigma_3 = 0$

   incompressibility: $\lambda_1 = \lambda_2 = \lambda$, $\lambda_3 = \lambda^{-2}$

   Equation A.1 gives

$$\sigma_1 = \frac{nk\Theta}{3}\sqrt{N}\left(\lambda\mathcal{L}^{-1}\left\{\frac{\lambda}{\sqrt{N}}\right\} - \lambda^{-2}\mathcal{L}^{-1}\left\{\frac{1}{\lambda^2\sqrt{N}}\right\}\right) \tag{A.10}$$

   or

$$f_1 = \frac{nk\Theta}{3}\sqrt{N}\left(\mathcal{L}^{-1}\left\{\frac{\lambda}{\sqrt{N}}\right\} - \lambda^{-3}\mathcal{L}^{-1}\left\{\frac{1}{\lambda^2\sqrt{N}}\right\}\right) \tag{A.11}$$

$$f_2 = f_1 \tag{A.12}$$

$$f_3 = 0 \tag{A.13}$$

3. pure shear

   boundary condition: $\sigma_3 = 0$

   incompressibility: $\lambda_1 = \lambda$, $\lambda_2 = 1$, $\lambda_3 = \lambda^{-1}$

   The results are

$$f_1 = \frac{nk\Theta}{3}\sqrt{N}\left(\mathcal{L}^{-1}\left\{\frac{\lambda}{\sqrt{N}}\right\} - \lambda^{-2}\mathcal{L}^{-1}\left\{\frac{1}{\lambda\sqrt{N}}\right\}\right) \tag{A.14}$$

$$f_2 = \frac{nk\Theta}{3}\sqrt{N}\left(\lambda^{-1}\mathcal{L}^{-1}\left\{\frac{1}{\sqrt{N}}\right\} - \lambda^{-2}\mathcal{L}^{-1}\left\{\frac{1}{\lambda\sqrt{N}}\right\}\right) \tag{A.15}$$

$$f_3 = 0 \tag{A.16}$$

The force-stretch relation of Equation A.7 can also be found from direct differentiation of the strain energy function according to

$$f_t = \sum_{i=1}^{3} \frac{\delta W}{\delta \lambda_i}\frac{\delta \lambda_i}{\delta \lambda_t} \tag{A.17}$$

where the $\frac{\delta \lambda_i}{\delta \lambda_t}$ terms provide the incompressibility constraint for λ_i expressed as functions of the imposed stretch, λ_t, determined by the incompressibility condition for each state of deformation. For example, in uniaxial extension Equation A.17 expands to

$$f_1 = \frac{\delta W}{\delta \lambda_1}\frac{\delta \lambda_1}{\delta \lambda_1} + 2\frac{\delta W}{\delta \lambda_2}\frac{\delta \lambda_2}{\delta \lambda_1} \tag{A.18}$$

because $\lambda_2 = \lambda_3$. When the exact strain energy expression is given the force-stretch relations are determined using Equation A.18. All force-stretch relations used in the simulations reported in this thesis appear below along with the parameters used to fit each model.

1. Mooney-Rivlin

   $C_1 = .15$, $C_2 = .015$

   uniaxial $\quad f = 2(\lambda - \lambda^{-2})(C_1 + C_2\lambda^{-1})$

   biaxial $\quad f = 2(\lambda - \lambda^{-5})(C_1 + C_2\lambda^{2})$

   pure shear $\quad f = 2(\lambda - \lambda^{-3})(C_1 + C_2)$

2. Ogden

   $\alpha_1 = 1.3$, $\mu_1 = .61803$, $\alpha_2 = 5.$, $\mu_2 = .00118$,$\alpha_3 = -2.$, $\mu_3 = -.00981$

   uniaxial $\quad f = \sum_n \mu_n\lambda^{-1}(\lambda^{\alpha_n} - \lambda^{-\frac{\alpha_n}{2}})$

   biaxial $\quad f = \sum_n \mu_n\lambda^{\alpha_n - 1}(1 - \lambda^{-3\alpha_n})$

   pure shear $\quad f = \sum_n \mu_n\lambda^{-1}(\lambda^{\alpha_n} - \lambda^{-\alpha_n})$

3. Wang-Guth

$N = 82.$, $\frac{nk\Theta}{3} = .09$

uniaxial $f = \frac{nk\Theta}{3}\sqrt{N}\left(\mathcal{L}^{-1}\left\{\frac{\lambda}{\sqrt{N}}\right\} - \lambda^{-\frac{3}{2}}\mathcal{L}^{-1}\left\{\frac{1}{\sqrt{\lambda N}}\right\}\right)$

biaxial $f = \frac{nk\Theta}{3}\sqrt{N}\left(\mathcal{L}^{-1}\left\{\frac{\lambda}{\sqrt{N}}\right\} - \lambda^{-3}\mathcal{L}^{-1}\left\{\frac{1}{\lambda^2\sqrt{N}}\right\}\right)$

pure shear $f = \frac{nk\Theta}{3}\sqrt{N}\left(\mathcal{L}^{-1}\left\{\frac{\lambda}{\sqrt{N}}\right\} - \lambda^{-2}\mathcal{L}^{-1}\left\{\frac{1}{\lambda\sqrt{N}}\right\}\right)$

4. Flory-Rehner

This form was not used to determine Figure 2.9, the constants are approximate.

$\frac{nk\Theta}{4} = 5.5$, $N = 64.$

uniaxial $\frac{f}{\frac{nk\Theta}{4}\sqrt{N}} = \mathcal{L}^{-1}\left\{\frac{\lambda}{\sqrt{N}}\right\}$

$$+(\lambda - 4\lambda^{-2})(8\lambda^{-1} + \lambda^2)^{-\frac{1}{2}}\mathcal{L}^{-1}\left\{\frac{(8\lambda^{-1}+\lambda^2)^{\frac{1}{2}}}{3\sqrt{N}}\right\}$$

biaxial $\frac{f}{\frac{nk\Theta}{4}\sqrt{N}} = \mathcal{L}^{-1}\left\{\frac{\lambda}{\sqrt{N}}\right\}$

$$+\frac{1}{3}(\lambda - 8\lambda^{-5})(8\lambda^{-4} + \lambda^2)^{-\frac{1}{2}}\mathcal{L}^{-1}\left\{\frac{(8\lambda^{-4}+\lambda^2)^{\frac{1}{2}}}{3\sqrt{N}}\right\}$$

$$+\frac{2}{3}(\lambda - 2\lambda^{-5})(7\lambda^2 + 2\lambda^{-4})^{-\frac{1}{2}}\mathcal{L}^{-1}\left\{\frac{(7\lambda^2+2\lambda^{-4})^{-\frac{1}{2}}}{3\sqrt{N}}\right\}$$

pure shear $\frac{f}{\frac{nk\Theta}{4}\sqrt{N}} = \mathcal{L}^{-1}\left\{\frac{\lambda!}{\sqrt{N}}\right\}$

$$+\frac{8}{3}(\lambda - \lambda^{-3})(8\lambda^{-2} + \lambda^2)^{-\frac{1}{2}}\mathcal{L}^{-1}\left\{\frac{(8\lambda^{-2}+\lambda^2)^{\frac{1}{2}}}{3\sqrt{N}}\right\}$$

$$+\frac{2}{3}(\lambda - 2\lambda^{-3})(6 + \lambda^2 + 2\lambda^{-2})^{-\frac{1}{2}}\mathcal{L}^{-1}\left\{\frac{(6+\lambda^2+2\lambda^{-2})^{-\frac{1}{2}}}{3\sqrt{N}}\right\}$$

5. Flory-Erman

$\xi k\Theta = .3$, $\frac{\mu}{\xi} = .1$, $\kappa = 100.$

uniaxial $f = \xi k\Theta\left[\lambda - \lambda^{-2} + \left(\frac{\mu}{\xi}\right)(\lambda K_1 - \lambda^{-2}K_2)\right]$

$K_1 = \hat{K}_1(\lambda^2)$, $K_2 = \hat{K}_2(\lambda^{-\frac{1}{2}})$

biaxial $f = \xi k\Theta\left[\lambda - \lambda^{-5} + \left(\frac{\mu}{\xi}\right)(\lambda K_1 - \lambda^{-5}K_3)\right]$

$K_1 = \hat{K}_1(\lambda^2)$, $K_3 = \hat{K}_3(\lambda^{-4})$

pure shear $f = \xi k\Theta\left[\lambda - \lambda^{-3} + \left(\frac{\mu}{\xi}\right)(\lambda K_1 - \lambda^{-3}K_3)\right]$

$K_1 = \hat{K}_1(\lambda^2)$, $K_3 = \hat{K}_3(\lambda^{-2})$

$K_i = B_i[\dot{B}_i(B_i + 1)^{-1} + \kappa^{-1}(\lambda_i^2\dot{B}_i + B_i)(B_i + \kappa\lambda_i^{-2})^{-1}]$

$$\dot{B}_i = B_i[(\lambda_i^2 - 1)^{-1} - 2(\lambda_i^2 + \kappa)^{-1}]$$
$$B_i = \kappa^2(\lambda_i^2 - 1)(\lambda_i^2 + \kappa)^{-2}$$

6. Eight Chain

$N = 26.5$, $\frac{nk\Theta}{3} = .09$

uniaxial $f = \frac{nk\Theta}{3}\sqrt{N}\left(\mathcal{L}^{-1}\left\{\frac{\lambda_{chain}}{\sqrt{N}}\right\}\right)\left(\frac{\lambda-\lambda^{-2}}{\lambda_{chain}}\right)$

biaxial $f = \frac{nk\Theta}{3}\sqrt{N}\left(\mathcal{L}^{-1}\left\{\frac{\lambda_{chain}}{\sqrt{N}}\right\}\right)\left(\frac{\lambda-\lambda^{-5}}{\lambda_{chain}}\right)$

pure shear $f = \frac{nk\Theta}{3}\sqrt{N}\left(\mathcal{L}^{-1}\left\{\frac{\lambda_{chain}}{\sqrt{N}}\right\}\right)\left(\frac{\lambda-\lambda^{-3}}{\lambda_{chain}}\right)$

$$\lambda_{chain} = \frac{1}{\sqrt{3}}\, I_1^{\frac{1}{2}}$$

Appendix B

State of deformation dependence

The strain energy expression for the eight chain model proposed in Chapter 2 (Equation 2.35) is a function of non-negative integer order I_1 terms. The role of these terms in predicting the state of deformation dependence displayed by rubber data can be illustrated by consideration of the first five terms which represent first, second, third, fourth and fifth order functions of I_1. The approximate uniaxial and biaxial force-stretch relations are written using the five strain energy terms and differentiating according to Equation A.17.

$$\textit{uniaxial} \qquad I_1 = \lambda^2 + 2\lambda^{-1}$$

$$f = nk\Theta(\lambda - \lambda^{-2})\left[1 + \frac{1}{5N}I_1 + \frac{11}{175N^2}I_1^2 + \frac{19}{875N^3}I_1^3 + \frac{519}{67375N^4}I_1^4\right] \qquad \text{(B.1)}$$

$$\textit{biaxial} \qquad I_1 = 2\lambda^2 + \lambda^{-4}$$

$$f = nk\Theta(\lambda - \lambda^{-5})\left[1 + \frac{1}{5N}I_1 + \frac{11}{175N^2}I_1^2 + \frac{19}{875N^3}I_1^3 + \frac{519}{67375N^4}I_1^4\right] \qquad \text{(B.2)}$$

In Figure B1 the uniaxial force-stretch data have been compared to the first five terms in the eight chain model by plotting the individual decomposed terms from the prediction above as well as the total force represented by the sum of these five terms. The eight chain model parameters as reported above were used. This exercise has been repeated for the biaxial expression and data in Figure B2. From these figures it is seen that the first order I_1 term captures the initial response of the material in both deformation states. The higher order I_1 terms are responsible for providing the upturn in the curves at stretches in excess of 4.0 for the uniaxial simulation and earlier, at roughly 3.0, for the biaxial test. The trend established by these first five terms is that as the order of the I_1 term increases more of an upturn in force at large extensions is provided. In uniaxial extension the upturn is delayed as compared to its occurrance in the biaxial response. This aspect of the contribution from the non-linear I_1 terms is responsible for predicting the correct state of deformation dependence.

It is clear from Figures B1 and B2 that the five term approximation given above does not reach the force levels of the data in either deformation state at the largest

stretches and that the complete eight chain model is comprised of a large summation of such terms of increasing I_1 order. Clearly many of these terms are needed to fully capture the uniaxial and biaxial behavior of the material; the use of five terms in the series does not fully present the desired response. The complete inverse Langevin function used in the eight chain model provides the large number of terms required while limiting the number of adjustable parameters to two.

The above illustration was repeated with a strain energy expression of I_2 and I_2^2. The results appear in Figures B3 and B4 for uniaxial and biaxial cases, respectively. While first and higher order I_2 terms do show a state of deformation dependence, these terms alone can not capture the uniaxial and biaxial data successfully. In uniaxial extension the I_2 type terms do not capture the upturn in the force-stretch curve and therefore have little effect when used together with a linear I_1 term; these same terms grossly overpredict the biaxial response. Used together, first order I_1 and I_2 terms can probably achieve a reasonable fit to the biaxial data which is why the Mooney-Rivlin formulation does reasonably well in uniaxial compression. However, from Figures B1 and B2 it is clear that I_2 type terms are not needed to capture the deformation response when the nonlinear I_1 type terms are present in a physically meaningful representation.

In conclusion it is clear that the first invariant, I_1, as it appears in the eight chain model is clearly able to predict the response of the data. While other terms such as integer powers of the second invariant and non-integer powers of both functions similarly show a state of deformation dependence their inclusion is not needed. A good fit to all of the deformation states requires several terms and is easily accomplished using the eight chain model with its two physical parameters.

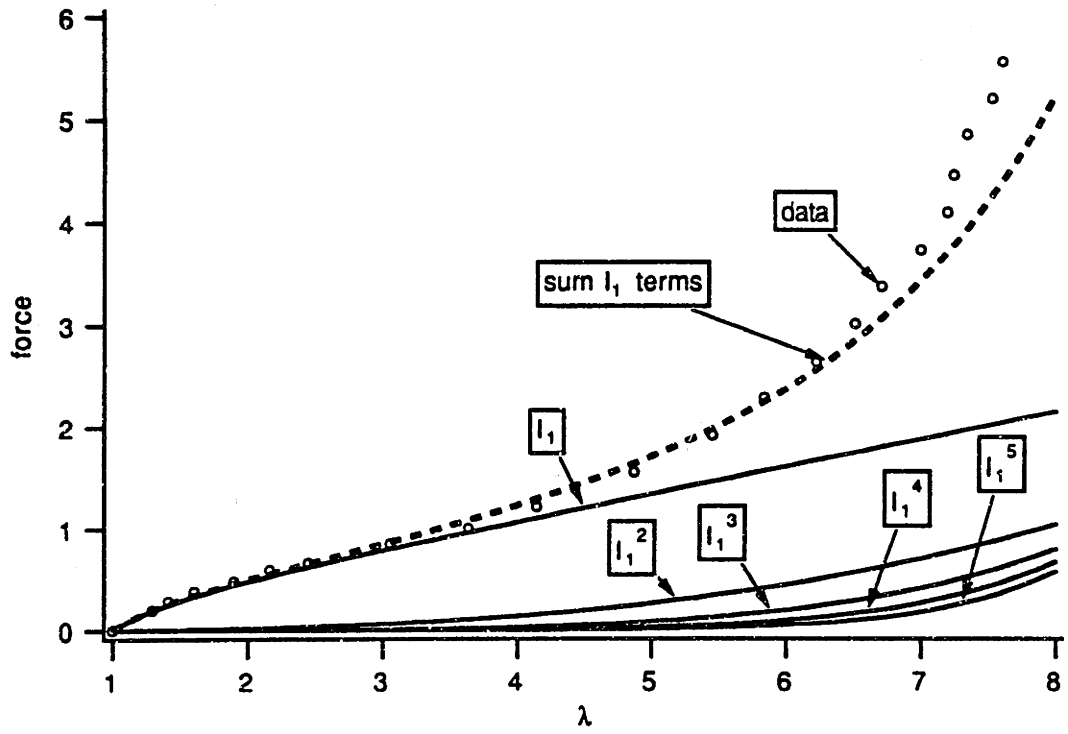

Figure B1: Predictions of the first five terms in the eight chain strain energy expression and comparison with data for uniaxial extension.

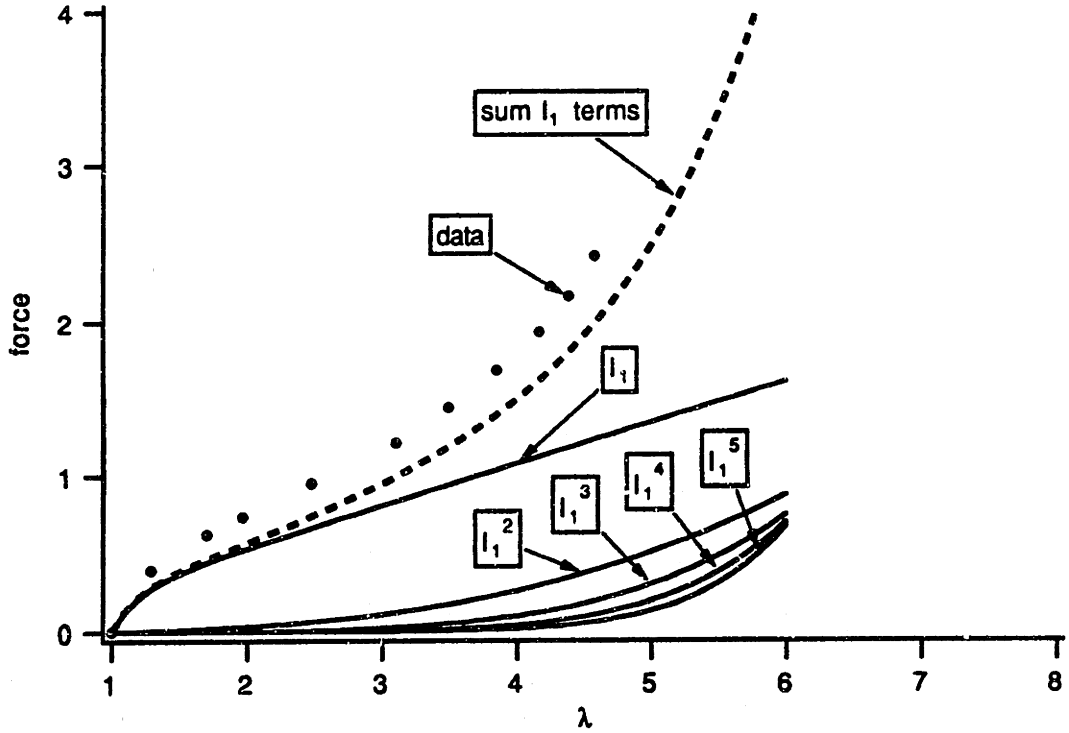

Figure B2: Predictions of the first five terms in the eight chain strain energy expression and comparison with data for biaxial extension.

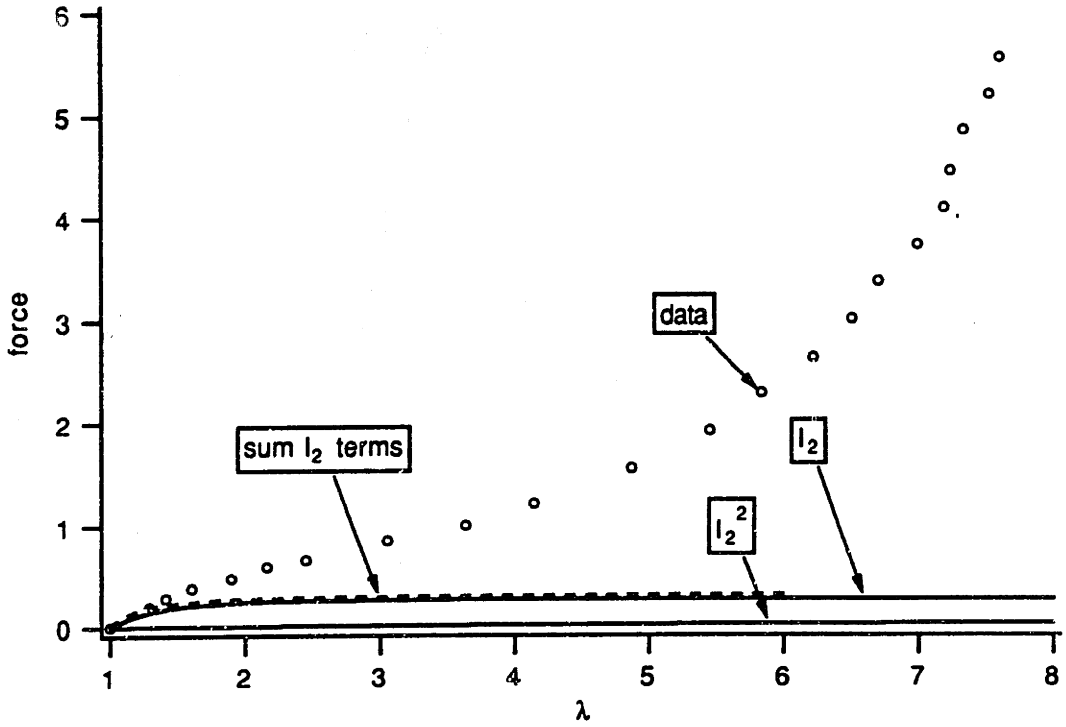

Figure B3: Predictions of first and second order I_2 terms in the eight chain strain energy expression and comparison with data for uniaxial extension.

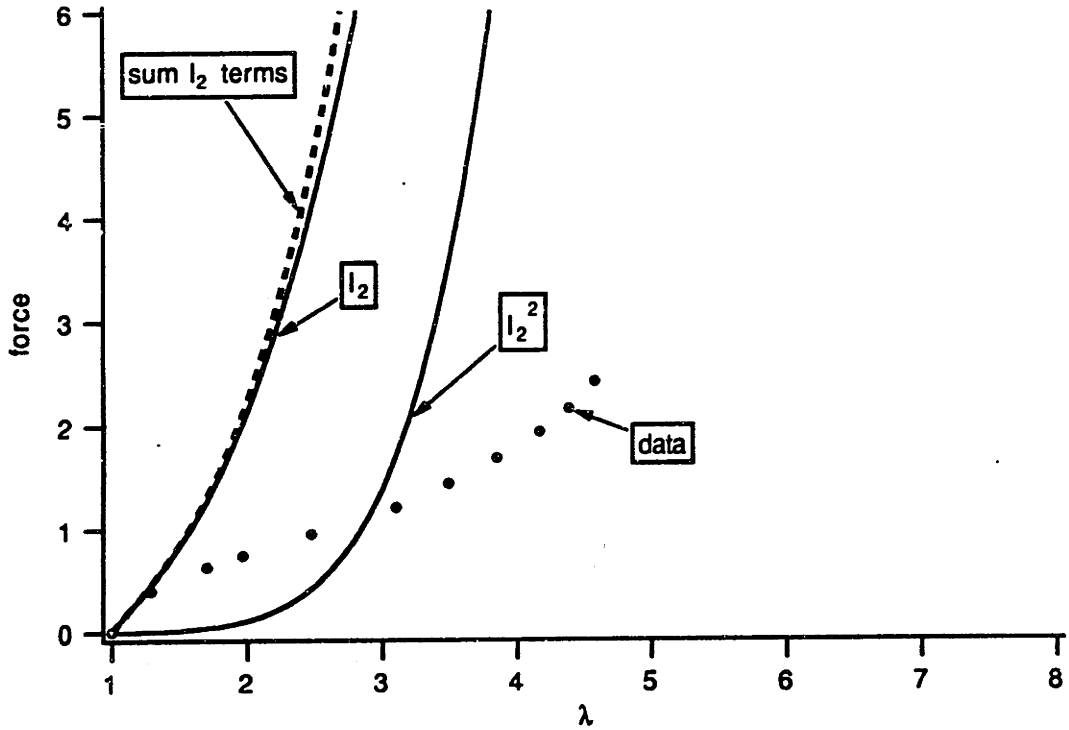

Figure B4: Predictions of first and second order I_2 terms in the eight chain strain energy expression and comparison with data for biaxial extension.